APPLIED COMPUTATIONAL ELECTROMAGNETICS SOCIETY JOURNAL

April 2022
Vol. 37 No. 4
ISSN 1054-4887

The ACES Journal is abstracted in INSPEC, in Engineering Index, DTIC, Science Citation Index Expanded, the Research Alert, and to Current Contents/Engineering, Computing & Technology.

The illustrations on the front cover have been obtained from the ARC research group at the Department of Electrical Engineering, Colorado School of Mines

Published, sold and distributed by: River Publishers, Alsbjergvej 10, 9260 Gistrup, Denmark

APRIL 2022 REVIEWERS

Hristos T. Anastassiu
Thomas Bauernfeind
Behrokh Beiranvand
Arkaprovo Das
Nebojsa Doncov
Asma Ejaz
Mohamed Hameed
Zi He
Mohamed Khalifa
Arvind Kumar
Wang-Sang Lee
Fabrizio Loreto
Daniel Marcsa
Anton Menshov
Nitin Saluja
Khalil Sayidmarie
Surinder Singh
Margarita Tecpoyotl-Torres
Hamid Torpi
Yunus Uzun
Marsellas Waller
Chao-Fu Wang
Salah I. Yahya
Shihyuan Yeh

THE APPLIED COMPUTATIONAL ELECTROMAGNETICS SOCIETY JOURNAL

Vol. 37 No. 4 April 2022

TABLE OF CONTENTS

Field Distribution Analysis Based on Improved Differential Algorithm for Dual Port Radiation Device

Shiqi Wang, Shaojun Fang, and Peng Chen

Department of Information Science and Technology
Dalian Maritime University, Dalian, Liaoning 116026, China
1609900643@qq.com, fangshj@dlmu.edu.cn, chenpeng213@126.com

***Abstract* –** With the continuous development of science and technology, the requirement of signal source is higher and higher. Single port signal source is difficult to meet experimental requirements of radiation spatial field distribution. In this paper, a dual port radiation device for changing the field distribution is proposed. The dual port radiation device is mainly composed of the DC to 6 GHz experimental radiation device, amplifier, attenuator, and the phase shifter. After adding two different excitation signals to the dual port, the field distribution of the radiation device is calculated by improved differential algorithm and simulated by CST software. The simulated results are in good agreement with the calculated results. The innovation of this research lies in the dual port and controlling the field distribution of the radiation space freely.

***Index Terms* –** Field distribution, dual port, signal source, differential algorithm.

I. INTRODUCTION

With the increasing use of electronic chips and devices, electromagnetic radiation effect and its protection have become the focus of attention [1]. Signal source plays an important role in the detection and experiment of communications as well as in the biological field of studying the effect of electromagnetic radiation on cells. Field distribution is a highly important factor to ensure the validity of test results for electromagnetic field facilities [1]. Field uniformity is also addressed and required in some standards and works [2–4]. At present, there are many kinds of signal sources designed by existing technology, but there are still some problems, such as small frequency range adjustment, high noise, power and phase adjustment, and so on. Most of them are single port signal transmission rather than dual port signal sources, which are not suitable for analyzing the internal field distribution and controlling the field pattern. Most existing sources can provide a frequency range of 30 MHz to 3 GHz and higher frequency [5–7]. In [6], a radio frequency (RF) signal source with 40–160 MHz output frequency range is designed based on direct digital frequency synthesizer (DDS). In [7], a 143.4–151.5 GHz high DC-RF efficiency signal source in CMOS is introduced. In [8], a measurement of reflection coefficient of an 8.2–12.4 GHz RF signal source is introduced. In [9], a 0.01–70 GHz ultra-wideband and high output power signal source module is applied to RF and microwave test instruments. Some studies have shown that multi-port can provide better performance and meet requirements than single port [9–11]. In [10], a dual control and dual output current source from 0 to 12 A is designed for semi-conductor laser diode to meet the high power and high stability requirements. In [11], a dual-port intermodulation generator is introduced, which can be worked at 710 and 2550 MHz. In [12], a four-port high-frequency system for a 0.14-THz dual-sheet-beam hole-grating backward-wave oscillator is presented. The published paper [13] proposed a cylindrical coaxial radiation device with single port excitation in a small size. And the field distribution is not uniform in the frequency range. In recent years, based on the research of DC to 6 GHz broadband electromagnetic radiation experimental device, the field distribution in the radiation device is studied.

Because the field distribution in the single port radiation device is not very uniform, and it is not easy to control the internal field distribution, in order to solve the above technical problems and better control the distribution and uniformity of the electromagnetic field in the DC to 6 GHz radiation device, a dual port radiation device is proposed in the article. The proposed dual port radiation device is mainly composed of the DC to 6 GHz broadband experimental radiation device, amplifier, attenuator, and the phase shifter. The dual port radiation device uses the DC to 6 GHz experimental radiation device as the carrier of electromagnetic wave. By adding two signals with different amplitude and phase to the dual port radiation device, electromagnetic fields with different power and phase can be generated in the radiation space. In this way, the electromagnetic field in the radiation space can be

Submitted On: August 8, 2021
Accepted On: March 8, 2022

https://doi.org/10.13052/2022.ACES.J.370401

freely controlled and changed to provide uniform electromagnetic field with good broadband characteristics. We use the CST Microwave Studio software to make the simulation [12–21]. Due to the large number of frequency points to be simulated, the simulation time of CST software is longer, and the memory space occupied is larger, which is not conducive to the research. Therefore, we propose an improved differential algorithm to calculate it, which saves simulation time and reduces memory space. Details of the analysis of field distribution are given and the related key parameters are discussed.

II. PRINCIPLES OF THE PROPOSED DEVICE

The configuration of the proposed dual port radiation device is shown in Figure 1. It consists of a DC to 6 GHz broadband electromagnetic radiation device, a broadband signal source, two adjustable amplifier modules, attenuators, and phase shifters. They are all controlled by a micro-controller and powered by a power supply module. It can be seen in Figure 1 that the broadband signal source generates two signals and passes through the amplifiers, attenuators, and phase shifters into signals with different power P_1, P_2 and phase φ_1, φ_2. The cell dish is 35 mm in diameter and 10 mm in height and it is used to place cells. The cell dishes are placed in the inner conductor of the electromagnetic radiation device. These two different signals are added to the dual port of the radiation device respectively. Sinusoidal source signal is used for single port excitation. We can control the output frequency of the signal source according to the input data and input the data into the microcontrollers through the keyboard. And we can control the gain of dual port adjustable gain amplifiers, such as A-way and B-way and the last dual port output of the phase shifter, respectively. There is a wave detection device that can feedback the field strength of the experimental space. The integrated phase locked loop

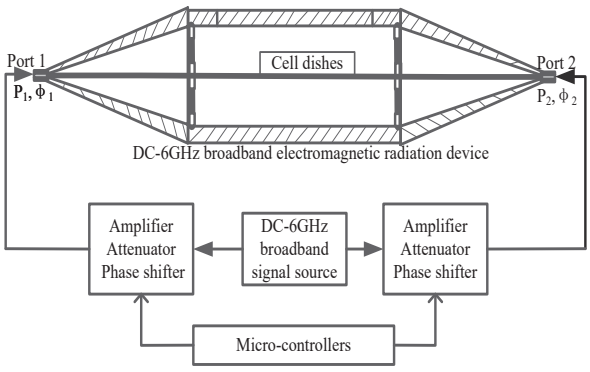

Fig. 1. Structure of a dual port radiation device.

module has the advantage of low noise characteristics and saving development time. The amplifier module uses chip-compatible variable attenuator to achieve its gain control, while the micro-controllers will connect the keyboard and screen to input the required frequency and the power. In this way, we can change the power and phase of the signal source. By adding it to the two ports of the radiation device, two broadband signals with different power and phase can be generated to change the distribution of internal electromagnetic field.

III. DIFFERENTIAL ALGORITHM ANALYSIS AND SIMULATION

A. Differential algorithm analysis

The electromagnetic field values of each discrete point in the device are different, and the degree of variation is also different [12]. The field distribution of the TEM mode is solved by the two-dimensional Laplace equations, as shown in the following equation:

$$\nabla_i^2 \varphi(x,y) = 0, \tag{1}$$

where φ is the scalar potential and ∇ is the Laplacian operator.

Given the initial value of each point, the electromagnetic field formula is analyzed and discretized, and the distribution of electric field is obtained in the following equations:

$$E_x(i,j) = \frac{\varphi_{(i-1,j)} - \varphi_{(i+1,j)}}{2\delta}, \tag{2}$$

$$E_y(i,j) = \frac{\varphi_{(i,j-1)} - \varphi_{(i,j+1)}}{2\delta}, \tag{3}$$

where E_x is the electric field in the x direction, E_y is the electric field in the y direction, and δ is the grid size.

Differential algorithm is used to calculate the electromagnetic field distribution. In the calculation process, the phase and power (amplitude) are introduced by setting the initial amplitude and phase of the input signal. And the phase and power are further calculated by iteration. The frequency set in program calculation is 6 GHz. The 3-D field distribution of single port signal source by differential algorithm is shown in Figure 2. Figure 2 (a) shows the E_x field distribution and Figure 2 (b) shows the E_y field distribution, where a is half of the cross-sectional length of outer conductor plate and b is half of the cross-sectional length of outer conductor plate. x is the position coordinate in the length direction of the cavity and y is the position coordinate in the height direction of the cavity. As can be seen from Figure 2 (a), the peak value of field strength appears at $x = 0.4a$ $y = 0.776b$, $x = 0.6a$ $y = 0.782b$, $x = 0.6a$ $y = 0.28b$, and $x = 0.4a$ $y = 0.274b$. As can be seen from Figure 2 (b), the peak value of field strength appears at $x = 0.5a$ $y = 0.992b$, $x = 0.5a$ $y = 0.504b$, and $x = 0.5a$ $y = 0.006b$.

Field distribution of single port signal source in X-Y view by differential algorithm is shown in

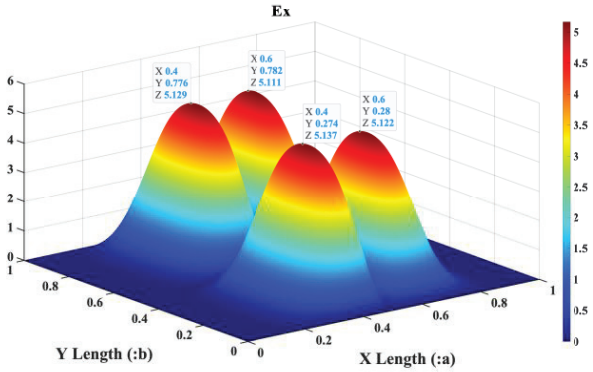

(a) E_x

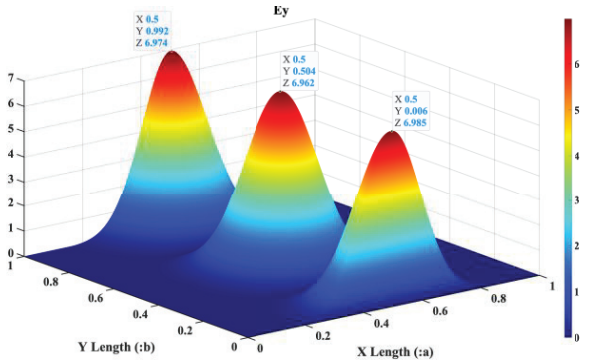

(b) E_y

Fig. 2. 3-D field distribution of single port signal source by differential algorithm.

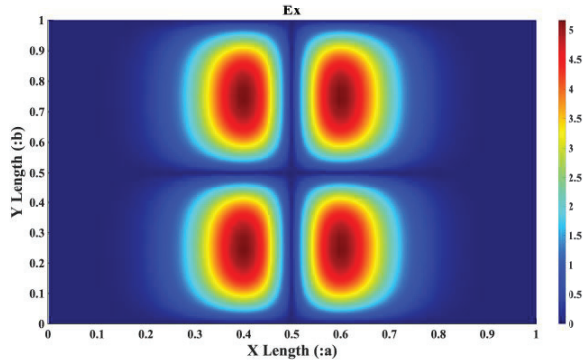

(a) E_x

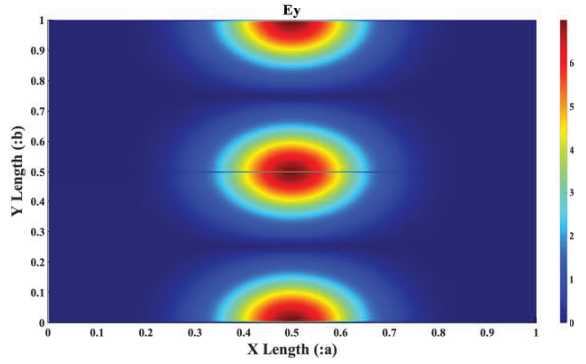

(b) E_y

Fig. 3. Field distribution of single port signal source in *X-Y* view by differential algorithm.

Figure 3. Figure 3 (a) shows the E_x field distribution and Figure 3 (b) shows the E_y field distribution. Figure 3 is the top view of Figure 2, respectively.

In order to observe the electric field distribution better, the field distribution of single port in one-dimension is shown in Figure 4. In Figure 4, the red dotted line shows the E_y field distribution and blue line shows the E_x field distribution of single port signal source in one-dimension. As can be seen from Figure 4, the peak value of E_y field strength appears at $x = 0.5a$, and the amplitude is 7. The peak value of E_x field strength appears at $x = 0.4a$ and $x = 0.6a$, and the amplitude is 5.

Figure 5 shows the field distribution of dual port in one-dimension. In Figure 5, the red dotted line shows the E_y field distribution and blue line shows the E_x field distribution of single port, the green line shows the E_y field distribution, and black dotted line shows the E_x field distribution of dual port. When the relative phase and amplitude of the dual port are changed, the E_x field distribution and E_y field distribution will also change. Because the field along the y direction is nearly unchanged, and the field along the x direction changes greatly in the

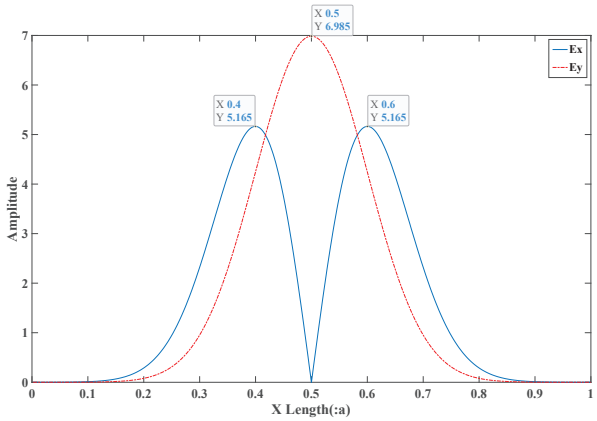

Fig. 4. Field distribution of single port signal source in one-dimension.

placement area of the radiation device, we focus on the field along the x direction.

When the amplitude is constant, the relative phase is changed and some parameters are selected, the field distribution in one-dimension is shown in Figure 5 (a), (c), (e), and (g). Figure 5 (a) illustrates that the relative phase is 90/180*pi and the relative amplitude is 1. Figure 5 (c)

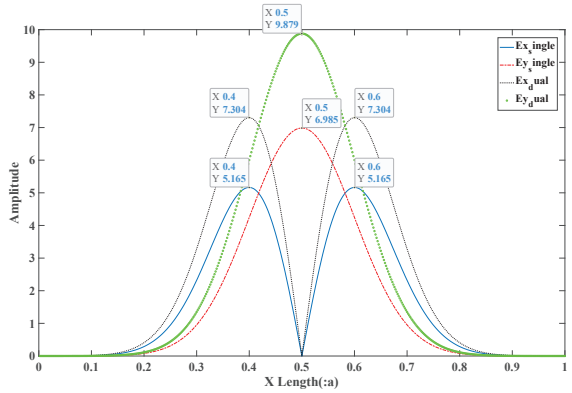

(a) Relative Phase = 90/180*pi
Relative Amplitude = 1

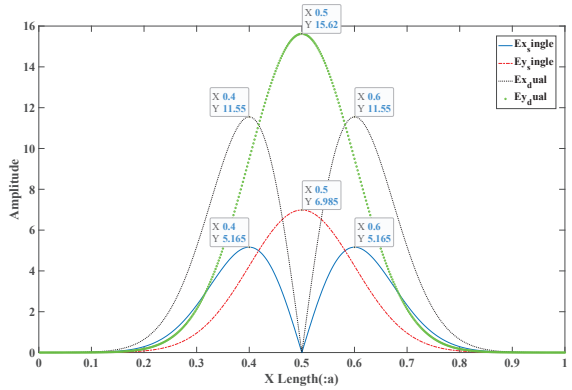

(b) Relative Phase = 90/180*pi
Relative Amplitude = 2

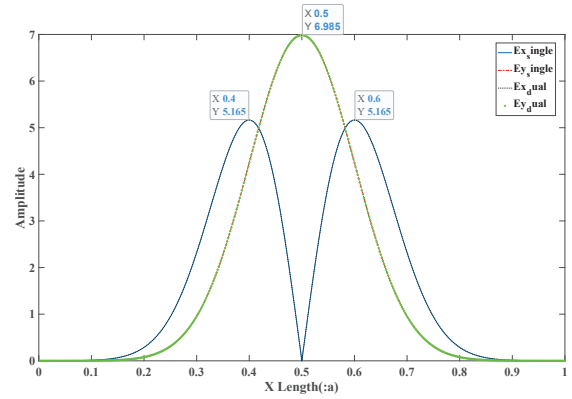

(c) Relative Phase = 120/180*pi
Relative Amplitude = 1

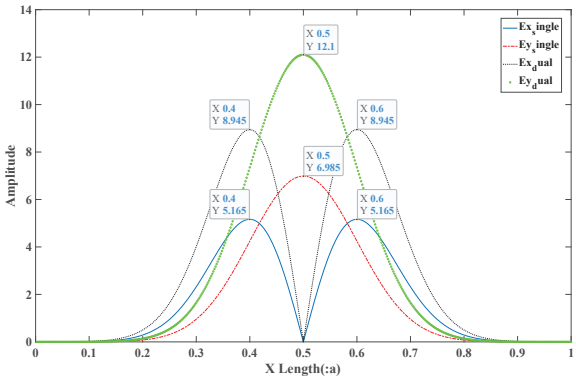

(d) Relative Phase = 120/180*pi
Relative Amplitude = 2

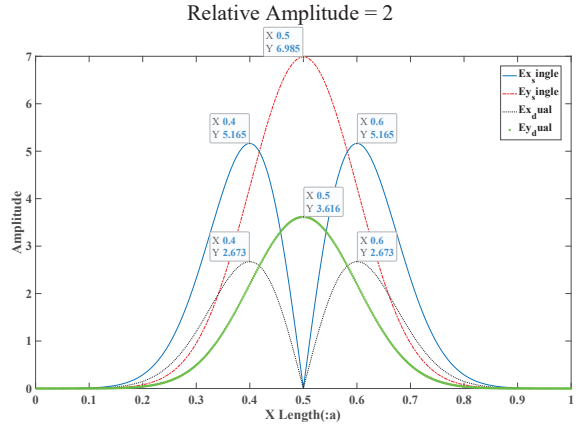

(e) Relative Phase = 210/180*pi
Relative Amplitude = 1

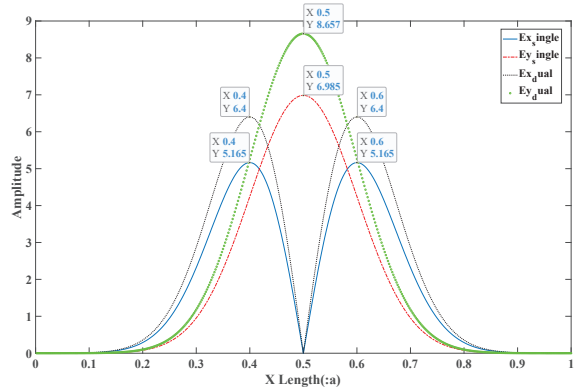

(f) Relative Phase = 210/180*pi
Relative Amplitude = 2

illustrates that the relative phase is 120/180*pi and the relative amplitude is 1. Figure 5 (e) illustrates that the relative phase is 210/180*pi and the relative amplitude is 1. And Figure 5 (g) illustrates that the relative phase is 360/180*pi and the relative amplitude is 1. When the amplitude is constant, the relative phase changes from 90/180*pi, 120/180*pi to 210/180*pi, the amplitude of E_x field and E_y field decrease by nearly half. While the relative phase changes from 210/180*pi to 360/180*pi, the amplitude of E_x field and E_y field is nearly doubled. It can be seen from the above three figures that when the relative phase changes, the amplitude of the field distribution changes periodically. The maximum amplitude is twice that of the single port.

When the phase remains constant, we change the relative amplitude and some parameters are selected,

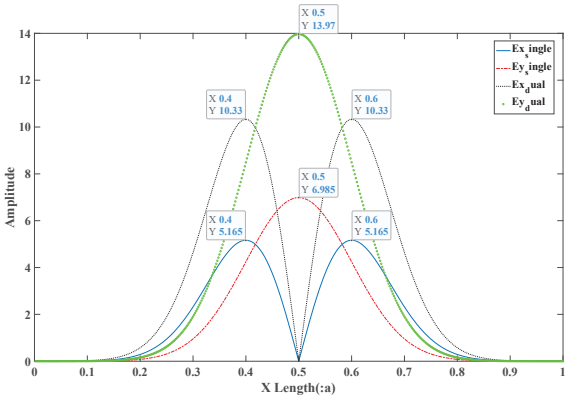

(g) Relative Phase = 360/180*pi
Relative Amplitude = 1

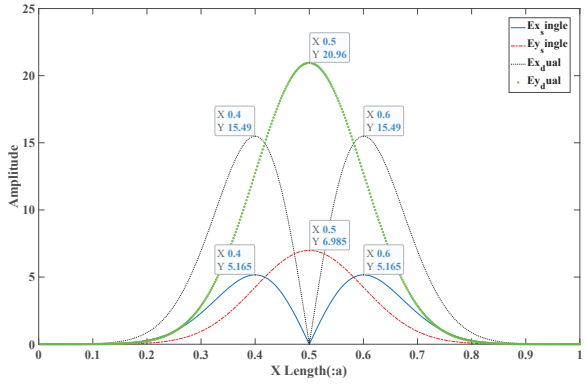

(h) Relative Phase = 360/180*pi
Relative Amplitude = 2

Fig. 5. Field distribution of dual port signal source in one-dimension when relative phase and amplitude change.

the field distribution in one-dimension is shown in Figure 5 (b), (d), (f), and (h). Figure 5 (b) illustrates that the relative phase is 90/180*pi and the relative amplitude is 2. Figure 5 (d) illustrates that the relative phase is 120/180*pi and the relative amplitude is 2. Figure 5 (f) illustrates that the relative phase is 210/180*pi and the relative amplitude is 2. And Figure 5 (h) illustrates that the relative phase is 360/180*pi and the relative amplitude is 2. Comparing Figure 5 (b), (d), (f), and (g) with (a), (c), (e), and (h), respectively, when the relative amplitude changes, the amplitude of field distribution causes corresponding changes, the relative amplitude has changed to two times the original one. And when the relative amplitude becomes twice, the amplitudes of E_x field and E_y field increase.

B. CST simulation

The commercial software CST Microwave Studio Suite TM 2013 could be used to simulate the inner field distribution of the device [22–26]. The meshing parameters of CST simulation are provided in Table 1 and the boundary conditions are PEC boundary.

Table 1: Meshing parameters of the structure

Meshing parameters	Values(mm)
Lower mesh limit	5
Min. mesh step	0.154755
Max. mesh step	0.505055
Meshcells	4,670,784

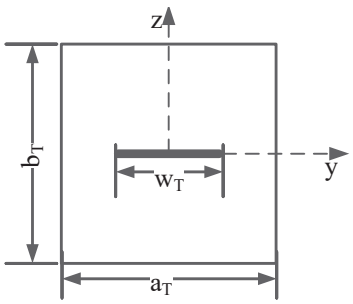

Fig. 6. Cross-sectional structure of the device.

Figure 6 illustrates the cross-sectional structure of the DC to 6 GHz wideband electromagnetic radiation device, and Table 2 lists the structural parameters in the CST simulation process. The dimensions are as follows: a_T = 20 cm, b_T = 20 cm, w_T = 13.12 cm, $L0$ = 40 cm, and $L1$ = 36.5 cm, where a_T is the cross-sectional length of outer conductor plate, b_T is the cross-sectional length of outer conductor plate, w_T is the cross-sectional width of inner conductor plate, $L0$ is the length of intermediate cavity of the device, and $L1$ is the length of conical cavity on the side. Moreover, the device has to be symmetrical and its characteristic impedance is chosen to be $Z_0 = 50\ \Omega$. The characteristic impedance of 50 Ω is provided by adjusting the ratio of the inner conductor to the outer conductor of the coaxial at the port. The reflection coefficient S_{11} is depicted in Figure 7. It depicts that the S_{11} is better than -10 dB in the frequency range of DC to 6 GHz.

When single port source was used in simulation, the other port was connected to the matching load. Field distribution of single port signal source is shown in Figure 8. Figure 8 (a) shows the E_x field distribution and Figure 8 (b) shows the E_y field distribution at 6 GHz. Figure 8 (c) shows that the electromagnetic field distribution at 3 GHz. It can be seen from Figures 3 and 8

Table 2: Simulation parameters of the structure

Structural parameters	a_T	b_T	w_T	$L0$	$L1$
Values (cm)	20	20	13.12	40	36.5

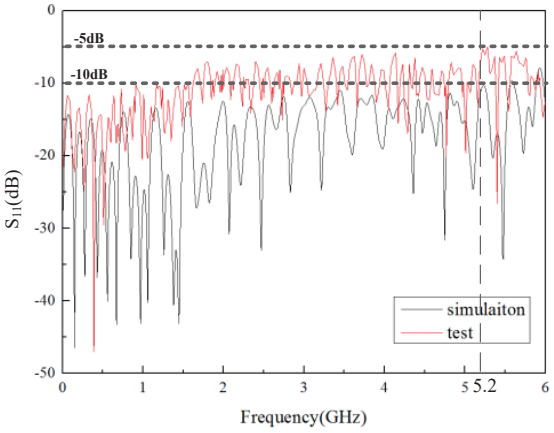

Fig. 7. Reflection coefficient S_{11} of the device.

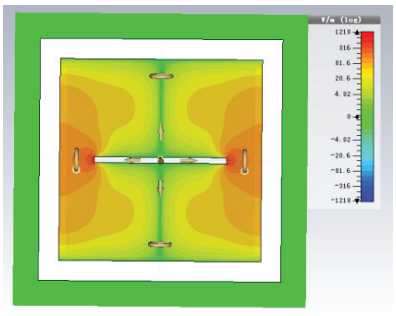

(a) E_x

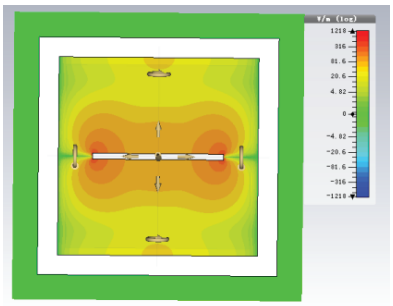

(b) E_y

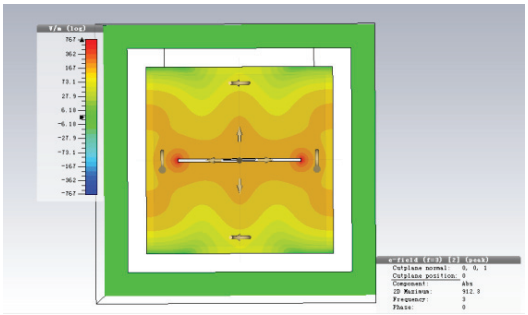

(c) Field distribution at 3 GHz

Fig. 8. Field distribution of single port signal source.

that the peak values of E_x appear on both sides, and the peak value of E_y appears in the middle. Compared with Figure 3, the simulated results are basically consistent with the calculated results, which shows that the established model is correct. From this point of view, it is consistent in Figures 3 and 8. There are some deviations between the simulated results and the calculated results in some places, which are related to the thickness error of the dielectric plate at the edge of the intermediate conductor.

When we add two different signal sources to ports of the device, the inner filed will be superimposed. Field distributions of dual port signal source are shown in Figures 9–12. Figures 9 and 10 illustrate the two different powers of the dual port signal source, which $P_2 = P_1$ in Figure 8 and $P_2 = 2 * P_1$ in Figure 10. Figure 9 (a) shows the E_x field distribution and Figure 9 (b) shows the E_y field distribution. Comparing Figure 8 with Figures 9 and 10, we can see that the strength of electromagnetic field has been superimposed on the radiation interface. Figure 11 illustrates the two different phases of the dual port signal source, which is $\phi_2 = \phi_1 - 90^\circ$. Figure 11 (a) shows the E_x field distribution and Figure 11 (b) shows the E_y field distribution. Comparing Figure 8 with Figure 11, we can see that the electromagnetic fields of

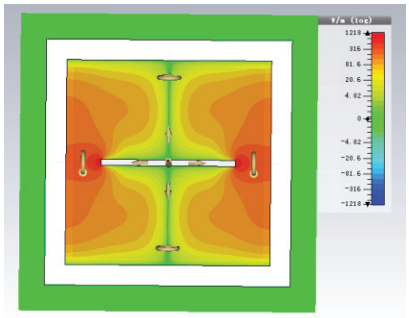

(a) E_x

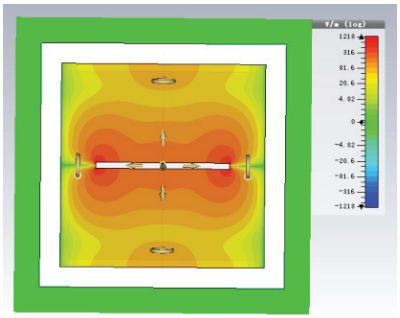

(b) E_y

Fig. 9. Field distribution of dual port signal source when $P_2 = P_1$.

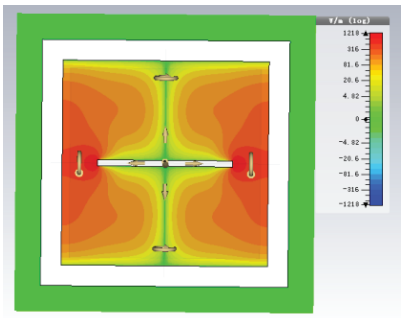

(a) E_x

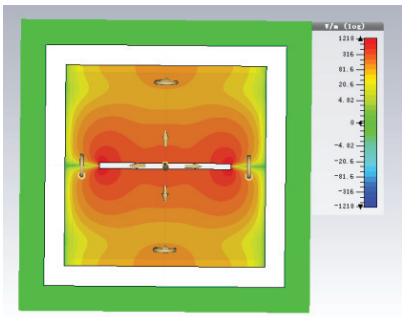

(b) E_y

Fig. 10. Field distribution of dual port signal source when $P_2 = 2 * P_1$.

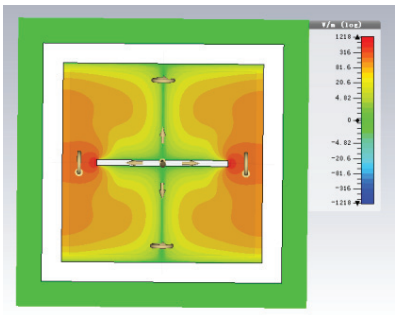

(a) E_x

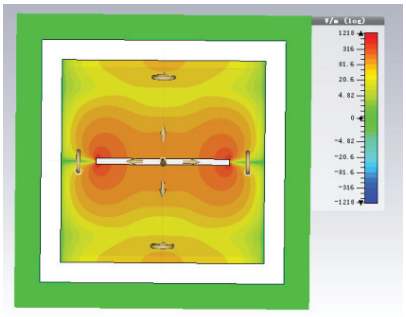

(b) E_y

Fig. 11. Field distribution of dual port signal source when $\phi_2 = \phi_1 - 90°$.

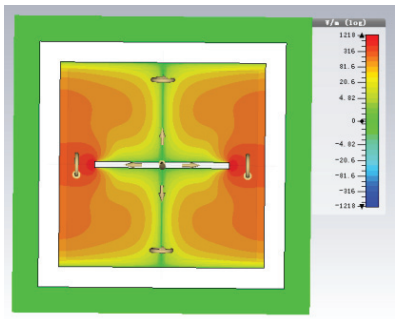

(a) E_x

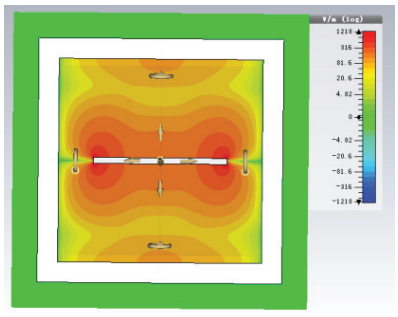

(b) E_y

Fig. 12. Field distribution of dual port signal source when $\phi_2 = \phi_1 - 90°$ and $P_2 = 2 * P_1$.

the same phase are superimposed and offset at the radiation interface. Figure 12 illustrates the two different powers of the dual port signal source, which are $P_2 = 2 * P_1$ and $\phi_2 = \phi_1 - 90°$. As can be seen from Figure 12, when we change the power of each port, the strength of electromagnetic field will be superimposed on the radiation interface. And when we change the phase of each port, the electromagnetic field will be superimposed and offset by the same phase. It can be seen from the simulated results and calculated results that the trend and results are consistent, which shows that this method is feasible. In this way, we can change and control the electromagnetic field precisely.

IV. COMPARISON OF THE SINGLE PORT DEVICE

Table 3 summarizes the performance comparison between the proposed dual port radiation device and previously reported designs for radiation experiments.

The proposed dual port radiation device shows the widest frequency range compared with other designs [17, 20] for the radiation frequency range. In the item of field distribution, the proposed dual port device can control the field distribution and ensure the uniformity of the field in the radiation space compared with [14] and [16]. In general, the proposed dual port device has

Table 3: Comparison between the proposed dual port radiation device and previously reported designs

Ref.	Structure	Frequency range (GHz)	Field distribution
[11]	Dual-port intermodulation generator	710–2550 MHz	
[12]	Four-port high-frequency system	0.14 THz	
[14]	Twin TEM cells	200 MHz	TEM
[16]	Twin TEM cells	1 GHz	TEM
[17]	TEM/GTEM cell		
[20]	Multi-step/piecewise linear TEM cell	DC to 1	TEM
This work	**Dual port device**	**DC to 6**	**Uniform TEM/TM/TE**

obvious advantages in the uniform field distribution and broadband aspect.

V. CONCLUSION

In this paper, a dual port radiation device is proposed, which can change the power and phase of the signal source. In this way, we can generate broadband signals with different power and phase to change the distribution of the electromagnetic field in the radiation space. Field distributions of the dual port radiation device for improved differential algorithm and CST simulation are provided. Its construction is given, and the related key parameters are discussed. Therefore, numerical and simulation analysis from DC to 6 GHz was carried out to define the usability of the system for well-controlled device. Based on the theoretical analysis and simulation calculations, the electromagnetic field distribution is generally shown. This characterization is assumed to be the fundamental prerequisite before considering the presence of cell dishes within the radiation device for radiation experiments of these new and widespread used telecommunication frequencies. Therefore, the proposed device can control the electromagnetic field in the radiation space. And the field distribution can be calculated with the proposed differential algorithm.

REFERENCES

[1] C. Baum, "Reminiscences of high-power electromagnetics," *IEEE Transactions on Electromagnetic Compatibility*, vol. 49, no. 2, pp. 211-218, May 2007.

[2] L. Yao, J. Huang, N. Kang, T. Shen, D. Liu, F. Zhang, and H. Sun, "Implementation of a measurement system on field uniformity of transient electromagnetic field," *IEEE Electromagnetic Compatibility Magazine*, vol. 5, no. 1, pp. 43-49, 2016.

[3] Electromagnetic Compatibility (EMC)-Part 4-3: Testing and Measurement Techniques- Radiated, Radio-Frequency, Electromagnetic Field Immunity Test, IEC 6l000-4-3: 2010, 2010.

[4] Electromagnetic Compatibility (EMC)-Part 4-20: Testing and Measurement Techniques- Emission and Immunity Testing in Transverse Electromagnetic (TEM) Waveguides, IEC61000- 4-20:2010, 2010.

[5] L. Yao, T. Shen, N. Kang, D. Liu, and J. Huang, "Time-domain simulation and measurement of a guided-wave EMP Simulator's field uniformity," *IEEE Transactions on Electromagnetic Compatibility*, vol. 55, no. 6, pp. 1187-1194, Dec. 2013.

[6] S. Chen, X. Han, and K. Chen, "The design of 40 160MHz RF signal source," *2011 International Conference on Electric Information and Control Engineering*, Wuhan, China, pp. 4598-4600, 2011.

[7] X. Meng, M. Zhou, B. Chi, and Z. Wang, "A 143.4-151.5 GHz high DC-RF efficiency signal source in 65nm CMOS," *2019 IEEE International Conference on Integrated Circuits, Technologies and Applications (ICTA)*, Chengdu, China, pp. 1-2, 2019.

[8] K. Furuya and T. Inoue, "Measurement of reflection coefficient of RF signal source using a mismatch power meter with loss-less dielectric," *Conference Digest Conference on Precision Electromagnetic Measurements*, Ottawa, Ontario, Canada, pp. 78-79, 2002.

[9] S. Zhang, G. Fan, Q. Li, and A. Zhao, "Design of a 0.01GHz–70 GHz high output power signal source module," *2017 Progress in Electromagnetics Research Symposium - Fall (PIERS - FALL)*, Singapore, pp. 2241-2246, 2017.

[10] H. Xue, Y. Che, W. Teng, Y. Ma, and L. Ge, "Design of dual control and dual output constant current source for semi-conductor laser diode," *2013 5th International Conference on Power Electronics Systems and Applications (PESA)*, Hong Kong, China, pp. 1-4, 2013.

[11] X. Chen, Y. He, and W. Cui, "Broadband Dual-Port Intermodulation Generator for Passive Intermodulation Measurements," *IEEE Microwave and Wireless Components Letters*, vol. 27, no. 5, pp. 518-520, May, 2017.

[12] X. Tang, Z. Yang, K. Khan, N. Muhammad, and Z. Ouyang, "Theoretical and cold-test investigation of a four-port high-frequency system for a 0.14-THz dual-sheet-beam backward-wave oscillator," *IEEE Transactions on Electron Devices*, vol. 65, no. 11, pp. 5068-5074, Nov. 2018.

[13] S. Wang, S. Fang, and P. Chen, "Design and research of DC-6GHz broadband electromagnetic radiation experimental device," *Journal of*

Electronics & Information Technology, vol. 41, no. 5, pp. 1092-1097, 2019.

[14] C. Zhang and J. Fu, "Research on field distribution of TEM mode in TEM cells," *Journal of Xi' An Jiaotong University*, vol. 30, no. 09, pp. 121-125, 1996.

[15] F. Dai, M. Wang, and D. Su, "A design of new twin TEM cells," *2005 IEEE International Symposium on Microwave, Antenna, Propagation and EMC Technologies for Wireless Communications,* Beijing, China, vol. 1, pp. 10-13, 2005.

[16] M. Wang, "Research of the uniformity of electromagnetic field based on FDTD method," *Journal of Guizhou University (Natural Science)*, vol. 30, no. 06, pp. 23-28, 2013.

[17] C. Song and X. Feng, "A new design and implementation of expanding testing space of a transverse electromagnetic cell," *2016 IEEE International Conference on Microwave and Millimeter Wave Technology (ICMMT)*, Beijing, China, pp. 967-969, 2016.

[18] V. Chechetkin, A. Korotkov, E. Golubenko, E. Sychugov, and P. Smirnov, "Investigation of the characteristics of the TEM cell model," *2019 Ural Symposium on Biomedical Engineering*, *Radioelectronics and Information Technology (USBEREIT),* Yekaterinburg, Russia, pp. 439-441, 2019.

[19] H. Cui, Y. Hu, and L. Pang, "Calculation and verification of uniform electromagnetic field for cell culture," *Tianjin society of Biomedical Engineering*, vol. 61, 2010.

[20] L. Yao, T. Shen, N. Kang, J. Huang, D. Liu, F. Zhang, and H. Sun, "Use of a reference point method to calibrate the field uniformity when testing with transient electromagnetic fields," *IEEE Transactions on Electromagnetic Compatibility*, vol. 59, no. 2, pp. 352-359, 2017.

[21] M. Arezoomand, M. Meybodi, and N. Noori, "Design of a TEM cell using both multi-step and piecewise linear tapering," 2016 8th International Symposium on Telecommunications (IST), Tehran, Iran, pp. 571-574, 2016.

[22] Z. Chen, Y. Deng, and D. Deng, "Research on field uniformity calibration method of GTEM cell," *Safety&EMC*, vol. 3, pp. 42-44+77, 2013.

[23] W. Zhang and Y. Cao, "Research and simulation analysis on radio propagation model in electromagnetic environment simulation," *Chinese Journal of Radio Science*, vol. 27, no. 3, pp. 538-542+550, 2012.

[24] W. Ju, Study on the critical frequency and the cause of higher order modes in the GTEM Cell [D]. Southeast University, 2016.

[25] G. Zhao, Q. Liu, and J. Wang, "Homogenization of microwave field in rectangular resonator," *Science & Technology Vision*, vol. 18, pp. 24+44, 2016.

[26] V. Sebera, A. Nasswettrová, and K. Nikl, "Finite element analysis of mode stirrer impact on electric field uniformity in a microwave applicator," *Drying Technology*, vol. 30, no. 13, pp. 1388-1396, 2012.

Shiqi Wang was born in Shenyang, China. She received the B.Eng. and M.Eng. degrees in information and communication engineering from Dalian Maritime University, Liaoning, China, in 2014 and 2017, respectively. She is currently working toward the Ph.D. degree with the Dalian Maritime University.

Her current research interests include wideband electromagnetic field, bioelectromagnetics, and optimization method.

Shaojun Fang received the Ph.D. degree in communication and information systems from Dalian Maritime University (DLMU), Liaoning, China, in 2001.

Since 1982, he has been with DLMU, where he is currently the Head Professor with the School of Information Science and Technology. His recent research interests include passive RF components, patch antennas, and computational electromagnetics. He has authored or coauthored three books and over 100 journal and conference papers. He was a recipient of the Best Doctor's Dissertation Award of Liaoning Province in 2002 and the Outstanding Teacher Award of the Ministry of Transport of China.

Peng Chen received the Ph.D. degree in communication and information systems from Dalian Maritime University (DLMU), Liaoning, China, in 2007.

He is currently an Associate Professor with the School of Information Science and Technology, DLMU. His current research interests include wireless sensor network, ultra-broadband wireless communication technology, and antenna.

Complementary Frequency Selective Surface with Polarization Selective Responses

Jian Jiao[1], Nianxi Xu[2], and Jinsong Gao[3]

[1]School of Physics
Changchun Normal University, Changchun 130032, China
xinhe7hl@126.com

[2]Key Laboratory of Optical System Advanced Manufacturing Technology
Changchun Institute of Optics, Fine Mechanics and Physics, Chinese Academy of Sciences, Changchun 130033, China xnxlzhy999@126.com

[3]Jilin Provincial Key Laboratory of Advanced Optoelectronic Equipment and Instruments Manufacturing Technologies, Changchun 130033, China gaojs@ciomp.ac.cn

Abstract – This paper reports the design and electromagnetic performance of a new complementary frequency selective surface (CFSS) which shows polarization selectivity and good angular stability. Each CFSS unit cell only consists of a thin substrate sandwiched by a square patch array and its complementary square slot array with lateral displacement. The polarization selectivity of the proposed CFSS is determined by the displacement introduced between two arrays. An equivalent circuit model has been developed for this structure to interpret its polarization selective feature. The CFSS structure has been analyzed with full-wave simulation. The polarization selectivity of the proposed structure was verified by experiment.

Index Terms – Frequency selective surface (FSS), complementary screen, polarization selective surface (PSS).

I. INTRODUCTION

Frequency selective surfaces (FSSs) are two-dimensional periodic arrays that have been widely used in a lot of applications, such as various microwave systems and antenna radomes [1, 2]. The FSSs with polarization selective response are called polarization selective surfaces (PSSs). The polarization selectivity is significant to anti-interference performance and detection capability. The PSSs are important in antenna applications and can be used in many fields, such as polarimetric imagining radars and communication satellites [3, 4].

There are so many ways to achieve linear polarizer. One classic way is to use parallel metal strip structure [5]. But its bandwidth should be widened by adding more layers. Some other linear polarizers are obtained by well-designed FSS structure [6]. Complementary frequency selective surface (CFSS) has many advantages in designing polarizer, such as good angular stability, low profile, and easy fabrication [7].

In this work, an alternative design of PSS based on CFSS structure is proposed. The PSS consists of a square patch array and a complementary square slot array separated by a thin substrate. An important parameter lateral displacement *DSX* is introduced. Its geometry and frequency responses are presented and explained from the circuit point of view. The measured transmissions, including normal and oblique incidence, are obtained. It is indicated that the proposed CFSS structure has polarization selectivity and its filtering performance is insensitive to the variation of the incident angle of illuminated wave. Polarization selectivity, low profile, and light weight make it a promising application in metamaterial polarizers on curved surfaces.

II. CFSS DESIGN AND CIRCUIT ANALYSIS SECTION FORMATTING

A. Design description

The proposed CFSS has two printed layers separated by a very thin dielectric substrate. On the top surface, there is a 2-D periodic array of metallic square patches, and on the bottom, there is a 2-D periodic array of complementary square slots. Figures 1 (a) and (b) show the unit cell of the proposed CFSS structure and its physical parameters. The period of the unit cell is $Dx = Dy = D$, and the length of square patch and slot is L. An important parameter, lateral displacement *DSX* along the x-axis, is introduced. And there is no lateral displacement *DSY* along the y-axis ($DSY = 0$) as shown in Figure 1 (a). That means the center of the square patch is shifted by *DSX*, along the x-axis, relative to the center of the square slot. Here, let $DSX = D/2$ in this work. Figure 1 (c) shows the

Submitted On: October 24, 2020
Accepted On: April 4, 2022

https://doi.org/10.13052/2022.ACES.J.370402

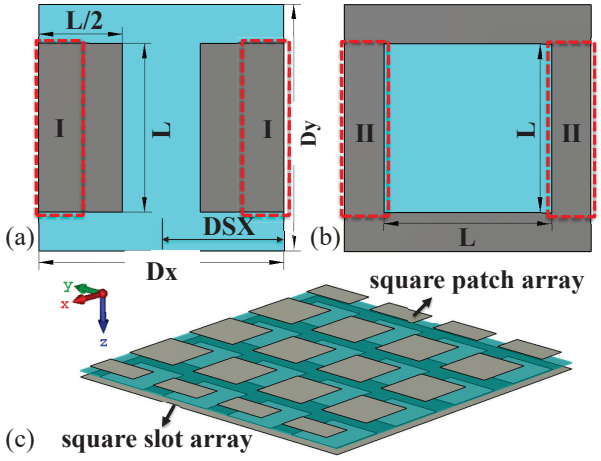

Fig. 1. The unit cell of the proposed CFSS design. (a) The unit cell of square patch array. (b) The unit cell of square slot array. (c) The topology of the proposed CFSS (3-D view). The inset in (c) is the coordinated system.

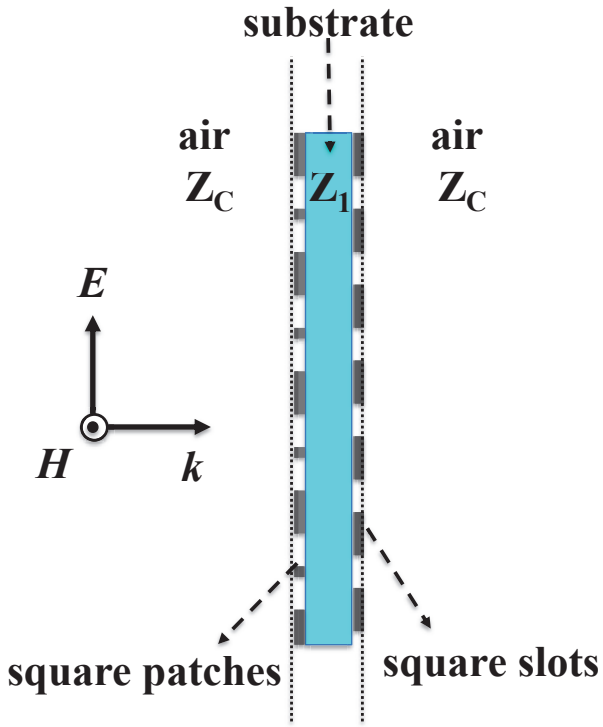

Fig. 2. Side view of the proposed CFSS array.

3-D view of the proposed CFSS array. The side view of the proposed CFSS array is shown in Figure 2.

B. Circuit analysis

We define that TE-polarization is that the incident *E*-field is parallel to the *y*-axis and that of TM-polarization is parallel to the *x*-axis. Figure 3 shows the plane view

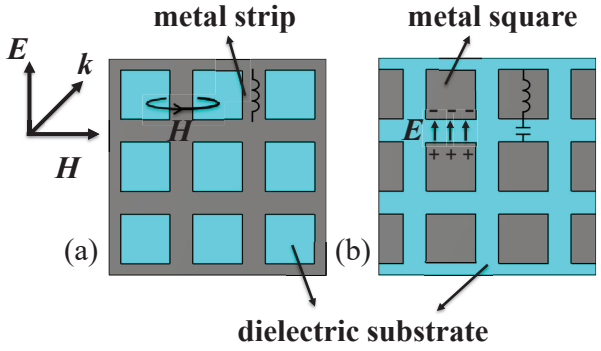

Fig. 3. Plan view of the proposed CFSS array and their equivalent circuit. (a) The square slot array. (b) The square patch array.

of the proposed CFSS illuminated by the TE polarized plane wave. The metallic strip of square slot array that acts as an inductor for magnetic field is perpendicular to the wire as shown in Figure 3 (a). Capacitance formed between the adjacent edges of two coplanar square patches and inductance is associated with square patch. Thus, the square patch array interacts with *E*-field and behaves as a series *LC* circuit as shown in Figure 3 (b) [8]. The substrate between square patches and square slots can be considered as a short transmission line. Hence, the proposed CFSS is equivalent to a parallel combination of inductor and a series *LC* circuit, as shown in Figure 4, where Z_C is the intrinsic impedance of air and Z_1 is the intrinsic impedance of the dielectric substrate. The thickness of the substrate *d* is relatively small, and its equivalent transmission line could be neglected in this work. The different transmission responses to TE- and TM-polarization incidence account for the electromagnetic coupling that occurs between square patches and square slots.

When a TE-polarized plane wave normally impinges on the composed CFSS structure, a strong coupling occurs around the metallic overlap area between I and II as shown in Figures 1 (a) and (b), which can be proved by the electric field distribution of square patch array and slot array at the resonance peaks shown in Figures 5 (a) and (b) where the *E*-field is concentrated on the overlap area.

The magnetic field induced by the current flowing on the square patch encircles the patch itself; hence, a portion of that field couples through the strips of the slot array because of overlap. Meanwhile, the current on the strips of square slot array produces a magnetic field that couples to the square patches. The mutual coupling between two layers is modeled as the mutual inductance as shown in Figure 4 (a) [9]. According to the transmission line and circuit theory, the CFSS sheet impedance

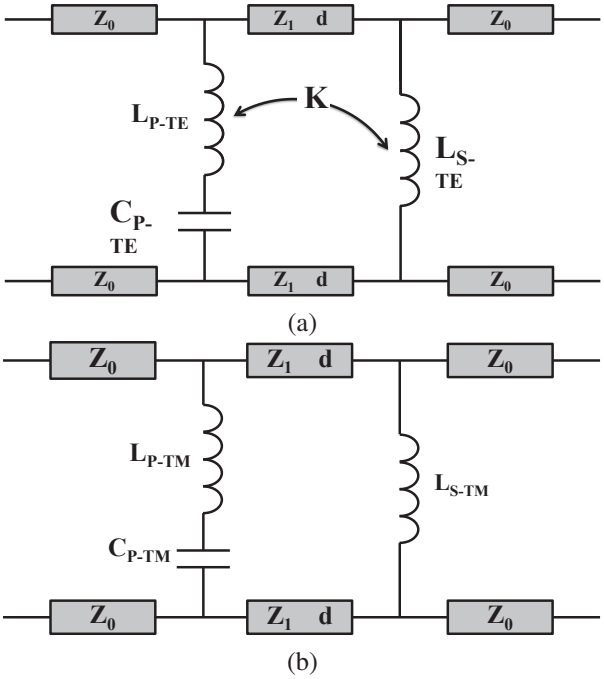

Fig. 4. The equivalent circuit model of the proposed CFSS. (a) TE wave incidence. (b) TM wave incidence.

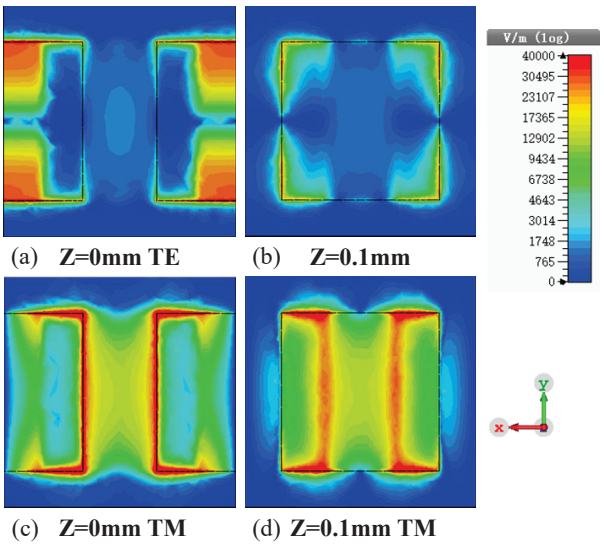

Fig. 5. The electric field distribution of the proposed CFSS at 24.5 GHz. (a) TE mode, the electric field distribution of square patch array. (b) TE mode, the electric field distribution of square slot array. (c) TM mode, the electric field distribution of square patch array. (d) TM mode, the electric field distribution of square slot array.

Z can be found as follows:

$$Z=\frac{j\omega L'_{s-\mathrm{TE}}\left(\frac{1}{j\omega C_{p-\mathrm{TM}}}+j\omega L'_{p-\mathrm{TE}}\right)}{\frac{1}{j\omega C_{p-\mathrm{TE}}}+j\omega L'_{p-\mathrm{TE}}+j\omega L'_{s-\mathrm{TE}}}+j\omega K. \quad (1)$$

Hence, the transmission zero frequency of the proposed CFSS in the TE-polarization case [10] is

$$\omega_{\mathrm{TE-null}}=\frac{1}{\sqrt{C_{p-\mathrm{TE}}\left(L_{p-\mathrm{TE}}-\frac{M^2}{L_{s-\mathrm{TE}}}\right)}}, \quad (2)$$

where $L'_{p-\mathrm{TE}}=L_{p-\mathrm{TE}}-M$, $L'_{s-\mathrm{TE}}=L_{s-\mathrm{TE}}-M$, and M is the mutual inductance.

When a TM-polarized plane wave normally incidents on the proposed CFSS, a weak coupling occurs between square patches and square slots. EM coupling between two layers can directly lead to the change of electromagnetic field distribution, which can be manifested by the electric field distribution at resonance shown in Figures 5 (c) and (d) where the E-field is concentrated on the gap between two square patches. The magnetic field induced by the current on the strips of square slot array is weak, and couples little to the patches, and vice versa. The coupling between the two complementary arrays would be ignored in this work as shown in Figure 4 (b). The CFSS sheet impedance Z can be found as follows:

$$Z=\frac{j\omega L_{s-\mathrm{TM}}\left(\frac{1}{j\omega C_{p-\mathrm{TM}}}+j\omega L_{p-\mathrm{TM}}\right)}{\frac{1}{j\omega C_{p-\mathrm{TM}}}+j\omega L_{p-\mathrm{TM}}+j\omega L_{s-\mathrm{TM}}}. \quad (3)$$

Hence, the resonant frequency of the proposed CFSS in the TM-polarization case [10] is

$$\omega_{\mathrm{TM-peak}}=\frac{1}{\sqrt{C_{p-\mathrm{TM}}\left(L_{p-\mathrm{TM}}+L_{s-\mathrm{TM}}\right)}}. \quad (4)$$

All the parameters, such as DSX, D, L, as well as the thickness and permittivity of the dielectric substrate, determine the performance of the CFSS. Optimizing the structure and adjusting the coupling K make the transmission peak of TM-polarization equal to the transmission null of TE-polarization, that is,

$$\omega_{\mathrm{TM-peak}}=\omega_{\mathrm{TE-null}}, \quad (5)$$

where the CFSS shows polarization selective performance with a certain bandwidth.

The transmission coefficient of the proposed CFSS can be achieved by the following expression:

$$T=\frac{2Z_{\mathrm{CFSS}}}{2Z_{\mathrm{CFSS}}+Z_C}, \quad (6)$$

where Z_{CFSS} is the impedance of the proposed CFSS structure.

A semi-analytic method is used to compute the values of the equivalent circuit parameters from the simulation. First, the transmission coefficient is obtained numerically by EM simulation, where commercial CST Microwave Studio is used in this work. Second, the least square method is applied to extract the equivalent lumped parameters of the equivalent circuit. Finally, the advanced design system (ADS) is used to test the extracted lumped parameters [11].

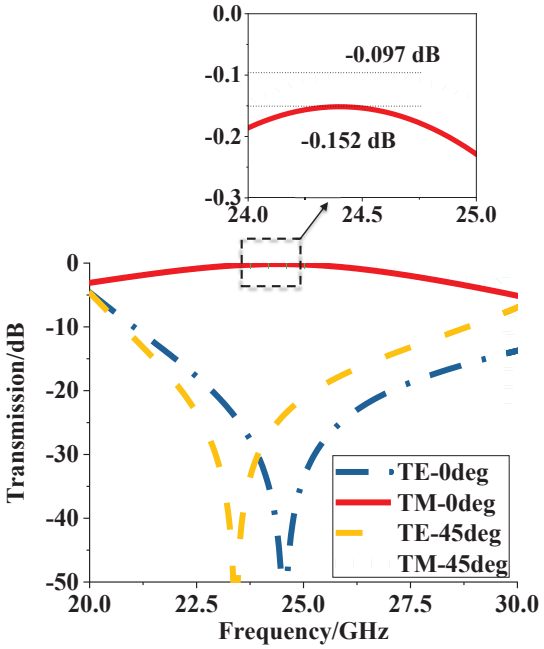

Fig. 6. The transmission responses of the CFSS.

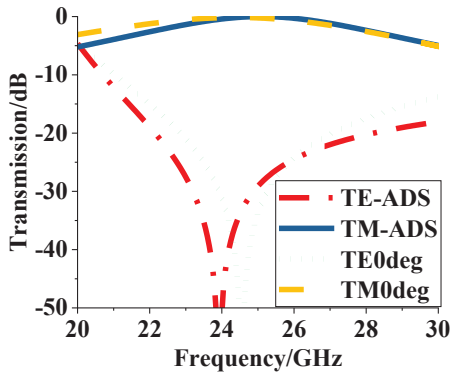

Fig. 7. Transmission of the equivalent circuit and CFSS structure.

III. SIMULATION RESULTS

In order to verify our design, a full-wave analysis of the CFSS is performed using the commercial CST Microwave Studio. The parameters of an optimized CFSS design are D = 6 mm, L = 4.1 mm, and DSX = 3 mm. A thin dielectric substrate, with thickness of 0.1 mm and permittivity of 3, is sandwiched between the two complementary arrays. And its transmission responses of normal incidence and 45° incident angle for both polarizations are plotted in Figure 6. It is shown that the proposed CFSS has polarization selectivity and angular stability between 22.5 and 27.5 GHz.

The equivalent lumped parameters of the proposed CFSS are calculated with the semi-analytic method

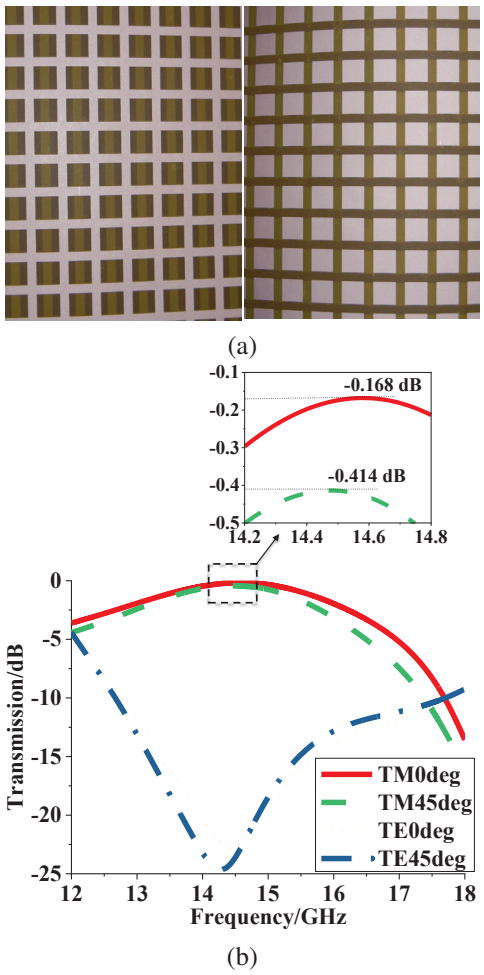

Fig. 8. (a) The CFSS prototype. (b) Its measured transmission responses.

described in Section II-B. The extracted parameters are L_{p-TE}= 212.64 pH, L_{s-TE}= 318.5 pH, C_{p-TE}= 0.3778 pF, K = 0.67, L_{p-TM}= 101.68 pH, L_{s-TM}= 410.18 pH, and C_{p-TM}= 0.0786 pF. The results of the equivalent circuit using ADS and EM simulation results using CST are plotted in Figure 7, in which the simulated results are in good agreement.

IV. EXPERIMENTAL VERIFICATION

A prototype was fabricated and its transmission responses were measured to validate the polarization selective performance. The parameters of the prototypes were re-optimized as L = 7.1875 mm and $Dx = Dy$ = 10 mm under the limitation that the measuring range available to us is 12-18 GHz. Each array was printed on a thin polyimide with a thickness of 0.0254 mm, a dielectric constant of 3, and a loss tangent of 0.005. They were aligned and combined by a layer of EVA glue with a thickness of 0.045 mm, a dielectric constant of 3, and

a loss tangent of 0.005. An Agilent N5224A vector analyzer and two horn antennas were used to measure the 400 mm $\times$ 400 mm CFSS prototype shown in Figure 8 (a). The left is the square slot array and the right is the square patch array. The measured transmission responses of normal incidence and an oblique incidence angle of 45° are plotted in Figure 8 (b). It indicates that the proposed CFSS has polarization selectivity and angular stability.

V. CONCLUSION

In this paper, we propose a new CFSS structure with polarization selectivity and angular stability. The structure is based on the idea of using electromagnetic coupling to make the transmission peak of one polarization wave coincide with the transmission null of the orthogonal polarization wave. The circuit analysis is used to explain its filtering mechanism. A prototype of the proposed CFSS has been fabricated and its performance has been verified through experiment. It could be applied in various polarizer applications.

ACKNOWLEDGMENT

The authors would like to acknowledge the support by the Natural Science Foundation of Changchun Normal University (Grant No. 004[2019]) and Changchun Normal University Doctoral Research Fund (Grant No. 001[2020]BS).

REFERENCES

[1] M. S. Samani, R. S. Shirazi, and G. Moradi, "Multi-band frequency selective surface design based on idea of clusters in cellular communication systems," *Applied Computational Electromagnetic Society (ACES) Journal*, vol. 30, no. 10, pp. 1079-1082, Oct. 2015.

[2] S. H. Wen and H. Y. Chen. "Design of a Jerusalem-cross slot antenna for wireless internet applications," *Applied Computational Electromagnetic Society (ACES) Journal*, vol. 33, no. 1, pp. 15-22, Jan. 2018.

[3] L. W. Guo, S. M. Li, X. Jiang, X. Liao, and L. Peng, "Ultra-wideband transmissive linear polarization device based on graphene," *Applied Computational Electromagnetic Society (ACES) Journal*, vol. 36, no. 7, pp. 914-921, Oct. 2021.

[4] B. Lin, W. Huang, L. Lv, J. Guo, Z. Wang, and R. Zhu, "Second-order polarization rotating frequency-selective surface," *IEEE Transactions on Antennas and Propagation*, vol. 69, no. 11, pp. 7976-7981, Nov. 2021.

[5] M. Joyal and J. Laurin, "A cascaded circular-polarization-selective surface at K band," 2011 *IEEE International Symposium on Antennas and Propagation (APSURSI), Spokane, WA*, pp. 2657-2660, Jul. 2011.

[6] X. Wu, Z. B. Pei, S. B. Qu, Z. Xu, P. Bai, J. F. Wang, X. H. Wang, and H. Zhou, "Design of metamaterial frequency selective surface with polarization selectivity," *Acta Phys. Sin.*, vol. 60, no. 11, pp. 279-283, Nov. 2011.

[7] J. Jiao, N. X. Xu, X. G. Feng, F. C. Liang, J. L. Zhao, and J. S. Gao, "Design and study of the active frequency selective surface based on the complementary screen," *Acta Phys. Sin.*, vol. 62, no. 16, pp. 364-369, Jul. 2013.

[8] K. Sarabandi and N. Behdad, "A frequency selective surface with miniaturized elements," *IEEE Trans. Antennas Propag.*, vol. 55, no. 5, pp. 1239-1245, May 2007.

[9] F. Bayatpur and K. Sarabandi, "Multipole spatial filters using metamaterial-base miniaturized-element frequency selective surfaces," *IEEE Trans. Microw. Theory Tech.*, vol. 56, no. 12, pp. 2742-2747, Nov. 2008.

[10] M. Moallem and K. Sarabandi, "Miniaturized element frequency selective surfaces for millimeter-wave to terahertz applications," *IEEE Trans. Terahertz Science Tech.*, vol. 2, no. 3, pp. 333-339, May 2012.

[11] H. A. Atallah, M. Alzubi, R. Hussein, and A. B. Abdlerhman, "Design of dual frequency coupled resonators using DGS and microstrip resonators for dual band WPT applications," *Applied Computational Electromagnetic Society (ACES) Journal*, vol. 36, no. 1, pp. 75-81, Jan. 2021.

Jian Jiao received the Ph.D. degree in optics from the Changchun Institute of Optics, Fine Mechanics and Physics, Chinese Academy of Sciences, China, in 2015.

She joined the School of Physics, Changchun Normal University, China, in 2019. Her research interests include frequency selective surface, and artificial electromagnetic material.

Nianxi Xu received the Ph.D. degree in optics from the Changchun Institute of Optics, Fine Mechanics and Physics, Chinese Academy of Sciences, China, in 2012.

He joined Key Laboratory of Optical System Advanced Manufacturing Technology Changchun Institute of Optics, Fine Mechanics and Physics, Chinese Academy of Sciences, China, in 2012. His research interests include frequency selective surface and functional thin films.

Jinsong Gao received the Ph.D. degree in optics from the Changchun Institute of Optics, Fine Mechanics and Physics, Chinese Academy of Sciences, China, in 2005. He was the Director of Key Laboratory of Optical System Advanced Manufacturing Technology Changchun Institute of Optics, Fine Mechanics and Physics, Chinese Academy of Sciences, China, from 2008 to 2017. He has been the Director of Jilin Provincial Key Laboratory of Advanced Optoelectronic Equipment and Instruments Manufacturing Technologies since 2017. His research interests include optical thin films, frequency selective surface, and functional thin films.

The Spatial Distributions of Radiation Emitted from a Sinusoidal Current Filament and a Dipole Antenna

Edmund K. Miller

Los Alamos National Laboratory (Retired)
e.miller@ieee.org

***Abstract* –** While the analytical and numerical tools for determining the basic properties of a variety of antenna types have been long-established, there remains some continuing curiosity about how electromagnetic radiation is launched by such a simple antenna as a dipole. The following article discusses this problem in both the frequency domain and time domain. The sinusoidal current filament (SCF) is investigated first as a prototype of a wire dipole. The length-wise distribution of radiated power for the SCF is obtained from the distributed radiation resistance of Schelkunoff and Feldman, the induced electromotive force (IEMF) method, and the far-field analysis of radiation sources (FARS) developed by the author.

The FARS approach is next used to analyze a frequency-domain numerical model of a dipole antenna, producing results similar to those for the SCF for a dipole of near-zero radius. Differentiating the decaying on-surface Poynting vector (PV) produces results comparable to those from FARS to explicitly demonstrate the power loss caused by radiation of the propagating current and charge. The lobed distributed radiated power is shown to be closely correlated with the square of the dipole current, confirming the cause of the radiation to be due to a partially reflected charge as the current and charge form standing waves on the dipole. Application of a time-domain version of FARS yields a smoothed length-wise distribution of radiated energy as opposed to the lobed variation of the frequency domain.

***Index Terms* –** Charge reflection, dipole radiation, differentiated Poynting vector (DPV), distributed radiation resistance, far-field analysis of radiation sources, IEMF method, NEC, Poynting vector, sinusoidal current filament, TWTD.

I. INTRODUCTION

How electromagnetic fields are radiated from such a simple antenna as a wire dipole seems to have been periodically revisited over the years. Perhaps, the first discussion related to this problem is due to Poynting who introduced the concept of electromagnetic power flow with a vector that bears his name. Streamline plots of Poynting vectors (PVs) near a dipole reveal the flow of power from the feedpoint along the antenna where they successively leave the antenna to become far-field radiation [1]. Computation of the power flow along the antenna exhibits a monotonic decrease down the arms of the dipole to its ends where the charge is reflected and the current becomes zero.

While the PV streamlines reveal a tantalizing image of power flow extending from the antenna feedpoint to the far field, their interpretation can be misleading. If the streamlines are constructed such that each represents the same amount of power flow, each will reach a different point on the far-field sphere with their angular separation dependent on the radiation pattern. Tracing them back to the dipole itself, each seems to bend away from it along its length at a different location. This might be interpreted to mean that a given angular steradian on the far-field sphere receives its power solely from a particular and different area of the antenna.

But numerical evaluation of the electric and magnetic fields around the antenna at any specific angle and distance involves integrating over its entire surface. This implies, to the contrary, that the charge and current distribution over the entire antenna potentially have some effect on the radiation at any given location in the far field. These two observations cannot both be true. Thus, some other interpretation is needed to establish the quantitative origin of where and how radiated power originates from over the antenna. The purpose of the following discussion is to provide some different ways of doing so. Two different but related kinds of radiating sources are considered: the sinusoidal current filament (SCF) and a dipole antenna consisting of a perfect electric conductor (PEC). This paper is motivated in part by a recent article by Jackson [1] who referred to the radiation emitted by a dipole antenna saying it somehow "ultimately shakes free" as the current propagates down its length.

The following discussion provides physical and computational demonstrations for how, why, and where the radiated power leaves, or shakes free, from the

Submitted On: January 4, 2022
Accepted On: May 5, 2022

https://doi.org/10.13052/2022.ACES.J.370403

dipole. This is done using various analytical procedures to determine the radiated-power density on a per-unit-length basis. The dipole results are obtained using Numerical Electromagnetics Code (NEC) [2], a well-validated computer model based on the thin-wire electric-field integral equation solved using the method of moments [3]. The moment method, widely used in the engineering electromagnetics community, involves sampling an unknown source such as a current distribution using basis functions and sampling boundary conditions using testing functions. While this procedure is representative of any electromagnetic numerical model, whether formulated using the differential or integral forms of Maxwell's equations, it has come to be typically associated with an integral-equation formulation.

While modeling linear objects such as wires, 6-10 samples per wavelength usually provide acceptably accurate results, the numerical results that follow use 20 samples per wavelength. This higher sampling rate is used for both the SCF and NEC dipole to ensure an acceptable accuracy for the far-field results and for their numerical comparisons. Note that the spatial density of the emitted radiated power in the frequency domain (FD) or radiated energy in the time domain (TD) can be expressed in two ways. One is on a per wavelength basis (FD) or on a per segment basis for either domain. The total power or energy can conveniently be normalized to 1 W or 1 J, respectively.

II. THE SINUSOIDAL CURRENT FILAMENT

The SCF has served as a surrogate for a wire antenna in the pre-computer era. It has the advantage of having closed-form expressions for its near and far fields and it closely approximates the current on an actual PEC thin-wire dipole. In a 1942 article [4], Schelkunoff and Feldman introduced the concept of a distributed radiation resistance, $R_{rad,SF}(x)$. Their analysis used the SCF as an analytical model

$$I(x) = I_o \sin\left[k\left(L - |x|\right)\right], -L \le x \le L, \tag{1}$$

while conducting experimental measurements to confirm their results using a wire antenna. They derived an expression for $R_{rad,SF}$ given by

$$R_{\mathrm{rad,SF}}(x) = \frac{60L}{L^2 - x^2}, \tag{2}$$

where they restricted the length $2L$ of the antenna to an integral number of half-wavelengths and the feedpoint is at a current antinode. Further examination of their work [3] shows that eqn (1) can be generalized to

$$R_{\mathrm{rad,SF}}(x) = 30\frac{1}{\sin\beta\left(L - |x|\right)} \left[\frac{\sin\beta\left(L-x\right)}{L-x} - 2\frac{\sin\beta x}{x}\cos\beta L + \frac{\sin\beta\left(L+x\right)}{L+x}\right]. \tag{3}$$

The radiated-power density is then given by

$$p_{\mathrm{rad}}(x) = \frac{1}{2}I^2(x)R_{\mathrm{rad,SF}}(x) = 15I(x)\left[\frac{\sin\beta\left(L-x\right)}{L-x} - 2\frac{\sin\beta x}{x}\cos\beta L + \frac{\sin\beta\left(L+x\right)}{L+x}\right]. \tag{4a}$$

In the following discussion, both the SCF and wire dipoles are divided into N equal-length segments for numerical purposes using the method of moments [3]. The radiated power per segment of an SCF having N segments of length $2L/N$ is then

$$p_{\mathrm{rad/seg}}(x_i) = \frac{1}{2}I^2(x_i)R_{\mathrm{rad,SF}}(x_i)\Delta x, \tag{4b}$$

where Δx is the segment length. This expression provides a useful confirmation for two other methods described below to obtain the spatial distribution of power radiated by the SCF.

The SCF distributed radiation resistance $R_{rad,SF}(x)$ from eqn (3) varies with its length L due to the slope discontinuity in the current that can occur at the origin $x = 0$. The SCF current in the range $-1 \le x \le +1$ for $L = 10l/2$ or $5.0l$ wavelengths and $L = 11l/2$ or 5.5 wavelengths is plotted in Figure 1 with $N = 101$ and 111 segments, respectively. This value of N was used to produce a symmetric distribution about the origin. The current slope at the origin for $L = 5.0$ has a sharp discontinuity at the origin, while for $L = 5.5$, there is no slope discontinuity. The distributed radiation resistances for these two cases are plotted in Figure 2. The 5-wavelength SCF becomes infinite at the origin, a point necessarily omitted in the plot. The 5.5-wavelength SCF, on the other hand, exhibits a smooth minimum there.

The radiated-power density from eqn(4) is plotted in Figure 3 where a striking difference is seen between the two SCF lengths. The current-slope discontinuity at the origin for the 5-wavelength case and the corresponding peak it causes in the $R_{rad,SF}(x)$ results in a sharp doublet in the radiated-power distribution. This doublet in

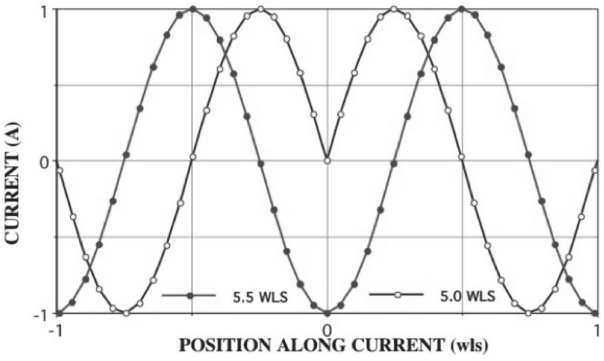

Fig. 1. The center portions of sinusoidal current filaments an even and odd number of half wavelengths long.

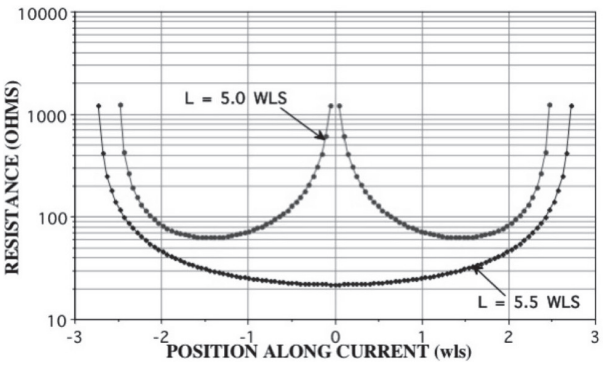

Fig. 2. The distributed radiation resistances from Schelkunoff and Feldman of sinusoidal current filaments an even and odd number of half wavelengths long.

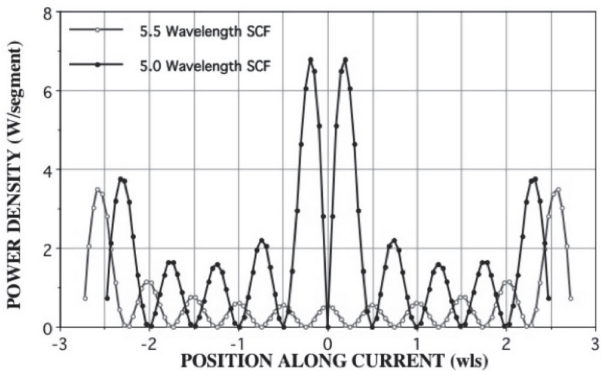

Fig. 3. The distributed radiated-power densities per segment for sinusoidal current filaments an even and odd number of half wavelengths long from eqn (5).

radiated power is due to charge-density maxima caused by the current-slope discontinuity at the origin. Similar but smaller effects occur for other SCF lengths while becoming zero only when n is an odd integer. The lobed structure of the radiated power will be explained after results for a dipole antenna are also presented.

Another way to determine the radiated-power distribution for the SCF is the induced electromotive force (IEMF) method. The IEMF method involves using the tangential electric field $E_x(x)$ along the SCF as given by

$$E_x(x) = \frac{j\eta_o I_o}{4\pi k\rho}\frac{e^{-jkr}}{r} \left\{ k\cos(kx) - (1+jkr)\frac{(x-x)^2}{r^2}[\sin(kx)] \right\}_{x=-L}^{x=L}. \quad (5)$$

Having the field along each current segment the associated supplied power for segment i can then be obtained from

$$p_{\text{IEMF/seg}}(x_i) = \frac{1}{2}\int_{\Delta x_i} I(x)\,Re[E_x(x)]\,dx \approx \frac{1}{2} I(x_i)\,Re[E_x(x_i)]\,\Delta x. \quad (6)$$

Note that the IEMF result is an input quantity and so is opposite in sign to a positive radiated power. For comparison purposes here, however, the IEMF results are plotted as a positive quantity.

The IEMF power results from eqn (6) for the 5.0- and 5.5-wavelength SCFs are compared with the $R_{rad,SF}(x)$ results of Figures 3 and 4 where they can be seen to be graphically indistinguishable. Concerning this agreement, it is worth noting that eqn (5) can be written as

$$p_{\text{rad/seg}}(x_i) = \frac{1}{2} I^2(x_i) R_{\text{rad,SF}}(x_i)\,\Delta x = -\frac{1}{2} I(x_i) E_x(x_i)\,\Delta x \approx -p_{\text{IEMF/seg}}(x_i) \quad (7)$$

and that the two methods are essentially equivalent. This result confirms the validity of the distributed radiation-resistance concept of Schelkunoff and Feldman.

An alternate approach to evaluating the radiated-power distribution of the SCF is far-field analysis of radiation sources (FARS) [4]. As its name implies, FARS is based on the far field that for the SCF can be written as [5]

$$E_{\text{rad},\theta}(\theta) = j\eta_o \frac{I_o e^{-jkr}}{2\pi r}\left[\frac{\cos(kL\cos\theta) - \cos(kL)}{\sin\theta}\right], \quad (8a)$$

or

$$E_{\text{rad},\theta}(\vartheta) = j\eta_o \frac{I_o e^{-jkr}}{2\pi r}\frac{1}{\sin(\theta)} \left[e^{(jkL)\cos(\theta)} + e^{-(jkL)\cos(\theta)} - 2\cos(kL)\right] \quad (8b)$$

where $E_{rad,\theta}$ is the θ component of the electric field. Note that the bracketed terms in eqn (8b) have the appearance of three point sources located at the ends and center of the SCF. This has led to speculation that the SCF radiates from only those three locations, but this is not the case as shown by Figure 3 and elsewhere [6] due to the $\sin(\theta)$ in the denominator of eqn (8).

The implementation of FARS involves evaluating the far radiated field in a slightly modified way compared to the usual computation of the radiated power from some object. This is done by developing the far-field power on an incremental basis in the context of the moment method. The incremental *FARS* power, $p_{i,FARS}(\theta,\varphi)$ for segment s_i in observation direction θ,φ is

$$p_{i,\text{FARS}}(\theta,\varphi) = \lim r\to\infty \left(r^2\frac{1}{2\eta} Re[e_i(\theta,\varphi)\cdot E^*(\theta,\varphi)]\right) \quad (9)$$

where $\vec{e}_i(\theta,\varphi)$ is the electric field due to source (or segment) i and η is the medium impedance while the total electric field for N sources or segments, denoted by

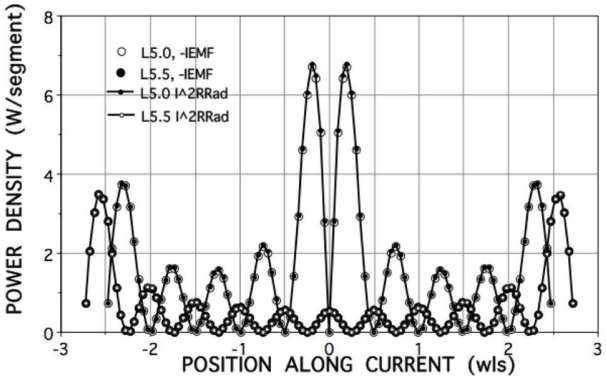

Fig. 4. The $I^2(x)R_{rad,SF}(x)$ and IEMF distributed radiated-power densities for sinusoidal current filaments an even and odd number of half wavelengths long.

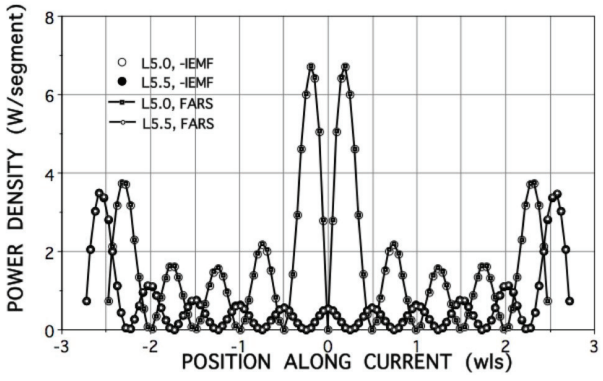

Fig. 5. The IEMF and FARS distributed radiated-power densities for sinusoidal current filaments an even and odd number of half wavelengths long.

$E(\theta,\varphi)$, is

$$E(\theta,\varphi)=\sum_{1}^{N} e_i(\theta,\varphi). \tag{10}$$

The total power contributed by segment i, denoted as $P_{i,FARS}$, comes from integrating the incremental result $p_{i,FARS}(\theta,\varphi)$ over all θ,φ to obtain

$$P_{i,\mathrm{FARS}}=\int_0^{\pi}\int_0^{2\pi} p_{i,FARS}(\theta,\varphi)\sin\theta d\theta d\varphi, \tag{11}$$

as the total power coming from segment i.

Finally, the total radiated power is obtained from integrating the $P_{i,FARS}$ samples over all N sources, or

$$P_{FARS}=\sum_{1}^{N} P_{i,FARS}. \tag{12}$$

Note that the FARS computation differs from a conventional evaluation of the total far-field power only in defining the intermediate quantity $P_{i,FARS}$, the individual contribution of each incremental source, to the total radiated or scattered power. Note also that there is no constraint that each $P_{i,FARS}$ be positive, with a negative value indicating that a particular segment is reducing the total radiated power.

III. THE NEC DIPOLE

Next considered is a comparison of FARS results for the SCF and an NEC-modeled dipole antenna presented in Figure 6. The NEC radiated power is slightly less than that for the SCF since the NEC current decays in amplitude away from the feedpoint.

The normalized, on-surface real component of the PV for a 10-wavelength NEC dipole is shown in Figure 7, as computed from the conjugate product of the wire charge density and current divided by 2. A longer dipole is used here to exhibit more clearly the decay in power flow along the dipole due to radiation. Power flow to the right is shown as positive and to the left is shown as negative in this graph. The normalized complex current

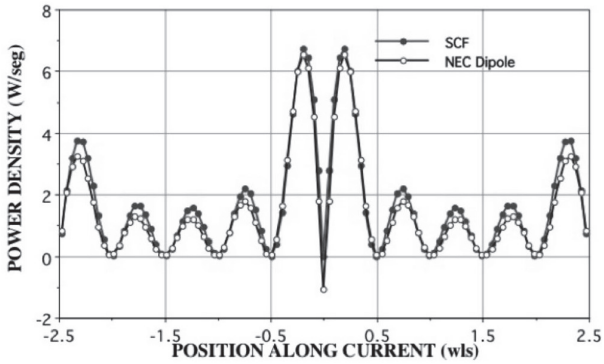

Fig. 6. A comparison of the FARS radiated-power density for a 1-A, 5-wavelength sinusoidal current filament, and an NEC dipole having a current maxima of 1 A.

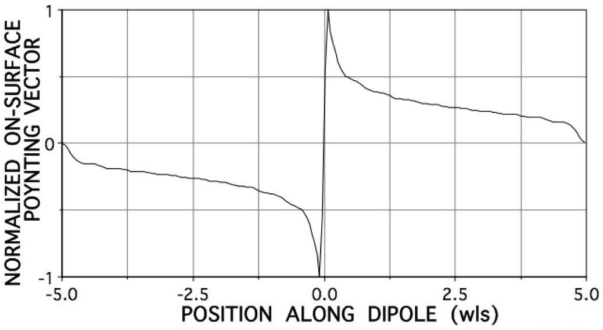

Fig. 7. The normalized on-surface Poynting vector $\mathrm{PV}_{jj}(x)$ along a center-fed, 10-wavelength dipole.

on the dipole is plotted in Figure 8 where the real part decays substantially more than the quadrature, or imaginary, component.

There is a slight oscillation in the PV of Figure 7, the effect of which is emphasized by differentiating it to pro-

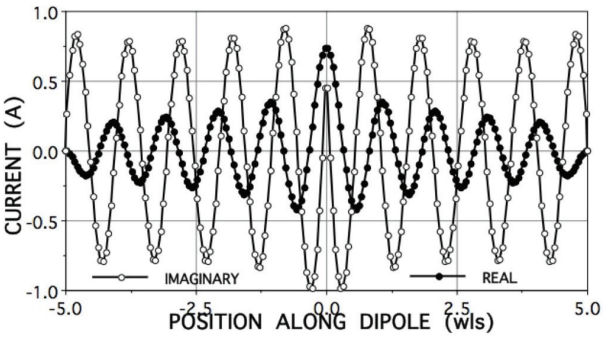

Fig. 8. The normalized complex current on a 10-wavelength dipole antenna.

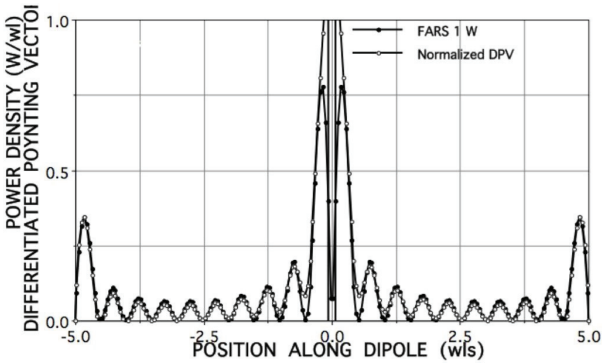

Fig. 9. Normalized DPV and FARS radiated-power densities for a 10-wavelength, center-fed dipole.

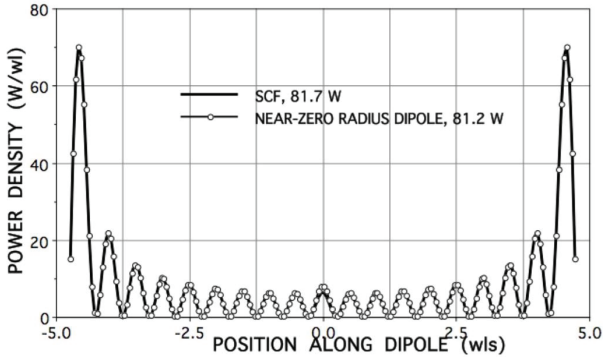

Fig. 10. FARS power densities for a 9.5-wavelength SCF and NEC dipole with maximum currents of 1 A.

duce the loss rate of radiated power with distance from the feedpoint as presented in Figure 9. Also included for comparison is the FARS radiated-power density, with the end maxima of the differentiated PV (DPV) normalized to the FARS result. Observe that the FARS result, being based entirely on the far field, does not explicitly include the effect of the input power provided by the exciting voltage at the antenna feedpoint as does the

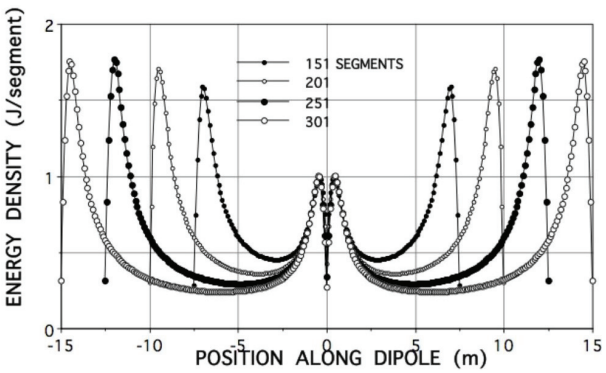

Fig. 11. The energy densities of dipoles of 151-301 0.1-m long segments excited by a Gaussian voltage pulse.

IEMF method. The agreement between the two methods for determining the quantitative absolute (FARS) or relative (DPV) radiated-power distribution is within a few percent, providing mutual validation for both.

FARS results for an NEC dipole of decreasing radius were obtained for comparison with an SCF [3]. The NEC results converged to within 1% of the SCF values for a dipole radius of 10^{-20} wavelengths.

FARS has also been implemented in the TD [7, 8] using the computer model thin-wire time domain (TWTD) [9]. A result for several dipoles of different lengths with center feedpoints is presented in Figure 11 where the excitation is a Gaussian pulse with a half-amplitude width of about 13 time steps, Δt, and with the segment length $\Delta x = c\Delta t$. The energy density is a smooth function of position in contrast with the frequency-domain result.

A comparison of a 10-m center-fed dipole radiating 1 J in the TD, a normalized version of the 101-segment curve of Figure 11, and a 10-wavelength dipole radiating 1-W in the FD is shown in Figure 12. The standing-wave nature of the frequency-domain dipole presents a distinctive contrast compared with the time-domain result.

IV. ACCELERATED CHARGE AND RADIATION

Three methods for determining where and how much radiation originates from an SCF have been presented above: the Schelkunoff-Feldman radiation resistance, a closely related procedure, the IEMF method, and FARS. Two, the DPV and FARS, have been shown to provide the same kind of information for a PEC dipole. Since charge acceleration is known to be the cause for electromagnetic radiation, the question remains about where and why does this occur on a PEC object? The answer to this question for an SCF is clear: Being a purely standing wave with zero net power propagation along its length, charge is accelerated due to an applied

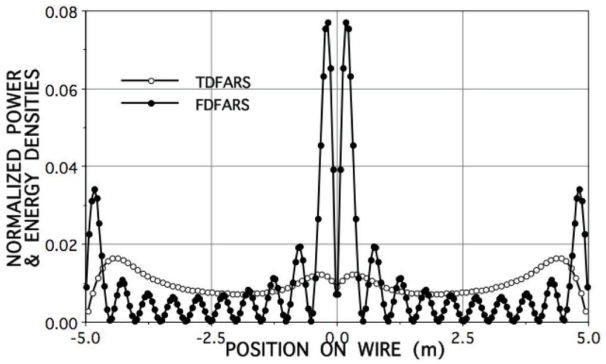

Fig. 12. Comparison of frequency-domain and time-domain FARS for a 10-m center-fed dipole radiating a total power of 1 W or energy of 1 J, respectively.

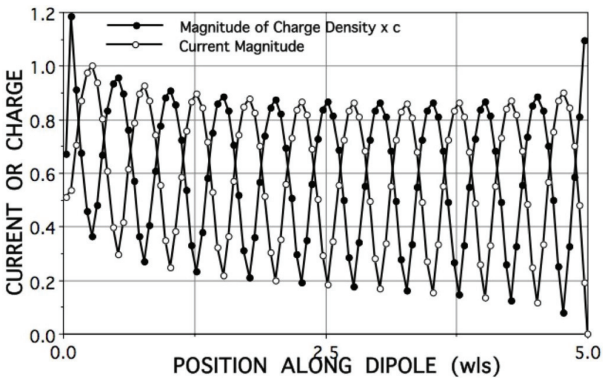

Fig. 13. The magnitudes of the standing-wave current and charge distributions on half of a 10-wavelength, center-fed dipole antenna.

electric field as demonstrated by the IEMF method, with the result corroborated by FARS.

Where charge acceleration occurs on a PEC needs some further discussion. It is clear that charge is set into motion, or accelerated, at the feedpoint where an exciting electric field is applied. In addition, the current goes to zero at the ends of a finite-length antenna where the charge is completely reflected and is thus consequently accelerated, as well. But both the frequency-domain and time-domain versions of FARS show that radiation and accompanying charge acceleration must occur all along the interior length of a dipole. So the question to be considered is what is the cause of this interior acceleration.

A related phenomenon provides the answer. It has been observed that the current propagating down a wire of constant radius decays in amplitude, with the cause being attributed to power loss due to radiation. This result of this decay is exhibited by the on-surface PV in Figure 7 where the power flow decays in an oscillatory but monotonic fashion with increasing distance from the feedpoint. Because charge is conserved, the conclusion follows that some portion of the outward-propagating charge and current is reflected back toward the feedpoint. This reflection and associated charge acceleration thus account for the radiation that takes place down the arms of the dipole antenna.

This raises the additional question about what causes the charge reflection itself to occur. It is known that the total current on an infinite biconical antenna is independent of distance from the feedpoint [5], i.e., there is no reflection because the bicone wave impedance is independent of position. An infinite wire or cylinder of constant radius by contrast has a variable, distance-dependent, wave impedance and so a partial reflection of a propagating current occurs. This accounts for what can be described as "propagation radiation" as shown by the FARS results in Figures 9 and 10 where radiation lobes occur at half-wavelength intervals. On the other hand, for a dipole antenna excited by a short-pulse electric field, there is no standing wave. Instead, the propagation radiation is a smooth, continuous curve extending between the feedpoint and wire ends as shown in Figures 11 and 12 as obtained using TWTD [9].

The cause of the lobed, standing-wave radiation power in the FD is simply explained. The counter-propagating sine waves of current and charge produce standing waves of the kind shown for one-half of a 10-wavelength dipole in Figure 13. The peaks and minima of the current and charge magnitudes are interleaved. The plot of the FARS radiated-power density and the square of the normalized current in Figure 14 shows that their lobe maxima are aligned. This is because current maxima are produced when opposite-signed, counter-propagating charge waves meet. The partial reflection of opposite-signed charges moving in opposite directions produces additive radiated electric fields, resulting in the FARS maxima. Charge maxima, on the other hand, occur when same-signed charge waves meet. Their partial reflections produce canceling radiated electric fields that result in FARS minima. These results demonstrate why and where the radiation originates from the PEC dipole.

Observe that the effective propagation speed of the current and charge waves on the PEC wire is approximately at the speed of light in the medium in which the dipole is located, a fact that deserves some additional discussion. Observe that when modeling in the TD, charge and current pulses are found to move at approximately the speed of light along a uniform-radius, straight wire. However, this phenomenon does not require any physical charge to move at near-light speed. Instead, it arises from the fact that the fields launched from the feedpoint

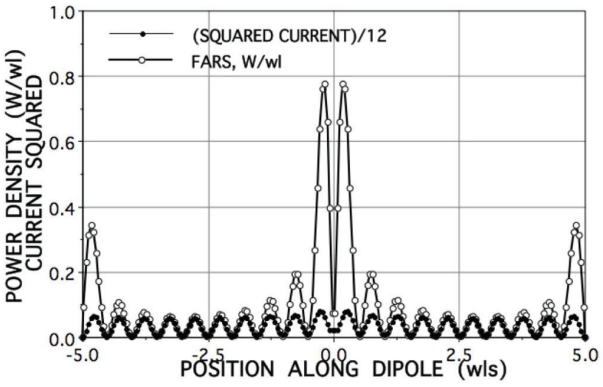

Fig. 14. The FARS power density in W/wavelength for a 10-wavelength, center-fed dipole together with the square of the current normalized to the inner FARS lobes.

of an impulsively excited wire propagate along the wire near or at the speed of light of the medium in which the wire is located. The magnetic and electric fields associated with these pulses must terminate on the wire as required by the boundary conditions of a PEC. This process can be analogized in various ways [9] or as a row of falling dominos. Each domino moves very little but with the overall effect propagating along the entire row.

Since the tangential electric field on the wire surface is zero, there is only a radial field that terminates at the charge on its surface. Similarly, since the normal magnetic field on the wire surface is zero, there is only a tangential, or azimuthal, magnetic field that terminates at the current on its surface. Thus, the moving charge and its accompanying current are attached to the propagating fields. When the field propagation is interrupted by ends, bends, loads, junctions, etc., some or all of the propagating fields and *Q*/*I* pulses are reflected with the reflected field lines developing bends as discussed in Chapter 2.

While the magnetic field lines are closed around a wire antenna since there is no magnetic charge, the radiated electric fields from finite objects must eventually form closed lines as well to "break off" from it. This is easily visualized for an impulsively excited object in the TD. After enough time has passed, the object must return to overall charge neutrality which means that there are no remaining electric or magnetic fields attached to its surface. Closure of the electric fields occurs when opposite-signed charges can neutralize each other as they pass moving in opposite directions.

It is reasonable to ask whether the equivalent sources used in boundary-value problems match physical reality, i.e., whether their computed results match measurements. The computed radiated fields have been found to match the measured radiation and scattering patterns within their respective numerical and experimental uncertainties since the beginning of electromagnetics as a discipline. Measurements of near-field interactions and input impedance are somewhat more experimentally difficult to determine, but they also have confirmed analytical and computational results. One of the more demanding checks on computations is measurement of the source distribution on an object. Examples of frequency-domain measurements for current distributions can be found in the literature such as 10–15.

REFERENCES

[1] J. D. Jackson, "How and antenna launches its input power into radiation: the pattern of the Poynting vector at and near an antenna," *American Journal of Physics*, vol. 74, no. 4, pp. 280-288, 2006.

[2] S. A. Schelkunoff and C. B. Feldman, "On radiation from antennas," *Proceedings of the I.R.E.*, pp. 511-516, Nov. 1942.

[3] E. K. Miller, "Comparison of the radiation properties of a Ssinusoidal current filament and a PEC dipole of near-zero radius," *IEEE Antennas and Propagation Society Magazine*, vol. 48, no. 4, pp. 37-47, Aug. 2006.

[4] E. K. Miller, "PCs for AP and other EM reflections," *IEEE AP-S Magazine*, vol. 41, no. 2, pp. 82-86, Apr. 1999a; vol. 41, no. 3, pp. 83-88, Jun. 1999b.

[5] C. A. Balanis, *Antenna Theory*, Harper & Row, New York, 1982, pp. 118-124.

[6] E. K. Miller, "The incremental far field and degrees of freedom of the sinusoidal current filament," *IEEE Antennas and Propagation Society Magazine*, vol. 49, no. 4, pp. 13-21, Aug. 2007.

[7] E. K. Miller and G. J. Burke, "A multi-perspective examination of the physics of electromagnetic radiation," *Applied Computational Electromagnetics Society (ACES) Journal*, vol. 16, no. 3, pp. 190-201, 2001.

[8] E. K. Miller, "Time-domain far-field analysis of radiation sources," *IEEE Antennas and Propagation Society Magazine*, vol. 53, no. 5, pp. 81-97, Oct. 2011.

[9] E. K. Miller, "Exploring electromagnetic physics using thin-wire time-domain (TWTD) modeling," *Proceedings of 14th Annual Review of Progress in Applied Computational Electromagnetics*, Naval Postgraduate School, Monterey, CA, pp. 583-588, 1998.

[10] C. S. Baird, "What is the speed of electricity," *Science Questions with Surprising Answers,* Feb. 19, 2014.

[11] R. W. P. King and T. T. Wu, "Current measurement-1965-currents, charges, and near fields of cylindrical antennas," *Radio Science*, vol. 69D, no. 3, pp. 429-446, 1965.

[12] W. D. Smith, "Numerical analysis of normal mode helical dipoles antennas," PhD Dissertation, Iowa State University, 1971.

[13] T. Yokoyama, T. Hoashi, K. Murata, S. Egashira, K. Egashira, and T. Nakamiya,, "Design of multi-band antenna using different radius wires," *PIERS Online*, vol. 5, no. 3, 2009.

[14] T. Ishizone, S. Adachi, K. Taira, Y. Mushiake, K. Mitazaki, "Measurement of antenna current distribution in an anisotropic plasma," *IEEE Transactions on Antennas and Propagataion*, pp. 678-679, Sep. 1969.

[15] S. Egashira, M. Taguchi, and A. Sakitani, "Consideration on the measurement of current distributionon bent wire antennas," *IEEE Transactions on Antennas and Propagation*, vol. 36, no. 7, pp. 918-926, Jul. 1988.

[16] Y. S. H. Khraisat and K. A. Hmood, "Distribution of symmetrical dual and triple feeding full-wave dipole antenna," *Modern Applied Science*, vol. 5, no. 6, pp. 126-132, Dec. 2011.

Edmund K. Miller received the Ph.D. degree in electrical engineering from the University of Michigan in 1965 with an emphasis on computational electromagnetics (CEM), a rapidly developing field at the time.

His working career has been quite varied including employment at four universities (Michigan Technological University, University of Michigan, Kansas University, and Ohio University), three companies (MBAssociates, Rockwell International Science Center, and General Research Corporation, all in California), and two national laboratories (Lawrence Livermore and Los Alamos from which he retired in 1993). He has served two terms on the IEEE Antennas and Propagation Society (AP-S) Administrative Committee and has twice been an APS Distinguished Lecturer.

Dr. Miller was elected as IEEE Fellow in 1984 and received the IEEE Third Millennium Medal in 2000. He was the recipient (with others) of the 1988 Best Paper Award from the IEEE Education Society. Between 1985 and 2002, he served on the editorial board of IEEE Potentials Magazine as Editor or Associate Editor for which he wrote a regular column "On The Job." He also wrote a column for the AP-S Magazine "PCs for AP and Other EM Reflections" from 1984 to 2000. He was an organizer, served as its first president, and is a Fellow of the Applied Computational Electromagnetics Society (ACES) for which he served two terms on its Board of Directors. His research interests include CEM, applied signal processing, visual electromagnetics, and promoting the incorporation of accuracy statements in published CEM numerical results. He has published numerous articles dealing with his major interest, the physics of electromagnetic radiation, and recently completed a draft book on the topic with the title "Charge Acceleration and the Spatial Distribution of Radiation Emitted by Antennas and Scatterers."

3D Dynamic Ray-tracing Propagation Model with Moving Scatterer Effects

Gang Liu[1], Tao Wei[2], and Chong-Hu Cheng[2]

[1]College of Physics and Electronic Engineering Taishan University,
Tai'an 271000, China
gd0713liugang@163.com

[2]College of Electronic and Optical Engineering & College of Microelectronics
Nanjing University of Posts and Telecommunications, Nanjing 210023, China
taotaotao110@163.com, chengch@njupt.edu.cn

Abstract – Ray-tracing propagation model (RTPM) has been widely used for predicting channel characteristics, whereas the scenarios considered are generally static. The complexity of RTPM is significantly increased due to the rapidly time-varying scenario resulted from moving scatterers. A three-dimensional (3D) dynamic RTPM considering moving scatterer effects is advanced in this paper. First, a simplified dynamic scenario preprocessing method based on the predefined active region and face transformation is proposed. The random movement of multiple scatterers can be enabled without repeated scenario modeling. Second, an efficient dynamic ray-tracing method based on self-adaptive ray-launching technique is advanced. The computational efficiency of the dynamic RTPM can be significantly improved due to the exclusion of repeated ray-tracing process over time. Finally, the feasibility and accuracy of the RTPM is verified by comparing the simulation results with the measurements performed in an indoor scenario with pedestrians.

Index Terms – Dynamic ray-tracing, moving scatterers, self-adaptive ray-launching technique.

I. INTRODUCTION

Dynamic scenarios (e.g., shopping mall, waiting hall, intelligent transportation, and intelligent plant) with moving scatterers (e.g., vehicles, machines, and pedestrians) are considered as one of the most important application scenarios for the B5G and 6G wireless communication systems [1–3]. Accurately predicting the channel characteristics in these scenarios is fundamental and crucial for system design. As a high performance solution, ray-tracing propagation model (RTPM) has been widely used in the prediction of channel characteristics [4–6]. However, these RTPMs are generally focused on the scenarios considering only static scatterers.

The research on the RTPM for dynamic scenarios with moving scatterers is still scarce. For a dynamic scenario with moving scatterers, the complexity of a RTPM is extremely increased and generally reflected in two aspects. The first one is the scenario preprocessing such as the dynamic and continuously temporal channel representation. This is because the scenario is required to be modeled repeatedly once the locations of scatterers are changed. The other one is that performing ray-tracing simulations at each discrete time instant is indeed computationally expensive. Several dynamic ray-tracing models with the movement of transceiver are described in [7–9], whereas the moving scatterer effects are not considered. An image-visibility-based preprocessing method for dynamic ray tracing in urban environments is introduced in [10]. The dynamic visibility region is established according to the movement trajectory of the transmitter and scatterers. However, the trajectory is a priori and the dynamic visible region has to be reconstructed once trajectory is changed. Several efficient dynamic ray-tracing models considering moving scatterer effects are introduced in [11] and [12]. The efficiency of the dynamic ray-tracing models can be improved by replacing the simulation at each discrete time instant with single simulation in the coherent time. However, the coherent time for different scenarios is required to be obtained from a large number of measurements.

In this paper, a three-dimensional (3D) dynamic RTPM with moving scatterer effects is advanced. In view of the two problems that resulted from the moving scatterers as mentioned above, first, a simplified scenario preprocessing method is proposed. Based on the predefined active region and face transformation, scenario modeling and date processing are required to be performed only once in the entire dynamic ray-tracing process. Moreover, a self-adaptive ray-launching (SARL) based dynamic ray-tracing method is advanced

Submitted On: November 2, 2021
Accepted On: May 8, 2022

https://doi.org/10.13052/2022.ACES.J.370404

to improve the computational efficiency by removing the redundant rays at each time instant.

II. 3D DYNAMIC RAY-TRACING PROPAGATION MODEL

In this section, a 3D dynamic RTPM is introduced from two aspects, including simplified dynamic scenario preprocessing and efficient dynamic ray-tracing method.

A. Simplified dynamic scenario preprocessing

Detailed scenario description such as the geometric structure and the layout of scatterers is necessary for RTPM. However, the random movement of scatterers leads to the real-time change of scenarios. Repeated scenario modeling and data processing result in the huge overhead of dynamic scenario preprocessing.

In order to simplify the dynamic scenario preprocessing, the static and moving scatterers are modeled independently. Static scatterers can be modeled according to the geometric structure and layout as same as the traditional RTPMs [13, 14]. However, for moving scatterers, an active region should be predefined according to the possible locations. Assuming that a moving scatterer can be modeled as a parallelepiped commonly used as one of the human and vehicle models [15, 16], the active region can be gridded as shown in Figure 1. All grids are required to be numbered without repetition and each grid is corresponding to a parallelepiped.

Second, space subdivision is performed to the whole scenario and the whole propagation space can be subdivided into many non-overlapping tetrahedrons. An instance of space subdivision for a room with a single scatterer is shown in Figure 2. Two types of faces are present in the scenario after space subdivision. The first one is called physical face (PF), i.e., the object surface. The PF property can be characterized by material parameters including the relative permittivity ε_r and the conductivity σ. The other one is called constructed face (CF). The faces are invisible and only used to assist the subsequent ray-tracing process. The material of CF is air and the corresponding parameters are $\varepsilon_r = 1$ and $\sigma = 0$.

The appearance and disappearance of a scatterer can be modeled rapidly using a simple method of face property transformation (FPT). As shown in Figure 3, if all PF of a scatterer is transformed into CF (i.e., the forward FPT), rays pass through the scatterer without changing the propagation direction since CF has no effect on the rays. This indicates that the scatterer is equivalent to disappearing in the scenario. Conversely, if all CFs of the scatterer are converted into PF (i.e., the inverse FPT), the incident rays are interacted with the scatterer such as the reflection and diffraction. This indicates that the scatterer is equivalent to appearing in the scenario.

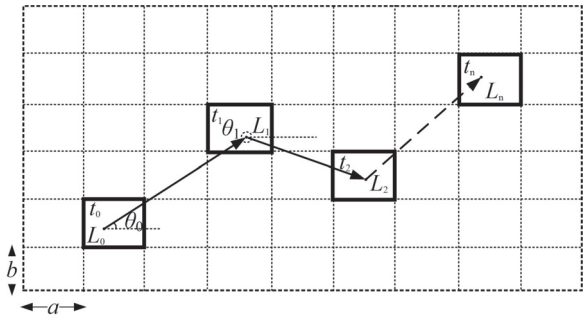

Fig. 1. Random movement of a scatterer in a predefined activeregion.

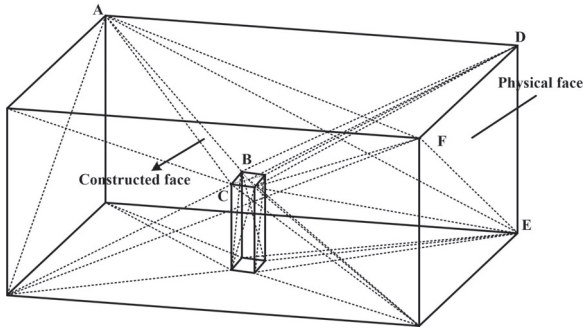

Fig. 2. An instance of space subdivision for a room with a single scatterer.

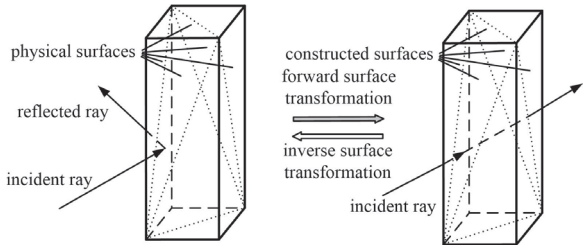

Fig. 3. The appearance and disappearance fora moving scatterer using FPT.

The data of scenario after space subdivision can be stored in a tree structure with the depth of five as shown in Figure 4. The whole space of a scenario is assumed to be subdivided into T tetrahedrons on the second layer. Each tetrahedron corresponds to four faces stored in the third layer. The fourth layer is a crucial layer. In addition to three child nodes representing three lines, five leaf nodes are divided into three parts including two adjacent tetrahedrons related to the common face, the unit normal vector, and the face types, wherein the ray-object interaction mechanism can be determined according to the face types. The fifth layer is consisted of two parts, i.e., the two endpoints of each line and line types including

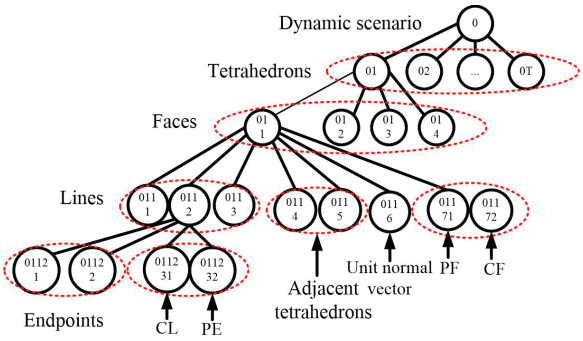

Fig. 4. Data structure of scenario preprocessing.

constructed lines (CLs) and physical edges (PEs). As a result, the adjacent relationship between tetrahedrons can be obtained efficiently by traversing the tree structure.

B. Efficient dynamic ray-tracing method

The computational efficiency can be significantly reduced if performing ray-tracing process to all rays at each time instant. An SARL method is introduced to exclude the repeated ray-tracing process.

First, the forward FPT is applied to all parallelepipeds and this is equivalent to no moving scatterers in the scenario. As mentioned above, the propagation space has been subdivided into a number of tetrahedrons. A ray emitted from a transmitting point $\boldsymbol{T}_m$ can be intersected with a face of the tetrahedron containing $\boldsymbol{T}_m$. The intersected face and the intersection point $\boldsymbol{I}$ can be determined as follows [17]:

$$\delta_i = \frac{\left\langle \vec{r}, \vec{u}_i \right\rangle}{\left\langle \vec{r}, \vec{n}_i \right\rangle}, i = 1,2,3,4 \tag{1}$$

$$\boldsymbol{I} = \boldsymbol{T}_m + \delta \vec{r}, \delta = \min\{\delta_i | \delta_i > 0\}, \tag{2}$$

where δ is the extension coefficient related to the i-th face. $\vec{r}$ denotes the unit vector in the propagation direction. $\vec{u}_i$ is the vector between $\boldsymbol{T}_m$ and one endpoint of the i-th face. $\vec{n}_i$ is the unit normal vector of the i-th face. The intersected face is corresponding to the minimum and positive extension coefficient. If the intersected face is PF and the roughness is assumed to be neglected, the ray is reflected and the reflected field can be given as [18]

$$\vec{\vec{E}}_r = \vec{\vec{E}}_i \widetilde{R} A_r(d_0) e^{-jkd_0}, \tag{3}$$

where $A_r(d_0)$ is the attenuation coefficient and can be expressed as

$$A_r(d_0) = \frac{d'}{d_0(d_0 + d')}, \tag{4}$$

where d' and d represent the distance from $\boldsymbol{I}$ to $\boldsymbol{T}_m$ and to a reference point on the reflected ray, respectively. The complex reflection coefficients $\widetilde{R}$ for perpendicular and parallel polarizations are given as

$$\widetilde{R}_\perp = \frac{\cos\theta_i - \sqrt{\widetilde{\varepsilon}_r - \sin^2\theta_i}}{\cos\theta_i + \sqrt{\widetilde{\varepsilon}_r - \sin^2\theta_i}} \tag{5}$$

$$\widetilde{R}_\parallel = \frac{\widetilde{\varepsilon}_r \cos\theta_i - \sqrt{\widetilde{\varepsilon}_r - \sin^2\theta_i}}{\widetilde{\varepsilon}_r \cos\theta_i + \sqrt{\widetilde{\varepsilon}_r - \sin^2\theta_i}}, \tag{6}$$

where $\widetilde{\varepsilon}_r$ is the complex relative permittivity expressed as

$$\widetilde{\varepsilon}_r = \varepsilon_r - j\frac{\sigma}{\omega\varepsilon_0}, \tag{7}$$

where ω is the angular frequency and ε_0 is the permittivity of vacuum.

Otherwise, if the intersected face is CF, the ray enters the adjacent tetrahedron without changing the propagation direction. Regardless of the intersected face being SF or CF, the intersection point $\boldsymbol{I}$ can be taken as the next transmitting point, and next intersection point $\boldsymbol{I}'$ can be determined from eqn (1) and (2). Consequently, the propagation path and received field of each ray can be determined.

In order to exclude the repeated ray-tracing process at each time instant, the sets of parallelepipeds intersected with rays are required to be recorded as

$$\text{ray\_scat}_k = \left[s_{k,1}, s_{k,2}, \ldots, s_{k,j}\right], k = 1,2,\ldots,K, \tag{8}$$

where $s_{k,j}$ is the jth parallelepiped intersected with the k-th ray. K denotes the total number of rays. Consequently, the ray set corresponding to each parallelepiped can be also obtained and represented as

$$\text{scat\_ray}_i = \left[r_{i,1}, r_{i,2}, \ldots, r_{i,l}\right], i = 1,2,\ldots,Q, \tag{9}$$

where $r_{i,l}$ is the l-th ray related to the i-th parallelepiped. Q is the total number of parallelepipeds.

The dynamic RTPM can enable multiple scatterers to move independently and randomly. It is assumed that N moving scatterers are present in a scenario. At the initial time t_0, the initial locations of the N moving scatterers can be randomly generated from the grid indices and the N moving scatterers corresponding to the grids can be constructed based on the inverse FPT. The rays required to be retraced can be obtained from the set of scat_ray since only the paths of rays intersected with the N moving scatterers are changed. As a result, the total field can be determined as

$$\vec{\vec{E}}_{\text{total}} = \sum_{m_1=1}^{M_1} \vec{\vec{E}}_{m_1} + \sum_{m_2=1}^{M_2} \vec{\vec{E}}_{m_2}, \tag{10}$$

where M_1 and M_2 denote the number of retained and retraced rays, respectively.

At time t_1, for the nth moving scatterer, a point can be randomly generated within the grid and taken as the start point $\boldsymbol{L}_{t_0}$. The speed v and direction angle θ can be generated according to the velocity models. For simplicity, assuming that the velocity $\vec{v}$ is constant in the time interval (t_1-t_0), the velocity can be expressed as

$$\vec{v} = v\vec{e}_r = v(\cos\theta \vec{e}_x + \sin\theta \vec{e}_y), \tag{11}$$

where $\vec{e}_r$, $\vec{e}_x$, and $\vec{e}_y$ denote the unit vectors of moving direction, x-axis direction, and y-axis direction, respectively. The reach point $\boldsymbol{L}_{t_1}$ can be determined as

$$\boldsymbol{L}_{t_1} = \boldsymbol{L}_{t_0} + \vec{v}(t_1 - t_0). \tag{12}$$

For multiple scatterers with different velocities, eqn (12) can be modified as

$$\{\boldsymbol{L}_1, \boldsymbol{L}_2, \ldots, \boldsymbol{L}_N\}_{t_1} = \{\boldsymbol{L}_1, \boldsymbol{L}_2, \ldots, \boldsymbol{L}_N\}_{t_0} + \{\vec{v}_1, \vec{v}_2, \ldots, \vec{v}_N\}(t_1 - t_0). \tag{13}$$

The grids containing the reach points represent the new locations of the N moving scatterers. The disappearance of moving scatterers at previous locations and the appearance of moving scatterers at new locations can be implemented using the forward and inverse FTP, respectively, and the scenario at time t_1 can be formed.

Similarly, the dynamic scenario with moving scatterers at each time instant can be determined. Furthermore, the total field at each time instant can be also obtained as eqn (10). Finally, the frame diagram of the 3D dynamic RTPM is shown in Figure 5. In view of the dynamic RTPM, the scenario modeling and space subdivision are required to be performed only once based on the predefined active region and FPT method, and, therefore, the dynamic scenario preprocessing can be significantly simplified. Moreover, only partial rays at each time instant are required to be retraced based on the SARL method and the efficiency of the dynamic ray-tracing process can be improved.

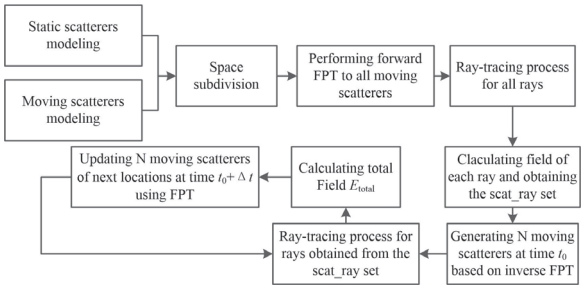

Fig. 5. The frame diagram of the 3D dynamic ray-tracing propagation model.

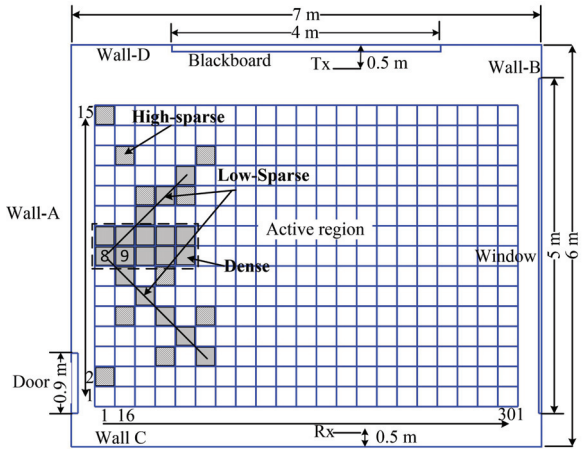

Fig. 6. 2D layout of the office with a predefined active region.

III. MODEL ANALYSIS

A. Scenario description

An indoor office scenario with pedestrians is considered in this paper. The size of the office is 7 m × 6 m × 2.5 m and the two-dimensional (2D) layout of the office with a predefined active region is shown in Figure 6. The office is composed of brick walls and the concrete ceiling and floor. There is no other furniture in the office except a wooden blackboard on the wall-D, a door on the wall-A, and a large glass window on the wall-B. Human body is modeled as a parallelepiped with the size of 0.3 m × 0.3 m × 1.7 m. The corresponding material parameters are listed in Table 1. The speed of pedestrians is assumed to be a constant of 0.5 m/s and pedestrians move from the left side to the right side of the office along a straight line. Vertically polarized omnidirectional antennas with the gain of 2.2 dBi are deployed at the transmitting and receiving sides. The transmitting antenna is 1.35 m above the floor level and 0.5 m from the wall-D. The frequency is 5.2 GHz and the transmitting power is 10 dBm. The height of receiving antenna is 0.85 m and the receiving antenna is 0.5 m from the wall-C.

B. Numerical results analysis

The received power can be expressed as [19]

$$P_r = \frac{\left|\vec{E}_{\text{total}}\right|^2 \lambda^2 G_r}{8\pi\eta}, \tag{14}$$

where $|.|$ is the modulus operator. λ and η denote the wavelength and the wave impedance in free space, respectively. G_r represents the receiving antenna gain. Considering a pedestrian (location 8 as shown in Figure 6) and two pedestrians (locations 8 and 9) move along a route perpendicular to the line between the

Table 1: Material parameters

Object	Relative permittivity	Conductivity (S/m)
Brick wall	4.0	0.343
Concrete ceiling and floor	6.14	1.005
Glass window	5.5	0.0
Wooden blackboard	2.1	0.05
Human body	38.5	2.4

Table 2: Simulation time comparisons (unit: s)

N	Method	Distribution		
		Dense	Low-sparsity	High-sparsity
2	RL	72.8	73.12	72.7
	SARL	7.69	8.48	8.18
5	RL	73.6	74.6	75.1
	SARL	9.2	9.61	9.67
10	RL	74.1	76.6	76.6
	SARL	9.63	11.14	11.27

transmitting and the receiving points. The time-varying received power is shown in Figures 7 and 8. The results show that the received power in the non-line-of-sight (NLOS) area is about 7 dB attenuation compared with the case of line-of-sight (LOS) due to the shadow effect of pedestrians. Furthermore, the received power for the scenario without pedestrians is also shown in Figure 8 as a reference. Up to 3 dB fluctuation of the received power compared with the case of empty room can be observed in the LOS area due to the multipath effect resulted from pedestrians. For the case of two pedestrians, a slightly offset in time is generated in the NLOS area. The simulation results show good agreement with the measurement results in [20] indicating the accuracy of the model.

In order to demonstrate the efficiency of the model, the simulation time of two dynamic RTPMs is investigated. The simulation has been carried out on a personal computer with the processor of Intel (R) core (TM) i5-7300hq CPU @ 2.50 GHz and the memory of 8 GB. The operating system is the 64-bit operating system of windows 10. Fortran computer language is used for the program implementation of the model and the running platform is Microsoft Visual Studio 2010. In the simulation, the total number of one hundred thousand source rays is traced at time t_0. The number of rays is a tradeoff between the computational accuracy and efficiency. For each time instant, the traditional ray-launching (RL) ray-tracing method is applied to all rays, whereas only the rays with changed paths are required to be retraced for the SARL ray-tracing method. The comparisons of simulation time between the traditional RL ray-tracing method and SARL ray-tracing method are listed in Table 2. Six dynamic scenarios considering different number of pedestrians (i.e., N = 2, 5, and 10) with multiple distributions (i.e., dense distribution, slight-sparsity distribution, and high-sparsity distribution) are considered.

First, the results indicate that the simulation time is positively correlated with the number of pedestrians for two methods since the number of ray-object intersection tests is increased with the number of pedestrians. In addition, the paths of rays can be more readily changed

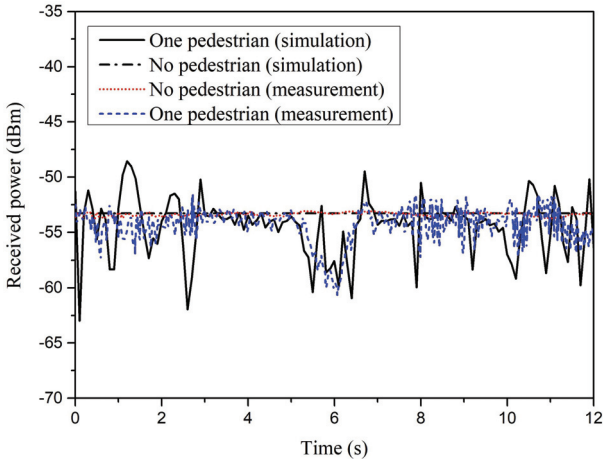

Fig. 7. The time-varying received power for empty room and single pedestrian.

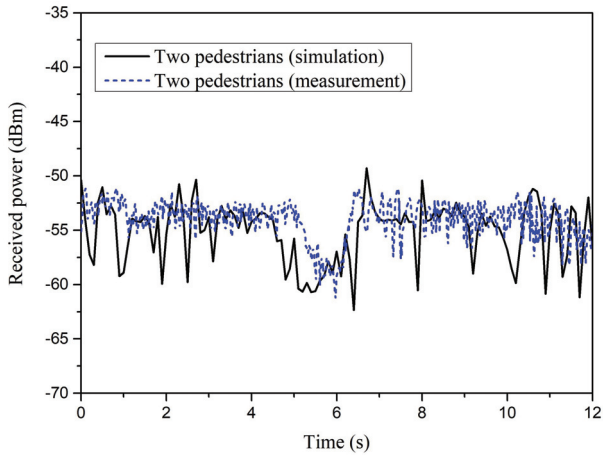

Fig. 8. The time-varying received power for two pedestrians.

with the increase of pedestrians. Second, more simulation time is required due to the increased dispersion degree of the distribution of moving scatterers. This is because the sparsely distributed scatterers lead to the paths of rays more likely to be changed especially for high-order reflection rays. Finally, the simulation time for RL is in the range of 72.7–76.6 s and is much higher than that for SARL in all scenarios due to the exclusion of repeated ray-tracing process. This indicates that the computational efficiency of dynamic ray-tracing model can be significantly improved using the SARL ray-tracing method.

IV. CONCLUSION

In this paper, an efficient 3D dynamic ray-tracing model has been advanced for the prediction of channel characteristics in the dynamic scenarios considering moving scatterers. In view of the moving scatterer

effects on the increased complexity dynamic scenario preprocessing and reduced efficiency of ray-tracing process, first, a simplified dynamic scenario preprocessing method based on the predefined active region and FPT has been introduced. The simultaneous movement of multiple moving scatterers can be performed without repeated scenario modeling and date processing. Furthermore, an SARL-based dynamic ray-tracing method has been described. The repeated ray-tracing process can be eliminated at each time instant. The dynamic RTPM has been applied into an indoor office scenario considering multiple pedestrians and various distributions. The accuracy of the model has been verified by comparing the simulation results with the measurements. Furthermore, the reduced simulation time for SARL method compared with traditional RL method indicate that the computational efficiency of the proposed model can be significantly improved.

REFERENCES

[1] C. Wang, J. Huang, H. Wang, et al., "6G oriented wireless communication channel characteristics analysis and modeling," *Chinese Journal on Internet of Things*, vol. 4, no. 1, 2020.

[2] B. Zong, C. Fan, X. Wang, et al., "6G technologies: Key drivers, core requirements, system architectures, and enabling technologies," *IEEE Vehicular Technology Magazine*, vol. 14, no. 3, pp. 18-27, 2019.

[3] W. Saad, M. Bennis, and M. Chen, "A vision of 6G wireless systems: Applications, trends, technologies, and open research problems," *IEEE Network*, vol. 34, no. 3, pp. 134-142, 2020.

[4] Z. Chen, H. Bertoni, and A. Delis, "Progressive and approximate techniques in ray-tracing based radio wave propagation prediction models," *IEEE Transactions on Antennas and Propagation*, vol. 52, no. 1, pp. 240-251, 2004.

[5] Z. Q. Yun, and M. F. Iskander, "Ray tracing for radio propagation modeling: Principles and applications," *IEEE Access*, vol. 3, pp. 1089-1100, 2015.

[6] F. Fuschini, E. M. Vitucci, et al., "Ray tracing propagation modeling for future small-cell and indoor applications: A review of current techniques," *Radio Science*, vol. 50, pp. 469-485, 2015.

[7] D. He, B. Ai, et al., "The design and applications of high-performance ray-tracing simulation platform for 5G and beyond wireless communications: A tutorial," *IEEE Communications Surveys & Tutorials*, vol. 21, no. 1, pp. 10-27, 2019.

[8] L. Azpilicueta, C. Vargas-Rosales, and F. Falcone, "Intelligent vehicle communication: deterministic propagation prediction in transportation systems," *IEEE Vehicular Technology Magazine*, vol. 11, no. 3, pp. 29-37, Sep. 2016.

[9] S. Hussain and C. Brennan, "Efficient preprocessed ray tracing for 5G mobile transmitter scenarios in urban microcellular environments," *IEEE Transactions on Antennas and Propagation*, vol. 67, no. 5, pp. 3323-3333, May 2019.

[10] S. Hussain, and C. Brennan, "A dynamic visibility algorithm for ray tracing in outdoor environments with moving transmitters and scatterers," *IEEE 2020 14th European Conference on Antennas and Propagation*, Copenhagen, Denmark, pp. 1-5, 2020.

[11] D. Bilibashi, E. M. Vitucci, and V. Degli-Esposti, "Dynamic ray tracing: Introduction and concept," *2020 14th European Conference on Antennas and Propagation*, Copenhagen, Denmark, pp. 1-5, 2020.

[12] F. Quatresooz, S. Demey, and C. Oestges, "Tracking of interaction points for improved dynamic ray tracing," *IEEE Transactions on Vehicular Technology*, vol. 70, no. 7, pp. 6291-6301, Jul. 2021.

[13] G. E. Athanasiadou and A. R. Nix, "A novel 3-D indoor ray-tracing propagation model: The path generator and evaluation of narrow-band and wideband predictions," *IEEE Transactions on Vehicular Technology*, vol. 49, no. 7, pp. 1152-1168, 2000.

[14] S. Lored, L. Valle L, and R. P. Torres, "Accuracy analysis of GO/UTD radio-channel modeling in indoor scenarios at 1.8 and 2.5 GHz," *IEEE Antennas and Propagation Magazine*, vol. 43, no. 5, pp. 37-51, 2001.

[15] M. Yang, Bo Ai, R He, et al., "Measurements and cluster-based modeling of vehicle-to-vehicle channels with large vehicle obstructions," *IEEE Transactions on Wireless Communications*, vol. 19, no. 9, pp. 5860-5874, 2020.

[16] M. Mohamed, M. Cheffena, et al., "A dynamic channel model for indoor wireless signals: Working around interference caused by moving human bodies," *IEEE Antennas and Propagation Magazine*, vol. 60, no. 2, pp. 82-91, 2018.

[17] G. Liu, J. She, W. Lu, et al., "3D deterministic ray tracing method for massive MIMO channel modelling and parameters extraction," *IET Communications*, vol. 14, no. 18, pp. 3169-3174, 2020.

[18] H. R. Anderson, "A ray-tracing propagation model for digital broadcast systems in urban areas," *IEEE Transactions on Broadcasting*, vol. 39, no. 3, pp. 309-317, 1993.

[19] A. Gifuni, "On the expression of the average power received by an antenna in a reverberation chamber," *IEEE Transactions on Electromagnetic Compatibility*, vol. 50, no. 4, pp. 1021-1022, Nov. 2008.

[20] Z. Castro, Karla, et al., "Measured pedestrian movement and bodyworn terminal effects for the indoor channel at 5.2 GHz," *European*

Transactions on Telecommunications, vol. 14, no. 6, pp. 529-538, 2004.

Gang Liu received the B.S. degree from Yantai University, Yantai, China, in 2011 and the Ph.D. degree from the Nanjing University of Post and Telecommunications, Nanjing, China, in 2021.

He has been with Taishan University, Tai'an, China, since 2021. His current research interests include wireless channel modeling, ray-tracing method and intelligent optimization algorithm.

Tao Wei received the B.S. and M.S. degrees from Guangxi Normal University, Guilin, China, in 2009 and 2014, respectively. He is currently working toward the Ph.D. degree with the Nanjing University of Post and Telecommunications (NJUPT), Nanjing, China.

His current research interests include frequency selective surfaces and polarization rotators.

Chong-Hu Cheng received the B.S., M.S., and Ph.D. degrees from Southeast University, Nanjing, China, in 1983, 1986, and 1993, respectively, all in electronic science and engineering.

From 1994 to 1996, he was a Postdoctoral Researcher with the Department of Information Electronics, Zhejiang University, Hangzhou, China. From 1996 to 1999, he served as a Lecturer with Hainan University, Haikou, China. From 1999 to 2001, he was a Research Fellow with the National Institute of Information and Communications Technology, Tokyo, Japan. He joined the College of Telecommunications and Information Engineering, Nanjing University of Posts and Telecommunications, as an Associate Professor, in 2001, and became a Full Professor in 2006. He has authored or co-authored more than 100 technical publications. His research interests include computational electromagnetics, small antennas, and microwave passive circuits. He is a member of the China Institute of Electronics, Antenna Society. He served as a Reviewer for several international journals, including the *IEEE Microwave and Wireless Component Letters* and *IET Electronics Letters*.

Study on Wide-angle Scanning Characteristics of Hemispherical Array

Linqian Du, Jianping Zhao, and Juan Xu*

School of Cyber Science and Engineering
Qufu Normal University, Qufu 273165, People's Republic of China
dlq6917@163.com, zjp-wlx@163.com, *xujuan125@163.com

Abstract – A kind of hemispherical antenna array based on shape conformal is studied in this paper. In order to solve the polarization problem during beam scanning of the array, the method of phase compensation is adopted. The omni-directional scanning of $0^\circ - 360^\circ$ in azimuth direction and wide-angle scanning of $-90^\circ$to 90° in elevation direction are realized. The gain of the array at each scanning angle is about 17 dB. To reduce the occlusion effect of array elements on radiation, the effective elements at different scanning angles are selected for thinned array arrangement. The power loss is reduced and the better scanning performance is achieved by using fewer elements.

Index Terms – Conformal array, wide-angle scanning, phase compensation, thinned array.

I. INTRODUCTION

In recent years, there have been a large number of studies on antenna arrays that can be conformal with carrier surfaces, such as cylindrical array [1, 2], spherical array [3, 4], and conical array [5–7]. Compared with the planar array, the conformal array can make full use of the surface of the carrier. Moreover, the conformal array is widely used in aircraft because it does not affect the aerodynamic performance of the carrier and can reduce the radar cross section.

In some occasions, the antenna array is required to carry out beam scanning [8, 9], which is commonly used in military fields such as radar and navigation. The scanning range of linear array and planar array is limited [10], and the gain of the array will decrease sharply with the increase of the scanning angle, which will greatly affect the performance of the array. The hemispherical array studied in this paper is consistent with geometrical surfaces such as aircraft fuselage and missile airframes, which can realize large angle scanning in azimuth and elevation directions while ensuring stable radiation characteristics. However, the polarization problem of the hemispherical array is serious during beam scanning. To solve this problem, Wen-Tao Li rotates the array elements to adjust their polarization in the main beam direction [11]. But the improvement of array polarization characteristics is limited when the number of array elements increases. Xin Li adopts the dual-polarization amplitude weighting method to reduce the cross-polarization [12]. But this method requires designing dual-polarization element, and the feed system and array structure are relatively complex.

In this paper, the method of phase compensation is used to solve the polarization problem. It does not need to design complex element or array structure. The operation is simple and the effect is remarkable. In addition, not all elements in a conformal array contribute to the main radiation and some elements may also have negative effects such as gain reduction and side lobe increase. Therefore, it is necessary to optimize the array and determine different effective elements at different scanning angles to achieve better scanning performance.

II. THEORETICAL METHOD

A. Phase compensation theory

As the common element in conformal arrays, patch antenna's main polarization direction is its normal direction, and the array elements in the conformal array are not on the same plane; so it is difficult to realize completely parallel polarization direction. As shown in Figure 1, two symmetrical electric fields of the same size seem to superimpose each other in the direction of the Z-axis, but from the center of symmetry, there is a 180° phase difference between them. This leads to the polarization cancelation of the array, which is reflected in beam instability and the sudden drop of gain.

Based on the above analysis, it is considered that 180° phase compensation for one of the symmetrical array elements on the same layer can improve the polarization problem. The phase compensation of the element can change its main polarization direction, so as to strengthen the main radiation of the array.

B. Optimization theory

Not all elements in a uniform conformal array contribute to the main radiation. Therefore, the array needs to be optimized. Thinned array is a kind of sparse array, which refers to the array formed after sparing some elements on the basis of uniform full array. If the

Submitted On: June 29, 2021
Accepted On: March 10, 2022

https://doi.org/10.13052/2022.ACES.J.370405

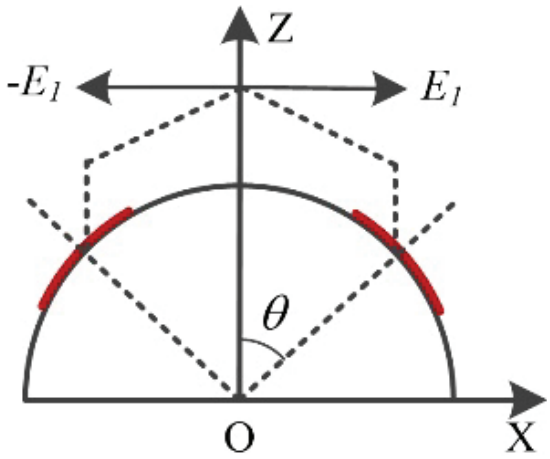

Fig. 1. Symmetric spherical elements distribution.

hemispherical array is thinly arranged, there are several advantages. First of all, different effective elements at each scanning angle can be selected. Second, thinned arrays do not change the arrangement of the whole array. In addition, it can reduce the power loss of the array with fewer elements and improve the width of main lobe and side lobe level at each scanning angle.

The thinned optimization of array follows certain principles. It is assumed that when the deviation angle is greater than $\theta_{\max}$, the contribution of the microstrip antenna to the main beam can be ignored, and the element is invalid. Then $\theta_{\max}$ is called the maximum effective radiation angle, and the effective lobe width of the element is $2\theta_{\max}$. The element will be thinned if its main beam direction is not within this range.

It is assumed that the maximum radiation direction of the array is (θ_0, φ_0), and the maximum radiation direction of any element in the array is (θ_n, φ_n). It can be determined whether the element is located in the effective region by judging whether the included angle β_n of the two main radiation directions is greater than $\theta_{\max}$. That is to judge whether eqn (1) is valid:

$$\cos\beta_n = [\sin\theta_0\cos\varphi_0, \sin\theta_0\sin\varphi_0, \cos\theta_0] \begin{bmatrix} \sin\theta_n\cos\varphi_n \\ \sin\theta_n\sin\varphi_n \\ \cos\theta_n \end{bmatrix} \geq \cos\theta_{\max} \tag{1}$$

III. SIMULATION AND OPTIMIZATION

A. Element designing

Conformal arrays are divided into shape conformal and structure conformal. To make the antenna completely fit with the curved carrier, this design adopts shape conformal. The antenna element is a rectangular patch antenna that is easily conformal, placed on a

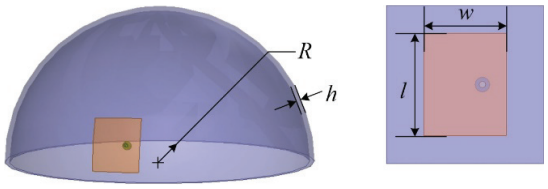

Fig. 2. Antenna element structure.

hemispherical substrate with a dielectric constant of 2.2, and the central frequency is 35 GHz. The substrate radius R is set to 2 times the wavelength. In order to simplify the feed network of the array, the antenna element adopts coaxial feed, and its geometry shape is shown in Figure 2.

According to the working frequency f of the antenna and the thickness h of the substrate, the width of the patch can be obtained by the following equation:

$$w = \frac{c}{f}\sqrt{\frac{2}{\varepsilon_r + 1}}, \tag{2}$$

where c is the speed of light and $\varepsilon_r$is the dielectric constant of the substrate. Considering the edge shortening effect, the length of the patch can be obtained from the following equation:

$$l = \frac{c}{2f\sqrt{\varepsilon_e}} - 2\Delta l, \tag{3}$$

where $\varepsilon_e$is the effective dielectric constant and Δl is the extension length:

$$\varepsilon_e = \frac{\varepsilon_r + 1}{2} + \frac{\varepsilon_r - 1}{2}\left(1 + \frac{12h}{w}\right)^{-\frac{1}{2}}, \tag{4}$$

$$\Delta l = 0.412h\frac{(\varepsilon_e + 0.3)(\frac{w}{h} + 0.264)}{(\varepsilon_e - 0.258)(\frac{w}{h} + 0.8)}. \tag{5}$$

According to the above formula, the basic parameters of the patch can be obtained. After the patch is conformal to the curved surface carrier, the final size is obtained after adjustment: $h = 0.254$ mm, $w = 2.675$ mm, $l = 3.24$ mm.

B. Array designing and simulation

There are many arrangement methods of hemispherical antenna arrays, such as concentric circle projection method, rectangular projection method, and regular icosahedral spherical division method. The antenna array obtained by the projection method is sparsely distributed in the elevation direction, resulting in a serious waste of space. And the design of the regular icosahedral spherical division method is complicated. Therefore, this paper considers the method of equal spacing distribution, in which the spacing is at least half the wavelength. The arrangement of array elements is shown in Figure 3. The distance between adjacent elements is same whether in azimuth direction or elevation direction.

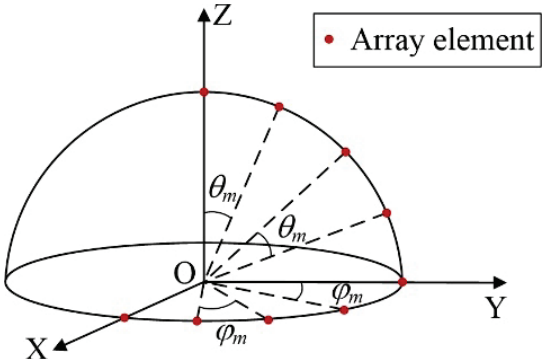

Fig. 3. The arrangement of array elements.

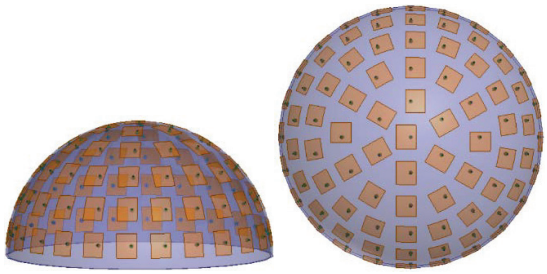

Fig. 4. Hemispherical antenna array. (a) Main view. (b) Top view.

Application programming interface (API) script is written in MATLAB and HFSS is called to complete automatic modeling. In this process, in order to achieve complete conformal array, the projection function is written to project the rectangular patch onto the substrate. In addition, the rotary and duplicate operation is used to complete the establishment of the whole model, so as to improve the modeling efficiency.

If the hemisphere is with a radius of $R = 2\lambda$, the final uniform antenna array is shown in Figure 4 after considering the influence of array elements mutual coupling. The array consists of $M = 6$ layers of rings and $N = 83$ elements in total. Each element uses coaxial feed alone. The distance between adjacent elements is $d = 0.5\lambda$.

The beam scanning characteristics of the hemispherical antenna array are studied. It can be found that in the scanning process of elevation direction, the pattern begins to depress from $\theta_0 = 30^\circ$, and the closer it is to $\theta_0 = 0^\circ$, the more serious the depression is. By phase compensation of the elements, it can be found that the depression disappears and the maximum radiation direction of the pattern is consistent with the expectation. Therefore, the polarization problem of the array has been solved. Figure 5 shows the 2D pattern in elevation direction before and after phase compensation when the beam direction is $(\theta_0, \varphi_0) = (0^\circ, 0^\circ)$. It can be seen from Figure 5 that the gain of the array has changed significantly, increasing from 15 to 17 dB. At the same time, it also verifies the correctness of the theory.

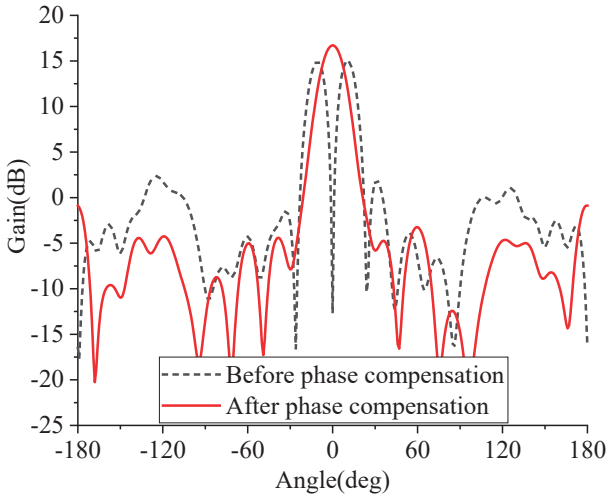

Fig. 5. Comparison before and after phase compensation at $(\theta_0, \varphi_0) = (0^\circ, 0^\circ)$.

After dealing with the polarization problem, the beam scanning performance of the array is analyzed again. Finally, the array can realize omni-directional scanning of $0^\circ - 360^\circ$ in azimuth direction and wide-angle scanning of -90° to 90° in the elevation direction. When the elevation direction is selected to be $\theta_0 = 60^\circ$,Figure 6(a) shows the 2D scanning pattern in azimuth direction. When the azimuth direction is selected to be $\varphi_0 = 0^\circ$, Figure 6 (b) shows the 2D scanning pattern in elevation direction.

It can be seen from Figure 6 that the gain of the hemispherical array is stable at about 17 dB during the beam scanning. With the increase of the scanning angle, the effective caliber of the hemispherical array remains unchanged, which is beneficial to the stable performance of the array during beam scanning. This gives the hemispherical array a very large scanning range.

C. Thinned optimization of the array

In a planar array, the maximum effective radiation angle is generally 60°. The performance of the array is compared when $\theta_{\max}$ is taken as different values by referring to the situation of the planar array. Figure 7 shows the 2D pattern in elevation direction of different $\theta_{\max}$ when (θ_0, φ_0) is $(0^\circ, 0^\circ)$ and $(60^\circ, 0^\circ)$.

It can be concluded by comparison that when $\theta_{\max}$ is different, the patterns at different scanning angles are also different. Generally, the pattern gain under three scanning angles is a little higher than that under full array, and the side lobe level is also slightly lower when

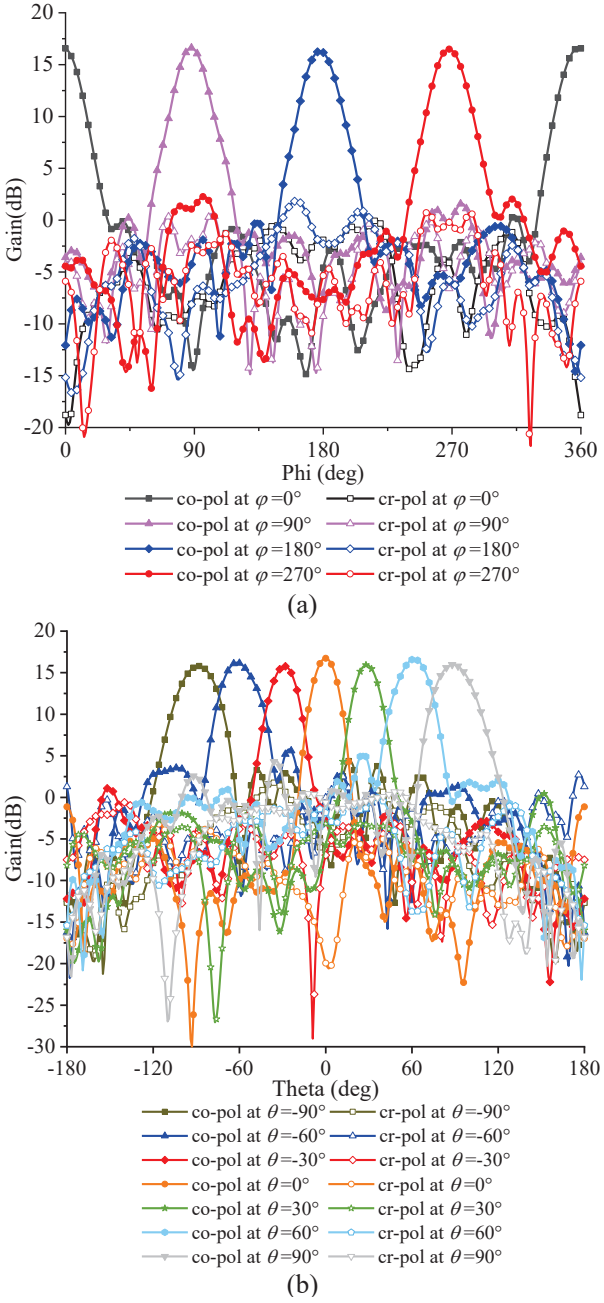

Fig. 6. Beam scanning pattern of the hemispherical array. (a) Azimuth direction. (b) Elevation direction.

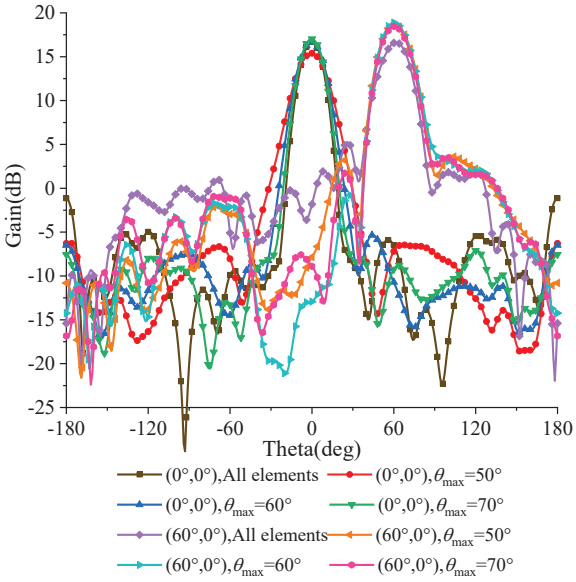

Fig. 7. 2D pattern in elevation direction of different $\theta_{\max}$.

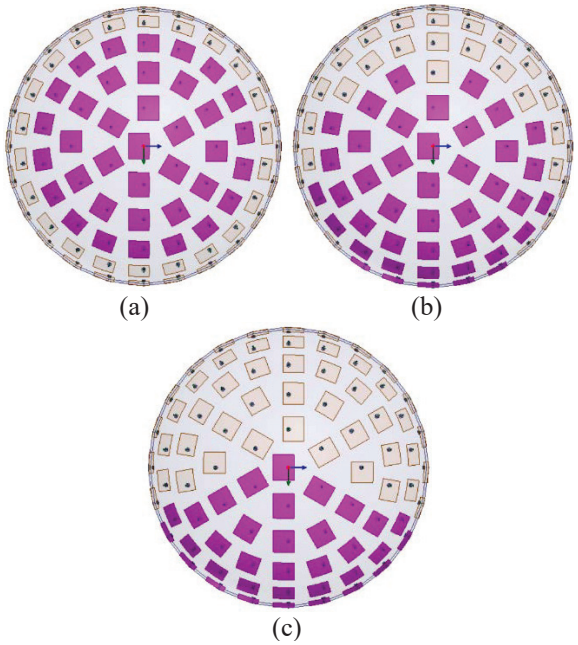

Fig. 8. Thinned array at different scanning angles.

$\theta_{\max} = 60°$. Figure 8 shows the thinned array under three scanning angles, in which the dark-colored selected part is the effective elements, while the light-colored unselected part is the invalid elements. The sparsity rates of the three are 55.4%, 48.2%, and 51.8%, respectively, all around 50%.

(a) $(\theta_0, \varphi_0) = (0°, 0°)$. (b) $(\theta_0, \varphi_0) = (30°, 0°)$. (c) $(\theta_0, \varphi_0) = (60°, 0°)$.

IV. CONCLUSION

In this paper, a hemispherical antenna array based on shape conformal is designed. The polarization problem during beam scanning of array is solved by the method of phase compensation, and omni-directional scanning in azimuth direction and wide-angle scanning in elevation direction are realized. The thinned array is used to achieve better scanning performance and reduce the power loss of the array.

ACKNOWLEDGMENT

This work was supported in part by the National Natural Science Foundation of China (61701278).

REFERENCES

[1] M. Liu, Z.-R. Feng, and Q. Wu, "A millimeter-wave cylindrical conformal phased microstrip antenna array," *2008 China-Japan Joint Microwave Conference*, pp. 150-153, 2008.

[2] T. K. Vo Dai, T. Nguyen, and O. Kilic, "A non-focal rotman lens design to support cylindrically conformal array antenna," *The Applied Computational Electromagnetics Society (ACES) Journal*, vol. 33, no. 2, pp. 240-243, Feb. 2018.

[3] D. Gibbins, M. Klemm, I. Craddock, A. Preece, J. Leendertz, and R. Benjamin, "Design of a UWB wide-slot antenna and a hemispherical array for breast imaging," *2009 3rd European Conference on Antennas and Propagation*, pp. 2967-2970, 2009.

[4] H.-S. Lin, Y.-J. Cheng, Y.-F. Wu, and Y. Fan, "Height reduced concave sector-cut spherical conformal phased array antenna based on distributed aperture synthesis," in *IEEE Transactions on Antennas and Propagation*, pp. 1-9, Apr. 2021.

[5] X.-J. Zhang, X.-P. Ma, and Q.-F. Lai, "Two kind of conical conformal GPS antenna arrays on projectile," *2009 3rd IEEE International Symposium on Microwave, Antenna, Propagation and EMC Technologies for Wireless Communications*, pp. 659-662, 2009.

[6] Z.-R. Li, L.-D. Tan, and X.-l. Kang. "A novel wideband end-fire conformal antenna array mounted on a dielectric cone," *The Applied Computational Electromagnetics Society (ACES) Journal*, vol. 31, no. 8, pp. 933-942, Aug. 2016.

[7] Y. Li, J. Ouyang, F. Yang, and P. Yang, "Synthesis of conical conformal array antenna using invasive weed optimization method," *The Applied Computational Electromagnetics Society (ACES) Journal*, vol. 28, no. 11, pp. 1025-1030, Nov. 2013.

[8] M. Arrebola, E. Carrasco, and J. A. Encinar, "Beam scanning antenna using a reflectarray as sub-reflector," *The Applied Computational Electromagnetics Society (ACES) Journal*, vol. 26, no. 6, pp. 473-483, Jun. 2011.

[9] A. Mahmoodi and A. Pirhadi, "Enhancement of scan angle using a rotman lens feeding network for a conformal array antenna configuration," *The Applied Computational Electromagnetics Society (ACES) Journal*, vol. 30, no. 9, pp. 959-966, Sep. 2015.

[10] Y.-B. Kim, S. Lim, and H. L. Lee, "Electrically conformal antenna array with planar multipole structure for 2-D wide angle beam steering," in *IEEE Access*, vol. 8, pp. 157261-157269, Aug. 2020.

[11] W.-T. Li, X.-W. Shi, Y.-Q. Hei, S.-F. Liu, and J. Zhu, "A hybrid optimization algorithm and its application for conformal array pattern synthesis," in *IEEE Transactions on Antennas and Propagation*, vol. 58, no. 10, pp. 3401-3406, Oct. 2010.

[12] X. Li, K. Gao, C. Li, C.-l. Li, and W. Chen, "Design of hemi-spherical conformal array with a wide-angle scanning," *2016 IEEE International Conference on Microwave and Millimeter Wave Technology (ICMMT)*, pp. 461-463, 2016.

Linqian Du was born in Jinan, Shandong Province, China, in 1996. She received the B.S. degree in engineering from Qufu Normal University, China, in 2019. In the same year, she was admitted to Qufu Normal University and became a graduate student.

Her research interest is the wide-angle scanning of conformal arrays.

Jianping Zhao was born in Heze, Shandong Province, China, in 1964. He received the B.S. degree in physics from Qufu Normal University, Qufu, China, in 1985. In 1988, he studied in Wuhan University for master's degree in radio and information engineering.

Since 1985, he has worked with Qufu Normal University. He was promoted to Associate Professor in 1997 and Professor in 2002. Since 1992, he has been the Director of the Radio Teaching and Research Section. He has been engaged in application of electronic technology and scientific research in communication and information system of electronic information engineering and communication engineering.

Juan Xu was born in Jining, Shandong Province, China, in 1982. She received the Ph.D. degree in electronic science and technology from the Nanjing University of Science and Technology, Nanjing, China, in 2016.

Since 2016, she has been working with Qufu Normal University. She has been an Associate Professor since 2019. Her research interests include simulation, design, and experimental measurement of new high performance RF, microwave and millimeter wave passive devices, antennas, and antenna arrays.

Metasurface Superstrate-based MIMO Patch Antennas with Reduced Mutual Coupling for 5G Communications

Sthembile P. Dubazane, Pradeep Kumar, and Thomas J. O. Afullo

Discipline of Electrical, Electronic and Computer Engineering
University of KwaZulu-Natal, Durban 4041, South Africa
213526437@stu.ukzn.ac.za, pkumar_123@yahoo.com, afullot@ukzn.ac.za

***Abstract* –** Multiple-input multiple-output (MIMO) systems have several advantages, such as providing high capacity, spatial diversity, etc. MIMO antennas suffer with high mutual coupling (m-coupling) between the ports. In this paper, the metasurface with negative permeability (MNG) is designed and utilized for m-coupling reduction of a two-port rectangular microstrip MIMO antenna (Antenna 1). Two metasurface superstrate-based MIMO antennas with reduced m-coupling for fifth generation (5G) are proposed. The first design (Antenna 2) is constructed using a single metasurface superstrate suspended above the two-port MIMO microstrip antenna. The second design (Antenna 3) is constructed using a double metasurface superstrate layers suspended above the two-port MIMO microstrip antenna. Both metasurface-based MIMO antennas achieve significant m-coupling reduction over the entire bandwidth. The edge-to-edge separation between the two patches is $0.29\lambda_0$. The proposed Antenna 3 obtains the reduced m-coupling of -44 dB along with the wide bandwidth of $5.92 - 6.2$ GHz and a maximum gain of 6.79 dB. The proposed antennas are suitable for extended sub-6 GHz 5G applications with the operating frequency band of 5.9–6.1 GHz.

***Index Terms* –** Permeability, permittivity, metasurface, mutual coupling.

I. INTRODUCTION

Multiple-input multiple-output (MIMO) systems refer to the systems where the transmitting end and the receiving end are equipped with the multiple antenna elements. The use of multiple antennas results in significant increase in channel capacity, higher spectral efficiency, and reduced fading without requiring additional bandwidth and transmission power. Hence, the most modern wireless devices are anticipated to employ MIMO technology in wireless communication systems. For low correlation and suitable isolation, a distance of at least $0.5\lambda_0$ (where λ_0 is the free space wavelength at the operating frequency) is required between antenna elements [1]. Due to miniaturization of most modern wireless devices, compact and dense antenna systems with much smaller distances are preferred, which results in high m-coupling between the antenna elements. M-coupling is generally as a result of surface waves or radiated waves and it degrades the antenna performance by deteriorating the radiation characteristics of the antenna system.

To reduce m-coupling, several decoupling methods or techniques have been proposed, which include, but are not limited to, electromagnetic band-gap (EBG) structures [2], defected ground structures (DGS) [3], metamaterials structures [4], decoupling networks [5], etc. The major drawback of these techniques are that these are mostly three dimensional structures; hence, they introduce fabrication difficulties and high cost. In this paper, a planar two-dimensional metasurface is used for m-coupling reduction. Metasurface is two-dimensional structure with properties equivalent to metamaterials. Metasurface structures are planar, thin, and practical for implementation; hence, they have been getting antenna researchers' attention in the recent years.

Various techniques have been used to reduce m-coupling between the antenna elements. Employment of decoupling networks (DNs) is one of the methods that have been highly utilized for m-coupling reduction. They work on the principle of transforming cross-admittance to a completely imaginary value by utilizing discrete elements and step-up transmission lines [6–11]. In [7], a coupled resonator decoupling method is used to decouple the coupled dual-band antennas. In the lower band ($2.4 - 2.48$ GHz), a maximum m-coupling reduction of 7 dB was achieved, while for the upper band ($5.15 - 5.135$ GHz), the m-coupling remains the same and is not reduced. In [9], an LTE700/WWAN MIMO antenna system is decoupled using a DN which consists of a suspended transmission line with two terminals shorted to the ground and a capacitor loaded at the center of the line. In the lower band ($704 - 960$ MHz), the m-coupling was reduced by 9 dB, while in the

Submitted On: December 9, 2021
Accepted On: May 3, 2022
https://doi.org/10.13052/2022.ACES.J.370406

upper band (1710 − 2170 MHz), the m-coupling was not reduced.

One of the other highly used techniques for m-coupling reduction is by the employment of EBG structures. The EBG structures are formed by a periodic arrangement of dielectric and metallic elements. The EBG structure can either block electromagnetic waves at specific frequencies or provide a medium to pass and transmit electromagnetic waves [12]. The most commonly used EBG structure for m-coupling reduction is the mushroom-like EBG structure [13–20]. In [14], the mushroom-like EBG structure was introduced between the two monopole antennas. A maximum m-coupling reduction of 13.4 dB was achieved.

In [15], a planar compact EBG structure was introduced between the two square microstrip patches with an edge-to-edge separation $0.75\lambda_0$ for achieving a maximum m-coupling reduction of 6 dB. The major drawbacks with EBG structures are that they can be largely associated with the fabrication complexities due to their vertical via placement. Moreover, they require thicker substrates, which results in an increase in size of antenna structure.

DGS is another m-coupling reduction technique that is widely employed. It introduces periodic or non-periodic slits or defects on the antenna's ground plane to suppress the ground current between the antenna elements. Different DGS structural arrangements have been used to reduce m-coupling in different antenna arrays [21–27]. In [22], a dumbbell-like DGS was inserted between two multiband microstrip antenna array elements. A maximum m-coupling reduction of 6 dB was achieved. In [24], a slit pattern without a via was etched on the ground plane between two PIFA antennas with an edge-to-edge separation of 0.116 λ_0. A maximum m-coupling reduction of 10 dB was achieved. The main disadvantage of utilizing DGS for m-coupling reduction is that a segment of the propagating energy is leaked, which leads to the electromagnetic interference with the adjacent circuitry. Moreover, the introduced defect might lead to a distorted radiation pattern of the antenna structure.

The last technique that will be discussed is the employment of metamaterial structures to reduce m-coupling between the antenna elements. The usage of metamaterial structures for m-coupling reduction has grown popular over the years due to their ability to manipulate electromagnetic waves [28–33]. In [29], a spiral metamaterial resonator was printed on the microstrip antenna substrate between the two array elements. A maximum m-coupling reduction of 5.5 dB was achieved. In [32], a 3D dual-band metamaterial array structure was loaded on the top of a dual-band microstrip antenna array for m-coupling reduction. A maximum m-coupling reduction of 3 dB was achieved. The major drawback of using metamaterials for m-coupling reduction is that they are frequently used as 3D structures, which introduces problems in terms of fabrication complexity and high cost. In most recent designs, where metasurface is employed for m-coupling reduction in array antenna systems, antenna mismatches can be seen. This then requires further antenna matching techniques to be utilized for improving antenna parameters and fabrication difficulties.

In this paper, the design, simulation, fabrication, and measurement of the metasurface-based antennas are presented. Two metasurface-based antennas, i.e., Antenna 2 and Antenna 3 are presented and their results are analyzed. The first design, i.e., Antenna 2 is achieved by suspending a single metasurface substrate on the top of the microstrip antenna, while the second design, i.e., Antenna 3 is achieved by suspending a double metasurface substrate on the top of the microstrip antenna.

II. DESIGN AND GEOMETRY OF METASURFACE-BASED MIMO ANTENNAS

Two metasurface superstrate-based antennas are presented in this paper. The proposed designs utilize the MNG metasurface which is equivalent to the medium with negative permeability. The metasurface is designed using periodic split ring resonators (SRR). The MNG metasurface is designed such that it rejects wave propagation at the center frequency and, hence, reduces the m-coupling between the antenna elements. The first design employs a single metasurface superstrate suspended over the radiating antenna elements. In this design, the m-coupling is reduced from −29 to −61 dB, while the gain is significantly reduced from 4.79 to 1.69 dB. The second design employs a double metasurface superstrate suspended over the radiating antenna elements. In this design, the m-coupling between the antenna elements is reduced from −24 to −46 dB, while the gain is increased from 4.71 to 6.79 dB.

A. Antenna 1

To demonstrate the effectiveness of the metasurface superstrate-based antenna designs, a two-element MIMO rectangular microstrip antenna is designed. This antenna is designed using the transmission line model of analysis. The antennas for MIMO systems require separate feeding for every antenna element [34, 35]. The antenna structure is simulated and optimized using the CST Microwave Studio. This antenna is designed for the resonant frequency of 6 GHz in the sub-6 GHz band. Sub-6 GHz band is the frequency range below 6 GHz and is defined as frequency range 1 (FR1) in fifth generation (5G) technology for various ISM applications [36, 37]. Recently, some antennas have been designed for sub-6 GHz applications 38–40.

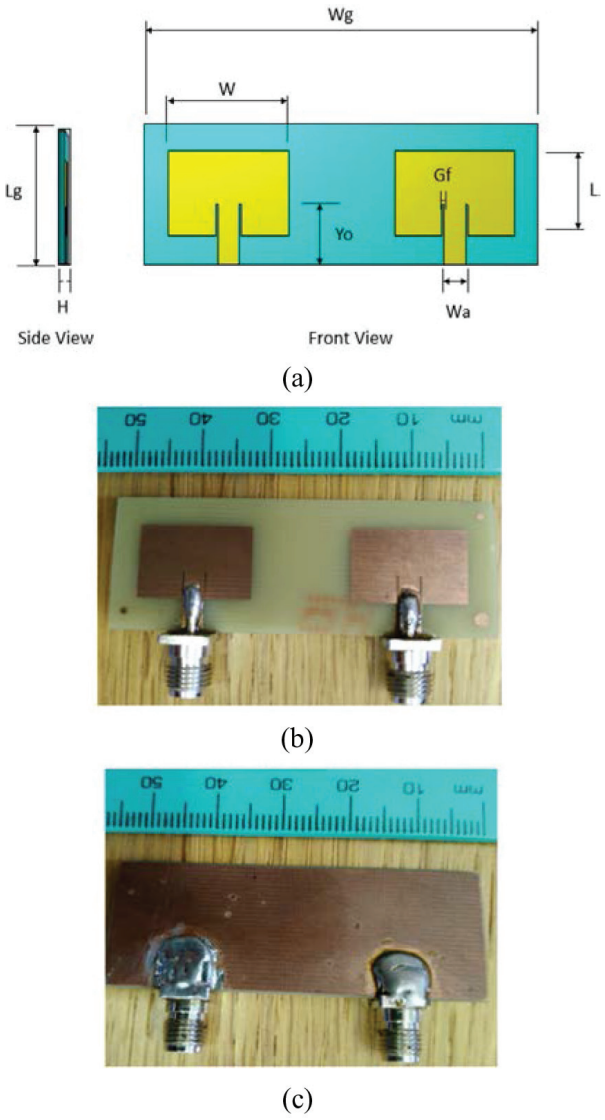

Fig. 1. Two-port MIMO microstrip antenna (Antenna 1). (a) Antenna configuration. (b) Top view of fabricated Antenna 1. (c) Bottom view of fabricated Antenna 1.

The 5G frequency bands are regularly updated and new bands are availed in different countries. Recently the 3rd Generation Partnership Project (3GGP) extended the 5G FR1 band from (410 MHz − 6 GHz) to (410 MHz − 7.125 GHz), hence introducing 1200 MHz additional spectrum [41]. In 2020, the Federal Communication Commission (FCC) also permitted the usage of 6 GHz band (5.925−7.125 GHz) for unlicensed use. This was done with certain regulations and standards to protect incumbent licensed services from interference [42-45]. This approval of 6 GHz for unlicensed use has introduced a new market for 6 GHz wireless solutions like the new Wi-Fi 6E which is an extension for Wi-Fi 6 which operates at the (2.4 and 5 GHz) bands [42].

Table 1: Dimensional parameters of the MIMO antenna and the metasurface unit cell

Parameter	Value (mm)	Parameter	Value (mm)
Wg	55	Wgm	7.844
Lg	20.382	Lgm	7.844
W	16.3	Wm1	5.06
L	11.3822	Lm1	5.06
Wa	2.89	Wm2	2
Yo	4.2112	G1	1
Gf	0.083781	G2	0.5
H	1.5	H	1.5
Ws	65	Hs1	6.5
Ls	33.862	Hs2	3

The two-port MIMO rectangular microstrip antenna is depicted in Figure 1. It is printed on an FR-4 substrate with a dielectric constant of 4.4, a loss tangent of 0.002, and a substrate thickness of 1.5 mm. The top view and bottom view of fabricated Antenna 1 are shown in Figures 1 (b) and (c), respectively. The thickness of the copper layer is 0.035 mm. The dimensional parameters of the antenna and metasurface unit cell are listed in Table 1.

B. Metasurface

The dielectric properties of the dielectric material can be utilized to improve the performance of the microstrip antenna [46, 47]. Metasurface-based antenna designs have been previously utilized [48–52]. In [51], a metasurface superstrate is suspended above an antenna array for m-coupling reduction purposes. A mutual coupling reduction of 19 dB is achieved. In [52], a metasurface superstrate is also utilized to reduce the m-coupling of an antenna array. Maximum m-coupling reduction of 25 dB is achieved. In both designs, the employment of metasurface superstrates results in significant antenna mismatches. In [51], when the metasurface superstrate is employed, the reflection coefficient is significantly increased from −30 to −9 dB, while in [52], the reflection coefficient is increased from −20 to −5 dB. To combat the antenna mismatches, a U-shaped slot was etched on all elements of the antenna array. However, introducing the slots to an antenna changes the path of the current distribution which can result in changes in radiation patterns and impedance. Additionally, the introduction of the U-slot increases fabrication cost and complexities. The design conducted in this paper does not require additional matching methods, which means that it is inexpensive to fabricate and the structure is less complex. In addition to that, this design can be implemented in already existing antenna designs because it does not change the original structure of the antenna.

The decoupling metasurface is designed using SRR to achieve a negative permeability medium. They are

formed by a pair of metal loops printed on a dielectric substrate with gaps or slits 180° from each other. The split gap between the rings results in a capacitance, while the metal loops result in an inductance, hence forming an *LC* circuit. This *LC* circuit is responsible for producing the resonant frequency of the metasurface, while the magnetic field induced in SRR is responsible for creating negative permeability. The metasurface unit cell is depicted in Figure 2. It consists of lossless copper loops printed on an FR-4 substrate with dielectric constant of 4.4, a thickness of 1.5 mm, and a loss tangent of 0.002. The optimized dimensions of the unit cell are listed in Table 1.

The negative frequency region and the resonant frequency of the designed SRR unit cell are as the result of the physical dimensions of the ring and the size of the slip gap between the rings. During the design and optimization of the unit cell, the dimensions of the rings and split gaps are varied to obtain the desired resonant frequency, permeability, and permittivity. In this design, the optimization parameters are selected to be G1 and G2. The real and imaginary values of permittivity (ε) and permeability (μ) of the SRR unit cell are extracted using CST Microwave Studio. However, the real parts are the ones of significant concern in this design. Figure 3 depicts the real part of permittivity and permeability. It can be observed that the real part of permeability is negative in the 6-GHz frequency range, while the real part of permittivity is positive in the same frequency range. The real part of permeability while varying split gap 1 (G1) is depicted in Figure 4. From Figure 4, it can be observed that varying G1 changes the resonant frequency as well as the permeability of the unit cell. The designed metasurface is used in the reference microstrip antenna; it introduces the region with negative permeability and positive permittivity.

In this region, the wave number is given by [51, 52]

$$\boldsymbol{k} = \boldsymbol{k_o}.\sqrt{-|\mu_r|.|\varepsilon_r|} = \boldsymbol{jk_o}.\sqrt{|\mu_r|.|\varepsilon_r|}. \quad (1)$$

From eqn (1), it can be observed that k is purely imaginary, resulting in the electric field of the x-component

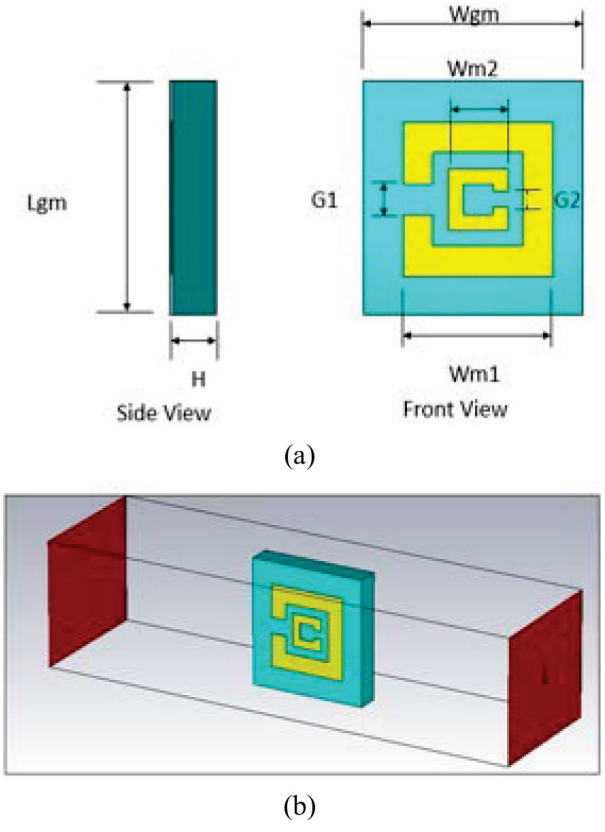

Fig. 2. Metasurface unit cell. (a) Geometry. (b) CST simulation model.

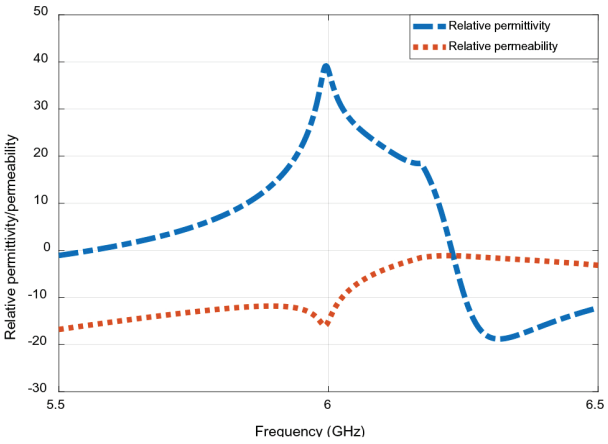

Fig. 3. Relative permittivity (ε_r) and relative permeability (μ_r) of the metasurface unit cell.

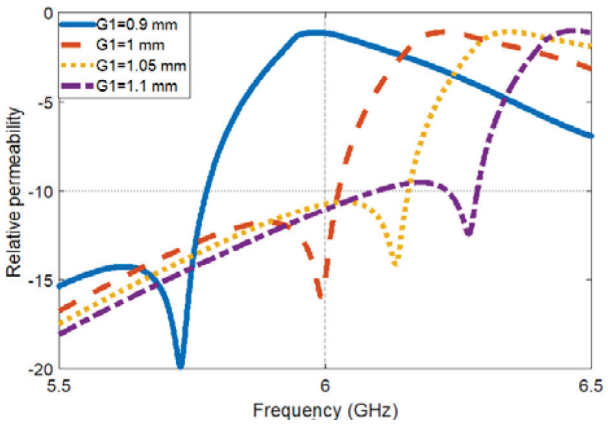

Fig. 4. Real part of permeability with different values of G1.

$(A_o e^{jkx})$ to be expressed as [51, 52]

$$A_o e^{jkx} \cdot e^{jwt} = A_o e^{j(jk_o \cdot \sqrt{|\mu_r| \cdot |\varepsilon_r|})x} \cdot e^{jwt}, \quad (2)$$

and

$$A_o e^{j(jk_o \cdot \sqrt{|\mu_r| \cdot |\varepsilon_r|})x} \cdot e^{jwt} = A_o e^{-k_o \cdot \sqrt{|\mu_r| \cdot |\varepsilon_r|}x} \cdot e^{jwt}. \quad (3)$$

This shows that the electromagnetic wave propagating along the negative x-component direction is evanescent. This means that the m-coupling resulting from the surface waves can be rejected.

C. Antenna 2

This design utilizes a single metasurface superstrate suspended above the antenna to reduce m-coupling between the two microstrip antenna elements. The metasurface superstrate is made up of periodic SRR unit cells printed on one side of an FR-4 substrate with a dielectric constant of 4.4 and a loss tangent of 0.002. The unit cells are placed at a distance (D) from each other. The CST model of this design is depicted in Figure 5 (a). The top view and bottom view of fabricated Antenna 2 are shown in Figures 5 (b) and (c), respectively. The optimized design parameters of Antenna 2 are listed in Table 1.

D. Antenna 3

This design utilizes a double metasurface superstrate to reduce m-coupling between two microstrip antenna elements. The substrate ($W_s \times L_s \times H$) is made up of 4×8 SRR unit cells. Each metasurface substrate uses four dielectric poles to provide mechanical support. Figure 6 (a) depicts the CST model of Antenna 3. The top view of fabricated Antenna 3 and the combined fabricated Antenna 3 are shown in Figures 6 (b) and (c), respectively. The optimized dimensions of Antenna 3 are listed in Table 1.

III. RESULTS AND DISCUSSION

All the three antennas, which include the reference microstrip antenna (Antenna 1), the single suspended metasurface superstrate antenna (Antenna 2), and the double suspended metasurface substrate antenna (Antenna 3), are simulated using CST Microwave Studio. The antenna parameters which include reflection coefficient, radiation patterns, m-coupling, gain, and envelope correlation coefficient (ECC) are assessed, compared, and discussed. Figure 7 depicts the reflection coefficients of the antennas. From Figure 7, it can be seen that the reflection coefficient of Antenna 2 have significantly increased from -24 to -14 dB, which indicates that this antenna is not well matched, when compared to the reference antenna (Antenna 1). Additionally, a major bandwidth reduction of 49% at the frequency range of $6.05 - 6.15$ GHz can be seen from the $S11$ parameter, while a bandwidth reduction of 43% can be seen from $S22$ parameter. Antenna 3 can be seen to

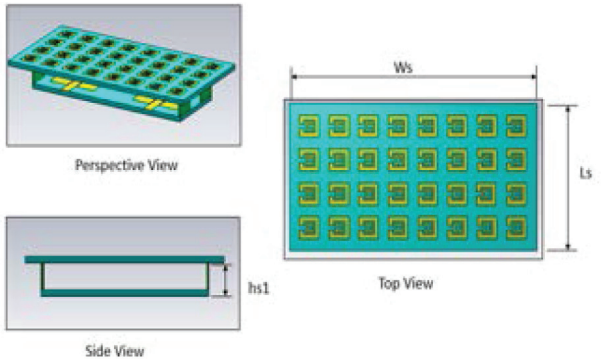

(a)

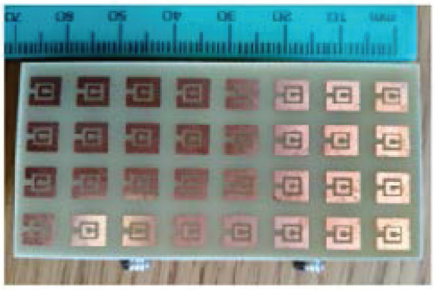

(b)

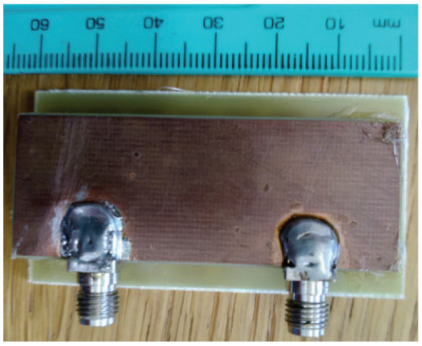

(c)

Fig. 5. Single suspended metasurface antenna (Antenna 2). (a) Antenna configuration. (b) Top view of fabricated Antenna 2. (c) Bottom view of fabricated Antenna 2.

be well matched with a bandwidth enhancement of 38% and 17% at the frequency range of $5.92 - 6.2$ GHz for $S11$ and $S22$ parameters, respectively.

The m-coupling of the antennas is depicted in Figure 8. It can be seen that the m-coupling of Antenna 1 is drastically improved using the two mutual decoupling methods. Both Antenna 2 and Antenna 3 show m-coupling reduction over the entire bandwidth. Antenna 2 shows a maximum m-coupling of -60.6 dB from -29 dB, which is equivalent to a total m-coupling reduction of 31.6 dB. Antenna 3 shows a maximum

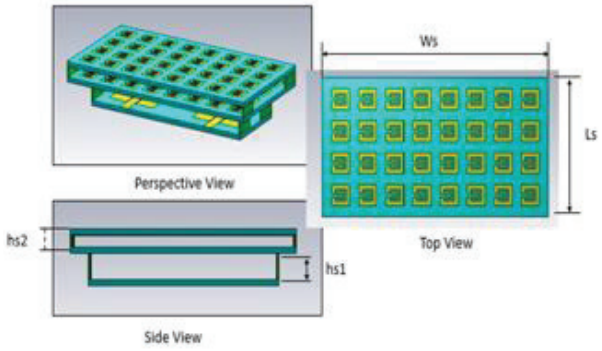

(a)

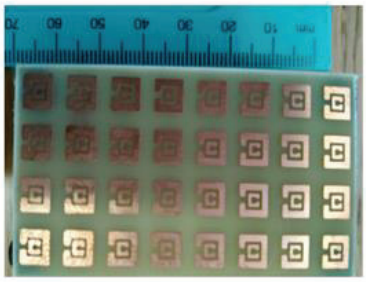

(b)

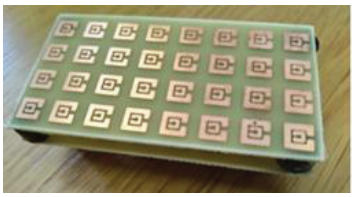

(c)

Fig. 6. Double suspended metasurface antenna (Antenna 3). (a) Antenna configuration. (b) Top view of fabricated Antenna 3. (c) Combined Antenna 3.

m-coupling reduction of −46 dB from −24 dB, which is equivalent to a total m-coupling reduction of 22 dB.

Figure 9 depicts the reflection coefficient of Antenna 2 with respect to various metasurface suspension heights (hs1). During the design of the metasurface-based antenna, hs1 is varied to obtain the optimal reflection coefficient and mutual coupling at the desired resonant frequency. It can be seen that varying hs1, the resonant frequency and the *S*-parameters can be optimized.

Figures 10 (a)-(c) depict the simulated and measured *S*-parameters of Antenna 1, Antenna 2, and Antenna 3, respectively. Both simulated and measured results confirm the suitability of these antennas for mid-band 5G communication. Minor discrepancies can be seen between the simulated *S*-parameters and the measured *S*-parameters, and these discrepancies can be attributed to soldering residue, vector network analyzer calibration, fabrication, and assembly error.

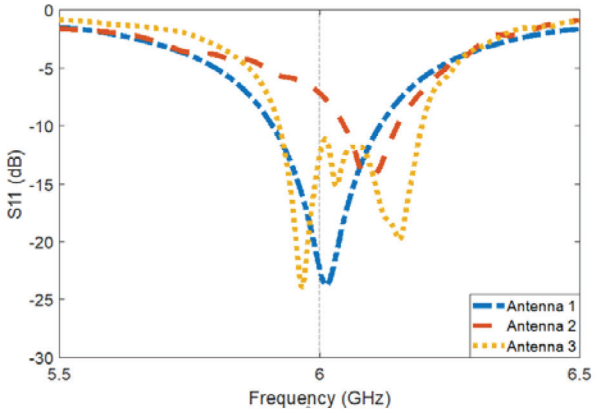

(a)

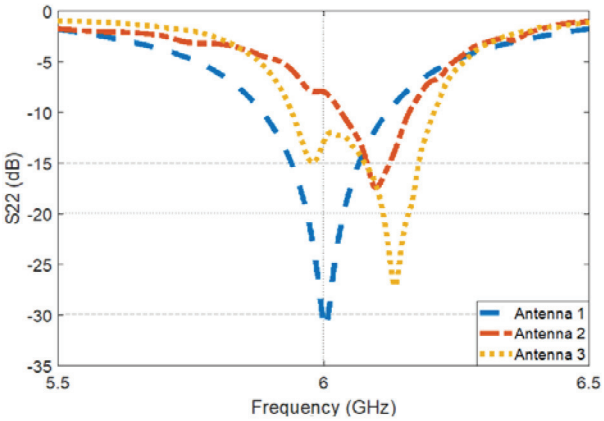

(b)

Fig. 7. Reflection coefficient of the antennas: (a) at port-1; (b) at port-2.

The radiation patterns of the antennas in the *H*-plane (Phi = 0°) and *E*-plane (Phi = 90°) at 6 GHz are depicted in Figure 11. Table 2 presents the radiation pattern parameters of the antennas which include main lobe direction, 3 dB beamwidth, total efficiency, radiation efficiency, maximum gain, and maximum directivity.

From Figure 11, it can be observed that the radiation pattern in the *E*-plane of Antenna 2 is highly distorted, while that of Antenna 3 can be seen to be more directive when compared to that of Antenna 1. This can also be seen that there is major gain increase of 2.09 dB. There is a slight decrease in the 3 dB beamwidth and an increase in maximum directivity of Antenna 3. Meanwhile, the *H*-plane radiation patterns of antennas are highly maintained. From Table 2, it can be observed that Antenna 2 shows a major decrease in total efficiency from 70% to 26%. This shows that Antenna 2 is poorly matched, while Antenna 3 also shows a decrease in total efficiency from 70% to 55% when compared to Antenna 1. This is still acceptable due to the fact that the efficiency is still greater than 50%.

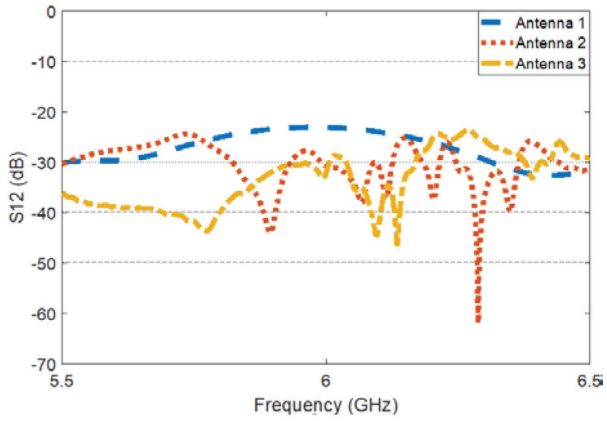

(a)

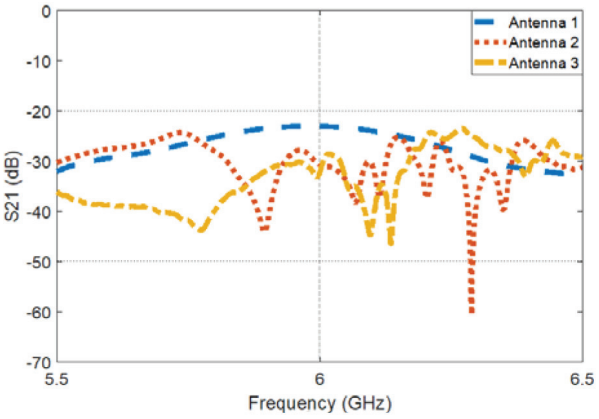

(b)

Fig. 8. M-coupling coefficient of the antennas. (a) $S12$. (b) $S21$.

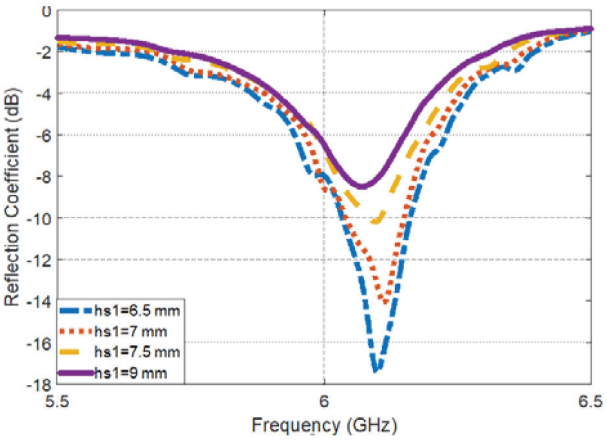

Fig. 9. Reflection coefficient of Antenna 2 with respect to different hs1 values.

Figure 12 depicts the realized gain for all three antennas. It can be observed that Antenna 2 shows a significant gain reduction over the entire bandwidth.

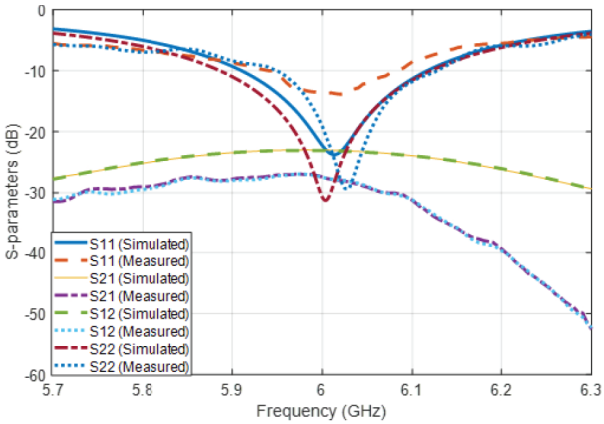

(a)

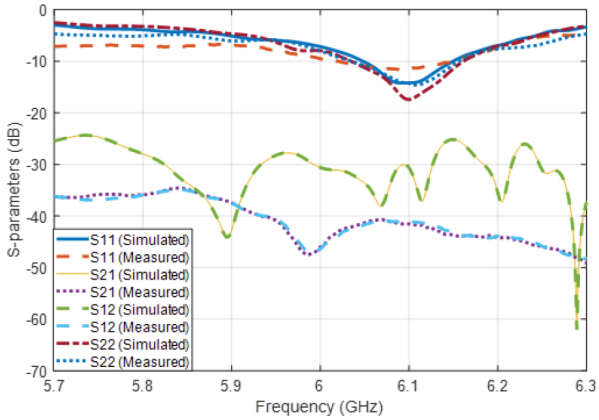

(b)

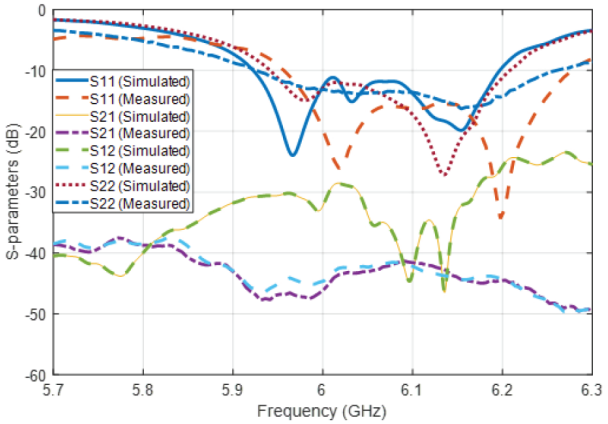

(c)

Fig. 10. Simulated and measured S-parameters of (a) Antenna 1, (b) Antenna 2, and (c) Antenna 3.

At 6 GHz, the gain of the antenna is reduced from 4.7 to 1.69 dB, which is equivalent to a gain reduction of 3.01 dB, while Antenna 3 shows a gain value 6.79 dB which is equivalent to a significant gain increase of 2.09 dB when compared to the reference antenna.

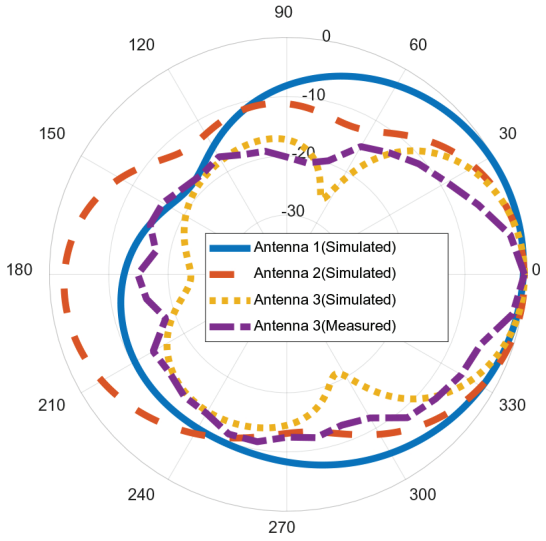

(a)

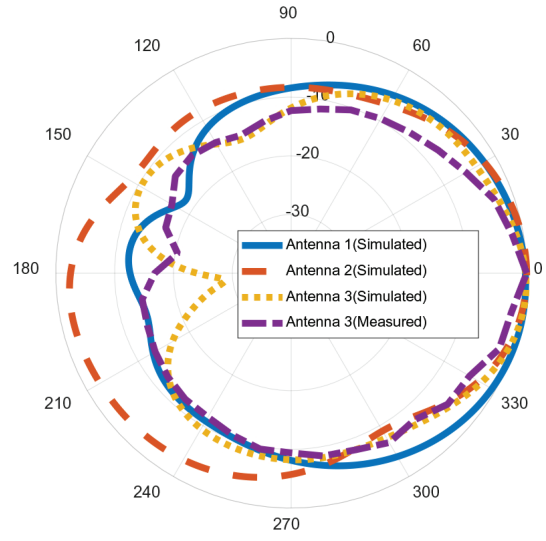

(b)

Fig. 11. Radiation patterns of the antennas. (a) *H*-plane. (b) *E*-plane.

This is attributed to the major m-coupling reduction that was achieved.

The ECC is also an important parameter to consider for any MIMO systems. It is also used to check the m-coupling in MIMO antenna systems. For a two-port MIMO antenna, the ECC can be calculated from *S*-parameters using the following equation [4]:

$$\rho_e = \frac{|S^*_{11}S_{12} + S^*_{21}S_{22}|}{(1-(|S_{11}|^2+|S_{21}|^2))(1-(|S_{12}|^2+|S_{12}|^2))}. \quad (4)$$

Table 2: Main lobe direction (in degrees), **3** *dB* beamwidth (in degrees), total efficiency, radiation efficiency, maximum gain (in **d***B*), and maximum directivity (in **d***Bi*)

Antenna parameters	**Antenna 1**	**Antenna 2**	**Antenna 3**
Main lobe direction (phi = 0°)	11	1	6
Main lobe direction (phi = 90°)	12	3	0
3-dB Beamwidth (phi = 0°)	93.1	65.4	53.9
3-dB Beamwidth (phi = 90°)	99.1	61.9	50.1
Total efficiency	70%	26%	55%
Radiation efficiency	75%	32%	55%
Maximum gain	4,7	1.69	6.79
Maximum directivity	6.12	6.6	9.24

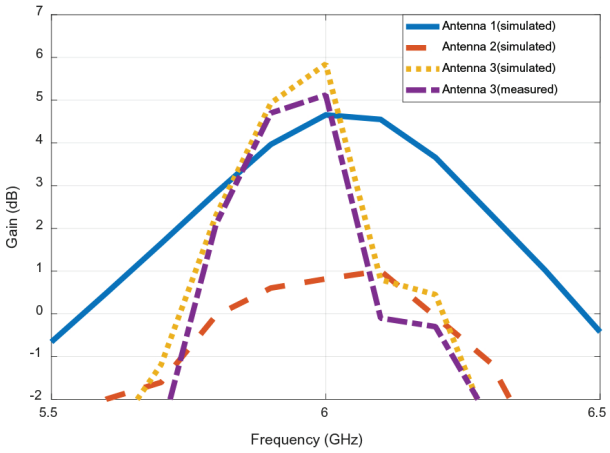

Fig. 12. Realized gain of the antennas.

Figure 13 depicts the ECCs of all three antennas. It can be seen that at 6 GHz, the ECC is less than 0.01, which demonstrates that two microstrip antenna elements are not correlated and that the m-coupling is well reduced.

Antenna 1 achieves maximum m-coupling reduction of 32 dB, while Antenna 2 achieves the maximum m-coupling reduction of 22 dB, 39% bandwidth increase, and a 2.09 dB gain enhancement. Table 3

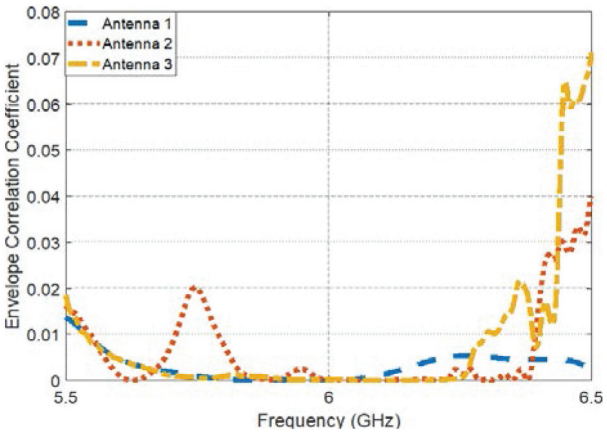

Fig. 13. Envelope correlation coefficient of the reference antenna and the proposed antennas.

Table 3: Comparison of the proposed antenna with the related works

Ref.	Size	Bandwidth	Method used	Edge to edge separation	m-coupling reduction	Gain enhancement
[1]	78 ×60 mm^2	4.85–5.1 GHz (approx.)	MTM	0.25	5.5 dB	-
[9]	130 × 80 mm^2	704–960 MHz, 1.7–2.17 GHz	DN	0.1	9 dB	-
[15]	480 × 160 mm^2 (approx.)	2.35–2.45 GHz	EBG	0.75	6 dB	-
[23]	140 × 100 mm^2	11.82–12.2 GHz (approx.)	Parasitic patches	0.72	9 dB	-
[24]	43 ×43 mm^2	2.27–2.35 GHz	DGS	0.116	10 dB	-
Proposed Antenna 3	65 ×33.862 mm^2	5.92–6.2 GHz	MTS	0.29	22 dB	2.09 dB

compares the proposed metasurface-based antenna (Antenna 3) with the other decoupling methods. The techniques that are referenced and compared are the recent mutual decoupling techniques and they include DN, EBG, DGS, and MTM structures. It can be seen from the table that the proposed work is quite effective in reducing m-coupling when compared to other listed works. Moreover, the proposed structure also shows some other advantages when compared to other works such as bandwidth enhancement and gain improvement.

IV. CONCLUSION

In this paper, two metasurface superstrate-based antennas with reduced m-coupling between the ports have been proposed. The first metasurface-based antenna, i.e., Antenna 1 is constructed using a single metasurface superstrate that is suspended above the two radiating antenna elements. The second metasurface based antenna, i.e., Antenna 2 is constructed using a double metasurface superstrate which is also suspended above the two antenna elements. The metasurface superstrate is made up of periodic SRRs printed on a FR-4 dielectric substrate. The metasurface is used for introducing a negative permeability medium, which converts the electromagnetic propagating waves into evanescent, hence rejecting m-coupling. It was shown that both antennas, i.e., Antenna 1 and Antenna 2 achieve significant m-coupling reduction over the entire bandwidth. Antenna 2 showed an m-coupling reduction of 31.6 dB, while Antenna 3 showed an m-coupling reduction of 22 dB, a 38% increase in bandwidth, and a gain enhancement of 2.09 dB. The low m-coupling, wide bandwidth, and high gain properties make Antenna 3 suitable for extended sub-6 GHz 5G wideband MIMO systems.

REFERENCES

[1] M. M. Bait-Suwailam, O. F. Siddiqui, and O. M. Ramahi, "Mutual coupling reduction between microstrip patch antennas using slotted-complementary split-ring resonators," *IEEE Antennas Wirel. Propag. Lett.*, vol. 9, pp. 876-878, 2010. doi: 10.1109/LAWP.2010.2074175.

[2] G. Expósito-Domínguez, J. M. Fernández-González, P. Padilla, and M. Sierra-Castañer, "EBG size reduction for low permittivity substrates," *Int. J. Antennas Propag.*, vol. 2012, pp. 1-8, 2012. doi: 10.1155/2012/106296.

[3] D. Guha, S. Biswas, M. Biswas, J. Y. Siddiqui, and Y. M. M. Antar, "Concentric ring-shaped defected ground structures for microstrip applications," *IEEE Antennas Wirel. Propag. Lett.*, vol. 5, pp. 402-405, 2006. doi: 10.1109/LAWP.2006.880691.

[4] B. C. Pan, W. X. Tang, M. Q. Qi, H. F. Ma, Z. Tao, and T. J. Cui, "Reduction of the spatially mutual coupling between dual-polarized patch antennas using coupled metamaterial slabs," *Sci. Rep.*, vol. 6, pp. 1-8, 2016. doi: 10.1038/srep30288.

[5] M. Alibakhshikenari *et al.*, "A comprehensive survey on various decoupling mechanisms with focus on metamaterial and metasurface principles applicable to SAR and MIMO antenna systems," *IEEE Access*, vol. 8, pp. 192965-193004, 2020. doi: 10.1109/ACCESS.2020.3032826.

[6] L. Zhao and K. Wu, "A decoupling technique for four-element symmetric arrays with reactively loaded dummy elements," *IEEE Trans. Antennas Propag.*, vol. 62, pp. 4416-4421, 2014. doi: 10.1109/TAP.2014.2326425

[7] L. Zhao and K. Wu, "A dual-band coupled resonator decoupling network for two coupled antennas," *IEEE Antennas Propag. Mag.*, vol. 7,

pp. 2843-2850, 2015. doi: 10.1109/TAP.2015.2421973

[8] C. F. Ding et al., "Novel pattern-diversity-based decoupling method and its application to Multielement MIMO Antenna," *IEEE Trans. on Antennas and Prop.*, vol. 66, pp. 4976-4985, 2018. doi: 10.1109/TAP.2018.2851380

[9] W. Chen and H. Lin, "LTE700 / WWAN MIMO antenna system integrated with decoupling structure for isolation improvement," *2014 IEEE Antennas and Prop. Society Int. Symp. (APSURSI),* pp. 178-182, 2014.

[10] M. S. Khan, A. Capobianco, A. I. Najam, I. Shoaib, E. Autizi, and M. Farhan, "Compact ultra-wideband diversity antenna with a floating parasitic digitated decoupling structure," *IET Microw., Antennas Propag.*, vol. 747, 2014. doi: 10.1049/iet-map.2013.0672

[11] R. Xia, S. Qu, S. Member, P. Li, Q. Jiang, and Z. Nie, "An efficient decoupling feeding network for microstrip antenna array," *IEEE Antennas Wirel. Propag. Lett.*, vol. 14, pp. 871-874, 2015. doi: 10.1109/LAWP.2014.2380786

[12] I. Nadeem and D. Choi, "Study on mutual coupling reduction technique for MIMO antennas," *IEEE Access*, vol. 7, pp. 563-586, 2019. doi: 10.1109/ACCESS.2018.2885558.

[13] I. Mohamed and M. Abdalla, "Reduced size mushroom like EBG for antenna mutual coupling reduction," *32nd Natl. RADIO Sci. Conf.*, pp. 57-64, 2015. doi: 10.1109/NRSC.2015.7117815

[14] V. Ionescu, M. Hnatiuc, and A. TopalA, "Optimal design of mushroom-like EBG structures for antenna mutual coupling reduction in 2.4 GHz ISM band," *2015 E-Health Bioeng. Conf. EHB*, pp. 19-22, 2015. doi: 10.1109/EHB.2015.7391559.

[15] F. Benykhlef and N. Boukli, "EBG structures for reduction of mutual coupling in patch antennas arrays," *J. Commun. Softw. Syst.*, vol. 13, pp. 9-14, 2017. doi: 10.24138/jcomss.v13i1.242.

[16] X. Jiang et al., "A low mutual coupling MIMO antenna using EBG structures," Prog. In Electrom. Research Symp., 2017. doi: 10.1109/PIERS.2017.8261823

[17] A. Suntives and R. Abhari, "Miniaturization and isolation improvement of a multiple-patch antenna system using electromagnetic bandgap," *Microw. Opt. Technol. Lett.*, vol. 55, no. 7, pp. 1609-1612, 2013. doi: 10.1002/mop.27621

[18] S. Ghosh, S. Member, T. Tran, and T. Lengoc, "Dual-layer EBG-based miniaturized multi-element," *IEEE Antennas Propag.*, vol. 62, pp. 3985-3997, 2014. doi: 10.1109/TAP.2014.2323410

[19] B. Mohamadzade and M. Afsahi, "Mutual coupling reduction and gain enhancement in patch array antenna using a planar compact electromagnetic bandgap structure," *IET Microwaves, Antennas Propag.*, pp. 1719-1725, 2017. doi: 10.1049/iet-map.2017.0080.

[20] J. Lee, S. Kim, and J. Jang, "Reduction of mutual coupling in planar multiple antenna by using 1-D EBG and SRR structures," *IEEE Trans. Antennas Propag.*, vol. 63, pp. 4194-4198, 2015. doi: 10.1109/TAP.2015.2447052

[21] A. Dharmarajan et al, "A high gain UWB human face shaped MIMO microstrip printed antenna with high isolation," *Mult. Tools and App.*, 2022. doi: 0.1007/s11042-021-11827-7

[22] F. Zulkifli, E. Rahardjo, and D. Hartanto, "Mutual coupling reduction using dumbbell defected ground structure for multiband microstrip antenna array," *Prog. Electromagn. Res. Lett.*, vol. 13, 29 2010. doi:10.2528/PIERL09102902

[23] Q. C. Zhang, J. D. Zhang, and W. Wu, "Reduction of mutual coupling between cavity-backed slot antenna elements," *Prog. Electromagn. Res. C*, vol. 53, no. 27, 2014. doi: 10.2528/PIERC14052908.

[24] C. Y. Chiu et al., "Reduction of mutual coupling between closely-packed antenna elements," *IEEE Trans. on Antennas and Prop.*, vol. 55, no. 6, pp. 1732-1738, 2007. doi: 10.1109/TAP.2007.898618

[25] M. I. Ahmed, A. Sebak, E. A. Abdallah, and H. Elhennawy, "Mutual coupling reduction using defected ground structure (DGS) for array applications," *2012 15th Int. Symp. Antenna Technol. Appl. Electromagn.,* 2012. doi: 10.1109/ANTEM.2012.6262354.

[26] G. Dadashzadeh, A. Dadgarpour, F. Jolani, and B. S. Virdee, "Mutual coupling suppression in closely spaced antennas," *IET Microwaves, Antennas Propag.*, vol. 5, 2011. doi: 10.1049/iet-map.2009.0564.

[27] F. G. Zhu, J. Xu, and Q. Xu, "Reduction of mutual coupling between closely-packed antenna elements using defected ground structure," *Proc. - 2009 3rd IEEE Int. Symp. Microwave, Antenna, Propag. EMC Technol. Wirel. Commun.*, pp. 1-4, 2009. doi: 10.1109/MAPE.2009.5355659..

[28] Q. L. Zhang, Y. T. Jin, J. Q. Feng, X. Lv, and L. M. Si, "Mutual coupling reduction of microstrip antenna array using metamaterial absorber," *2015 IEEE MTT-S Int. Microw. Work. Ser. Adv. Mater. Process. RF THz Appl.,* 2015. doi: 10.1109/IMWS-AMP.2015.7324947

[29] H. Kondori, M. A. Mansouri-birjandi, and S. Tavakoli, "Reducing mutual coupling in microstrip

array antenna using metamaterial spiral resonator," *Int. J. Comput. Sci. Issues*, vol. 9, 2012.

[30] A. A. Odhekar et al., "Mutual coupling reduction using metamaterial structure for closely spaced microstrip antennas," *IJCA Proceedings on Int. Conf. on Comm. Technology*, pp. 9-11, 2013.

[31] A. H. Jabire et al., "Metamaterial based design of compact UWB/MIMO monopoles antenna with characteristic mode analysis," *Appl. Sci.*, vol. 11, no. 4, 1542, 2021. doi: 10.3390/app11041542

[32] S. Luo and Y. Li, "A dual-band antenna array with mutual coupling reduction using 3D metamaterial structures," *ISAP 2018 - 2018 Int. Symp. Antennas Propag*., pp. 5-6, 2018.

[33] K. Yu, Y. Li, and X. Liu, "Mutual coupling reduction of a MIMO antenna array using 3-D novel meta-material structures," *The Applied Computational Electromagnetics Society (ACES) Journal*, vol. 33, 758, 2018.

[34] P. Kumar and J. L. Masa-Campos, "Dual polarized monopole patch antennas for UWB applications with elimination of WLAN signals," *Adv. Electromag.*, vol. 5, no. 1, pp. 46-52, 2016. doi: 10.7716/aem.v5i1.305

[35] P. Kumar and J. L. Masa-Campos, "Dual polarized microstrip patch antennas for ultra wideband applications, *Microw. and Opt. Tech. Lett.,* vol. 56, no. 9, pp. 2174-2179, 2014. doi: 10.1002/mop.28504

[36] A. Kapoor et al., "Compact wideband-printed antenna for sub-6 GHz fifth-generation applications," *Int J Smart Sensing Intell Syst*, vol. 13, pp. 1-10, 2020. doi: 10.21307/ijssis-2020-033

[37] P. Kumar et al., "Flexible substrate based printed wearable antennas for wireless body area networks medical applications," *Radioelectro. and Comm. Sys*., vol. 64, no. 7, pp. 337-350, 2021. doi: 10.3103/S0735272721070013

[38] R. Mishra et al., "Compact high gain multiband antenna based on split ring resonator and inverted F slots for 5G industry applications," *The Applied Computational Electromagnetics Society (ACES) Journal*, vol. 36, no. 8, pp. 999-1007, 2021. doi: 10.47037/2021.ACES.J.360808999

[39] T. O. Olawoye and P. Kumar, "A high gain microstrip patch antenna with slotted ground plane for sub-6 GHz 5G communications, *Int. Conf. on Adv. in Big Data, Comp. and Data Comm. Sys.,* pp. 1-6, 2020. doi: 10.1109/icABCD49160.2020.9183820

[40] B. W. Ngobese and P. Kumar, "A high gain microstrip patch array for 5 GHz WLAN applications," *Adv. Electromag.*, vol. 7, no. 3, pp. 93-98, 2018. doi: 10.7716/aem.v7i3.783

[41] "Unlinced use of the 6 GHz Band, (report and order futher notice of propsed rulemaking ET Docket N0. 18-295, GN Docket No. 17-1823)," Washington, D.C 20554, 2020.

[42] "5G Spectrum public policy position," (2016). [Online]. Available: https://www.gsma.com/spectrum/wp-content/uploads/2016/06/GSMA-5G-Spectrum-PPP.pdf

[43] "5G frequency bands, channels for FR1 & FR2," 2021. https://www.electronics-notes.com/articles/connectivity/5g-mobile-wireless-cellular/frequency-bands-channels-fr1-fr2.ph

[44] D. Rowell, "The 6 GHz network?: Bigger channels, stronger signal, faster data," 2020. https://www.hpe.com/us/en/insights/articles/the-6-ghz-network-bigger-channels-stronger-signal-faster-data-2007.html.

[45] T. Lee, "What you should know about Wi-Fi 6 and the 6-GHz band," 2019. https://www.testandmeasurementtips.com/what-you-should-know-about-wi-fi-6-and-the-6-ghz-band/.

[46] N. Hussain et al., "A high-gain microstrip patch antenna using multiple dielectric superstrates for WLAN applications," *The Applied Computational Electromagnetics Society (ACES) Journal*, vol. 35, no. 2, 2020.

[47] R. S. Saxena et al., "Effects of dielectric substrate material microstrip antenna for limited band applications," *Journal of Physics: Conference Series*, 012124, pp. 1-6, 2021. doi: 10.1088/1742-6596/2070/1/012124

[48] N. Hussain and I. Park, "Performance of multiple-feed metasurface antennas with different numbers of patch cells and different substrate thicknesses," *The Applied Computational Electromagnetics Society (ACES) Journal*, vol. 33, no. 1, pp. 49-55, 2018.

[49] S. Dubazane et al., "Metasurface based MIMO microstrip antenna with reduced mutual coupling" *IEEE Africon*, pp. 1-7, 2021. doi: 10.1109/AFRICON51333.2021.9570916

[50] L. N. Nguyen, "A new metasurface structure for bandwidth improvement of antenna array," *The Applied Computational Electromagnetics Society (ACES) Journal,* vol. 36, no. 2, pp. 139-144, 2021.

[51] Z. Wang, L. Zhao, Y. Cai, S. Zheng, and Y. Yin, A meta-surface antenna array decoupling (MAAD) method for mutual coupling reduction in a MIMO antenna system, *Sci. Rep.*, 2018. doi: 10.1038/s41598-018-21619-z

[52] J. Tang *et al.*, "A metasurface superstrate for mutual coupling reduction of large antenna arrays," *IEEE Access*, vol. 8, 126859, 2020. doi: 10.1109/ACCESS.2020.3008162.

Sthembile Promise Dubazane was born in South Africa, on 27 June 1995. She received the B.Sc. degree in electronic engineering from the University of KwaZulu-Natal, South Africa, in 2017. She is currently working toward the M.Sc. degree in electronic engineering with the University of KwaZulu-Natal, South Africa.

She has a great passion for learning and hopes to conduct her Ph.D. degree studies in near future. Her research areas include antennas, MIMO systems, etc.

Pradeep Kumar received the bachelor's, M.Eng., and Ph.D. degrees in electronics and communication engineering in 2003, 2005, and 2009, respectively. He completed his postdoctoral studies from Autonoma University of Madrid, Spain.

He is currently working with the University of KwaZulu-Natal, South Africa. His current research areas include design and analysis of microstrip antennas, antenna arrays, wireless communications, etc.

Thomas J. O. Afullo received the B.Sc. degree (Hons.) in electrical engineering from the University of Nairobi, Kenya, in 1979, the M.Sc. degree in electrical engineering from the University of West Virginia, USA, in 1983, and the Ph.D. degree in electrical engineering from Vrije Universiteit Brussel, Belgium, in 1989.

He is currently a Professor with the Discipline of Electrical, Electronic and Computer Engineering, University of KwaZulu-Natal, Durban, South Africa, and a former Academic Leader. He was with Kenya Post and Telecommunication Corporation as a Senior Executive Engineer from 1985 to 1986. He was a Senior Lecturer and the Head of the Department of Electrical and Communication Engineering, Moi University, Kenya, from 1991 to 1994. He was a Lecturer with the University of Botswana from 1996 to 2002, an Associate Professor with UDW/UKZN from 2003 to 2010, and has been a Professor with UKZN since 2012. His research interests include radio wave propagation, antenna design, cognitive radio, and power line communication.

A Novel Double-layer Low-profile Multiband Frequency Selective Surface for 4G Mobile Communication System

Şakir Balta[1] and Mesut Kartal[2]

[1]Department of Electronics and Communication Engineering, Faculty of Electrical and Electronics
Istanbul Technical University, Istanbul, Turkey
sakirbalta@itu.edu.tr

[2]Department of Electronics and Communication Engineering, Faculty of Electrical and Electronics
Istanbul Technical University, Istanbul, Turkey
kartalme@itu.edu.tr

Abstract – A novel double-layer multiband, low-profile frequency selective surface (FSS) for IMT-Advanced (4G) mobile communication system is presented in this article. On aspired to a minimum transmission coefficient of −10 dB for surface materials when the frequency bands targeted for blocking are stopped. For this project, we chose the dielectric substrate FR4 (loss-tangent = 0.02; dielectric constant = 4.54) and a thickness of 1 mm. Dodecagonal rings, upright bars, and square frame make up the FSS unit cell. The desired frequency responses of the FSS were intended to avoid being changed according to the angle of incidence of the electromagnetic waves. The FSS design is proposed as a symmetrical structure to make it polarization-independent and is aimed to stop 800, 900, 1800, 2100, and 2600 MHz frequencies to prevent harmful effects to human health and interference effects at these frequencies. With a cell size of 0.17λ, the planned FSS is quite small and, thus, has a low sensitivity at the angle of the incident wave. In addition, FSS geometry was manufactured by a printed circuit board (PCB) and measured in a non-reflective environment after being studied in Ansys high-frequency structure simulator (HFSS) software. By comparing the analysis and measurement results of the design, the success of the FSS to the frequencies to be stopped has been verified. The effect of each patch on different frequencies has been examined by drawing the surface current density graphs of the design.

Index Terms – Ansys HFSS, frequency selective surface (FSS), FR4, GSM, 4G IMT-Advanced, PCB.

I. INTRODUCTION

Communication systems are constantly diversifying to meet our needs and finding solutions to our problems with the use of different frequencies. The IMT-Advanced 4G GSM mobile communication system, which is currently widely used in mobile communication, also provides high-speed communication by using frequency bands of 800, 900, 1800, 2100, and 2600 MHz. The widespread usage of these new frequency bands gives rise to information security and interference problems between neighboring wireless networks. In addition, the use of each different frequency is a threat to human health. Advanced signal processing techniques and antenna designs attempt to solve these problems. At any time in a daily struggle whereas at home or at the office, exposure to these frequencies is inevitable by reason of not having a prevention system [1]. On the other hand, penetration of a radio frequency (RF) signal to inside of a building can result in interference problems and reduction on communication speed and quality [2].

An important approach to solving all these problems is to isolate the frequency bands used by wireless networks from each other [3]. Periodic arrays of conductive patches or apertures placed on a dielectric medium exhibit reflection and transmission properties that vary with frequency [4]. Antenna and microwave fields have so many applications such as multiband microwave antennas, artificial magnetic conductors, polarizers, radomes, beam splitters, absorber surface designs, etc. Frequency-selective surfaces at various wireless communication systems have begun to be investigated because of finding solutions to problems such as interference, security, signal strength weakening [5], etc. Latest researches on FSS focus on areas with the substrate-integrated waveguide [6], miniaturized frequency selective surfaces (MEFSS) [7], multiband [8], and active [9].

FSS expands a wide range of resonance frequencies. Therefore, many other currently using frequencies are included unintentionally. This leads to importance of minimizing the interference of incoming radio frequency waves, which needs to be prevented on these convergent

Submitted On: August 18, 2021
Accepted On: April 4, 2022

https://doi.org/10.13052/2022.ACES.J.370407

frequency bands. Hence, designing a structural surface material at other frequencies with decent transmission characteristics is crucial [10, 11]. On the other side, there is not enough research on multi-resonant FSS structures that prevent frequency bands of 800, 900, 1800, 2100, and 2600 MHz. In this work, a design is proposed with the goal of achieving a transmission coefficient (S_{21}) of the material in the extinguishing band of at least -10 dB. This design also targets a transmission coefficient (S_{11}) of the transmission band that is near to 0 dB. Another goal for this design is to be very compact, and low sensitivity to incoming wave angle is also a key characteristic.

Two different types of surface waves occur in FSSs. The first type of surface wave, in the condition that the distance between periodic geometries is greater than half of the resonance wavelength, undesired emissions occur in the dielectric layer, called surface waves [12]. The surface waves tend to propagate at frequencies where undesired radiation occurs when they come to the dielectric surface at an angle less than the critical angle and they cause radiation. The second type of surface waves occurs at frequencies that contain a limited number of periodic elements and where the distance between periodic elements is less than half of the resonance wavelength, 20%-30% lower than the resonance frequency [13]. FSS geometries should be placed quite frequently and periodically in order to prevent scattering in the surface waves and to increase the performance at the targeted frequencies.

Generally, wave equation solutions for FSS geometries are done by methods with numerical solutions, whereas solving basic FSS geometries are possible by using Floquet's theory and periodic boundary conditions analytically [10]. Computer technology is developing swiftly. Therefore, applications for numerical analysis methods are now available in this area. Finite-difference time-domain (FDTD) method [14], finite element method (FEM) [15], and method of moments (MoM) are used [16] for obtaining numerical solution methods in FSS geometry analyses.

The design phase is the crucial part for determining the analysis of the FSSs which is finalized with "finite element method" throughout the numerical analysis procedure. Moreover, calculation of transmission and reflection coefficients is done in the preferred frequency range. Such structures with the "FEM" [15] can be analyzed by using Ansys high-frequency structure simulator (HFSS) program.

If we compare our work with similar studies in the literature, the innovations we have brought to the literature are clearly seen. As seen in previous designs, FSS cells are generally designed to block a single frequency [17, 18]. However, in this study, we applied a unique design that blocks these five different frequency bands for the first time in the literature. When we look at the S_{21} graph plotted in the sample article [19], based on the response of the design only to relatively distant frequencies such as 2.4 and 5.8 GHz, it is seen that FSS has a much wider band than ours and affects other frequency regions as well. Our study gives much narrower band responses to the five different frequencies, without affecting frequencies outside of the operating frequencies. If the simulation results and measurement results are compared, it is seen that, unlike other studies [20], simulation results and measurement results are extremely similar and there is no frequency shift in our study.

II. DESIGN OF THE FSS

A. The decision of the structure

The desired frequency responses of the FSS to be designed have been wanted not to be changed depending on the angle of incidence of electromagnetic wave. IMT-Advanced 4G GSM frequencies are 800, 900, 1800, 2100, and 2600 MHz [21]. Because the 4G frequency bands are in close proximity to one another, it has been particularly challenging to design without affecting transmission characteristics at the transmission bands as much as possible, which is why the FSS is designed to be multi-resonant. In this study, simple FSS geometries are curved, whose periods are much smaller relative to the wavelength, and miniature FSS geometries were obtained; thus, the stability of the surfaces has been increased. The sensitivity of this relatively tiny design to the incident wave angle is quite low. The period of the geometry was obtained as 0.17 times the smallest resonance wavelength (λ at 800 MHz). Thus, the stability of the FSS for different angles of incidence of the electromagnetic wave is increased and unwanted emission is provided at much higher frequencies [6]. It has been observed that the obtained FSS exhibits a stable frequency characteristic behavior to the electromagnetic wave which is up to an angle of incidence of 60° to surface normal. For the FSS that has more than one stop band, the resonant geometries of the FSS are placed into the unit cell as hybrid or nested or in different layers.

The interference between resonant geometries is particularly the most important problem encountered at this stage. In this study, new design techniques have been introduced for the solution of the issue. As suggested from the knowledge from the first technique, the interference effect decreases proportionally with the square of the distance. To control the distance between resonant geometries, nested geometries were used in the design. The interference effect can be avoided by keeping the interior geometry distance between interlocking geometries with a high degree of miniaturization as large as possible. Patch-type FSS is selected because it provides

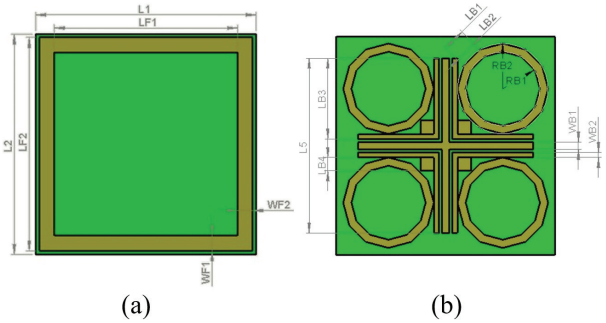

Fig. 1. FSS unit dimensions: (a) the top layer of FSS with dimensions; (b) the bottom layer of FSS with dimensions.

a stop band response, which is in line with the design's goal.

A double-layer FSS unit cell is shown in Figure 1. Square patches are used on the top layer to prevent the 800 MHz frequency, "L" bars are integrated on the bottom layer to be effective at 900 and 1800 MHz frequencies, cross is integrated to stop the 2100 MHz frequency, and dodecagons are used to support the stopping characteristics at 2600 MHz and other frequencies in this FSS unit cell.

B. Dimension of the proposed structure

Electrical properties and thicknesses of dielectric substrates change the frequency characteristics of FSSs. For the dielectric layers to have a minimum effect on the frequency response of the FSS, these layers' electrical properties must be stable and their dependence on ambient temperature is not desired to be high. The costs and difficulties in obtaining these substrates are other important issues to consider. All of this information led to the selection of FR4 as the dielectric material in the design. A 1-mm dielectric with a dielectric constant of 4.54 and a loss tangent of 0.02 has been developed. Different FSS/dielectric arrangements will influence the frequency selective response to a different extent and improve the stability of FSS performance over a range of incident angles. In order to make the FSS less sensitive to different angles of incidence, the dielectric layer thickness, the dielectric constant, and the loss tangent values were selected at their optimal levels.

There are two layers in the proposed FSS: a top layer and a bottom layer. Figure 1 and Tables 1 and 2 show the dimensions of the patch elements.

III. RESULTS AND DISCUSSION

The simulation results in this study were repeated in the ANSYS Electronic Desktop 2020 R2 program for 631 points between 0.5 and 3 GHz. Here, it is aimed to make a one-to-one comparison with the measurement

Table 1: Dimensions of the top layer's structures

Dimensional names	Symbol	Value in (mm)
A single substrate length	L1	65
Other substrate lengths	L2	65
Small square's length	LF1	52
Length of big square	LF2	63
Big square's length	WF1	5.5
Width of lower edge	WF2	5.5

Table 2: Dimensions of the bottom layer's structures

Dimensional names	Symbol	Value in (mm)
Outer dodecagon radius	RB2	13.46
Inner dodecagon radius	RB1	11
Outer dodecagon length	LB1	6.98
Inner dodecagon length	LB2	5.70
Outer rectangle length	LB3	24
Small square length	LB4	4
Cross length	LB5	52
Cross width	WB1	2.2
Outer rectangle width	WB2	1.5

results. HFSS simulates an infinitely periodic unit cell using the Floquet ports and periodic boundaries defined in the software, by making use of the real-life adaptation of Floquet's theorem. Once a Floquet port is defined, a set of modes known as Floquet modes represent areas on the port boundary. Floquet modes are plane waves with a propagation direction determined by the phase, frequency, and geometry of the periodic structure. The design presented a multiband behavior. At each desired frequency band, simulations are run for both TE and TM polarizations, while the incident wave's angle ranges from 0° to 60°. Because the frequency bands of 800 and 900 MHz are adjacent, these two frequency bands were both suppressed by the same structure. Attenuation of at least 10 dB for wide oblique incidence angles was achieved in all frequency bands using multilayer geometries.

On the basis of simulation results for different incidence angles and each desired frequency band, the S_{11} parameters of the proposed FSS in TE polarization are shown in Figure 2.

Based on simulation findings at different incidence angles and in each required frequency band, S_{21} parameters of the proposed FSS in TE polarization are shown in Figure 3 and Table 3.

Based on simulation results at varied incidence angles and each target frequency band, S_{11} parameters of the proposed FSS in TM polarization have been illustrated in Figure 4. S_{21} parameters of the proposed FSS in

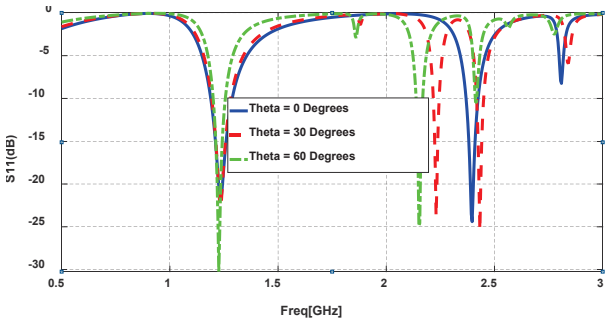

Fig. 2. Simulated reflection coefficient (S_{11}) for TE polarization at various incidence angles.

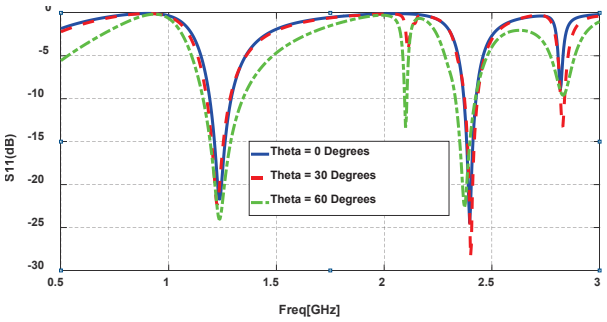

Fig. 4. Simulated reflection coefficient (S_{11}) at different incidence angles for TM polarization.

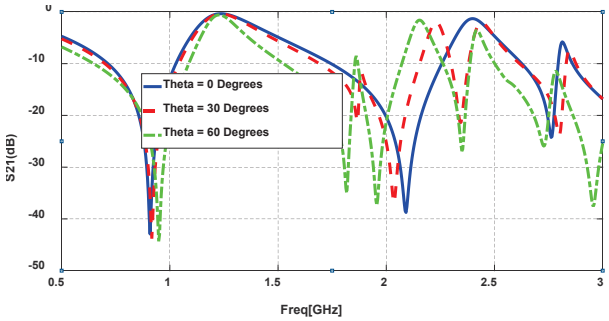

Fig. 3. Simulated transmission coefficient (S_{21}) for TE polarization at various incidence angles.

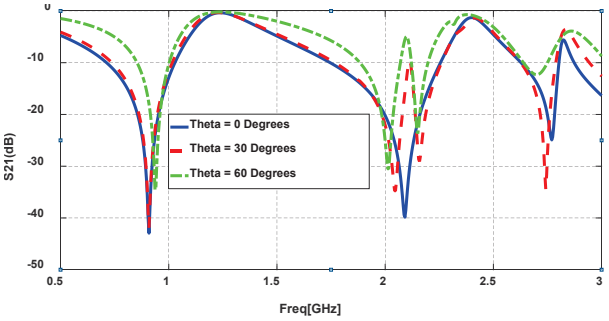

Fig. 5. Simulated transmission coefficient (S_{21}) at different incidence angles for TM polarization.

TM polarization are shown in Figure 5 and Table 4 based on the simulation results at different incidence angles and in each desired frequency band. When the simulation results for both incidence wave angles varies from 0° to 60°, whereas the FSS has a consistent frequency behavior, with attenuation of up to 44 dB in the IMT-Advanced frequency bands.

After simulations, the FSS was fabricated by using 65 mm × 65 mm FR4 dielectric, with a thickness of 1 mm, a relative dielectric constant of 4.54, and a loss tangent of 0.02. The top layer and the bottom layer of the produced FSS are shown in Figures 6 and 7. After the FSS was produced, the measurement setup is shown in Figure 8, and Figure 9 was prepared in order to make measurements. The Vivaldi antenna capable of radiating in the frequency ranges of 600 MHz and 3 GHz was positioned as a transmitter at a distance of about 1.5 m from the FSS surface, and an identical Vivaldi antenna at the same distance on the receiver side and the measurement results of the E8362C model belonging to Agilent Technologies company, shown in Figure 8, were collected with a Network Analyzer that can operate in the frequency range of 10 MHz to 20 GHz.

On the basis of the measurement results at different incidence angles and in each desired frequency band, the S_{21} parameters of the proposed FSS in TE polarization are shown in Figure 10. Measurement and simulation results for different incidence angles at each desired band

Table 3: Transmission coefficient at different frequencies and incidence angles for TE polarization

Frequencies (MHz)					
Angle (degrees)	800 MHz	900 MHz	1800 MHz	2100 MHz	2600 MHz
0	−15	−41	−13	−38	−11
30	−15	−44	−14	−18	−11
60	−16	−26	−32	−10	−14

Table 4: Transmission coefficient at different frequencies and incidence angles for TM polarization

Frequencies (MHz)					
Angle (degrees)	800 MHz	900 MHz	1800 MHz	2100 MHz	2600 MHz
0	−15	−43	−13	−39	−10
30	−15	−44	−12	−15	−11
60	−8	−20	−9	−10	−10

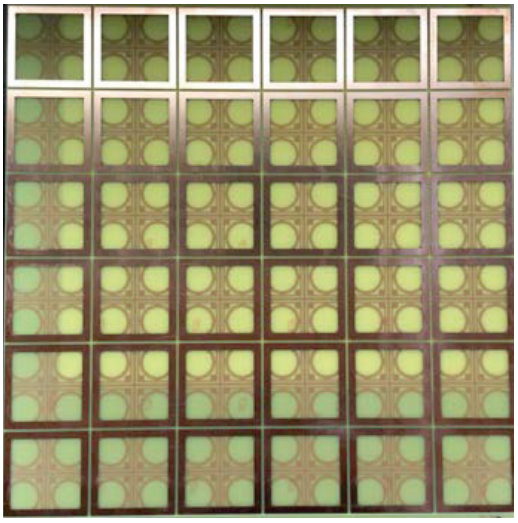

Fig. 6. Top layer of the fabricated FSS.

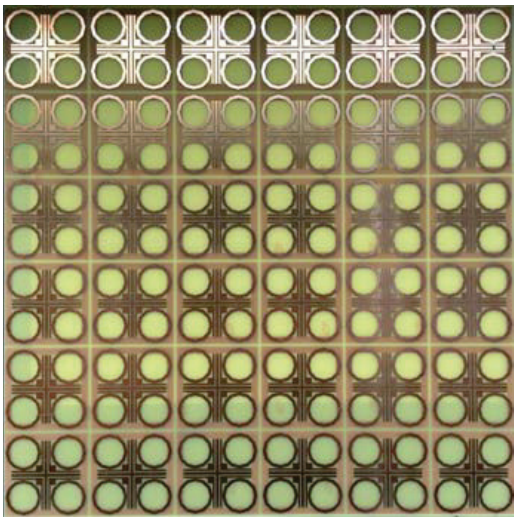

Fig. 7. Bottom layer of the fabricated FSS.

are also presented in Figure 11. Figure 12 shows the S_{21} parameters of the proposed FSS in TM polarization. For each desired band, Figure 13 shows the comparison of the measurement and simulation results in TM polarization for different incidence angles.

On comparing measurement and simulation results, it can be seen that for both TE and TM polarizations, measurements and simulations yield similar results, i.e., the FSS has a stable frequency behavior while the incident wave's angle ranges from 0° to 60°, and more than 20 dB of attenuation is observed in the IMT-Advanced bands.

Figure 14 shows surface currents for IMT-Advanced mobile communication system resonant frequencies of

Fig. 8. The measurement room and measurement setup.

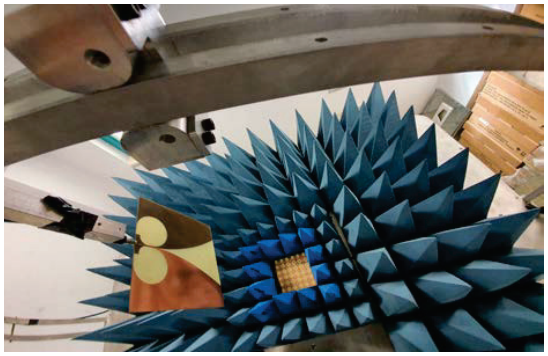

Fig. 9. The measurement setup.

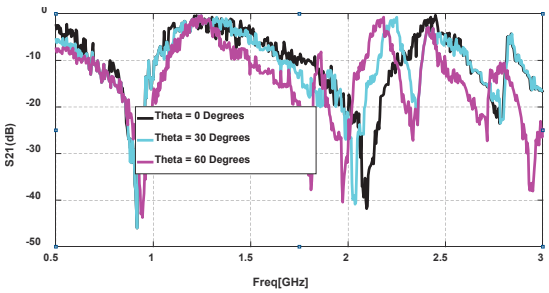

Fig. 10. Measured transmission coefficient (S_{21}) at different incidence angles for TE polarization.

800, 900, 1800, 2100, and 2600 MHz. In the figure, we can see that for each different resonant frequency, surface currents of varying magnitudes occur on different surface elements.

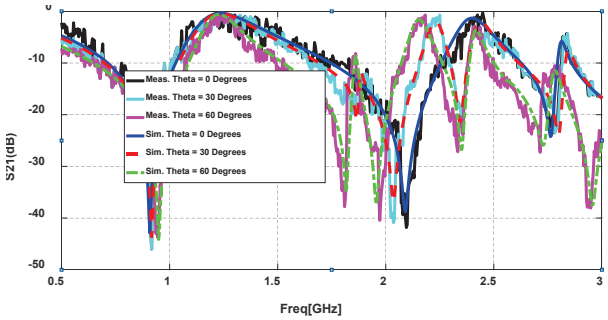

Fig. 11. Measured and simulated transmission coefficient (S_{21}) at different incidence angles for TE polarization.

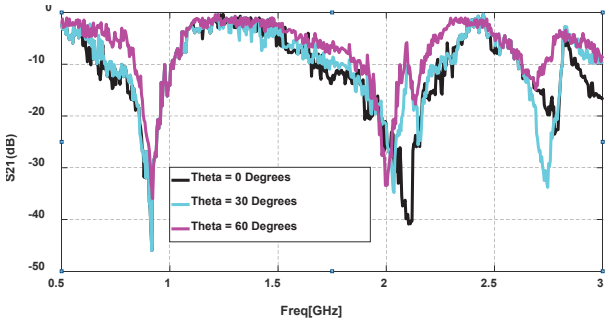

Fig. 12. Measured transmission coefficient (S_{21}) at different incidence angles for TM polarization.

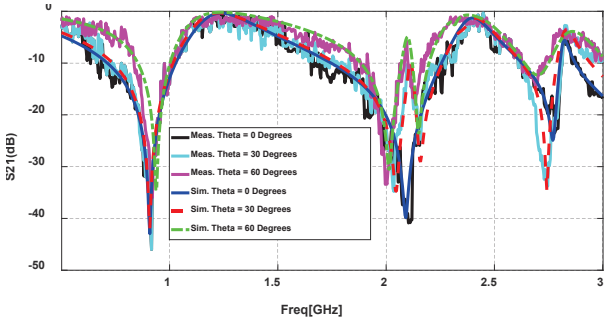

Fig. 13. Measured and simulated transmission coefficient (S_{21}) at different incidence angles for TM polarization.

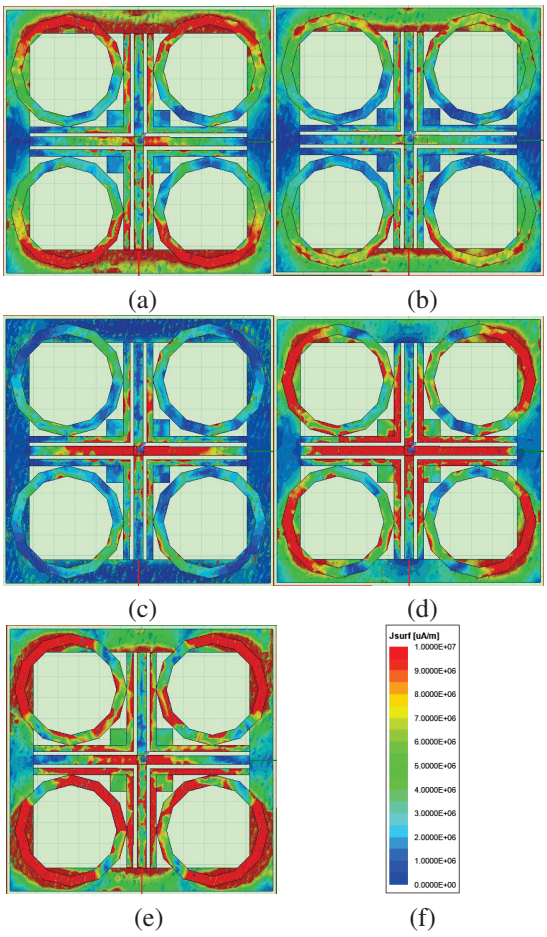

Fig. 14. FSS surface currents. Notice how resonance peaks differ for patches at each 4G frequencies: (a) surface current at 800 MHz; (b) surface current at 900 MHz; (c) surface current at 1800 MHz; (d) surface current at 2100 MHz; (e) surface current at 2600 MHz; (f) scale.

IV. CONCLUSION

A novel double-layer low-profile multiband frequency selective surface (FSS) for a 4G IMT-Advanced mobile communication system has been designed in this research. The suggested FSS performed admirably as a band-stop filter, resonating at frequencies of 800, 900, 1800, 2100, and 2600 MHz. For TE and TM polarizations at each target frequency band, simulations and experiments were carried out while the incoming wave angle varied from 0° to 60°. A double layer FSS was used to achieve the requisite minimum attenuation of 10 dB for large oblique incidence angles throughout all frequency bands. By reducing the thickness of the FSS and using sub-wavelength periodic structures, the design became low-profile and reacted as a higher order band-stop response with minimal sensitivity to incident wave angles.

REFERENCES

[1] B. Döken and M. Kartal, "Triple band frequency selective surface design for global system for mobile communication systems," *IET Microw. Antennas Propag.*, vol. 10, no. 11, pp. 1154-1158, Apr. 2016.

[2] R. Ma, Q. Guo, C. Hu, and J. Xue, "An improved WiFi indoor positioning algorithm by weighted fusion," *Sensors*, vol. 15, pp. 21824-21843, 2015.

[3] F. C. G. da Silva Segundo and A. L. P. S. Campos, "Compact frequency selective surface with dual band response for WLAN applications," *Microwave and Optical Technology Letters*, vol. 57, no. 2, pp. 265-268, 2015.

[4] G. H. Sung, K. W. Sowerby, M. J. Neve, and A. G. Williamson, "A frequency-selective wall for interference reduction in wireless indoor environments," *IEEE Antennas and Propag. Mag.*, vol. 48, no. 5, pp. 29-37, Oct. 2006.

[5] S. Armour, A. Doufexi, B. S. Lee, A. Nix, and D. Bull, "The impact of power limitations and adjacent residence interference on the performance of WLANs for home networking applications," *IEEE Trans. Consumer Electron.*, vol. 47, no. 3, pp. 502-511, 2001.

[6] S. M. A. M. H. Abadi, M. Li, and N. Behdad, "Harmonic-suppressed miniaturized-element frequency selective surfaces with higher order bandpass responses," *IEEE Trans. on Antennas Propag.*, vol. 62, no. 5, pp. 2562-2571, May 2014.

[7] G. Meng and N. Behdad, "A dual-band, inductively coupled miniaturized-element frequency selective surface with higher order bandpass response," *IEEE Trans. on Antennas Propag.*, vol. 64, no. 8, pp. 3729-3734, August 2016.

[8] G. Schennum, "Frequency-selective surfaces for multiple-frequency antennas.," *Microwave Journal*, vol. 16, no. 5, pp. 55-57, 76, 1973.

[9] C. Gu, B. S. Izquierdo, S. Gao, J. C. Batchelor, E. A. Parker, and F. Qin, "Dual-band electronically beam-switched antenna using slot active frequency selective surface," *IEEE Trans. on Antennas Propag.*, vol. 65, no. 3, pp. 1393-1398, Mar. 2007.

[10] B. A. Munk, *Frequency Selective Surfaces: Theory and Design*, John Wiley & Sons, New York, 2000.

[11] C. J. Davenport, J. M. Rigelsford, J. Zhang, and H. Altan, "Periodic comb reflection frequency selective surface for interference reduction," *Loughborough Antennas & Propagation Conference (LAPC)*, pp. 615-618, 2013.

[12] E. F. Kent, B. Doken, and M. Kartal, "A new equivalent circuit based fss design method by using genetic algorithm," *2nd International Conference on Engineering Optimization*, 2010.

[13] M. Philippakis, C. Martel, D. Kemp, R. Allan, M. Clift, S. Massey, S. Appleton, W. Damerell, C. Burton, and E. Parker, "Application of FSS structures to selectively control the propagation of signals into and out of buildings," *Ofcom ref. AY4464A*, 2004.

[14] C. Mias, C. Tsakonas, and C. Oswald, "An investigation into the feasibility of designing frequency selective windows employing periodic structures, (Ref. AY3922)," *Final Report for the Radio Communications Agency*, Nottingham Trent University, 2001.

[15] I. Bardi, R. Remski, D. Perry, and Z. Cendes, "Plane wave scattering from frequency-selective surfaces by the finite-element method," *IEEE Transactions on Magnetics.*, vol. 38, no. 2, 641-644, 2002.

[16] M. Kominami, H. Wakabayashi, S. Sawa, and H. Nakashima, "Scattering from a periodic array of arbitrary shaped elements on a semi infinite substrate," *Electronics and Communications in Japan (Part I: Communications)*, vol. 77, no. 1, 85-94, 1994.

[17] M. Idrees, S. Buzdar, S. Khalid, M. A. Khalid, "A miniaturized polarization independent frequency selective surface with stepped profile for shielding applications," *Applied Computational Electromagnetics Society (ACES) Journal*, vol. 31, no. 5, pp. 531-536, 2016.

[18] H. Ahmad, M. Rahman, S. Bashir, W. Zaman, and F. C. Seman, "Miniaturized frequency selective radome operating in the X-Band with wideband absorption," *Applied Computational Electromagnetics Society (ACES) Journal*, vol. 34, no. 12, pp. 1915-1921, Dec. 2019.

[19] B. Döken and M. Kartal, "Dual layer convoluted frequency selective surface design in the 2.4 GHz and 5.8 GHz ISM bands," *Applied Computational Electromagnetics Society (ACES) Journal*, vol. 33, no. 4, pp. 413-418, 2021.

[20] Z. Yu and W. Tang, "A third-order bandpass three-dimensional frequency selective surface with multiple transmission zeros," *Applied Computational Electromagnetics Society (ACES) Journal*, vol. 35, no. 12, pp. 1548-1555, 2020.

[21] Ş. Balta and M. Kartal, "A novel multilayer multiband frequency selective surface for IMT advanced 4G mobile phone service and airborne radar systems," *9th International Conference on Recent Advances in Space Technologies (RAST),* pp. 527-531, 2019.

Şakir Balta was born in 1986. He received the B.S. degree in electronics and communication engineering in 2009 and the M.S. degree in 2013. He is currently working toward the Ph.D. degree in electronics and communication engineering with Istanbul Technical University, Istanbul, Turkey.

He is still a Chief Researcher with TÜBİTAK (The Scientific and Technological Research Council of Turkey), Kocaeli, Turkey. His research interest includes antenna and FSS design, RF and microwave design engineering, circuit design, logic design, FPGAs (Field Programmable Gate Arrays), as well as modeling, design, simulations, and analysis, and CAD techniques in high frequency region.

Mesut Kartal received the M.S. degree in 1993 and the Ph.D. degree in 2000.

He is still a Professor with Istanbul Technical University, Department of Electronics and Communication Engineering. His research interest includes remote sensing, antenna and FSS design, inverse problems, RF and microwave design engineering, as well as modeling, design, simulations, and analysis, and CAD techniques in high frequency region.

Application of the Multi-element Grid in EMC Uncertainty Simulation

Jinjun Bai[1], Kaibin Guo[1], Jingchao Sun[2], and Ning Wang[1]

[1]College of Marine Electrical Engineering
Dalian Maritime University, Dalian 116026, China
baijinjun@dlmu.edu.cn,guokaibin123123@163.com,n.wang@ieee.org

[2]Traction & Control State Key Lab
CRRC Dalian R& D Co., Ltd, Dalian, 116052, China
sunjingchaofirst@126.com

Abstract – Uncertainty analysis is a research hotspot in the field of electromagnetic compatibility (EMC) simulation. The stochastic collocation method (SCM) is considered particularly suitable for uncertainty analysis in the EMC field because it is characterized by a high level of computational efficiency and accuracy while requiring no replacement solver. However, the post-processing process of the SCM is too complex, which will seriously limit its application in many industrial environments such as real-time simulation analysis. Multi-element grid (MEG) is a novel uncertainty analysis method recently for successful application in another area. It is proved that its calculation accuracy is same as the SCM, and its post-processing process is facile. This paper introduces the MEG to the EMC field and makes a detailed comparison between it and the SCM in performance, aiming to apply uncertainty analysis to solve more practical EMC engineering problems.

Index Terms – Electromagnetic compatibility, uncertainty analysis, stochastic collocation method, multi-element grid.

I. INTRODUCTION

Uncertainty analysis theory has been developed and perfected in the field of computational fluid dynamics (CFD) [1] and introduced into the field of electromagnetic compatibility (EMC) simulation in previous years. Gradually, it has become a hot research issue in the field of EMC simulation.

EMC simulation has its unique characteristics. One is that the time of simulation is usually long due to the frequent use of the finite element method. Therefore, the uncertainty analysis methods with slow convergence speed are not competitive, such as the Monte Carlo method (MCM) [2, 3]. The reason is that too much time cost is unacceptable. However, the calculation accuracy of MCM is the highest; so its simulation results are usually used as standard data in theoretical research to verify the accuracy of other uncertainty analysis methods, and this paper is no exception.

Another characteristic of EMC simulation is that its calculation needs the help of commercial simulation software in most cases. On this premise, the uncertainty analysis method which needs to change the previous solver cannot be used normally, such as the perturbation method [4], the stochastic Galerkin method [5, 6], and the stochastic testing method [7]. At the same time, there are still some uncertainty analysis methods, such as the moment method [8] and the stochastic reduced order models [9]. There are no restrictions in terms of application, but their accuracy is not ideal. Thus, these methods are also difficult to promote.

The stochastic collocation method (SCM) is an efficient uncertainty analysis method based on generalized polynomial chaos theory [10–12]. It has the advantages of high calculation accuracy, high calculation efficiency, and no need to change the solver. From this point of view, the SCM is an ideal uncertainty analysis method in the EMC field at this stage. However, the post-processing process of the SCM is extremely complex, resulting in the following problems in engineering application. First, in the process of real-time simulation, very long post-processing time will affect the response speed of subsequent control operations. Second, the SCM has high algorithm complexity and needs to store a large number of sampling points information. From the perspective of algorithm implementation and storage, it is not easy to write into the one-chip computer; so it is difficult to realize industrial application.

The multi-element grid (MEG) is a novel uncertainty analysis method, which also has the characteristics of high computational efficiency and no need to change the solver [13]. It has been applied successfully in the control area, and its outstanding advantage is that the post-processing process is simple. This paper aims to use

Submitted On: December 31, 2021
Accepted On: May 6, 2022

https://doi.org/10.13052/2022.ACES.J.370408

this novel method to solve typical EMC simulation problems and provide a better uncertainty analysis method for EMC field.

The remainder of this paper is organized as follows. In Section II, the framework of the SCM is briefly introduced. Section III presents the application of the MEG in EMC simulation in detail. Section IV validates the algorithm's accuracy by using crosstalk simulation example. Shielding effect simulation example of anechoic chamber is shown in Section V. The prospect of further application of the MEG is discussed in Section VI. Section VII summarizes this paper.

II. OUTLINE OF THE SCM

In the actual electromagnetic environment, randomness and cognitive limitations are inevitable; so it is impossible to realize accurate simulation completely using deterministic parameter models. It is more appropriate to use a random variable model to describe random events in practical engineering, shown as follows:

$$\xi = \{\xi_1, \xi_2, \ldots, \xi_n\}, \tag{1}$$

where ξ_i represents a random variable with probability density, and ξ is the set of all random variables.

When the probability density function of the random variable is known, the orthogonal polynomial corresponding to the random variable can be obtained by three-term recurrence formula [10]

$$\pi_{r+1}(\xi_i) = (\xi_i - \alpha_r)\pi_r(\xi_i) - \beta_r \pi_{r-1}(\xi_i), \tag{2}$$

$$\pi_{-1}(\xi_i) = 0, \pi_0(\xi_i) = 1, \tag{3}$$

where $\pi_r(\xi_i)$ is the orthogonal polynomial of one-dimensional random variable ξ_i. The intermediate variables can be calculated by the following formula:

$$\alpha_r = \frac{\langle \xi_i \pi_r, \pi_r \rangle}{\langle \pi_r, \pi_r \rangle}, \tag{4}$$

$$\beta_0 = \langle \pi_0, \pi_0 \rangle, \beta_r = \frac{\langle \pi_r, \pi_r \rangle}{\langle \pi_{r-1}, \pi_{r-1} \rangle}. \tag{5}$$

The internal product calculation formula is

$$\langle x(\xi_i), y(\xi_i) \rangle = \int x(\xi_i) y(\xi_i) \,\mathrm{pdf}(\xi_i)\, d\xi_i, \tag{6}$$

where $\mathrm{pdf}(\xi_i)$ represents the probability density function of the random variable ξ_i.

For the SCM, the collocation points corresponding to the one-dimensional random variable are the zero points of orthogonal polynomial in formula (2). In the multidimensional case, the collocation points are the tensor product of one-dimensional collocation points [11].

In SCM, the uncertainty analysis result is the sum of orthogonal polynomials

$$U(\xi) = \sum_{r=0}^{M} c_r \pi_r(\xi), \tag{7}$$

where c_r is the constant to be solved.

A single deterministic EMC simulation is implemented at each collocation point q_i to obtain the corresponding result $U_{\mathrm{EMC}}(q_i)$. The fitting of formula (7) is realized based on the least square method to obtain the constant c_r. It can be seen that the result of the SCM is in the form of a random variable polynomial. Finally, the statistical results such as expectation, standard deviation, and worst-case estimation are obtained by sampling the random variables in formula (7).

Obviously, in the whole calculation process, only deterministic simulation is required at each collocation point; thus, the SCM has the advantage of no need to change the original solver. At the same time, the generalized polynomial chaos theory ensures the fast convergence speed of the SCM, so that the required collocation points are far lower than the collocation points required by the MCM, which ensures that the SCM has high computational efficiency [11, 12].

It is worth noting that the SCM can only obtain statistical results after fitting and sampling calculation. Therefore, the implementation of the SCM requires a long post-processing process, which will have an adverse impact on calculation efficiency and algorithm promotion.

III. IMPLEMENTATION OF THE MEG IN EMC SIMULATION

In MEG, it is also necessary to construct the orthogonal polynomial under the three-term recurrence formula, and it is also necessary to select the zero points of the orthogonal polynomial to ensure the fastest convergence speed. At the same time, in the case of multi-dimensional random variables, the way to select the zero points is still in the form of a tensor product. In other words, under the same random variables model, the collocation points of the SCM are exactly the same as those required by the MEG.

It is more convenient for the MEG to give uncertainty statistic results. After a single deterministic EMC simulation at each selected zero point, the expectation result can be expressed as follows:

$$E(U) = \sum_{i=1}^{M} w_i \times U_{\mathrm{EMC}}(q_i). \tag{8}$$

Similarly $U_{\mathrm{EMC}}(q_i)$ represents the result of a single simulation at the selected point q_i. As the selected configuration points are exactly the same as the SCM, the total number M is also consistent with formula (7). w_i expresses the weight proportion of $U_{\mathrm{EMC}}(q_i)$, and its calculation is the core idea of the MEG algorithm. When the random variables model is one-dimensional, the weight calculation formula is as follows:

$$w_i = \int L^2(\xi, q_i)\,\mathrm{pdf}(\xi) d\xi, \tag{9}$$

where $L(\xi, p_i)$ represents the Lagrange interpolation polynomial constructed by each selected point and its

single simulation results

$$L(\xi, q_i) = \prod_{\substack{0 \le k \le M \\ k \ne i}} \frac{\xi - q_k}{q_i - q_k}. \tag{10}$$

If the random variables model is multidimensional, the weight can be directly obtained by multiplying the one-dimensional weight in the form of a tensor product. For example, if there are only two random variables, and their one-dimensional weights are only three, namely w_1, w_2, and w_3. The results in tensor product form are as follows:

$$\begin{bmatrix} w_1 w_1 & w_1 w_2 & w_1 w_3 \\ w_2 w_1 & w_2 w_2 & w_2 w_3 \\ w_3 w_1 & w_3 w_2 & w_3 w_3 \end{bmatrix}. \tag{11}$$

Similarly, the variance results can be calculated in the same way

$$\sigma(U) = \sum_{i=1}^{N_d} w_i \times [U_{EMC}(\xi_i) - E(U)]^2. \tag{12}$$

It can be seen that the MEG also has the advantage of no need to change the original solver and has the same computational efficiency as the SCM. Meanwhile, the MEG is more concise in the post-processing stage of uncertainty analysis.

IV. SIMULATION EXAMPLE OF PARALLEL CABLE CROSSTALK

This section presents a benchmark calculating example in [11] to verify the accuracy of the MEG. It is a crosstalk simulation example with three uncertain parameters as shown in Figure 1.

The first uncertain parameter is the voltage source value, which satisfies the following formula:

$$E_m(\xi_1) = 1 + 0.1 \times \xi_1. \tag{13}$$

Its probability density function is supposed as follows:

$$\mathrm{pdf}(\xi_1) = \begin{cases} \frac{1}{2}\sin(\frac{3\pi}{2}\xi_1) + (1 - \frac{1}{3\pi}), 0 \le \xi_1 \le 1 \\ 0, \qquad \text{other values} \end{cases}. \tag{14}$$

Obviously, this probability density function satisfies the following conditions:

$$\begin{cases} \mathrm{pdf}(\xi_1) \ge 0 \\ \int_{-\infty}^{+\infty} \mathrm{pdf}(\xi_1)\, d\xi_1 = 1 \end{cases}. \tag{15}$$

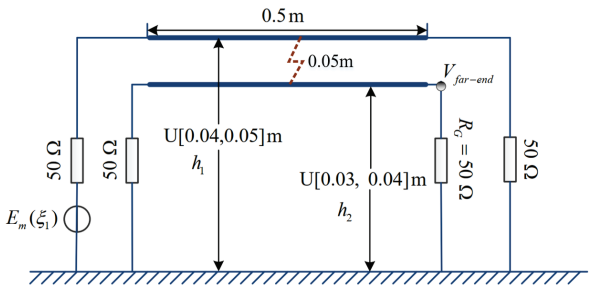

Fig. 1. Benchmark calculating example in [11].

The other two uncertainty parameters are the heights of two cables, and both of them have a uniform distribution. Their random variable models are shown as follows:

$$\begin{cases} h_1(\xi_2) = 0.045 + 0.005 \times \xi_2 \\ h_2(\xi_3) = 0.035 + 0.005 \times \xi_3 \end{cases}, \tag{16}$$

where ξ_2 and ξ_3 are the random variables with the uniform distribution $[-1, 1]$.

The longitudinal distance along the paper between the two cables is 0.05 m, and the frequency range of crosstalk results is from 1 to 100 MHz. The other detailed information of the model is completely consistent with [11]. For MEG, the third-order chaotic polynomial of random variable ξ_1 is $\xi_1^3 - 1.4360\xi_1^2 + 0.5513\xi_1 - 0.0465$, the collocation points are $\{0.8546, 0.4642, 0.1172\}$. The third-order chaotic polynomials of random variables ξ_2 and ξ_3 are $\xi_i^3 - \frac{3}{5}\xi_i$, and both collocation points are $\left\{\frac{\sqrt{15}}{5}, 0, -\frac{\sqrt{15}}{5}\right\}$. Finally, calculate formulas (9)–(12), respectively.

Figures 2 and 3 show expectation results and standard deviation results of the MEG in calculating the crosstalk voltage, respectively. As a comparison, the simulation results of the MCM and the SCM are also given.

Taking the calculation results of the MCM as standard data, the feature selective validation (FSV) method [14] is used to evaluate the differences between the calculation results of other uncertainty analysis methods, so as to judge the accuracy of the algorithm. The FSV value between the MCM and the MEG in expectation results is 0.0092, and that between the MCM and the SCM is 0.0211. It presents that the accuracy of the MEG is slightly better than the SCM, and both of them are at an "Excellent" level. Meanwhile, the FSV value between the MCM and the MEG in standard deviation results is 0.0232, and that between the MCM and the SCM is 0.0873. Similarly, the same conclusion as the expectation results can be obtained.

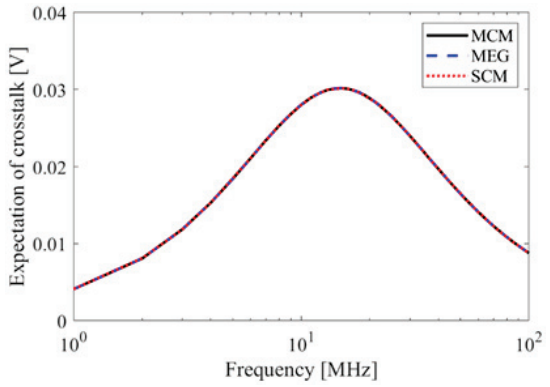

Fig. 2. Expectation results of the crosstalk voltage from 1 to 100 MHz.

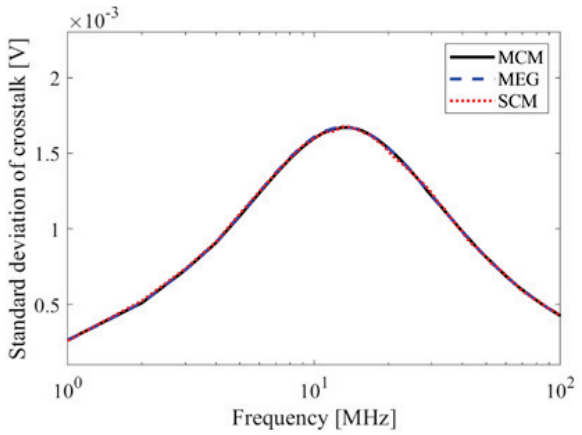

Fig. 3. Standard deviation results of the crosstalk voltage from 1 to 100 MHz.

Table 1: Simulation time comparison of the MCM, the MEG, and the SCM

	Simulation times	Processing time	Total time
MCM	12,000	0 s	12.75 h
MEG	27	0.7 s	1.73 min
SCM	27	0.98 h	1.01 h

Table 1 provides the comparison of three uncertainty analysis methods in simulation time. The MCM needs 12,000 deterministic simulations to ensure convergence, so that its computational efficiency is the lowest. With the increase of single deterministic simulation time, the disadvantage of the low computational efficiency of the MCM will become more apparent. In contrast to the MEG and the SCM, the convergence can be ensured by implementing deterministic simulation at each configuration point; so it only needs to be carried out $3 \times 3 \times 3 = 27$ times. The simulation time of this part is about 102 s. However, the SCM takes much more time to implement post-processing than the MEG. Although this time will not change with the time of deterministic simulation, it is enough to prove that the implementation of the MEG is more convenient.

To sum up, in this calculating example, the MEG is better than the SCM in computational efficiency of post-processing, and other performances of them are consistent.

V. SHIELDING EFFECT SIMULATION EXAMPLE IN ANECHOIC CHAMBER

Figure 4 shows the model of the anechoic chamber, and its size is $3.9 \times 3.9 \times 3.3$ m^3. The shielding material is carbon loaded foam with low conductivity. It is assumed that it has geometric parameter uncertainty

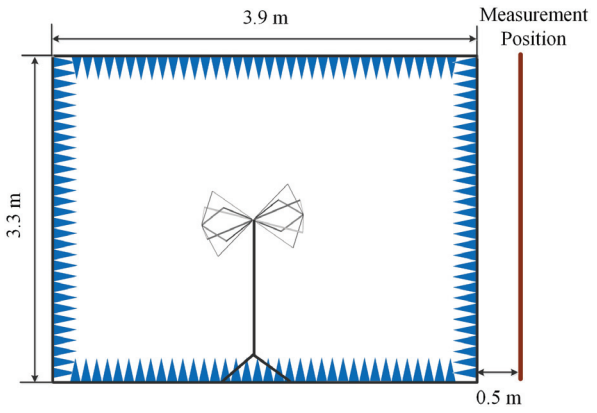

Fig. 4. Anechoic chamber model.

and material parameter uncertainty. The height h_s of the absorber cone is uniform distribution of [0.33,0.37] m. The relative dielectric constant ε_r of the shielding material is uniform distribution of [0.96,1], and the conductivity σ_s of the shielding material is uniform distribution of [0.53,0.57] S/m. The random variable models are shown as follows:

$$\begin{cases} h_s(\xi_1) = 0.35 + 0.02 \times \xi_1 \\ \varepsilon_r(\xi_2) = 0.98 + 0.02 \times \xi_2 \\ \sigma_s(\xi_3) = 0.55 + 0.02 \times \xi_3 \end{cases}, \tag{17}$$

where ξ_1, ξ_2, and ξ_3 are consistent with the meaning of symbols in formulas (13) and (15).

There is a biconical antenna in the center of the darkroom, which emits 240 MHz spherical wave. The measurement position is 0.5 m away from the right wall, and the simulation output is the electric field intensity. In order to better show the change of results, it is expressed in decibels

$$E_{\text{final}} = 20 \times \log_{10}(E_{\text{norm}}). \tag{18}$$

Figure 5 shows the distribution of electric field intensity value at the test point without considering the parameter uncertainty. It can be seen that the variation range of electric field intensity is close to 40 dBV/m, and its change range is large. Therefore, it is more meaningful to pay attention to the maximum and minimum values when considering parameter uncertainty.

Considering the parameter uncertainty in formula (16), the MEG and the SCM are used for simulation, and their results are presented in Table 2. The results are the mean value of maximum $M_{\max}$, the standard deviation of maximum $\sigma_{\max}$, the mean value of minimum $M_{\min}$, and the standard deviation of minimum $\sigma_{\min}$ at the position to be measured. It is shown that the accuracy of the MEG is the same as the SCM. The mean equivalent area method (MEAM) is an effectiveness evaluation method for EMC uncertainty simulation results. The MEAM value of the MEG and the SCM in maximum results is 0.9035, and

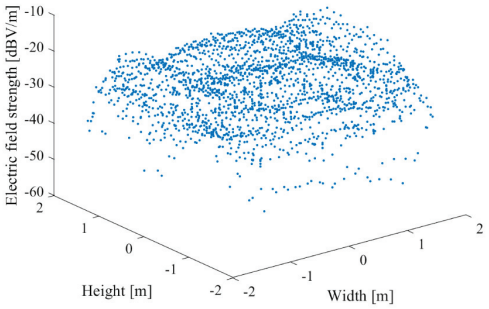

Fig. 5. Electric field intensity at test position when $h_s = 0.35$, $\varepsilon_r = 0.98$, and $\sigma_s = 0.55$.

Table 2: Simulation results comparison of the MEG and the SCM

	MEG	SCM
$M_{\max}$**[dBV/m]**	-14.4987	-14.4980
$\sigma_{\max}$ **[dBV/m]**	0.0481	0.0460
$M_{\min}$**[dBV/m]**	-152.5319	-152.5318
$\sigma_{\min}$**[dBV/m]**	0.0364	0.0361

that in minimum results is 0.9195. It is also proved that the uncertainty analysis results of the MEG and the SCM are very similar. More details about the MEAM can be found in [15].

The number of deterministic simulations required by the MEG and the SCM is 27, and the simulation time is 2.08 h. For post-processing time, the MEG takes 0.34 s and the SCM takes 7.23 min. Therefore, the conclusion is exactly the same as that in Section IV.

It is worth noting that the uncertainty analysis results of the MCM are not given in this section; the reason is that its estimated simulation time cost is unacceptable. When the number of deterministic simulations required by the MCM is still 12,000, the required simulation time is 38.5 days. More importantly, convergence may not be guaranteed under this simulation time. The MCM, the SCM, and the MEG are non-embedded uncertainty analysis methods, and the single EMC simulation process can be seen as a black box. Therefore, this paper proposes a third example, and the formula is as follows:

$$Ana(\xi) = \{\frac{h_s(\xi_1)}{1[\mathrm{m}]}\}^2 + e^{\frac{\varepsilon_r(\xi_2)}{1}} + 2 \times \frac{\sigma_s(\xi_3)}{1[\mathrm{S}/m]}. \quad (19)$$

Through the analytical value of formula (18), the accuracy of the SCM and the MEG is verified based on the analytical calculation results of the MCM. It is worth noting that each variable in formula (18) has eliminated the unit; so the abscissa in Figure 6 is unitless. Figure 6 gives the probability density results. According to probability theory, the closer the common area of the two

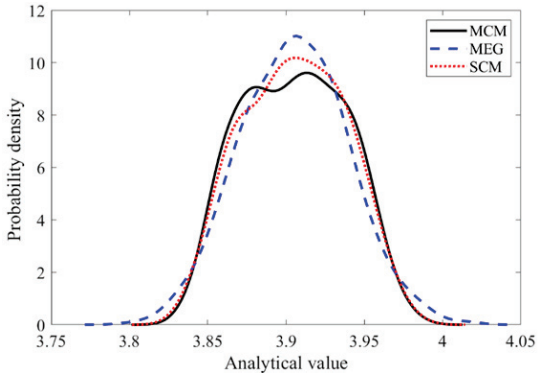

Fig. 6. Probability density result of the analytical value of formula (18).

curves is to 1, the more similar the results of the uncertainty analysis. When using the calculation results of the MCM as standard data, it can be clearly seen that both the SCM and the MEG are valid and accurate.

Furthermore, the SCM has been proved many times to have high calculation accuracy; so the calculation accuracy verification of the MEG in shielding effect simulation example in Figure 4 is guaranteed.

VI. COMPARISON OF THE MEG AND THE SCM IN INDUSTRIAL APPLICATION

First, the required storage space is compared. In crosstalk simulation example, storage space required by the MEG is 100 (Frequency number) $\times$ 27 (Number of matching points formed by tensor product) $\times$ 16 (Number of bytes required for real storage) + 9 (Weight values calculated in advance) $\times$ 16 (Number of bytes required for real storage) = 42.33 KB. Storage space required by the SCM is 100 (Frequency number) $\times$ 3200 (Number of collocation points) $\times$ 36 (9 calculated values of multidimensional Lagrange interpolation + 27 matching points formed by tensor product) $\times$ 16 (Number of bytes required for real storage) = 175.27 MB. In shielding effect simulation example, storage space required by the MEG is 2 (Maximum and minimum) $\times$ 27 (Number of matching points formed by tensor product) $\times$ 16(Number of bytes required for real storage) + 9 (Weight values calculated in advance) $\times$ 16 (Number of bytes required for real storage) = 0.98 KB. Storage space required by the SCM is 2 (Maximum and minimum) $\times$ 1600 (Number of collocation points) $\times$ 36 (9 calculated values of multidimensional Lagrange interpolation + 27 matching points formed by tensor product) $\times$ 16 (Number of bytes required for real storage) = 1.76 MB.

Obviously, the MEG needs less storage space, and it is easier to use one-chip computer to store information, so as to further realize industrial application.

Second, in order to generate uniformly distributed collocation points satisfying ξ_2 and ξ_3, the post-processing stage of the SCM needs to use the rand function, which can be completed by one-chip computer under specific conditions. To obtain collocation points satisfying ξ_1, a more complex function is needed, and even the cumulative probability density equation needs to be solved by inverse solution. In this case, one-chip computer is obviously unable to complete.

Therefore, the MEG is easier to realize industrial application than the SCM in terms of algorithm implementation and storage implementation.

VII. CONCLUSION

In this paper, a novel uncertainty analysis method called MEG is introduced to solve the problem of EMC simulation. It verifies that the MEG is as good as the SCM in both calculation accuracy and calculation efficiency by two typical EMC calculating example. Finally, through quantitative calculation, it is verified that the MEG is easier to be realized in one-chip computer, so as to complete industrial application scenarios such as online real-time prediction.

REFERENCES

[1] D. Xiu and G. E. Karniadakis, "The wIENERaSKEY pOLYNOMIAL cHAOS FOR sTOCHASTIC dIFFERENTIAL eQUATIONS," *Journal on Scientific Computing*, vol. 24, no. 2, pp. 619-644, 2002.

[2] S. A. Pignari, G. Spadacini, and F. Grassi, "Modeling field-to-wire coupling in random bundles of wires," *IEEE Electromagnetic Compatibility Magazine*, vol. 6, no. 3, pp. 85-90, 2017.

[3] H. Xie, J. F. Dawson, J. Yan, AC. Marvin, and M. P. Robinson, "Numerical and analytical analysis of stochastic electromagnetic fields coupling to a printed circuit board trace," *IEEE Transactions on Electromagnetic Compatibility*, vol. 62, no. 4, pp. 1128-1135, 2020.

[4] Y. Zhang, C. Liao, H. Rui, Y. Shang, and H. Zhou, "Analysis of nonuniform transmission lines with a perturbation technique in time domain," *IEEE Transactions on Electromagnetic Compatibility*, vol. 62, no. 2, pp. 542-548, 2020.

[5] P. Manfredi, D. V. Ginste, I. S. Stievano, D. D. Zutter, and F. G. Canavero, "Stochastic transmission line analysis via polynomial chaos methods: An overview," *IEEE Electromagnetic Compatibility Magazine*, vol. 6, no. 3, pp. 77-84, 2017.

[6] F. Canavero, "Generalized decoupled polynomial chaos for nonlinear circuits with many random parameters," *IEEE Microwave & Wireless Components Letters*, vol. 25, no. 8, pp. 505-507, 2015.

[7] Z. Zhang, T. A. El-Moselhy, I. M. Elfadel, et al., "Stochastic testing method for transistor-level uncertainty quantification based on generalized polynomial chaos," *IEEE Transactions on Computer-Aided Design of Integrated Circuits and Systems*, vol. 32, no. 10, pp. 1533-1545, 2013.

[8] R. S. Edwards, A. C. Marvin, and S. J. Porter, "Uncertainty analyses in the finite difference time domain method," *IEEE Transactions on Electromagnetic Compatibility*, vol. 52, no. 1, pp. 155-163, 2010.

[9] Z. Fei, Y. Huang, J. Zhou, and X. Qian, "Uncertainty quantification of crosstalk using stochastic reduced order models," *IEEE Transactions on Electromagnetic Compatibility*, vol. 59, no. 1, pp. 228-239, 2016.

[10] T. Wang, Y. Gao, and L. Gao, "Statistical analysis of crosstalk for automotive wiring harness via the polynomial chaos method," *Journal of the Balkan Tribological Association*, vol. 22, no. 2, pp. 1503-1517, 2016.

[11] J. Bai, G. Zhang, D. Wang, A. P. Duffy, and L. Wang, "Performance comparison of the SGM and the SCM in EMC simulation," *IEEE Transactions on Electromagnetic Compatibility*, vol. 58, no. 6, pp. 1739-1746, 2016.

[12] J. Bai, G. Zhang, A. P. Duffy, and L. Wang, "Dimension-reduced sparse grid strategy for a stochastic collocation method in EMC software," *IEEE Transactions on Electromagnetic Compatibility*, vol. 60, no. 1, pp. 218-224, 2018.

[13] B. Jia, M. Xin, and Y. Cheng, "Uncertainty propagation via multi-element grid," 2013 American Control Conference (ACC) Washington, DC, USA, Jun. 17-19, 2013.

[14] A. P. Duffy, A. Orlandi, and G. Zhang, "Review of the feature selective validation method (FSV). Part I-theory," *IEEE Transactions on Electromagnetic Compatibility*, vol. 60, no. 4, pp. 814-821, 2018.

[15] J. Bai, L. Wang, D. Wang, A. P. Duffy, and G. Zhang, "Validity evaluation of the uncertain EMC simulation results," *IEEE Transactions on Electromagnetic Compatibility*, vol. 59, no. 3, pp. 797-804, 2017.

Jinjun Bai received the B.Eng. degree in electrical engineering and automation in 2013, and the Ph.D. degree in electrical engineering in 2019 from the Harbin Institute of Technology, Harbin, China. He is currently a Lecturer with Dalian Maritime University. His research interests include uncertainty analysis methods in EMC simulation, EMC problem of electric vehicles, and the validation of CEM.

Kaibin Guo received the bachelor's degree from Shandong Jiaotong University. He is currently studying at Dalian Maritime University for a master's degree. His major is in electrical engineering. The main research direction is electric vehicle lithium battery SOC estimation.

Jingchao Sun received the B.Eng. and M.Eng. degrees in electrical engineering from Dalian Maritime University, Dalian, China, in 2009 and 2012, respectively, where she is currently working toward the Ph.D. degree. She is currently an Electrical Engineer with the Dalian Electric Traction Research and Development Center, China CNR Corporation Ltd., Dalian, China. Her current research interests include unmanned crafts and their intelligent modeling and control.

Ning Wang (S'08-M'12-SM'15) received the B.Eng. degree in marine engineering and the Ph.D. degree in control theory and engineering from the Dalian Maritime University, Dalian, China, in 2004 and 2009, respectively. From September 2008 to September 2009, he was financially supported by China Scholarship Council to work as a joint-training Ph.D. student at the Nanyang Technological University (NTU), Singapore. In view of his significant research at NTU, he received the Excellent Government-funded Scholars and Students Award in 2009. From August 2014 to August 2015, he worked as a Visiting Scholar with the University of Texas at San Antonio. His research interests include self-learning modeling and control, unmanned (marine) vehicles, machine learning and autonomous systems. Dr. Wang received the Nomination Award of Liaoning Province Excellent Doctoral Dissertation, and also won the State Oceanic Administration Outstanding Young Scientists in Marine Science and Technology, the China Ocean Engineering Science and Technology Award (First Prize), the Liaoning Province Award for Technological Invention (First Prize), the Liaoning Province Award for Natural Science (Second Prize), the Liaoning Youth Science and Technology Award (Top10 Talents), the Liaoning BaiQianWan Talents (First Level), the Liaoning Excellent Talents (First Level), the Science and Technology Talents the Ministry of Transport of the P. R. China, the Youth Science and Technology Award of China Institute of Navigation, and the Dalian Leading Talents.

Modeling the Insertion Loss of Structured Ethernet Cabling Standard using the Scattering Parameters

Olusegun Ogundapo and Charles Nche

School of Engineering, American University of Nigeria, PMB 2250, Yola-Nigeria
olusegun.ogundapo@aun.edu.ng, charles.nche@aun.edu.ng

Abstract **–** A method of simulating the insertion loss of different channel configurations of structured Ethernet cabling with reference to standard specifications is presented. The method can aid cable engineers in the study of the performance of Ethernet cabling systems during standardization in order to have a view of what to expect in real life. The paper considered the standard category 8 cabling system as a case study. The method presented used the scattering parameters implemented in Matrix Laboratory (MATLAB) to model the insertion loss of standard category 8 cabling system. The insertion loss simulation results provided good agreements with the standard category 8 cabling system. The method presented will serve as a basis to cable engineers who want to study future structured cabling systems under standardization to aid the design of prototype Ethernet cables.

Index Terms **–** Category 8 cabling, Ethernet cables, insertion loss, scattering parameters, structured cabling.

I. INTRODUCTION

Cable engineers and designers often seek for a way of simulating cable performance with reference to the specifications provided [1, 2] during standardization. The ability to effectively simulate and predict the cable performance is not only needed to have a view of what to expect in real life but also to aid the design and manufacture of the cables. There is the need for cable engineers to study the characteristics of the cable by simulating their performance using the specifications and data provided before their eventual prototype design. This research used the category 8 cabling standard as a case study to model the insertion loss based on the specifications and data provided by the IEEE Task Force on standardization of the cable [2, 3]. Although a method of predicting the insertion loss of the structured Ethernet cabling system has been provided in [4], this paper extends it further by providing simulations, which enhances the study of the effects of patch cord and backbone cable lengths on the insertion loss of different channel configurations. This is to enable a comparison between the different channel configurations.

Insertion loss (attenuation) is a measure of the decrease in signal strength along the length of a transmission line or channel [5]. When it comes to transmitting data over twisted pair wired channels, Ethernet is the technology widely used [6]. Ethernet is now used in Internet of Things for homes, industries, public places, etc. [7]. The 40GBASE-T is the next generation following the 10-Gigabit Ethernet over twisted pair cabling [8]. The 40GBASE-T system is being supported by category 8 twisted pair cable and is expected to have a maximum length of 30 m [9]. The Telecommunications Industry Association (TIA) in collaboration with the International Organization for Standardization/International Electro-Technical Commission (ISO/IEC) worked on creating the category 8 cabling and connector specifications under the IEEE 802.3bq task force [8]. The effort of the IEEE 802.bq Task Force with the TIA and the ISO/IEC resulted in the publication of the category 8 cabling standard which specifies how the 40GBASE-T cabling system is expected to operate with two connectors at a maximum frequency of 2000 MHz [1, 3]. These specifications provided by the ISO/IEC and the TIA for the category 8 standard will be used to provide a method of simulating the channel insertion loss of the structured cabling using the scattering parameters.

The scattering parameters have been used extensively for modeling, characterization, and design of microwave devices and networks. It has also been applied to transmission line network behavior design and analysis [10, 11]. The major advantage of scattering parameters is that it permits flexibility in design and can be used to analyze cascaded cable performance [11]. The category 8 topology has been specified to consist of two connectors that have effects on the overall loss and the insertion loss deviation due to the channel. These losses due to the connectors will be factored into the channel insertion loss modeling using the scattering parameters which presently does not have expressed provisions for it. The demand for higher Gigabit Ethernet cabling system was driven by the need for increasing access

Submitted On: August 27, 2021
Accepted On: March 21, 2022

https://doi.org/10.13052/2022.ACES.J.370409

speeds across networks and higher rate throughput by data centers [13]. This is due to increasing demand for data bandwidth in the area of visualization, cloud computing, big data analytics, video-on-demand, etc. [9, 13].

The S-parameters can be expressed in terms of transmission line wave propagation characteristics as [14]

$$\lfloor S \rfloor = \frac{1}{D_s}\begin{bmatrix} S_{11} & S_{12} \\ S_{21} & S_{22} \end{bmatrix} \quad (1)$$

$$\lfloor S \rfloor = \frac{1}{D_s}\begin{bmatrix} \left(Z_c{}^2 - Z_e{}^2\right).\sinh\gamma_k l & 2.Z_c.Z_e \\ 2.Z_c.Z_e & \left(Z_c{}^2 - Z_e{}^2\right).\sinh\gamma_k l \end{bmatrix}. \quad (2)$$

In eqn (1) and (2), Z_e is the characteristics impedance of the test equipment in ohms, Z_c is the cable or patch cord impedance in ohms, γ_k is the propagation constant, and l is the cable length in meters.

$$D_s = 2.Z_c.Z_e.\cosh\gamma_k l + \left(Z_c{}^2 + Z_e{}^2\right).\sinh\gamma_k l. \quad (3)$$

The propagation constant (γ_k) is given in [4] and [15] as

$$\gamma_k = \alpha_k + \beta_k. \quad (4)$$

The phase constant (β_k) is expressed in [4] and [15] as

$$\beta_k = \frac{2\pi f_k.10^6}{V_{pk}} \quad (\text{Radian/m}), \quad (5)$$

where the velocity of propagation constant (V_{pk}) is given in [15] as

$$V_{pk} = \frac{100}{\left(494 + \frac{36}{f_k}\right).10^{-9}} \quad (\text{m/sec}). \quad (6)$$

The attenuation (A_{tk}) for 100-m cable is expressed in [12] and [15] as

$$A_{tk} = \left(1.80.\sqrt{f_k} + 0.005.f_k + 0.25/f_k\right). \quad (\text{dB}), \quad (7)$$

Therefore, the attenuation constant per meter is

$$\alpha_k = \left(\frac{0.01.A_{tk}}{20.\log(e)}\right) \quad (\text{Neper/m}). \quad (8)$$

The mathematical relationship between the S-parameters and the T-parameters that can be used to convert S-parameters to T-parameters and vice versa is expressed in [10] and [14] as

$$S = \begin{bmatrix} S_{11} & S_{12} \\ S_{21} & S_{22} \end{bmatrix} \quad (9)$$

$$S = \frac{1}{T_{22}}\begin{bmatrix} T_{12} & T_{11}T_{22} - T_{12}T_{21} \\ 1 & -T_{21} \end{bmatrix} \quad (10)$$

$$T = \begin{bmatrix} T_{11} & T_{12} \\ T_{21} & T_{22} \end{bmatrix} \quad (11)$$

$$T = \frac{1}{S_{21}}\begin{bmatrix} S_{12}S_{21} - S_{11}S_{22} & S_{11} \\ -S_{22} & 1 \end{bmatrix} \quad (12)$$

$$\text{Insertion loss } (\alpha_L) = -20.\log_{10}|S_{21}|\,\text{dB}. \quad (13)$$

This research, therefore, provides a method that can be used to simulate the channel insertion loss of structured cabling standard and also study the effects of patch cords and cable lengths on the insertion loss. Different channel configurations were compared with each other to observe the effect on the insertion loss. All these simulations are in reference to the category 8 (40GBASE-T) cabling specifications using scattering parameters implemented in Matrix Laboratory (MATLAB).

II. MATERIALS AND METHODS

A. Category 8 channel configuration

The schematic diagram of the category 8 channel configuration as presented in [1], [2], and [4] is shown in Figure 1.

Note: $A1$ and $A2$ are the equipment cords or patch cords; $C1$ and $C2$ are the hardware connectors; B is horizontal cabling under consideration.

The maximum length requirement as given in [1] is

$A + C$ (see Table 1)

B: 24 m (79 ft).

The specifications considered for this research are presented in [2]–[4] as follows:

$$\text{Channel insertion loss} = 2 \times \text{connecting hardware IL} + \text{cable IL} + \text{ILD}_{\text{channel}}(\text{dB}), \quad (14)$$

where IL means the insertion loss and $\text{ILD}_{\text{channel}}$ is the insertion loss deviation due to the channel.

The backbone cabling insertion loss for a 100-m length is

$$\text{Cable IL } (100\text{ m}) = 1.8 \times \sqrt{f} + 0.005 \times f + \left(0.25/\sqrt{f}\right) \text{ (dB), for:}$$

$$1\ (\text{MHz}) \le f\,(\text{MHz}) \le 2000\ (\text{MHz}). \quad (15)$$

The insertion loss due to the connecting hardware is as follows:

$$0.02 \times \sqrt{f}\ (\text{dB}) \text{ for:}$$

$$1\,(\text{MHz}) \le f(\text{MHz}) \le 500(\text{MHz}), \quad (16)$$

$$0.008 \times \sqrt{f} + 0.00029 \times f + 0.5 \times 10^{-6} \times f^2\ (\text{dB}) \text{ for}$$

$$500\ (\text{MHz}) > f\,(\text{MHz}) \le 2000\ (\text{MHz}). \quad (17)$$

The patch cord insertion loss is

$$\text{Patch cord cable } (\text{IL}) = 1.2 \times (\text{cable IL}) \quad (\text{dB}). \quad (18)$$

The insertion loss deviation due to the channel is

$$\text{ILD } (\text{channel}) = 0.0324 \times \sqrt{f}\ (\text{MHz}) \quad (\text{dB}). \quad (19)$$

The modifications provided to the insertion loss deviation of the channel to ensure good agreement with the category 8 cable specifications are

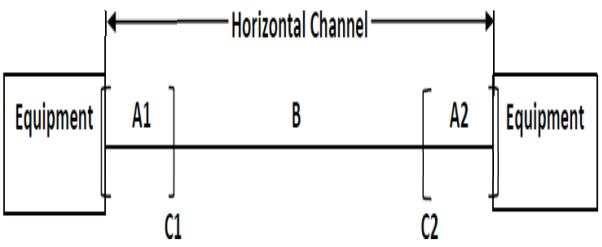

Fig. 1. Category 8 horizontal channel configuration.

Table 1: Cord thickness (AWG) and maximum length allowed

Cord (AWG)	$A + C$ (m)
22-23	8
24	6
26	4

$0.00362 \times \sqrt{f}$ (dB) for:

$$1\ (\text{MHz}) \le f\,(\text{MHz}) \le 500\ (\text{MHz}) \tag{20}$$

$$2.662 \times 10^{-3} \times \sqrt{f} + 3.19 \times 10^{-5} + 5.5 \times 10^{-8} \times f^2 \ (\text{dB}) \text{ for } 500\,(\text{MHz}) > f\,(\text{MHz}) \le 2000\ (\text{MHz}). \tag{21}$$

The overall channel insertion loss of category 8 (40GBASE-T) cabling system was determined using eqn (13).

B. Application of the scattering parameters to model the channel configuration

The schematic diagram of the scattering parameters method for predicting the insertion loss of the category 8 channel configuration is shown in Figure 2.

In Figure 2, the S-parameters of the first patch cord, backbone cable, and second patch cord are taken as S_1, S_2, and S_3 respectively.

To model the category 8 channel, the asymptotic impedances of the channel components are presented in [12] as cable asymptotic impedance (Z_{cba}) = 104.5 ohms, patch cord asymptotic impedance (Z_{cda}) = 95.5 ohms, and equipment asymptotic impedance (Z_e) = 100 ohms. These asymptotic impedances of the cable and patch cords are multiplied with a heuristic impedance equation which has been proven extensively to describe very well the mean characteristics impedance values. This heuristic impedance equation is expressed in [12] and [14] as

$$Z_h = \left[1 + 0.055.\frac{(1-j)}{\sqrt{f_h}}\right]. \tag{22}$$

Therefore, the new characteristic impedances of the cable and patch cords are calculated as

$$Z_{cbah} = Z_{cba} \times Z_h \ (\Omega) \tag{23}$$

$$Z_{cdah} = Z_{cda} \times Z_h \ (\Omega). \tag{24}$$

The S-parameters of the cable and patch cords can now be determined individually using eqn (2).

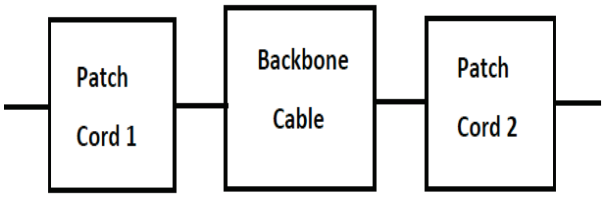

Fig. 2. Schematic diagram of the scattering parameter approach.

C. Concatenation of channel cables

The concatenation of the channel cables in Figure 2 can be achieved by converting the S-parameters obtained from the two patch cords and the backbone cable into T-parameters and multiplying them sequentially as

$$T = T_1 \times T_2 \times T_3. \tag{25}$$

The equivalent T-parameters obtained from eqn (25) are then converted back to S-parameters. The S-parameters from this conversion can be used to determine the insertion loss in decibels using eqn (13) in addition to the two connecting hardware insertion losses and the insertion loss deviation due to the channel.

III. RESULT OF THE MODELED STRUCTURED ETHERNET CHANNEL

The model simulation of the S-parameters from all the processes explained in Sections I and II was implemented in MATLAB to see if they agree with the category 8, 30m channel length prediction in [2]. The 3m-24m-3m and 1m-24m-5m channel configurations were used as samples for the S-parameter test simulation. The results of the MATLAB simulation in Figures 3 and 4 show very good agreement with the standard category 8 prediction, indicating that the model can now be used for a further analysis of the channel behavior.

A. Category 8 channel behavior under different configurations

This paper studies the effect of patch cords and cabling lengths on the channel insertion loss, which were not considered in [4].

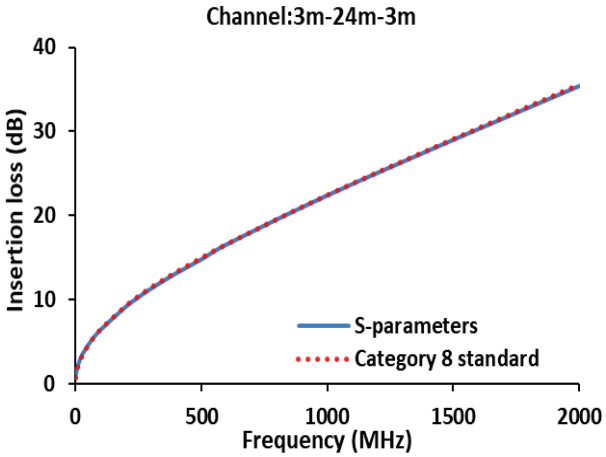

Fig. 3. Insertion loss for 3m-24m-3m channel.

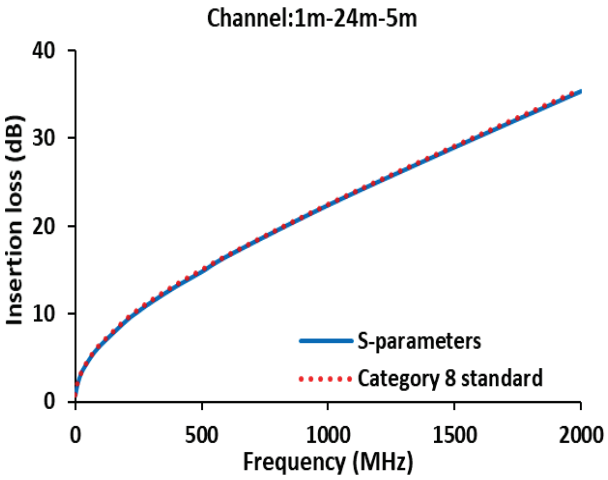

Fig. 4. Insertion loss for 1m-24m-5m channel.

The configurations considered are:

(i) 3m-24m-3m, 2m-24m-2m and 1m-24m-1m

(ii) 3m-24m-3m, 3m-22m-3m and 3m-20m-3m

(iii) 3m-10m-3m, 2m-10m-2m and 1m-10m-1m

(iv) 3m-24m-3m, 2m-10m-2m and 1m-3m-1m

IV. DISCUSSIONS

In Figure 5, the comparison of the 3m-24m-3m, 2m-24m-2m, and 1m-24m-1m channels shows that the insertion loss decreases with decreasing patch cords lengths. In Figure 6, the comparison of the insertion loss of the 3m-24m-3m, 3m-22m-3m, and 3m-20m-3m channels shows that the insertion loss decreases with decreasing backbone cable lengths, which reduces the overall channel length. The results in both Figures 5 and 6 indicate that the insertion loss reduces when there is a decrease in patch cords and backbone cabling lengths. Similarly, in Figure 7, the comparison of the 3m-10m-3m, 2m-10m-2m, and 1m-10m-1m channels shows a reduction in the overall insertion loss of the channels confirming that the channel insertion loss decreases with deceasing channel lengths. Finally, Figure 8 shows that a comparison of the 3m-24m-3m, 2m-10m-2m, and the 1m-3m-1m channels indicates that the highest channel length of 3m-24m-3m has the largest insertion loss, followed by the 2m-10m-1m and the 1m-3m-1m channels. This is a further confirmation that channel lengths affect the channel insertion loss of the category 8 configurations.

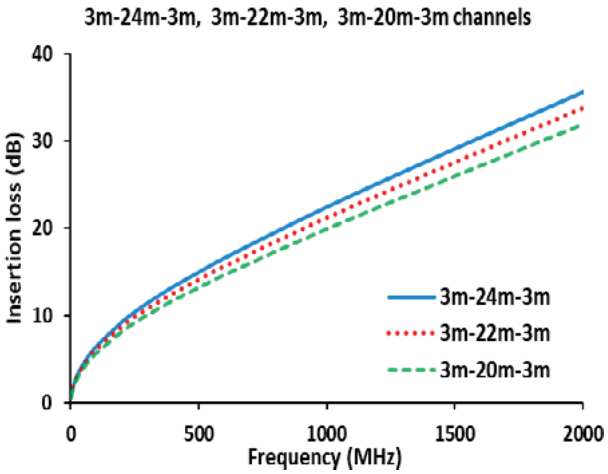

Fig. 6. Comparison of the 3m-24m-3m, 3m-22m-3m, and 3m-20m-3m channels.

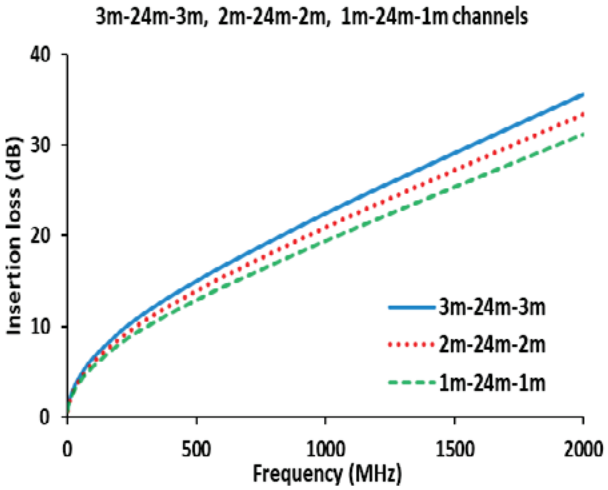

Fig. 5. Comparison of the 3m-24m-3m, 2m-24m-2m, and 1m-24m-1m channels.

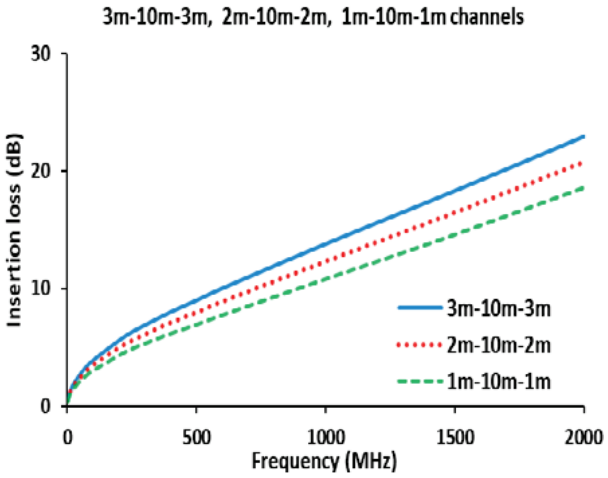

Fig. 7. Comparison of the 3m-10m-3m, 2m-10m-2m, and 1m-10m-1m channels.

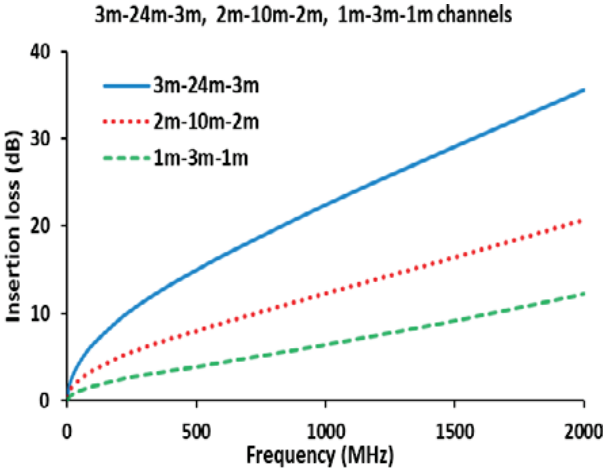

Fig. 8. Comparison of the 3m-24m-3m, 2m-10m-2m, and 1m-3m-1m channels.

V. CONCLUSION

This paper has presented a method that can be used by cable engineers to simulate the insertion loss of structured cabling standard and also study the effects of patch cord and backbone cable lengths on different channel configurations. The method can be used to predict the performance of different channel configurations of structured cabling standard which could aid the cable prototype design. The research used the category 8 cabling standard as a case study. The insertion loss prediction of the *S*-parameters model developed shows very good agreements with that of the category 8 cabling standard. The results also show that category 8 channel insertion loss reduces with decreasing channel lengths from either patch cords or backbone cabling or both. The method provided can be extended to predict the insertion loss of similar Ethernet cabling standards over structured cabling.

REFERENCES

[1] S. Vaden, "Inside the specifications of the new category 8 cabling standard," in *Cabling Installation and Maintenance Magazine*, vol. 24, no. 8, pp. 27-29, Aug. 2016.

[2] C. DiMinico, "40GBASE-T channel insertion loss," in *IEEE P802.3bq 40GBASE-T Task Force Study Group Public Area*, vol. 3, no. 11, Nov. 2016.

[3] ANSI/TIA-568-C2-1, Addendum 1, Balanced twisted pair cabling and components standard: specifications for category 8 cabling, vol. 6, no. 7, Jul. 2016.

[4] O. Ogundapo, A. Duffy, C. Nche, and J. Gow, "Scattering parameters approach to insertion loss prediction for 40 GBASE-T systems over structured cabling," *Proceedings of the World Congress on Engineering*, vol. 1, pp. 64-69, Jul. 2014.

[5] M. Guo, Q. Chen, D. Sang, Y. Zheng, and Y. Fu, "Dual polarized dual-band frequency selective rasorber with low insertion loss," *IEEE- Antennas and Wireless Propagation Letters*, vol. 19, no. 1, pp. 48-52, Jan. 2020.

[6] S. Buhr, X. Xu, M. Kreibig, and F. Ellinger, "A low power fast ethernet physical layer transceiver," *26th IEEE International Conference on Electronic Circuits and Systems (ICECS), Italy*, pp. 31-37, Nov. 2019.

[7] R. Eltom, E. Hamood, A. Mohammed, and A. Osman, "Early warning firefighting system using internet of things," *International Conference on Computer, Control, Electrical and Electronics Engineering (ICCCEEE), Khartoum*, pp. 28-35, Aug. 2018.

[8] F. Straka, "40 Gbits/s over twisted pair copper cable is on the way," in *Electronic Products Magazine*, vol. 56, no. 9, pp. 20-22, 2013.

[9] P. Mclaughlin "Category 8 questions answered," in *Cabling Installation and Maintenance Magazine*, vol. 23, no. 10, pp. 23-25, Oct. 2015.

[10] J. Dobrowolski, "Microwave network design using the scattering matrix," published by Artech House 2010.

[11] R. Allred and C. Furse, "Linearization of S-parameter cascading for analysis of multiple reflections," *Applied Computational Electromagnetic Society (ACES) Journal*, vol. 33, no. 12, Dec. 2018.

[12] J. Walling and A. Duffy, "The modeling of 4 pair data grade channels with the aim to use differential mode transmission parameters which are given in the standardized specification requirements," *57th International Wire and Cable Symposium, Rhode Island, USA*, pp. 532-540, Nov. 2008.

[13] J. Young, "The race to 40GBASE-T," in *COMMSCOPE publication*, vol. 3, no. 9, Sep. 2013.

[14] R. Papazyan, P. Petterson, H. Edin, R. Eriksson, and U. Gafvert., "Extraction of high frequency power cable characteristics from S-parameters measurements," in *IEEE Transactions on Dielectrics and Electrical Insulation*, vol. 11, no. 3, pp. 461-470, Jun. 2004.

[15] P. Kish, "Channel return loss results," in *IEEEP802.bq 40GBASE-T Task Force Study Group Area*, Nov. 2016.

Olusegun Ogundapo received the Ph.D. degree in electronic engineering from De Montfort University, United Kingdom, the M.Sc. degree in electrical engineering from Ahmadu Bello University, Zaria, and the B.Eng. degree in electrical and electronic engineering from the Federal University of Technology, Yola now Modibbo Adama University, Yola-Nigeria.

He is currently an Assistant Professor with the School of Engineering, American University of Nigeria, Yola-Nigeria. His research interests are in computational electromagnetics, wireless/wired communication media analysis, modeling, and optimization. Other interests are Internet of Things (IOT), model data, and network analytics.

Charles Nche is the formal Dean of the Graduate School and currently a faculty in the School of Engineering (SOE), American University of Nigeria (AUN), Nigeria. He received the Ph.D. degree in computer networks from Loughborough University of Technology, Britain. He holds an Electrical and Electronics Engineering degree and a Master's degree in digital communication systems.

He has worked for several companies, including BroadCom, Marconi, Mitel, etc. His research interest is centered on providing capacity, improving coverage, and increasing the efficiency of the network, using heterogeneous network (HETNET) and device-to-device communications (D2D). His other areas of interest include, but not limited to, high speed networks (40GBase-T System); wireless infrastructures and networks, resource allocation within 4G/5G networks using AI (ML and DL), and PV systems' performance.

A Novel Wideband and Multi-band Implantable Antenna Design for Biomedical Telemetry

Mohamed Behih[1], Farid Bouttout[1], Tarek Fortaki[2], and Christophe Dumond[3]

[1]Department of Electronics, University of Bordj Bou Arreridj, El-Anasser 34030, Algeria
mohamed.behih@univ-bba.dz, f.bouttout@univ-bba.dz

[2]Departement of Electronics, Batna 2 University, Batna 5000, Algeria
t.fortaki@univ-batna2.dz

[3]PRISME Institut, IUT of Chartres, University of Orleans, Orleans 45100, France
christophe.dumond@univ-orleans.fr

***Abstract* –** In this work, a novel multi-tracks wideband and multi-band miniaturized antenna design for implanted medical devices biomedical telemetry is proposed. This antenna entirely covers seven frequency bands which are the bands (401−406) MHz of the Medical Device Radiocommunications Service (MedRadio), the three bands (433.1−434.8), (868.0−868.6), and (902.8−928.0) MHz of the Industrial, Scientific, and Medical (ISM), and the three bands (608−614) MHz, and (1.395−1.400) and (1.427−1.432) GHz of the Wireless Medical Telemetry Service (WMTS). The antenna possesses a compact full size of ($19.5 \times 12.9 \times 0.456$) mm^3. The antenna miniaturization and impedance bandwidth enhancement are achieved using two techniques: the patch slotting and insertion of open-end slots in the ground plane, respectively. Prototype of proposed antenna with multi-tracks has been fabricated and tested in free space. The comparison between the simulated and measured reflection coefficient has been done and found in good agreement with each other. Furthermore, simulations of the proposed antenna implanted in the underneath the scalp in a realistic human model shows a wideband operation from 0.19 to 0.94 GHz, and from 1.38 to 1.54 GHz corresponding to return loss ($S_{11} \leq -10$ dB). Link budget calculation is performed to specify the range of telemetry considering both Specific Absorption Rate (SAR) restrictions and effective isotropic radiated power (EIRP) limitations. The designed implantable antenna with full ground plane presents an appropriate reflection coefficient for muscle implantation. Furthermore, the designed implanted muscle antenna may be also suitable for skin implantation.

***Index Terms* –** Biomedical telemetry, implanted antenna, ISM, MedRadio, multi-band, multi-tracks, wideband, WIMD, WMTS.

I. INTRODUCTION

Wireless body area network (WBAN), standardized by IEEE 802.15.6 [1, 2] is a promising wireless personal area network to connect low power devices placed on, inside, or around the human body for medical and non-medical ends. Implanted medical devices (IMDs) [2, 3] focus on various clinical purposes: diagnostic, monitoring, therapeutic, etc. [4]. The most modern of IMDs includes a communication mechanism for data exchange [4, 5]. In regard to the traditional limited near-field inductive coupling link [6], an implantable radiofrequency antenna has been integrated into the IMD to establish an effectiveness bidirectional wireless link between them and an exterior monitoring/control base-station for communication and/or physiological data transmission [5–7]. The biomedical telemetry using wireless IMDs (WIMDs) antenna has become more attractive for real-time remote monitoring and allowing telemedicine to improve the patient's life quality [2]. Nowadays, WIMDs are integrated in WBAN, where an on-body (or off-body) sensor node is used for linking the device to the exterior monitoring/control base-station that stands away from the body [4, 8, 9].

The implanted antennas in the heterogeneous lossy medium of the human body are designed for operation in specified frequency bands that face the challenge of size miniaturization while keeping good antenna radiation performances, i.e., high efficiency, high gain, and larger bandwidths [5] to establish an efficient telemetry communication. In addition, the specific absorption rate (SAR) restrictions for patient safety and the antenna biocompatibility also must be considered.

Large available bandwidth is an important factor to keep the implantable antenna performances stable and away from any frequency detuning due to the

Submitted On: April 10, 2021
Accepted On: March 10, 2022

https://doi.org/10.13052/2022.ACES.J.370410

dielectric properties modification caused by gender, age, health situation, etc. In addition to this, when such antennas cover several allocated frequency bands, they will allow to increase the WIMDs communication applications diversity. Furthermore, allocated telemetry frequency bands vary from a country to another. In spite of this, low frequencies are associated with relatively lower loss through the biological tissues [3], and the frequency bands in the range $(0.2-2)$ GHz are more efficient for both data transmission and wireless powering [10]. Thus, implantable antennas small enough to fit into WIMDs that cover the almost allocated bands widely within this frequency interval are more attractive. Such antennas are not widely reported in the literature.

Various implantable antennas have been proposed in the literature to cover various frequency bands of WIMDs biotelemetry applications [3, 5]. The developed antennas can be classified in three groups: (1) single narrow band [11] and single wideband [12–21], (2) dual narrow bands [22–25], dual lower wideband [26–28], dual higher wideband [29], and dual wideband [30–31], and (3) multi-narrow bands [32–34], multi-lower wideband [35–37], and multi-wideband [38].

Several miniaturization techniques of implantable patch antennas are reported in [39] such as slots insertion in the radiating patch, stacking [15, 22], and embedded open-end slots in the ground plane [26, 32, 34, 38]. The split ring resonator (SRR) technique is also used [11, 30, 40]. In spite of this, various methods have been proposed to enhance the gain, including the partial meandering of the patch [18], metamaterial array on the superstrate [17], lens and parasitic ring, and reactive impedance surface [19]. The ground plane slotting [26], stacking [21], and a capacitor at the open-end of the ground slot [38] are also used for the impedance bandwidth widening.

In [12] and [15], two muscle broadband implantable PIFA antennas have been proposed for covering the Medical Device Radiocommunications Service (MedRadio) band $(401-406)$ MHz, where the exhibited volumes of 399 and 448 mm^3 are relatively large. Similar study for the 2.45 GHz industrial, scientific, and medical (ISM) frequency band has been carried out in [20], where the occupied volume is 295.75 mm^3 and the impedance bandwidth is 220 MHz.

In [38], a quad-band implantable PIFA antenna for the underneath the scalp in the head muscle and other clinical applications has been proposed where the whole size of the antenna is 8.43 mm^3. Tests carried out on minced pork and the covered bands are MICS 403 MHz and ISM 915 MHz, both designed for telemetry, whereas the ISM 2.4 GHz is used for control signaling and the Midfield 1470 MHz is used for wireless power transfer.

In [22] and [24], two scalp dual bands implantable antennas have been proposed. For the first antenna, four frequency bands have been covered. Nevertheless, the simulated bandwidths inside a head model were relatively narrow. The second antenna has been proposed only for intracranial pressure monitoring. Furthermore, the exhibited SAR values were large.

In [32], a scalp triple band implantable PIFA antenna has been proposed. Although the volume is relatively small, the obtained impedance bandwidths were relatively narrow and the SAR has high values at considered frequencies. In [34], another triple band implantable antenna for deep tissue and skin implantations has been designed. The obtained measured impedance bandwidths were narrow and lower biotelemetry frequency bands are not covered.

Recently, in the reference [40], the authors proposed a flexible wideband loop antenna for wireless capsule endoscopy that covers all biotelemetry frequency bands within the range $(305-3500)$ MHz.

In this work, a novel multi-tracks wideband implanted antenna design is proposed for muscle WIMDs telemetry for frequencies up to 2 GHz. Since this allows miniaturization, high permittivity substrates are often used in the design of implantable antennas. However, this also has the effect of reducing the impedance bandwidth. For this reason, the choice was made to achieve miniaturization by an efficient design and to use a low permittivity substrate. Antenna's miniaturization is realized using path current lengthening principle and the optimized size of the design is 114.70 mm^3. The design procedure starts from an initial coax-feed PCB plate and consists of four steps, in which conducting regions of the patch and the ground plane are shaped by slotting.

The designed antenna performs multi-band operation and covers seven biomedical telemetry frequency bands with large bandwidths available and has the particularity of not having a superstrate.

The paper is organized as follows. In Section II, the antenna structure and the design and optimization process are presented. The fabricated prototype of the implantable antenna is also presented as well as a comparison of measured and simulated return loss in free space.

In Section III, tissues and implantation depth effects are investigated using two phantom models; a one-layer model which consists of skin or fat, and a three-layer model constituted of skin, fat, and muscle. Section IV presents antenna operation in two realistic implantations of human body; in the underneath the scalp and in the

muscle of the upper arm. Far-field gain radiation pattern, SAR restrictions, and link communication performances are investigated. Section V shows a comparison of the proposed antenna performances with those of recently published implantable antennas and Section VI summarizes the main results.

II. ANTENNA DESIGN AND OPTIMIZATION

A. Antenna structure

The side view and 3D view of the proposed antenna are represented in Figures 1 (a) and (b), respectively. The antenna is fed by a coaxial cable using a subminiature version A (SMA) connector with a characteristic impedance of 50 Ω and inner radius of 0.63 mm. The all-compact structure is covered with a thin layer of the polymer parylene-C (relative permittivity ε_r = 2.95, loss tangent tanδ = 0.013, and thickness = 20 μm) to guarantee the biocompatibility and the electrical isolation. Herein, the planar conductors consist of copper with thickness 18 μm and conductivity σ = 58 MS/m.

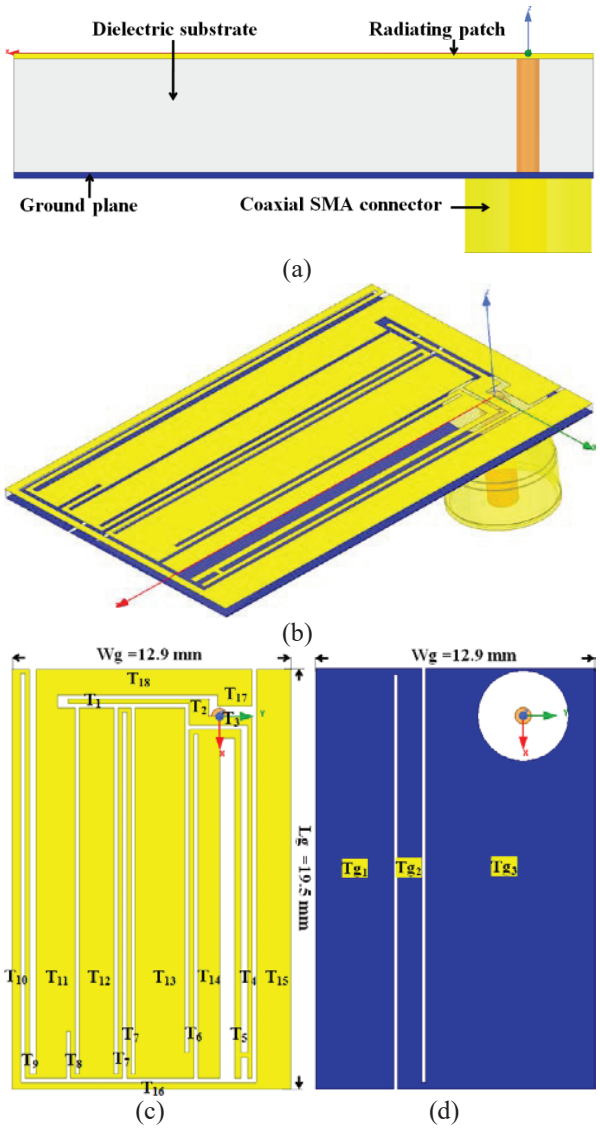

Fig. 1. The proposed antenna. (a) Side view. (b) 3D view. (c) Top view. (d) Ground plane.

Table 1: Various shaped patch tracks Ti, and sub-tracks ST_j, ground plane tracks Tg_k, and sub-tracks STg_l dimensions

Tracks and sub-tracks number	Dimensions [mm × mm]	Tracks and sub-tracks number	Dimensions [mm × mm]
T_1	0.2 × 5.6	ST_1 ($T_4 - T_5$)	0.2 × 0.3
T_2	1.2 × 0.9	ST_2 ($T_5 - T_{14}$)	0.4 × 0.7
T_3	0.4 × 2.0	ST_3 ($T_{14} - T_6$)	0.2 × 0.2
T_4	0.2 × 16.4	ST_4 ($T_6 - T_{13}$)	1.2 × 0.2
T_5	0.3 × 16.2	ST_5 ($T_{13} - T_7$)	0.2 × 0.2
T_6	0.2 × 15.6	ST_6 ($T_7 - T_7$)	0.2 × 0.2
T_7	17.2 × 0.2	ST_7 ($T_7 - T_{12}$)	0.2 × 0.2
T_8	17.2 × 0.2	ST_8 ($T_{12} - T_8$)	0.2 × 0.2
T_9	19.0 × 0.2	ST_9 ($T_8 - T_{11}$)	0.2 × 12.0
T_{10}	19.0 × 0.4	ST_{10} ($T_{11} - T_9$)	0.2 × 0.3
T_{11}	17.2 × 1.4	ST_{11} ($T_9 - T_{10}$)	0.2 × 0.2
T_{12}	17.2 × 1.6	ST_{12} ($T_{11} - T_{18}$)	1.0 × 0.6
T_{13}	17.2 × 2.3	Tg_1	19.5 × 3.6
T_{14}	16.2 × 1.0	Tg_2	19.5 × 1.1
T_{15}	19.5 × 1.6	Tg_3	19.5 × 7.8
T_{16}	0.3 × 10.9	STg_1 ($Tg_1 - Tg_2$)	0.3 × 0.2
T_{17}	1.7 × 1.6	STg_2 ($Tg_2 - Tg_3$)	0.3 × 0.2
T_{18}	1.2 × 8.4		

The antenna consists of three parts from the top to bottom: shaped patch with slotting, Cuflon substrate, and open-end slotted ground plane.

Part 1, the radiating patch: A detailed description of the antenna radiating shaped patch is given by Figure 1(c), where the radiating patch consists of 18 tracks T_i (i = 1 ,..., 18) obtained by slotting, and their optimized dimensions are given in Table 1. The various tracks are connected between them using a set of sub-tracks $ST_j(T_{i1} - T_{i2})$ of total number 12. The particular case of the sub-track occurred between tracks 4 and 5 and is located at a distance 1.2 mm from the track T_{16}.

Part 2, the dielectric substrate: A low permittivity and very low loss substrate is used, Cuflon with relative permittivity ε_r = 2.05, loss tangent $tan\delta$ = 0.00045, and dielectric thickness Thd = 0.38 mm. In addition to these frequency-uniform electrical properties [41], this substrate is relatively flexible, which allows freedom of the muscle movement and avoids injuries caused by sharp edges.

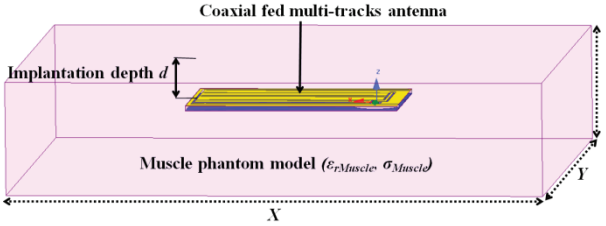

Fig. 2. 3D view of the implanted antenna in the muscle phantom model (X, Y, Z) = (110, 115, 25) mm.

Part 3, the ground plane: It consists of three tracks Tg_k ($k = 1, 2, 3$) and two sub-tracks STg_1 (Tg_1 - Tg_2), and STg_2 ($Tg_2 - Tg_3$) as shown in Figure 1 (d). The ground plane tracks and the sub-track dimensions are also given in Table 1.

B. Structure of the phantom model

For implantation, a single layer muscle human tissue phantom model is used, where the whole antenna is submerged in the phantom center at a distance $d = 4$ mm as shown in Figure 2. The phantom has a parallelepiped form of dimensions 110, 115, and 25 mm along the axes X, Y, and Z, respectively.

The dielectric properties of human tissues are frequency-dependent as demonstrated by the model of Gabriel *et al*. [42]. Herein, the model is implemented to generate the frequency-dependent conductivity and relative permittivity of the muscle, fat, and skin; the data are represented in Figure 3 for interest frequencies.

Fat and skin generated data will be used in Section III for studying tissues and implantation depth effects on implanted antenna performances.

C. Design process

It is not a quiet simple task to derive an exact straightforward theoretical model for the analysis and design of the proposed multi-track antenna, due to the complex form of its radiating element with irregular shape. Thus, we should make recourse to rigorous numerical methods.

To design, simulate and solve the corresponding electromagnetic problem, in a heterogeneous, complex, and non-uniform structure, the Ansys® HFSS, which is based on 3D full-wave finite element method (FEM) field solver is used.

Since our objective is to obtain closely multi-band operation for telemetry, we perform two techniques: 1) current path lengthening by inserting a slot in the radiating patch and 2) embedded open-end slots in the ground plane.

Now, the design procedure of the proposed implantable multi-track antenna is outlined. The design is accomplished in four steps by inserting slots in the radiating patch and open-end slots in the ground plane as shown in Figure 4. The corresponding reflection coefficients calculated with the antenna submerged at a distance $d = 4$ mm in the muscle phantom model were used to carry out the design (Figure 5).

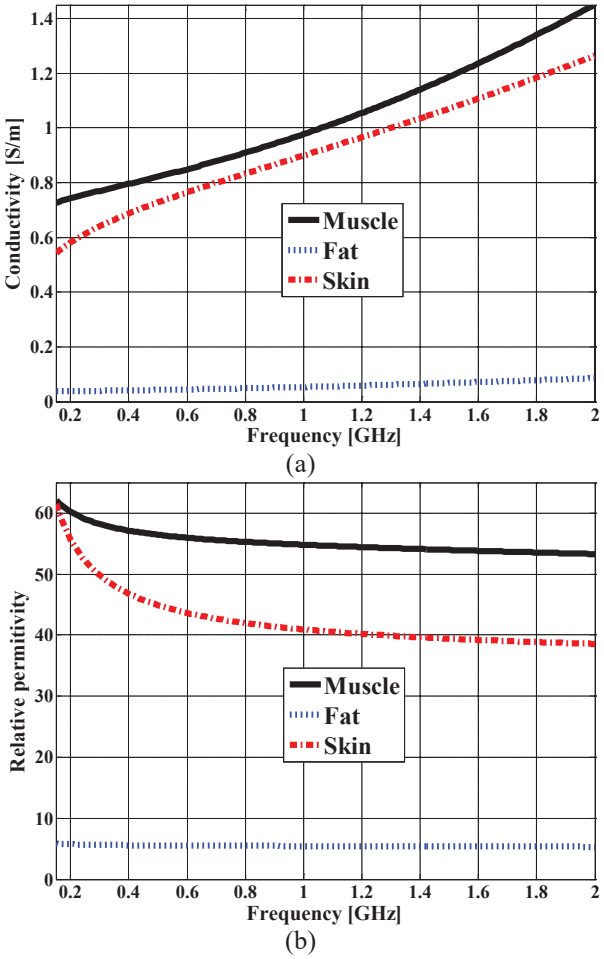

Fig. 3. Dielectric properties of the muscle, fat, and skin human tissues. (a) Conductivity σ [S/m]. (b) Relative permittivity ε_r.

[Step#1:] Start from an initial non-optimized design in which a microstrip antenna with full ground plane, where the antenna feed is fixed at the origin of the coordinate system as shown in Figure 4 (a). The dimensions are those of Figure 1 (c): $L_g \times W_g = 19.5 \times 12.9$ mm^2. From the results shown in Figure 5, step#1, it is seen from the computed reflection coefficient that the antenna does not resonate in the frequency band of interest (dc-2 GHz).

[Step#2:] Insert a meandered slot with variable sections of a minimum width; for example, 0.2 mm, in the radiating patch as shown in Figure 4 (b). This creates four resonance frequencies, as shown by the corresponding reflection coefficient. The impedance matching in this

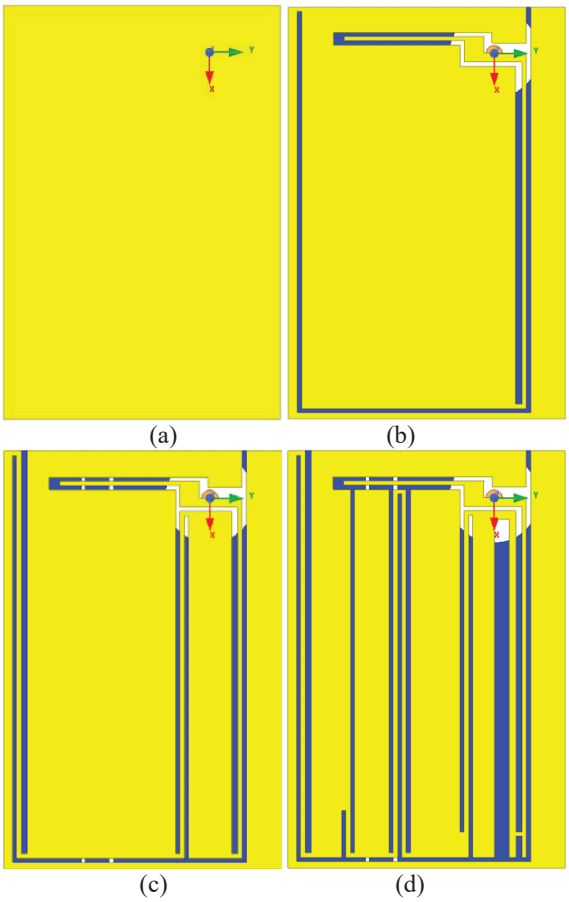

Fig. 4. Representation of the evolution of the patch and ground plane shapes with the four-step design process: (a) step #1; (b) step #2; (c) step #3; (d) step #4.

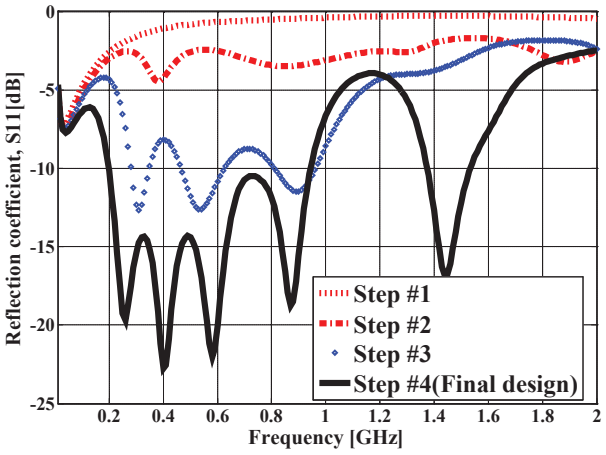

Fig. 5. The reflection coefficients (S_{11}) corresponding to the design process steps.

step is poor for the all created resonance frequencies as shown in Figure 5, step #2.

[Step#3:] The poor matching obtained in step #2 is improved for the first three resonances by inserting three other slots in parallel to the edges of the meandered slot introduced in the previous step as represented by Figure 4 (c). Also, the remaining fourth resonance frequency is shifted considerably to low without reaching its final target resonance frequency. For the fourth resonance frequency impedance matching enhancement, two parallel open-end slots are inserted in the ground plane. The reflection coefficient corresponding to this step is shown clearly in Figure 5, step #3.

[Step#4:] The poor obtained matching is reinforced again by inserting five other slots in the middle of the radiating patch, and another slot in parallel to the right edge of the meandered slot inserted before in step #2, as shown Figure 4 (d). A further shifting of the four resonance frequencies to their targeted counterparts is obtained with closer resonances. A fifth resonance frequency has been added in high frequencies. Finally, for resonance frequency tuning, adjustment of slots dimensions is performed. Results relative to reflection coefficient of this step are reported in Figure 5, step #4.

This marks the end of the antenna design and optimization. The final design yields a total impedance bandwidth of 0.90 GHz (0.20−0.94 and 1.37−1.53 GHz), and the obtained reflection coefficients (S_{11}) are −22.91, −18.46, −18.06, −18.65, −11.61, −12.08, and −16.68 dB at frequencies 403, 433, 611, 868, and 928 MHz and 1.395 and 1.432 GHz, respectively.

At this stage, we would say a word on the computation time. It is found that the computation time is highly depending on the antenna complexity which is directly related to the number of tracks of the radiating antenna. Hence, the computation time increases with the step number in the design process, detailed above in Section II-C. Later, in the simulations carried out in Section IV, computation time will increase again when the antenna is implanted in a realistic human model.

D. Ground plane open-end slotting effect

Figure 6 presents a comparison of the reflection coefficients of the final design with and without open-end slots inserted in the ground plane.

The open-end slots inserted in the ground plane enhance considerably the impedance bandwidth in higher frequencies. Otherwise, considering it is reported that an implantable antenna with full ground plane is preferred in some WIMDs, the designed antenna with full ground plane is still effective especially for the lower part of the targeted frequencies and remains a good candidate for such systems.

E. Free space measurements

To verify the performance of the designed implantable antenna in free space, a prototype of

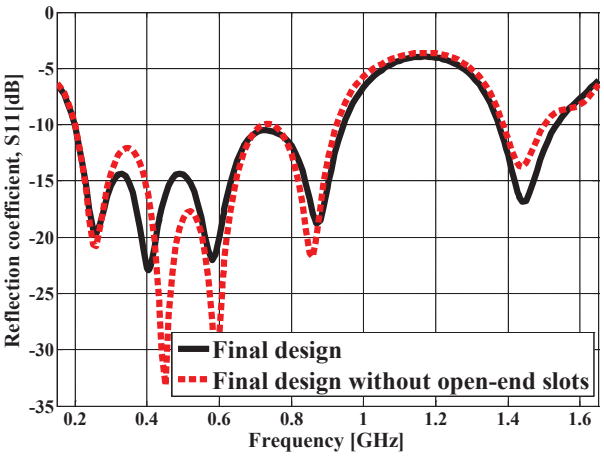

Fig. 6. Ground plane open-end slotting effect on impedance bandwidth enhancement.

the antenna was fabricated and appropriate measurement setup was used. A top and bottom view of the fabricated antenna and the measurement setup are shown, respectively, in Figures 7 (a) and (b).

The antenna consists of a coax-feed double-sided patch printed on a low permittivity and very low loss Cuflon substrate, with the same dielectric properties and thickness used in the simulation. A professional milling machine combined with high-precision 45° milling tools are used to engrave both the radiating patch and the ground plane. The antenna was connected to the vector network analyzer (VNA). A coaxial probe with an SMA connector that presents a characteristic impedance of 50 Ω is used to feed the antenna. Figure 8 displays a comparison of the measured and simulated return loss in free space.

Obviously, the antenna is not efficient in air, but according to the figure, we can see that numerical and experimental results are in a very good agreement. The measured resonance frequencies correspond to those predicted by the simulation, indicating that all current paths are present.

III. TISSUES AND IMPLANTATION DEPTH EFFECTS

In realistic implantation, the antenna is surrounded by various tissues that present different dielectric properties. The dielectric properties of all biological human tissues are frequency dependent. Examples of such characteristics are given for the muscle, fat, and skin in Figure 3 and will be used throughout this section. Furthermore, some types of tissues, such as the fat, possess variable thickness. To predict accompanied effects, simulations are performed into two main stages.

The first stage consists of one layer tissue with a total volume of 110 × 115 × 25 mm^3 in which the

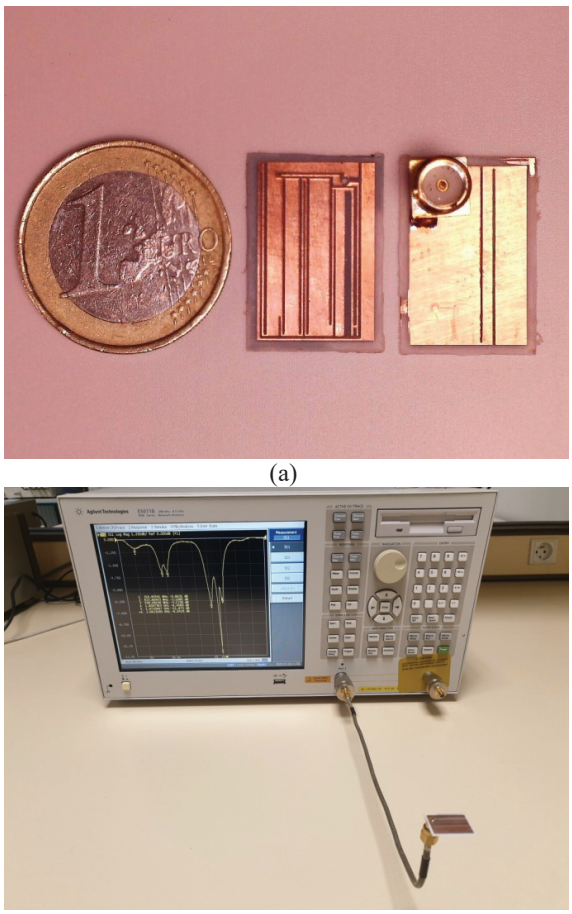

(a)

(b)

Fig. 7. (a) Fabricated antenna. (b) Measurement setup.

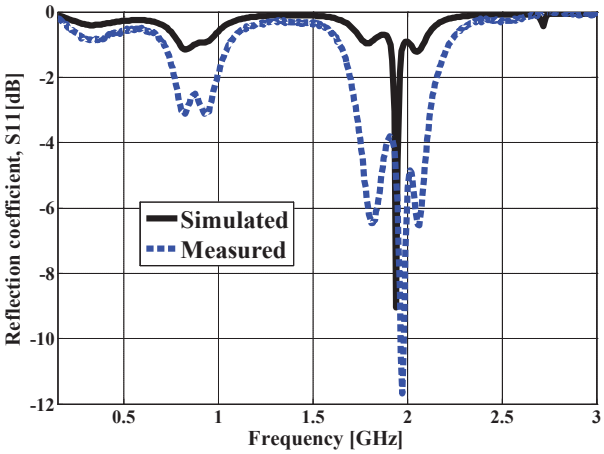

Fig. 8. Measured and simulated reflection coefficients (S_{11}) in air.

antenna implantation depth d_{oT} is set to 4 mm as shown in Figure 9 (a). Two different layers, skin and fat, are considered and the corresponding reflection coefficients

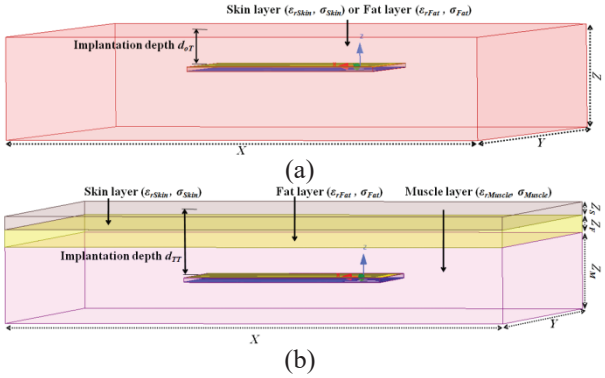

Fig. 9. Layered models used for tissues and depth effects study. (a) The one layered phantom model: skin or fat (X, Y, Z) = (110, 115, 25) mm. (b) The three layered phantom model: skin (X, Y, Z) = (110, 115, Z_S) mm, fat (X, Y, Z) = (110, 115, Z_F) mm, and muscle (X, Y, Z) = (110, 115, Z_M) mm.

Table 2: Various studied scenarios of a three-layer phantom model together with their physical dimensions

Scenario	**Layers thickness, and implantation depth [mm]**	**Implantation tissue**
1	Z_S = 1.3, Z_F = 1.7, Z_M = 22.0, d_{TT} = 4.0	Muscle
2	Z_S = 1.3, Z_F = 1.7, Z_M = 22.0, d_{TT} = 6.5	
3	Z_S = 2.0, Z_F = 10.0, Z_M = 13.0, d_{TT} = 15.0	
4	Z_S = 1.3, Z_F = 1.7, Z_M = 22.0, d_{TT} = 0.6	Skin
5	Z_S = 2.0, Z_F = 10.0, Z_M = 13.0, d_{TT} = 1.5	

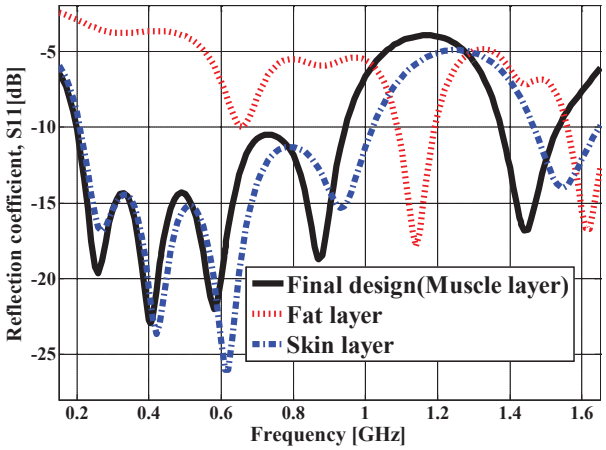

Fig. 10. Reflection coefficients (S_{11}) in one layer tissue phantom model.

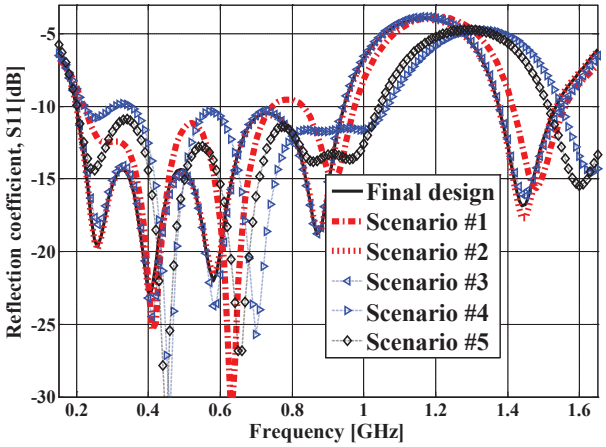

Fig. 11. Reflection coefficients (S_{11}) in a three-layer tissues phantom model.

are compared in Figure 10 to the one previously calculated in muscle layer. Results show that fat introduces an important shift of the resonance frequencies to higher frequencies due to lower values of relative permittivity of this human tissue layer and impedance mismatching is observed especially at lower frequencies. On the contrary, skin tissue layer introduces small modifications since it presents a closer permittivity with muscle.

The second stage consists of three layer tissues: muscle, fat, and skin, whose thicknesses are Z_M, Z_F, and Z_S, respectively, as shown in Figure 9 (b). The antenna implantation depth d_{TT}, in the layer of muscle, is defined as the distance between the radiating patch surface and the most close air−skin interface. Five scenarios corresponding to different values of implantation depth and layers thicknesses are given in Table 2 and are simulated. The whole volume of the structure is kept 110 × 115 × 25 mm^3 as in the first stage.

From the return loss results of the second stage scenario #1 given in Figure 11, we note that the use of three-layer human tissues phantom model shifts all implanted antenna resonance frequencies to higher frequencies with respect to the implantation in one layer muscle phantom model. Despite this shift, due to a lower permittivity of the media, a good impedance matching is maintained.

The obtained results of scenarios #2 and #3 presented in Figure 11 show that an appropriate increase in the implantations depth d_{TT} in the muscle allows reaching back the target resonance frequencies with very fine impedance matching level.

Furthermore, the designed skin implanted antenna of scenarios #4 and #5 present a good impedance matching for almost all target frequencies which are in this case, the MedRadio band (401−406) MHz, the ISM bands (433.1−434.8), (868.0−868.6), and

(902.8−928.0) MHz, and the Wireless Medical Telemetry Service (WMTS) band (608−614) MHz. The obtained results shown by scenarios #2, #3, #4, and #5 are in agreement with those presented by Lee *et al*. [43], where a skin- and muscle-implanted broadband PIFA antenna has been proposed for communication in the MICS band (402−405) MHz.

IV. ANTENNA OPERATION IN PRACTICAL IMPLANTATION

The proposed antenna is intended to be implanted in the muscles of the human body. To this end, two implantation tests have been simulated using the realistic human model of VHP-Female version 2.1 (age of 60 years old, height of 162 cm, and weight of 88 kg) of NEVA Electromagnetics, LLC [44]. This full body computational model of real human anatomy is constituted of 25 individual tissues distributed in 203 tissue parts. All inner tissues and organs are contained by the average body shell which is assigned as muscle tissue surrounded by fat and skin shells. For more accuracy, the individual dielectric properties of tissues [42] are used. Figure 12 shows two antenna implantation testing in the underneath the scalp (e.g., intracranial pressure monitoring) and in the upper arm muscle (e.g., blood pressure monitoring, and transcutaneous glucose monitoring). The antenna is implanted in the average body tissue at a depth of 5 and 11 mm from the close air−skin tissue surface for the first and the second implantation testing, respectively.

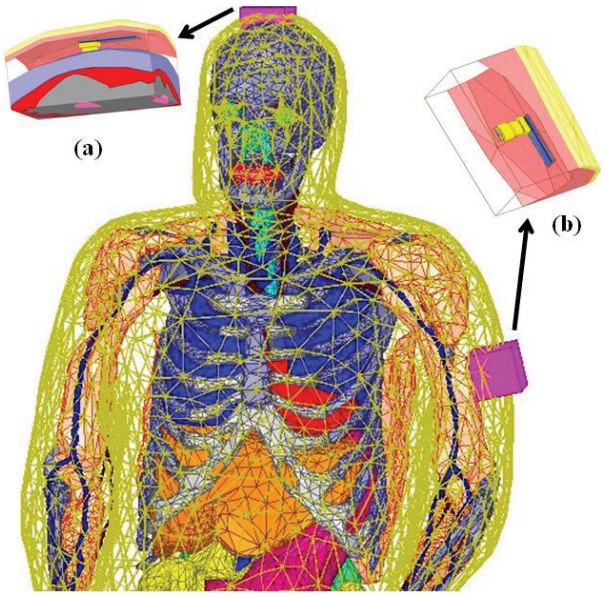

Fig. 12. Practical antenna implantation: (a) in the underneath the scalp; (b) in the upper arm.

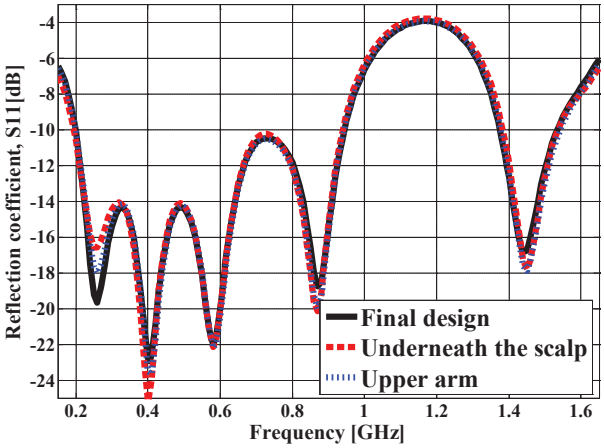

Fig. 13. Simulated reflection coefficients (S_{11}) of the antenna implantation tests in a realistic human body model.

A. Reflection coefficients

The simulated reflection coefficients of the two tests implantations are given in Figure 13, along with that of the final design already presented in Section II. Comparison of impedance bandwidth results shows that: 1) in the underneath the scalp implantation, the lower wideband (0.19−0.94) GHz is widened by 10 MHz toward lower limit bound, whereas the higher frequency band (1.38−1.54) GHz is shifted by 10 MHz toward upper limit bound, and 2) in the upper arm implantation, the impedance bandwidth of the lower wideband remains the same as the final design, whereas the impedance bandwidth of the higher band coincides with the underneath the scalp implantation. Thus, the exhibited total impedances bandwidth is of 0.91 and 0.90 GHz in the underneath the scalp and in the upper arm antenna implantation, respectively.

B. Far-field gain radiation pattern

An implanted antenna must be able to ensure communication requirements between the WIMDs and the external gateway/base-station. Thus, it is essential to obtain sufficient radiation power from the antenna implanted within the body. Figures 14 (a)−(g) present the simulated 3D far-field gain radiation patterns obtained for the two previous implantations together with the corresponding 2D far-field gain radiation patterns in *E* and *H* planes.

The corresponding values of the peak gain obtained in the underneath the scalp antenna implantation are −41.55, −39.58, −32.97, −30.52, −30.09, −27.69, and −27.35 dB. For in the upper arm, the corresponding values are −41.51, −40.00, −37.53, −41.05, −36.99, −25.93, and −25.24 dB at frequencies 403, 433, 611, 868, and 928 MHz and 1.395 and 1.432 GHz, respec-

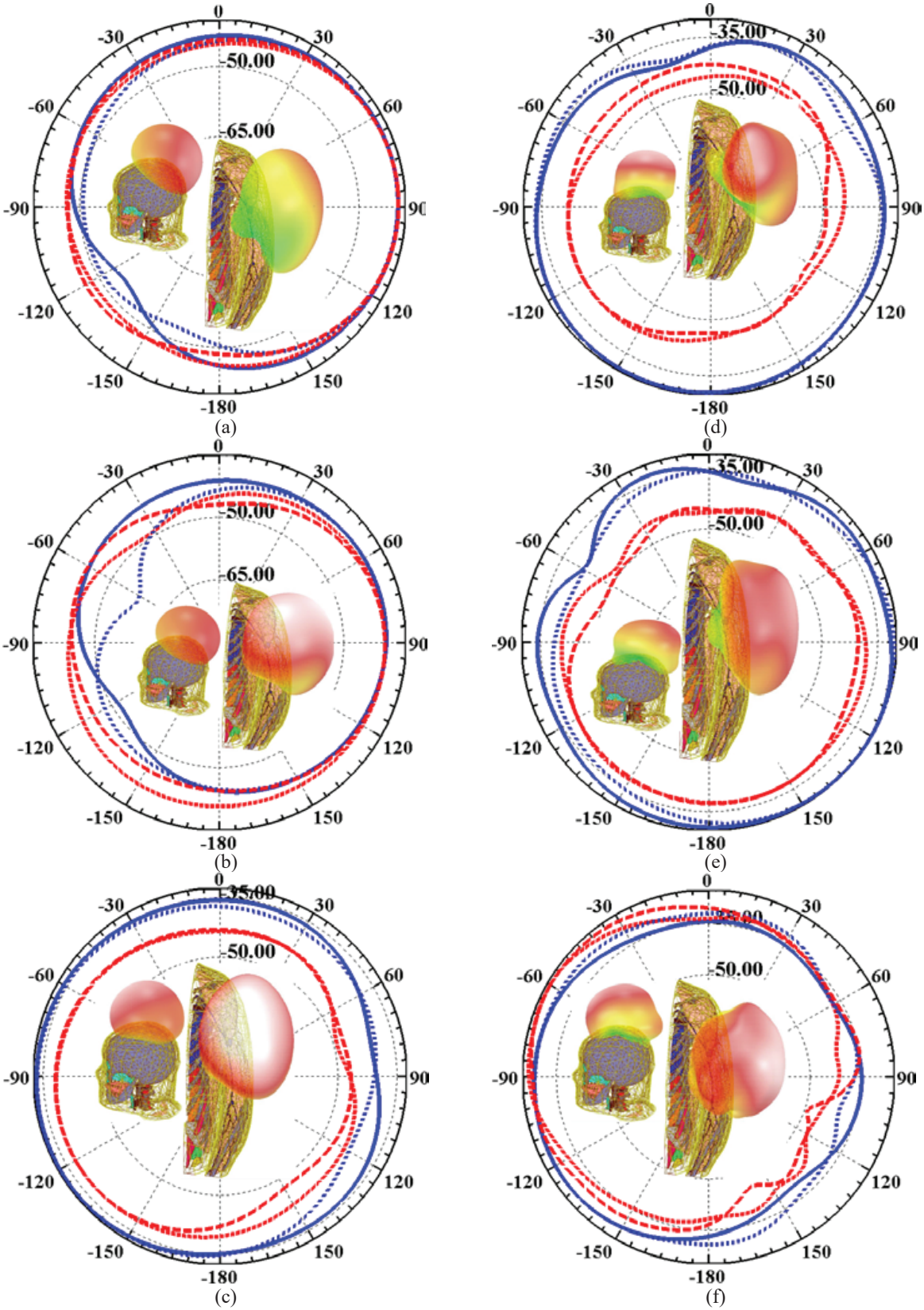

Fig. 14. *Continued.*

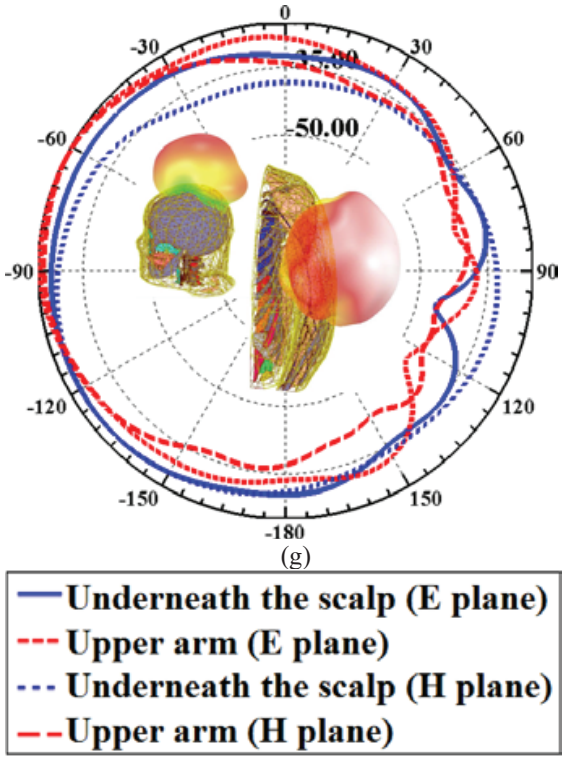

Fig. 14. Simulated 2D (*E* and *H* planes), and 3D far-field gain radiation patterns of antenna implantation tests in the underneath the scalp and in the upper arm at frequencies: (a) 0.403, (b) 0.433, (c) 0.611, (d) 0.868, (e) 0.928, (f) 1.395, and (g) 1.432 GHz.

tively. Note that, for both antenna implantation tests, the main radiated power is distributed toward the almost directions of the off-body environment.

This is valid for the all considered operating frequencies. Thus, the radiation characteristics of the proposed antenna are able to produce an effective wireless communication links between the interior and the exterior of the body. Besides, by comparison with the peak gain values obtained in the final design, a gain decreasing the overall considered frequency is observed. A maximum decrease of peak gain of 5 dB is noticed at the frequency 403 MHz. The decrease is probably due to the implantation depths and losses presented by the conductivity of the heterogeneous implantation testing mediums.

C. Safety considerations and electromagnetic interference

The patient safety is in priory. To this end, the general public exposure is restricted by IEEE C95.1-1999 and IEEE C95.1-2005 standards, in which the two limitations 1g averaged SAR $\leq$ 1.6 W/kg [45], and 10 g averaged SAR $\leq$ 2 W/kg [46] must be respected, respectively. Hence, the power incident to an implantable antenna should not exceed the corresponding value for each limitation. Assuming that the net-input power of the antenna is set to 1 W for the two practical implantation tests simulated previously in this section, the maximum 1-g averaged and 10-g averaged SAR and the corresponding maximum allowed net-input power values are listed in Table 3.

Table 3: Calculate maximum SAR values and corresponding permitted power

Model	Freq. [GHz]	Max SAR [W/kg]		Max net-input power [mW]	
		1 g-avg	10 g-avg	1 g-avg	10 g-avg
In the underneath the scalp	0.403	555.95	87.55	2.87	22.84
	0.433	563.44	86.65	2.83	23.08
	0.611	636.57	88.29	2.51	22.65
	0.868	624.63	90.53	2.56	22.09
	0.928	579.50	84.02	2.76	23.80
	1.395	599.58	81.31	2.66	24.59
	1.432	575.72	84.69	2.77	23.61
In the upper arm	0.403	554.54	89.57	2.88	22.32
	0.433	562.64	88.94	2.84	22.48
	0.611	635.47	89.97	2.51	22.22
	0.868	616.31	90.74	2.59	22.04
	0.928	571.37	84.44	2.80	23.68
	1.395	584.13	81.35	2.73	24.58
	1.432	547.41	83.84	2.92	23.85

Moreover, to mitigate EM interference with nearby services, the effective isotropic radiated power (EIRP) of a transmitter antenna is limited as mentioned by the following equation:

$$\mathrm{EIRP[dBm]} = P_{\mathrm{in}}[\mathrm{dBm}] + G[\mathrm{dBi}] \leq \mathrm{EIRP}_{\mathrm{max}}[\mathrm{dBm}], \quad (1)$$

where P_{in} is the net-input power, and G is the radiation gain of the antenna. The implanted antenna in transmitting serve the up-link, and the EIRP_{max} is set to -16, 7.85, 10.8, 11.85, 36, 22.2, and 22.2 dBm for frequencies 403, 433, 611, 868, and 928 MHz and 1.395 and 1.432 GHz, respectively [5, 22, 47].

The implanted antennas exhibit low gain values. Thus, the maximum net-input power remains limited by the SAR restrictions. For the two simulated implantation tests, the calculated value of the net-input power of 4 dBm (2.51 mW) allows to meet the patient safety restrictions of both the most (1-g averaged SAR $\leq$ 1.6 W/kg and less (10-g averaged SAR $\leq$ 2 W/kg) limitations of IEEE standards, and this is validated for all considered frequencies. In addition, this value is much greater than the limit of the input power of the implantable antennas, which is 25 μW [24, 29, 32, 34, 37].

Table 4: Parameters description of the link margin calculation

Transmission		
Freq [GHz]	Operating frequency	0.403, 0.43, 0.611, 0.868, 0.928, 1.395, 1.432
P_{Tx} [dBW]	Tx power	-46
G_{Tx} [dBi]	Tx antenna gain	Max gain (free space), mean gain (indoor)
L_{Txf} [dB]	Tx feeding loss	0
L_{Txm} [dB]	Tx impedance mismatch loss	0.3
L_{pol} [dB]	Polarization mismatch loss	2
Propagation scenarios		
LP_m ($m = 2$) [dB]	Free space	Path-loss exponent m and distance dependent
LP_m ($m = 1.5$) [dB]	Indoor LOS	
LP_m ($m = 3$) [dB]	Indoor NLOS	
dL [m]	Tx−Rx distance	To be calculated
d_0 [m]	Reference distance	1
λ [m]	Wavelength in free space	(3×10^8)/Freq
χ_σ [1]	Shadowing factor	0
Receiver		
G_{Rx} [dBi]	Rx antenna gain	2.15
L_{Rxf} [dB]	Rx feeding loss	0
L_{Rxm} [dB]	Rx mismatch loss	0
T_o [K]	Ambient temperature	293
k [1]	Boltzmann const.	1.38×10^{-23}
NF [dB]	Receiver noise figure	3.5
N_o [dB/Hz]	Noise power density	-199.95
Signal quality		
B_r [bps]	Bit rate	100×10^3
BER [1]	Bit error rate	1.0×10^{-5}
Eb/N_o [dB]	Ideal-PSK, ideal-BPSK	9.6
G_c [dB]	Coding gain	0
G_d [dB]	Fixing deterioration	2.5

D. Link communication performances

The link budget calculation allows evaluating the far-field communication link quality. It allows evaluating the communication performances between the WIMD antenna and the exterior gateway/base-station for envisaged communication requirements with including various transmission constraints. The link established between the transmitter designed antenna Tx and an exterior receiver antenna Rx is evaluated. The link margin (LM) is given as a function of the carrier to noise power density ratio (C/N_0) as detailed by the following equation [2, 20, 22]:

$$LM = \text{Link}\frac{C}{N_0} - \text{Required}\frac{C}{N_0} = (P_{Tx} + G_{Tx} + G_{Rx} - L_{Txf} - L_{Txm} - LP_m - L_{pol} - L_{Rxf} - L_{Rxm} - N_0) - \left(\frac{E_b}{N_0} + 10\log_{10} B_r - G_c + G_d\right), \quad (2)$$

where

$$LP_m = 10m\log_{10}\left(\frac{dL}{d_0}\right) + 20\log_{10}\left(\frac{4\pi d_0}{\lambda}\right) + \chi_\sigma, \quad (3)$$

and

$$N_0 = 10\log_{10}(kT_0(NF-1)). \quad (4)$$

Various parameter descriptions and their values used for LM calculation are listed in Table 4. The available transmitter power P_{Tx} is set to 25 μW and the transmitter gain G_{Tx} values considered are those obtained in the first practical test as described in Section IV-B. The considered receiver antenna is a well matched dipole antenna with impedance mismatch loss L_{Rxm} equal to 0 dB and gain G_{Rx} equal to 2.15 dB [22]. Also, the impedance mismatching loss L_{Txm} of the transmitter antenna is set to 0.3 dB, which is the maximum value calculated for all considered frequencies. The feeding losses L_{Txf} and L_{Rxf} of the transmitter and the receiver, respectively, are neglected. In addition, the obtained polarization is almost linear; thus, the polarization mismatch loss L_{pol} is taken 2 dB [11].

Three different propagation scenarios are considered to account for the propagation channel effects: (1) in the free space, (2) in the indoor line-of-sight (LOS), and (3) in the indoor non-line-of-sight (NLOS). To this end, the most suitable model of log-distance for the indoor loss estimation is used. For the first scenario communication channel, the transmitter gain G_{Tx} values are those simulated maximum values, whereas for the indoor channels, i.e., LOS and NLOS, the mean gains are more suitable [22] and their simulated values are considered for the LM calculation.

The shadowing factor χ_σ is neglected and the reference distance d_0 is set as 1 m for all three propagation scenarios. The signal quality parameter of the bit rate B_r is chosen to cover largely the requirements of the

clinical applications associated with practical tests simulated in Section IV. For example, the bit rate for the subcutaneous glucose sensor, and the intracranial pressure transmission is less than 10 kbps [4], and is of 7 kbps [29, 32, 37], respectively.

The other receiver Rx and signal quality parameter values adopted are those of references [2, 20]. These other signal quality parameter values are agreed from several WIMDs. The data communication between a transmitter and a receiver antennas remains possible when the LM $>$ 0 dB. Figure 15 illustrates the LM values calculated in function of transmitter−receiver distance *dL* for the three propagation scenarios.

The communication distances offered by the indoor LOS channel communication are larger than those obtained in the free space and in the indoor NLOS environments.

Due to the lack of LOS, the LM decrease is rapid in the indoor NLOS environments, which leads to low possible communication distance. Nevertheless, this distance communication remains sufficient in all the three channels. In the free space, the communication distance starts from 19 m at 403 MHz to reach 33.5 m at 611 MHz, and in the indoor LOS propagation scenario, the communication distance begins from 14 m at 403 MHz until and 45m at 868 MHz, and although the indoor NLOS is a rigorous propagation scenario, the communication can be established from the distance of 3.75 m at 433 MHz to 6.5 m at 868 MHz. Thus, the telemetry communication links between the proposed implantable antenna and an exterior gateway/base-station can be established in both the free space and in the indoor environments with practical distances.

V. COMPARISON WITH RECENTLY PUBLISHED IMPLANTABLE ANTENNAS

The performances of the proposed multi-track implantable antenna are compared with data brought from the literature. Various targeted operating frequency bands are considered for this comparison. The results are reported in Table 5.

Thanks to an efficient design combined with using a low permittivity substrate, the proposed antenna exhibits both low volume and broadband behavior. In addition, as it does not require any superstrate, the proposed configuration presents a very low thickness. Actually, the proposed antenna covers several telemetry frequencies with large available frequency bands, whereas voluminous antennas covering less number of operating frequency bands are noticed, as reported in published studies. Note that our obtained peak gain values are very near to those available from the literature in almost all cases. Note also that the obtained SAR values are very comparable to those in the literature with improvements in some cases and small degradation in other cases.

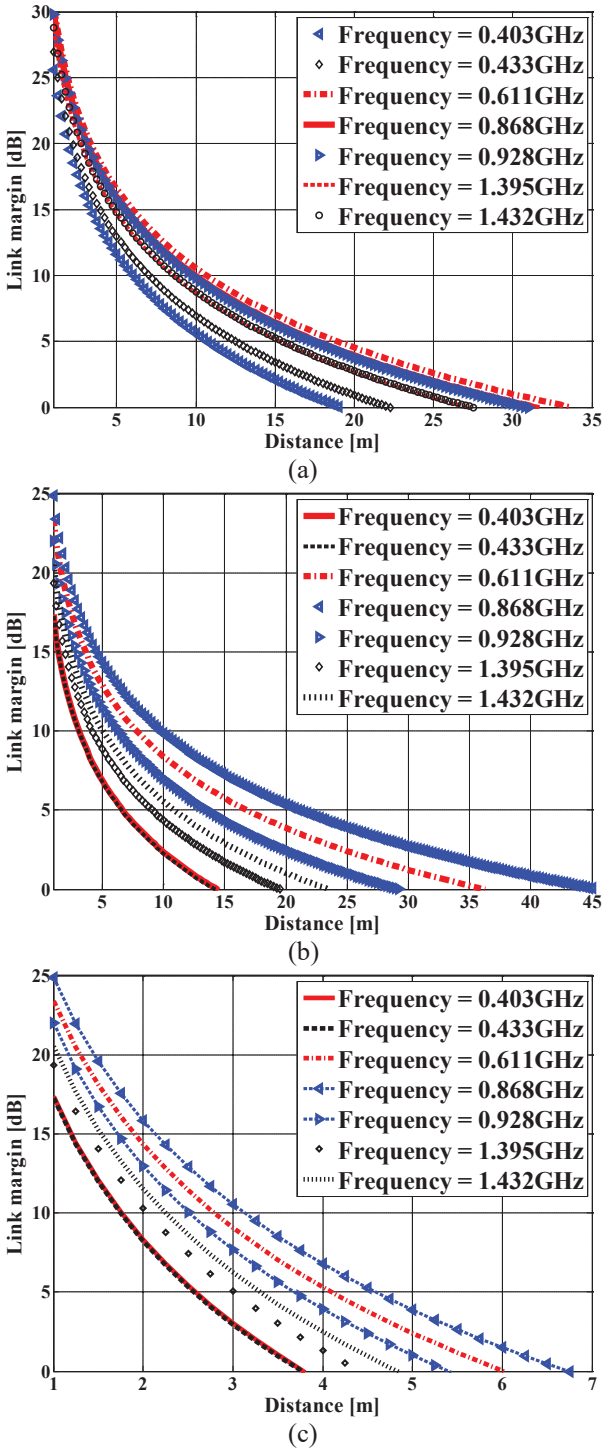

Fig. 15. Link margin LM calculation: (a) free space loss; (b) indoor LOS loss; (c) indoor NLOS loss.

Table 5: Comparison of the designed antenna performances with those of previous proposed implantable antennas from the literature

Ref.	Volume [mm^3]	Available bands [MHz]	Freq. [MHz]	Peak gain/ realized gain [dBi]	Max. SAR [W/kg] [input power = 1 W]		Substrate/ superstrate (ε_r, $tan\delta$)	Total thickness [mm]
					1-1999 1g-avg	1-2005 10g-avg		
[13]	560	360	400	G. −27.8	161	—	FR4 (4.4, 0.02)/RO3010 (10.2, 0.0035)	1.6
[22]	203.4	27	402	G. −36.9	324	66.6	Both: RO3210 (10.2, 0.003)	1.8
		28	433	G. −35.9	309	66.3		
		38	868	G. −35.1	297	66.0		
		40	915	G. −32.9	295	67.5		
[27]	248.92	100	402	G. −46	338	—	Both: RO3010 (10.2, –)	1.27
		300	2440	G. −19	482	—		
[32]	52.5	64	405	G. −40.8	665	93.2	Both: Rogers 6010 (10.2, 0.0035)	0.5
		91	915	G. −32.9	837	93.9		
		105	2450	G. −22.3	759	87.2		
[34]	21	80	915	G. −26.4	380	40.4	Both: RT/duroid 6010 (10.2, 0.0035)	0.5
		115	1900	G. −23	358	38.2		
		180	2450	G. −20.47	363	40.3		
[36]	254	150	401	G. −22	—	39.1	Both: RO3210 (10.2, 0.003)	2.45
			433	G. −23	—	39.5		
		52	1427	G. −17	—	58.7		
		102	2400	G. −16	—	76.8		
[37]	17.15	148	402 433	G. −30.5 G. −30	588 544	92.7 90.5	Both: RT/duroid 6010 (10.2, 0.0035)	0.377
		173	1600	G. −22.6	441	85.3		
		213	2450	G. −18.2	305	81.7		
[40]	404.14	3193	403	R.G. −34.3	216	—	Both: RO3010 (10.2, 0.0035)	1.235
			433	R.G. −30.6	213	—		
			868	R.G. −26.6	211	—		
			915	R.G. −26.0	205	—		
			2450	R.G. −18.4	203	—		
This work	114.70	750	403	G. −41.5	555	87.5	Cuflon (2.05, 0.00045)/No	0.456
			433	G. −39.5	563	86.6		
			611	G. −32.9	636	88.2		
			868	G. −30.5	624	90.5		
			928	G. −30.0	579	84.0		
		160	1395	G. −27.6	599	81.3		
			1432	G. −27.3	575	84.6		

VI. CONCLUSION

In this work, a novel miniaturized multi-track muscle implantable planar patch antenna has been proposed for WIMDs biomedical telemetry communications. The patch slotting and a pair of open-end slots in the ground plane techniques have been used to obtain a wideband and multi-band behavior. The miniaturized antenna compact volume of 114.70 mm^3 was implemented with a low relative permittivity substrate and does not require any superstrate. Seven telemetry allocated frequency bands are covered widely starting from the lower frequency band of MedRadio (401−406) MHz to the WMTS (1.427−1.432) GHz. A prototype of the proposed antenna has been fabricated, and the agreement between simulation and measurement was fully in free space.

Antenna's operation was investigated in two realistic implantations of human body, in the underneath the scalp and in the upper part of the arm.

Considering the three performance criteria, 1) optimized volume of the antenna, 2) total number of seven largely covered allocated frequency bands, and 3) peak gain values at considered frequencies at once, the proposed implantable antenna is very satisfactory compared to many recent proposed implantable antennas referenced in this work.

A model for the link communication distance is adopted and ascertained by performing computations for the cases of free space and indoor propagation environments.

With seven telemetry bands covered, the proposed implanted antenna is a candidate for various clinical applications of the head and arm. It can also be designed with a full ground plane and still cover five telemetry frequency bands. In addition, a second mode of antenna implantation, i.e., in the skin, can also be used with five operating frequency bands covered.

ACKNOWLEDGMENT

We would like to thank Mr. Erwan Fichou for his assistance in the manufacture of the antennas and the IUT of Chartres for his financial support.

REFERENCES

[1] P. S. Hall and Y. Hao, *Antennas and Propagation for Body Centric Wireless Communications*, Artech House, Norwood, 2012.

[2] K. S. Nikita, *Handbook of Biomedical Telemetry,* Wiley-IEEE, 2014.

[3] A. Kiourti and K. S. Nikita, "A review of in-body biotelemetry devices: Implantables, ingestibles, and injectables," *IEEE Transactions on Biomedical Engineering*, vol. 64, no. 7, pp. 1422-1430, Jul. 2017. doi: 10.1109/TBME.2017.2668612.

[4] A. K. Teshome, B. Kibret, and D. T. H. Lai, "A review of implant communication technology in WBAN: Progress and challenges," *IEEE Reviews in Biomedical Engineering*, vol. 12, pp. 88-99, Feb. 2019. doi: 10.1109/RBME.2018.2848228.

[5] K. Fujimoto and K. Ito, *Antennas for Small Mobile Terminals*, Artech House, Norwood, 2018.

[6] Z. N. Chen, D. Liu, H. Nakano, X. Qing, and Th. Zwick, *Handbook of Antenna Technologies*, Springer. Singapore, 2016.

[7] S. Bakogianni and S. Koulouridis, "An implantable planar dipole antenna for wireless MedRadio-Band biotelemetry devices," *IEEE Antennas and Wireless Propagation Letters*, vol. 15, pp. 234-237, Feb. 2016. doi: 10.1109/LAWP.2015.2439039.

[8] S. M. Huang, M. R. Tofighi, and A. Rosen, "Consideration for the design and placement of implantable annular slot antenna for intracranial pressure monitoring devices," *IEEE Antennas and Wireless Propagation Letters*, vol. 14, pp. 1514-1517, Jul. 2015. doi: 10.1109/LAWP.2014.2370940.

[9] C. Wang, L. Zhang, S. Wu, S. Huang, C. Liu, and X. Wu, "A dual-band monopole antenna with EBG for wearable wireless body area networks," *Applied Computational Electromagnetics Society (ACES) Journal*, vol. 36, no. 1, pp. 48-54, Jan. 2021. https://doi.org/10.47037/2020.ACES.J.360107.

[10] D. Nikolayev, M. Zhadobov, and R. Sauleau, "Impact of tissue electromagnetic properties on radiation performance of in-body antennas," *IEEE Antennas and Wireless Propagation Letters*, vol. 17, no. 8, pp. 1440-1444, Aug. 2018. doi: 10.1109/LAWP.2018.2848943.

[11] X. Y. Liu, Z. T. Wu, Y. Fan, and E. M. Tentzeris, "A miniaturized CSRR loaded wide-beamwidth circularly polarized implantable antenna for subcutaneous real-time glucose monitoring," *IEEE Antennas and Wireless Propagation Letters*, vol. 16, pp. 577-580, Mar. 2017. doi: 10.1109/LAWP.2016.2590477.

[12] A. Kiourti, J. R. Costa, C. A. Fernandes, and K. S. Nikita, "A broadband implantable and a dual-band on-body repeater antenna: Design and transmission performance," *IEEE Transactions on Antennas and Propagation*, vol. 62, no. 6, pp. 2899-2908, Jun. 2014. doi: 10.1109/TAP.2014.2310749.

[13] C. Tsai, K. Chen, and C. Yang, "Implantable wideband low-SAR antenna with c-shaped coupled ground," *IEEE Antennas and Wireless Propagation Letters*, vol. 14, pp. 1594-1597, Aug. 2015. doi: 10.1109/LAWP.2015.2413839.

[14] H. Li, Y. Guo, and S. Xiao, "Broadband circularly polarised implantable antenna For biomedical

applications," *Electronics Letters*, vol. 52, no. 7, pp. 504-506, Apr. 2016. doi: 10.1049/el.2015.4445.

[15] A. G. Miquel, S. Curto, N. Vidal, J. M. Lopez-Villegas, F. M. Ramos, and P. Prakash, "Multilayered broadband antenna for compact embedded implantable medical devices: Design and characterization," *Progress In Electromagnetics Research*, vol. 159, pp. 1-13, Apr. 2017. doi:10.2528/PIER16121507

[16] Y. Zhang, C. Liu, X. Liu, K. Zhang, and X. Yang, "A wideband circularly polarized implantable antenna for 915 MHz ISM-Band biotelemetry devices," *IEEE Antennas and Wireless Propagation Letters*, vol. 17, no. 8, pp. 1473-1477, Aug. 2018. doi: 10.1109/LAWP.2018.2849847.

[17] S. Das and D. Mitra, "A compact wideband flexible implantable slot antenna design with enhanced gain," *IEEE Transactions on Antennas and Propagation*, vol. 66, no. 8, pp. 4309-4314, Aug. 2018. doi: 10.1109/TAP.2018.2836463.

[18] R. Lesnik, N. Verhovski, I. Mizrachi, B. Milgrom, and M. Haridim, "Gain enhancement of a compact implantable dipole for biomedical applications," *IEEE Antennas and Wireless Propagation Letters*, vol. 17, no. 10, pp. 1778-1782, Oct. 2018. doi: 10.1109/LAWP.2018.2866233.

[19] G. Samanta and D. Mitra, "Miniaturised and radiation efficient implantable antenna using reactive impedance surface for biotelemetry," *IET Microwaves, Antennas & Propagation*, vol. 14, no. 2, pp. 177-184, Feb. 2020. doi: 10.1049/iet-map.2019.0132.

[20] X. Yang, H. Wong, and J. Xiang, "Polarization reconfigurable planar inverted-F antenna for implantable telemetry applications," *IEEE Access*, vol. 7, pp. 141900-141909, Oct. 2019. doi: 10.1109/ACCESS.2019.2941388.

[21] Z. Xia, H. Li, Z. Lee, S. Xiao, W. Shao, X. Ding, and X. Yang, "A wideband circularly polarized implantable patch antenna for ISM band biomedical applications," *IEEE Transactions on Antennas and Propagation*, vol. 68, no. 3, pp. 2399-2404, Mar. 2020. doi: 10.1109/TAP.2019.2944538.

[22] A. Kiourti and K. S. Nikita, "Miniature scalp-implantable antennas for telemetry in the MICS and ISM bands: Design, safety considerations and link budget analysis," *IEEE Transactions on Antennas and Propagation*, vol. 60, no. 8, pp. 3568-3575, Aug. 2012. doi: 10.1109/TAP.2012.2201078.

[23] J. Ung and T. Karacolak, "A dual-band meandered Dipole antenna for medical telemetry applications," *Progress In Electromagnetics Research C*, vol. 63, pp. 85-94, Apr. 2016. doi:10.2528/PIERC16012603

[24] S. A. A. Shah and H. Yoo, "Scalp-implantable antenna systems for intracranial pressure monitoring," *IEEE Transactions on Antennas and Propagation*, vol. 66, no. 4, pp. 2170-2173, Apr. 2018. doi: 10.1109/TAP.2018.2801346.

[25] A. O. Kaka, M. Toycan, S. D. Walker, and D. Kavaz, "Dual band, miniaturized, implantable antenna design with on-body antennas for wireless health monitoring," *Applied Computational Electromagnetics Society (ACES) Journal*, vol. 35, no. 4, pp. 443-452, Apr. 2020.

[26] L. Xu, Y. Guo, and W. Wu, "Dual-band implantable antenna with open-end slots on ground," *IEEE Antennas and Wireless Propagation Letters*, vol. 11, pp. 1564-1567, 2012. doi: 10.1109/LAWP.2012.2237010.

[27] M. Usluer, B. Cetindere, and S C. Basaran, "Compact implantable antenna design for MICS and ISM band biotelemetry applications," *Microwave and Optical Technology Letters*, vol. 62, no. 4, pp. 1581-1587, Apr. 2020. https://doi.org/10.1002/mop.32185.

[28] Y. Fan, H. Liu, X. Liu, Y. Cao, Z. Li, and M. M. Tentzeris, "Novel coated differentially fed dual-band fractal antenna for implantable medical devices," *IET Microwaves, Antennas & Propagation*, vol. 14, no. 2, pp. 199-208, Feb. 2020. doi: 10.1049/iet-map.2018.6171.

[29] F. Faisal and H. Yoo, "A miniaturized novel-shape dual-band antenna for implantable applications," *IEEE Transactions on Antennas and Propagation*, vol. 67, no. 2, pp. 774-783, Feb. 2019. doi: 10.1109/TAP.2018.2880046.

[30] H. Zhang, L. Li, C. Liu, Y.-X. Guo, and S. Wu, "Miniaturized implantable antenna integrated with split ring resonate rings for wireless power transfer and data telemetry," *Microwave and Optical Technology Letters*, vol. 59, no. 3, pp. 710-714, Mar. 2017. https://doi.org/10.1002/mop.30381

[31] L. Luo, B. Hu, J. Wu, T. Yan, and L-J. Xu, "Compact dual-band antenna with slotted ground for implantable applications," *Microwave and Optical Technology Letters*, vol. 61, no. 5, pp. 1314-1319, May 2019. https://doi.org/10.1002/mop. 31718.

[32] I. Gani and H. Yoo, "Multi-band antenna system for skin implant," *IEEE Microwave and Wireless Components Letters*, vol. 26, no. 4, pp. 294-296, Apr. 2016. doi: 10.1109/LMWC.2016.2538470.

[33] R. Das, Y. Cho, and H. Yoo, "High efficiency unidirectional wireless power transfer by a triple band deep-tissue implantable antenna," *2016 IEEE MTT-S International Microwave Symposium (IMS)*, San Francisco, CA, pp. 1-4, 2016. doi: 10.1109/MWSYM.2016.7540252.

[34] M. Zada and H. Yoo, "A miniaturized triple-band implantable antenna system for bio-telemetry applications," *IEEE Transactions on Antennas and Propagation*, vol. 66, no. 12, pp. 7378-7382, Dec. 2018. doi: 10.1109/TAP.2018.2874681.

[35] F. Huang, C. Lee, C. Chang, L. Chen, T. Yo, and C. Luo, "Rectenna application of miniaturized implantable antenna design for triple-band biotelemetry communication," *IEEE Transactions on Antennas and Propagation*, vol. 59, no. 7, pp. 2646-2653, Jul. 2011. doi: 10.1109/TAP.2011.2152317.

[36] C. K. Wu, T. F. Chien, C. L. Yang, and C. H. Luo, "Design of novel s-shaped quad-band antenna for MedRadio/WMTS/ISM implantable biotelemetry applications," *Int. J. Antennas Propag*., vol. 2012, Article ID 564092, 2012. doi:10.1155/2012/564092.

[37] I. A. Shah, M. Zada, and H. Yoo, "Design and analysis of a compact-sized multiband spiral-shaped implantable antenna for scalp implantable and leadless pacemaker systems," *IEEE Transactions on Antennas and Propagation*, vol. 67, no. 6, pp. 4230-4234, Jun. 2019. doi: 10.1109/TAP.2019.2908252.

[38] A. Basir and H. Yoo, "Efficient wireless power transfer system with a miniaturized quad-band implantable antenna for deep-body multitasking implants," *IEEE Transactions on Microwave Theory and Techniques*, vol. 68, no. 5, pp. 1943-1953, May 2020. doi: 10.1109/TMTT.2020.2965938.

[39] A. Kiourti and K. S. Nikita, "A review of implantable patch antennas for biomedical telemetry: challenges and solutions [wireless corner]," *IEEE Antennas and Propagation Magazine*, vol. 54, no. 3, pp. 210-228, Jun. 2012. doi: 10.1109/MAP.2012.6293992.

[40] Z. Jiang, Z. Wang, M. Leach, E. G. Lim, J. Wang, R. Pei, and Y. Huang, "Wideband loop antenna with split-ring resonators for wireless medical telemetry," *IEEE Antennas and Wireless Propagation Letters*, vol. 18, no. 7, pp. 1415-1419, Jul. 2019. doi: 10.1109/LAWP.2019.2918501.

[41] Available on 08.04.2021. https://www.craneae.com/microwave-solutions-substrates

[42] S. Gabriel, R. W. Lau, and C. Gabriel, "The dielectric properties of biological tissues," *Phys. Med. Biol.*, vol. 41, pp. 2231-2293, 1996. Available at: http://niremf.ifac.cnr.it/tissprop/

[43] C. M. Lee, T. C. Yo, F. J. Huang, and C. H. Luo, "Bandwidth enhancement of planar inverted-f antenna for implantable biotelemetry," *Microwave and Optical Technology Letters*, vol. 51, no. 3, pp. 749-752, Mar. 2009. https://doi.org/10.1002/mop.2418

[44] S. N. Makarov, G. M. Noetscher, J. Yanamadala, M. W. Piazza, S. Louie, A. Proko, A. Nazarian, and A. Nummenmaa, "Virtual human models for electromagnetic studies and their applications," *IEEE Reviews in Biomedical Engineering*, vol. 10, pp. 95-121, Dec. 2017. doi: 10.1109/RBME.2017.2722420.

[45] IEEE Standard for Safety Levels with Respect to Human Exposure to Radiofrequency Electromagnetic Fields, 3 kHz to 300 GHz, IEEE Standard C95.1, 1999.

[46] IEEE Standard for Safety Levels with Respect to Human Exposure to Radiofrequency Electromagnetic Fields, 3 kHz to 300 GHz, IEEE Standard C95.1, 2005.

[47] International Telecommunications Union-Radiocommunications (ITU-R), Radio Regulations, document SA 1346, ITU, Geneva, Switzerland. Available at: http://itu.int/home

Mohamed Behih was born in Bordj Bou Arreridj, Algeria, in 1981. He received the Engineer degree in electronic engineering and the Magister degree in communication from Setif University, Algeria, in 2004 and 2007, respectively. He is currently working toward the Doctor of Sciences degree in communication.

From 2010 to 2015, he was an Assistant Professor with the Electronics Department, University of Blida, Algeria. He is presently working as an Assistant Professor with Bordj Bou Arreridj University, Algeria. His researches focus on biomedical engineering, interaction between electromagnetic wave and human body, medical devices and biomedical telemetry, and antennas for wireless body area networks.

Farid Bouttout received the B.Sc. and M.Sc. degrees in electronic engineering from the University of Constantine, Constantine, Algeria, in 1994 and 1997, respectively, and the Ph.D. degree in electronic engineering from the University of Setif, Setif, Algeria, in 2001. He was granted three-year postdoc study on design of planar antennas for medical applications at the Commissariat à l'Energie Atomique (CEA) and at the University of Paris VI, France.

He is currently a Professor with the Electronics Department, University of Bordj Bou Arreridj. His current research interests include planar and cylin-

drical microstrip antennas and transmission lines, computational electromagnetics, high performance computing, neural networks, and fuzzy logic.

Tarek Fortaki was born on March 31, 1972, in Constantine, Algeria. He received the Engineer of Communication degree in 1995, the Master of Science degree in microwaves in 1999, and the Doctorate degree in microwaves in 2004, all from the Electronics Department, Faculty of Engineering Science, University of Constantine.

Currently, he is a Professor with the Electronics Department, Faculty of Technology, University of Batna 2. He has published more than 40 papers in refereed journals and more than 50 papers in conference proceedings. He serves as a Reviewer for several technical journals. His main research interests are in electromagnetic theory, numerical methods, and modeling of antennas and passive microwave circuits.

Christophe Dumond was born in Tulle, France, on October 22, 1966. He received the Ph.D. degree in optic communications and microwaves from the University of Limoges, France, in 1994. His works concern the electromagnetic answer of wire structures to fast transient perturbations.

In 2007, he joined the Institut Pluridisciplinaire de Recherche en Ingénierie des Systèmes Mécaniques et Energétique (PRISME), University of Orléans, France. His fields of research include fractal antennas, high Tc superconducting microstrip patch, phased arrays, and implantable antennas for bio-telemetry. He is also a teacher and head of the Electrical Engineering Department, Institut Universitaire de Technologie (IUT), Chartres, France.

A Compact Planar Monopole UWB MIMO Antenna Design with Increased Isolation for Diversity Applications

S. Kolangiammal[1], L. Balaji[2], and G. Vairavel[3]

[1,2]Department of Electronics and Communication,
Veltech Rangarajan Dr. Sakunthala R&D Institute of Science and Technology, Chennai 600062, India
[1]vtd582@veltech.edu.in, [2]drbalaji@veltech.edu.in

[3]SRM Institute of Science and Technology, Chennai 603203, India
vairavelg@protonmail.com

Abstract – A compact planar multiple input multiple output (MIMO) antenna with four elements spanning the ultra-wideband (UWB) is proposed for diversity applications. The unit cells are positioned orthogonally to lower the mutual coupling by replicating the single antenna three times. A 35 × 35 × 1.6 mm^3 UWB MIMO antenna is provided with a 50-Ω impedance microstrip line on a 1.6-mm thick FR4 substrate. In the radiator and ground plane, some modifications are made to achieve the operating limits of this antenna between the frequencies of 3.1-10.6 GHz, thereby covering the entire frequency spectrum of the UWB with compact size. We conclude from the calculated results that the proposed antenna has high performance characteristics appropriate for UWB wireless indoor communication and diversity applications with compact size.

Index Terms – Directive gain, diversity, envelope correlation coefficient, monopole, multiple input multiple output (MIMO), ultra-wideband antenna.

I. INTRODUCTION

In this developing age of technology, evolving technologies such as wireless communication must become more widely available and more reliable and faster. The ultra-wideband (UWB) technology can bring reliability and high data rate into the picture. It maintains a higher bandwidth while also having a low power density. The frequency range has been restricted to 3.1–10.6 GHz, with a bandwidth of 7.5 GHz.

A new approach is suggested in [1], where a four-element multiple input multiple output (MIMO) antenna with compact size is presented with low mutual coupling over an entire UWB range. This proposition suggests that we combine AFS miniaturizing techniques with MIMO orthogonal configuration, giving us both benefits. In [2], the designed antenna uses a novel integration-based orthogonal and asymmetric structure, four-directional decoupling and multiple-slot and slit (MSS) approaches. The symmetry in the structure and the four-directional escalators helps massively in reducing mutual coupling between antenna elements. The antenna's inter-element coupling is reduced by using polarization diversity between the elements. The isolation is further improved by using a decoupling structure with inverted L- and Z-shaped stubs [3].

A technique of creating numerous slits in the ground plane made us benefit from the combined use of inductance and capacitance [4]. The works [5–8] suggest that parasitic elements between antenna elements can reduce the effect of inter-elements coupling since they act as reflectors. The work [9] suggests a neutralization line in the antenna elements to diminish the effects of mutual coupling, reducing the need for extra space. The asymmetrical radiation pattern of quasi-self-complementary structured antenna helps to diminish mutual coupling without using any decoupling techniques [10–12]. The work [13] suggests combining a pair of inverted L antennas (ILAs) with the monopole antenna, and each ILA is fed in anti-phase excitement, which helps us achieve a pattern and polarization diversities. The UWB antenna in [14] has a stubbed ground plane that helps achieve high bandwidth impedance without employing any decoupling structures. In [15], to increase the isolation and minimization, metamaterial inspired isolators are used. The work [16] suggests the ground length is reduced to improve the impedance bandwidth.

The diminished mutual coupling and diminished correlation coefficient for the array envelope are achieved by folding a patch with wall support and feeding this folded patched monopole antenna in three-dimensional U-slotted shapes [17]. When two antennas are excited at different modes in a ground plane, the mutual coupling will be reduced, and the desired

Submitted On: March 29, 2021
Accepted On: February 26, 2022

https://doi.org/10.13052/2022.ACES.J.370411

radiation patterns can be achieved by not using any other decoupling structures [18]. The work [19] suggests that a VSWR value less than 2. Improvement in the impedance is achieved by etching the central patched metal. Beneath the radiator, a curve is inserted in the ground plane. The four-port diversity antenna in [20] is developed by repeating the unit cell and orthogonally positioning it to achieve high isolation. By varying the Sierpinski fractal, a better gain can be achieved [21]. The archetype Bowtie antenna is altered and aligned to improve the bandwidth through assailing the dipoles of patch and ground slot [22].

II. PROPOSED ANTENNA DESIGN

A. Single antenna design

The put-forward unit cell antenna with microstrip feed is modeled upon the FR4 substrate. The relative permittivity (ε_r) and loss tangent of the FR4 substrate are 4.3 and 0.025, respectively. The proposed antenna occupied a volume of 18 mm $\times$ 16 mm $\times$ 1.6 mm. The measurements of different parameters have been displayed in Table 1.

The antenna consists of a radiator (combining two hexagons, two ellipses, five circles, and two rectangles) at the front along with tapered microstrip feed and defected rectangular ground structure in the rear. The geometric specifications of the novelty radiator are as follows: It contains five adjacent tangential circles of radius 1.5 mm each, placed in a straight line, mounted atop an ellipse of major axis x_1= 7 mm and minor axis y_1= 1 mm, which, in turn, is again mounted upon another ellipse of major axis x_2= 7.5 mm and minor axis y_2= 1.4 mm. This whole setup is burdened upon two hexagons of radius 2 mm placed side by side on corners of a rectangle of 3 $\times$ 6 mm^2. In addition to this, a thin rectangle of dimensions 15 $\times$ 2 mm^2 passes through the array of five circles placed on top, which is used to lower the mutual coupling and enhance impedance matching performance. The inductive loading increases when the hexagons, ellipses, circles, and rectangles converge, raising the Q factor and resulting in a high inductive reactance, as shown by the following equation:

$$Q=\frac{\omega L}{R}=\frac{X_L}{R}. \quad (1)$$

The ground plane designed is a rectangular shape with a rectangular slot with dimensions 7 $\times$ 16 mm^2 used to improve the bandwidth and impedance matching. The capacitance impact between the radiator and the ground plane was reduced when the slot was included, resulting in a substantial gain in bandwidth. The feed line of dimensions 9 $\times$ 3 mm^2 is tapered to enhance current flooding near the radiator and obtain the required impedance bandwidth. Due to the modification in inductive reactance and capacitive reactance, both canceled with each other. Then the antenna behaved like a completely resistive load. A novelty concept of elliptical form radiator is an intelligent solution to bring a compact size UWB MIMO antenna. The final proposed antenna front and rear views are displayed in Figure 1. A fabricated single and MIMO antenna is displayed in Figure 2.

Table 1: Geometrical specifications of preferred monopole UWB unit cell antenna

Parameters	x_1	y_1	x_2	y_2	r_1	r_2
Units (mm)	7.5	1.4	7	1	2	1.5
Parameters	L	l_1	l_2	l_3	l_g	l_s
Units (mm)	18	9	2	15	7	1
Parameters	W	w_1	w_2	w_3	w_g	w_s
Units (mm)	16	3	1	2	16	7

The scattering parameters (S_{11}) of the antenna for both simulated and measured across the desired bandwidth and are below -10 dB; it is depicted in Figure 3. The couplings between small ground surface, connector

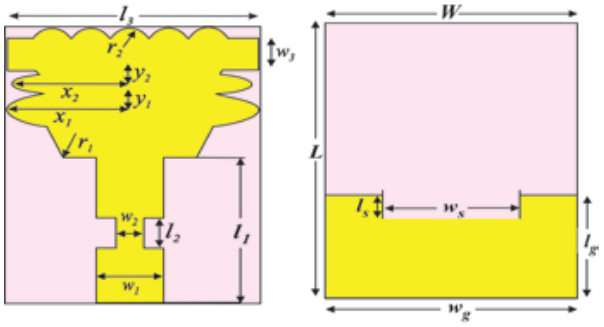

Fig. 1. Front and rear views of unit cell antenna.

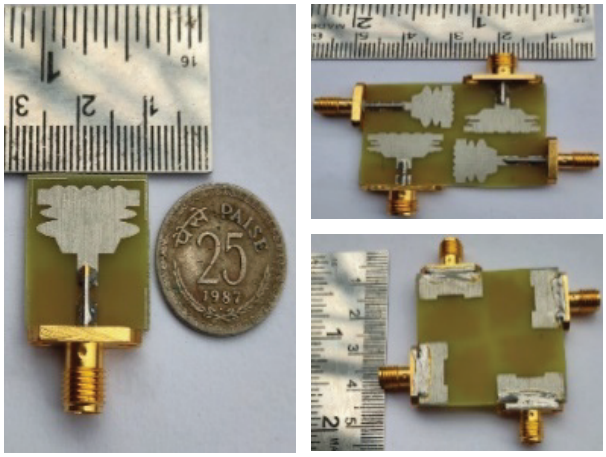

Fig. 2. Fabricated single and MIMO antenna.

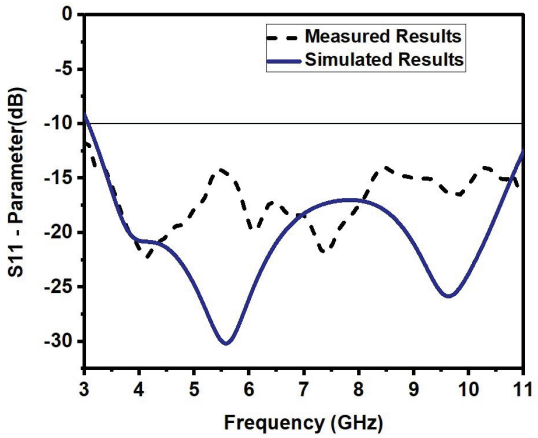

Fig. 3. Simulated and measured reflection coefficient of the monopole UWB unit cell antenna.

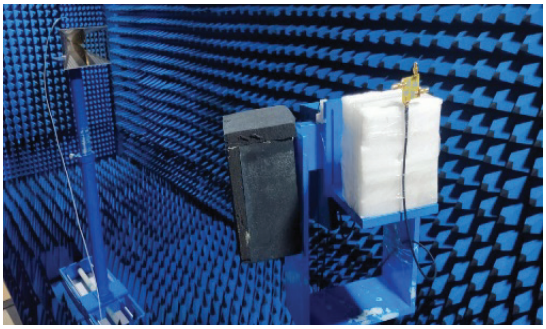

Fig. 4. Proposed UWB MIMO antenna measurement in anechoic chamber.

losses, and cable misalignment are the reasons for deviations in the measured *S*-parameters.

B. MIMO antenna design

The single antenna is replicated and grouped in an orthogonal pattern to design a multi-port antenna to attain high isolation. All radiating elements are arranged upon the same plane. Altogether, the total dimensions of the $L \times W \times hs$ of a four-port antenna are $35 \times 35 \times 1.6$ mm^3, *hs* representing the substrate's height. The measurement setup of the fabricated antenna with the anechoic chamber is depicted in Figure 4.

III. DIVERSITY PERFORMANCE ANALYSIS

CST Microwave Studio Software is used for designing and developing the proposed antenna by making parametric analysis and optimization [28]. Anritsu MS2703 vector network analyzer is used to measure propounded MIMO/diversity antenna performance.

A. Mutual coupling

The monopole UWB MIMO antenna incorporates four antennas that look very near to one another. As a result, one antenna would face interference due to the radiation of the other.

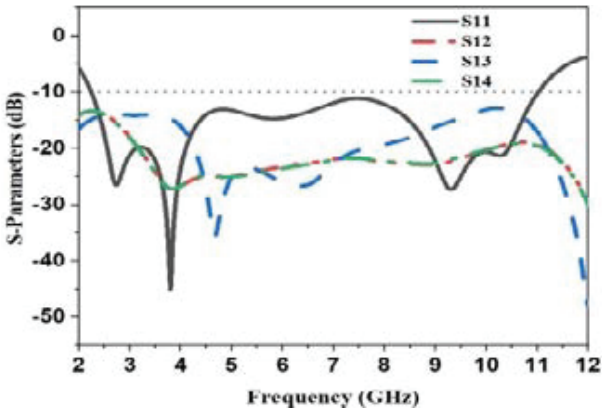

Fig. 5. *S*-parameter simulated results of monopole UWB MIMO antenna.

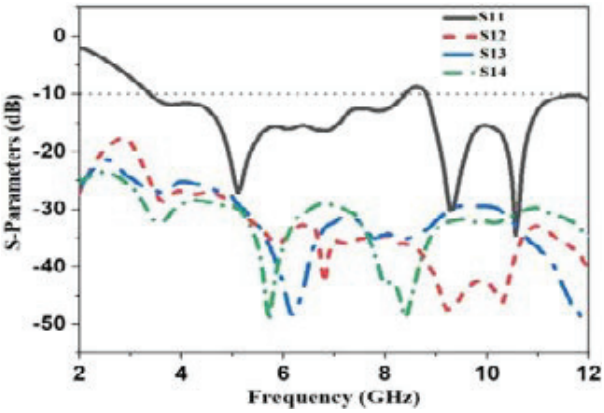

Fig. 6. *S*-parameter measured results of monopole UWB MIMO antenna.

The mutual coupling is reduced by assembling the modified ground structures, and identical antennas are arranged orthogonally. This antenna has been fabricated to offer mutual coupling less than −35 dB for the entire bandwidth range. Simulated and measured *S*-parameter results of monopole UWB MIMO antenna are depicted in Figures 5 and 6. Thus, we can see that impedance matching and high isolation are obtained using the etched ground plane with slot. Hence, the required result has been obtained.

B. Envelope correlation coefficient (ECC)

The correlation between the radiating elements is the important diversity parameter of the MIMO antenna. The degree of independence of the two antennas' radiation patterns is explained using the envelope correlation coefficient (ECC). Ideally, two antennas' radiation patterns are entirely independent of each other.

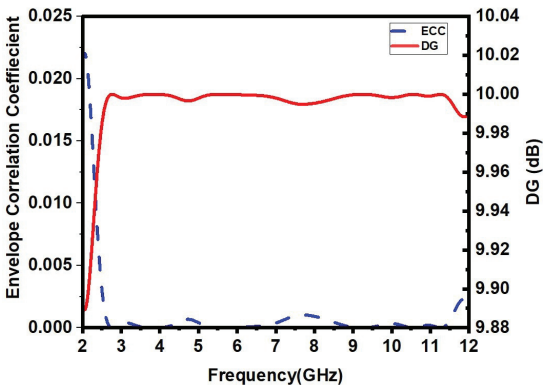

Fig. 7. Simulated diversity gain and ECC of monopole UWB MIMO antenna.

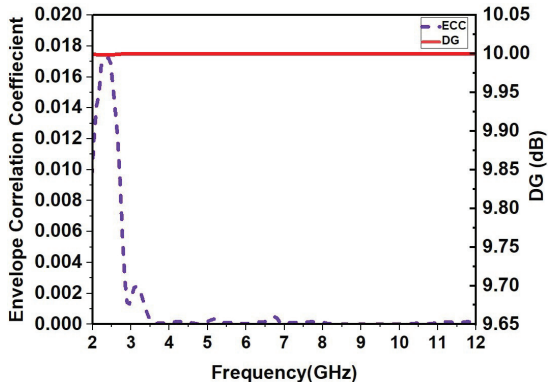

Fig. 8. Measured diversity gain and ECC of monopole UWB MIMO antenna.

The ECC should be 0, but its real value should not exceed 0.5. The ECC is calculated by substituting the *S*-parameters in eqn (2) [23]. From Figures 7 and 8, we discovered that ECC is much less than 0.001, which can also be regarded as a good ECC value.

$$\mathrm{ECC} = \frac{\left|S_{11}^{*}S_{12} + S_{21}^{*}S_{22}\right|^{2}}{\left(1-\left|S_{11}\right|^{2}-\left|S_{21}\right|^{2}\right)\left(1-\left|S_{22}\right|^{2}-\left|S_{12}\right|^{2}\right)}. \quad (2)$$

C. Diversity gain (DG)

The diversity gain (DG) of the monopole UWB MIMO antenna ought to be apex so that one can keep the wireless communication system more reliable and produce good quality. Its ideal value is 10 dB. Using the formula in eqn (3) [23], the value of the DG can be calculated for the proposed antenna. From Figures 7 and 8, we can evidence that the maximum value of DG is 9.999 dB.

$$\mathrm{DG} = 10\sqrt{1-\mathrm{ECC}^{2}}. \quad (3)$$

D. TARC

The ratio between the squared value of the reflected power and its incident power is called TARC. *N* port antenna's TARC ratio can be presented as in the following equation:

$$\Gamma_{a}^{t} = \frac{\sqrt{\sum_{i=1}^{N}\left|y_i\right|^{2}}}{\sqrt{\sum_{i=1}^{N}\left|x_i\right|^{2}}}, \quad (4)$$

where x_i represents incident signals and y_i represents reflected signals. The scattering matrix of 2×2 antenna arrays can be patterned as in the following equation:

$$\begin{bmatrix} y_1 \\ y_2 \end{bmatrix} = \begin{bmatrix} s_{11} & s_{12} \\ s_{21} & s_{22} \end{bmatrix} \begin{bmatrix} x_1 \\ x_2 \end{bmatrix}. \quad (5)$$

In the MIMO antenna, the phase of every excitation signal is arbitrary. The propagation environment contributes to further randomizing the signal phases before the signal reaches the receiver. So the MIMO channel signal is considered a random phase and independent and identically distributed. Gaussian random variables' sum or difference gives the Gaussian values, and reflected signals can be expressed as in the following equations [23]:

$$\begin{aligned} y_1 = S_{11}x_1 + S_{12}x_2 &= S_{11}\,x_0\,e^{j\theta 1} + S_{12}\,x_0\,e^{j\theta 2} \\ &= x_1\left(S_{11} + S_{12}\,x_0\,e^{j\theta}\right). \end{aligned} \quad (6)$$

$$\begin{aligned} y_2 = S_{21}x_1 + S_{22}x_2 &= S_{21}\,x_0\,e^{j\theta 1} + S_{22}\,x_0\,e^{j\theta 2} \\ &= x_1\left(S_{21} + S_{22}\,x_0\,e^{j\theta}\right). \end{aligned} \quad (7)$$

Therefore, TARC is described as follows in eqn (9):

$$\Gamma_{a}^{t} = \frac{\sqrt{\left(\left|x_1(S_{11}+S_{12}e^{j\theta})\right|^{2} + \left|x_1(S_{21}+S_{22}e^{j\theta})\right|^{2}\right.}}{\sqrt{2\left|x_1\right|^{2}}}, \quad (8)$$

$$\Gamma_{a}^{t} = \frac{\sqrt{\left(\left|(S_{11}+S_{12}e^{j\theta})\right|^{2} + \left|(S_{21}+S_{22}e^{j\theta})\right|^{2}\right.}}{\sqrt{2}} \quad (9)$$

The value of TARC must be less than -10 dB to attain the best operation in MIMO antennas. The received TARC is proven in Figure 9. It well agrees with the default standard values of TARC.

E. MEG

MEG is defined as the division of power obtained with the aid of a diversity antenna with power received by way of an isotropic antenna. Using the following relations [24], the MEG value is calculated for the MIMO antenna system. The MEG1 and MEG2 can be calculated from the following equation:

$$\mathrm{MEG}_i = 0.5\left(1 - \sum_{j=1}^{N} S_{ij}{}^{2}\right) \qquad i = 1,2. \quad (10)$$

For a better MIMO antenna system with equal power, the difference between MEG-1 and MEG-2

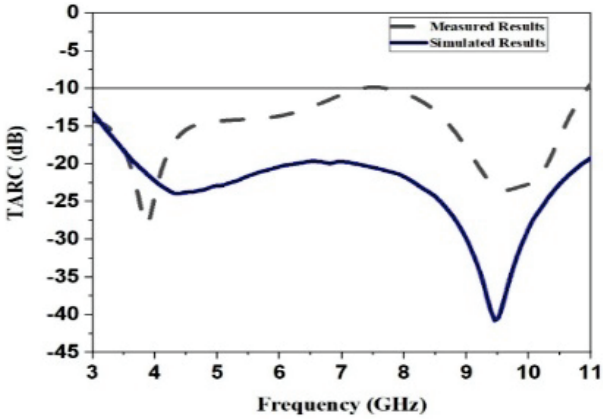

Fig. 9. TARC of the monopole UWB MIMO antenna.

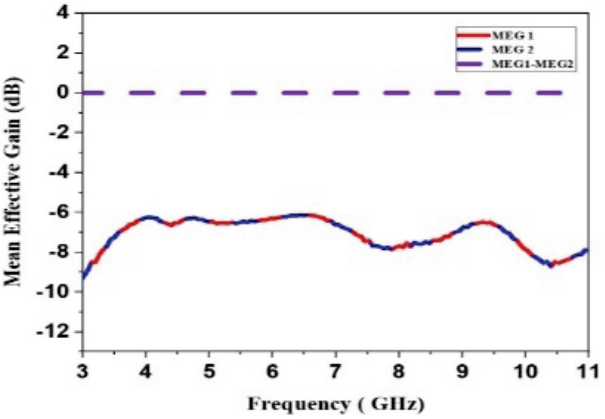

Fig. 11. Measured MEG of monopole UWB MIMO antenna.

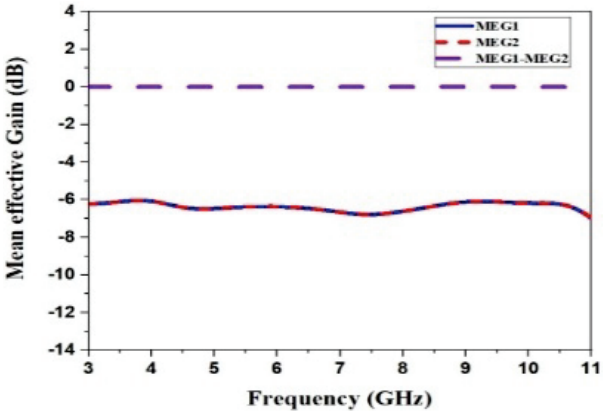

Fig. 10. Simulated MEG of monopole UWB MIMO antenna.

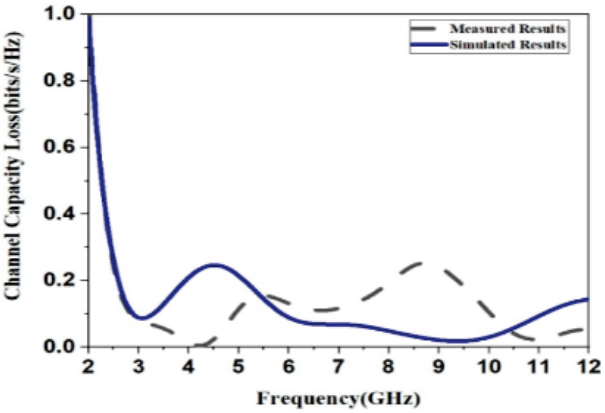

Fig. 12. CCL of the monopole UWB MIMO antenna.

should be equal to 0 dB. Figures 10 and 11 are well known to show that MEG-1 and MEG-2 are identical because the proposed radiator gives improved range overall performance.

F. CCL

Channel capacity loss (CCL) refers to the maximum message rate as far as the message transmits continuously through the communication channel without any losses. It can be estimated by the usage of the following components and expressed in the following equation [24]:

$$C_{\text{Loss}} = -\log_2 \det\left(\Psi^R\right), \tag{11}$$

$$\psi^{\text{R}} = \begin{bmatrix} \psi_{11} & \psi_{12} \\ \psi_{21} & \psi_{22} \end{bmatrix}, \tag{12}$$

where

$$\Psi_{11} = 1 - \left(|S_{11}|^2 + |S_{12}|^2\right),$$

$$\Psi_{21} = 1 - \left(|S_{22}|^2 + |S_{21}|^2\right),$$

$$\Psi_{12} = -\left(S^*_{11}S_{12} + S^*_{21}S_{22}\right),$$

$$\Psi_{21} = -\left(S^*_{22}S_{21} + S^*_{12}S_{11}\right).$$

The CCL value should not be greater than 0.4 bits/S/Hz ideally. Figure 12 shows the proposed MIMO antenna CCL value over the operating frequency range, and acceptable CCL values are achieved.

G. Multiplexing efficiency

Figure 13 indicates the multiplexing efficiency measured and simulated results of the proposed MIMO antenna. The multiplexing efficiency of the MIMO antenna is defined as the difference in the power required attaining a given capacity for an antenna under test concerning ideal reference MIMO antenna. As per eqn (13) [25], the MUX for a uniform angular power spectrum and high signal-to-noise ratio can be expressed as

$$\eta_{mux} = \sqrt{\eta 1 \eta 2 [1 - |ECC|^2]}. \tag{13}$$

Here, $\eta 1$ represents the total efficiency of antenna 1 and $\eta 2$ represents the total efficiency of antenna 2.

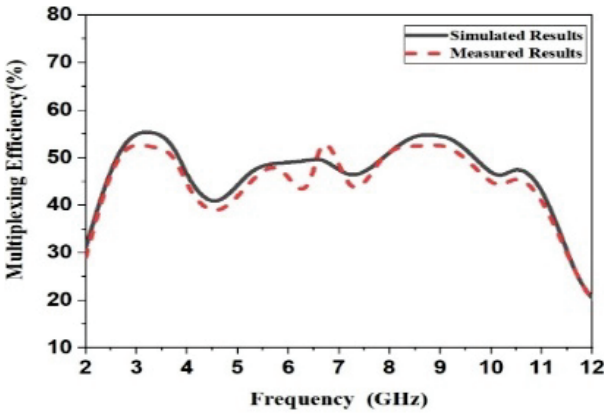

Fig. 13. Multiplexing efficiency of monopole MIMO ultra-wideband antenna.

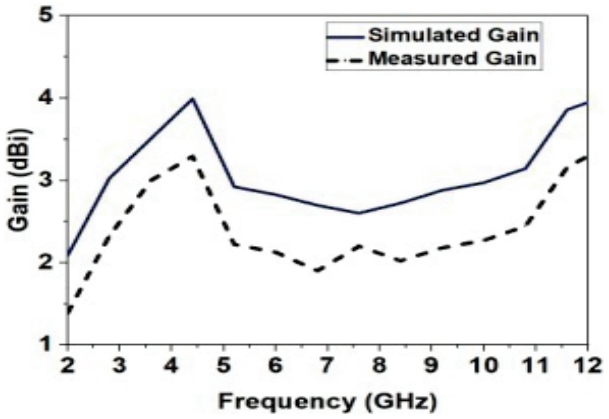

Fig. 14. The gain of monopole UWB MIMO antenna.

For the proposed antenna, measured and simulated gain is shown in Figure 14. From this, it is evident that simulated and measured gain changed in the range from 1.5 to 4 dBi. In [26], PSO and the curve fitting approaches are presented. Sierpinski's fractal antenna design can be modified to achieve a gain of 8.98 dB. For the proposed antenna, measured and simulated radiation efficiency is shown in Figure 15. Simulated and measured radiation efficiency changed from 75% to 90%.

H. Radiation patterns

The designed antennas' simulated and measured *H*-plane and *E*-plane radiation patterns at 3.8 GHz frequency are depicted in Figures 16 (a) and (b).

Using this pattern, we can see that the proposed MIMO antenna illustrates pattern diversity at the 3.8-GHz frequency band. The patterns at Port 1 and Port 3 are 180° rotated with each other; similarly, the patterns in Ports 2 and 4 are 180° rotated each other. The proposed antenna *H*-plane radiation pattern is omnidirectional, and the *E*-plane pattern is dumbbell-shaped [27].

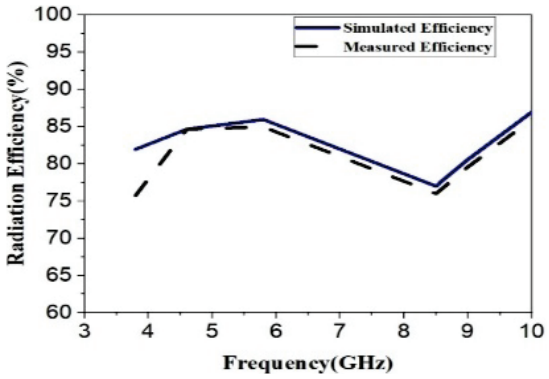

Fig. 15. Radiation efficiency of monopole UWB MIMO antenna.

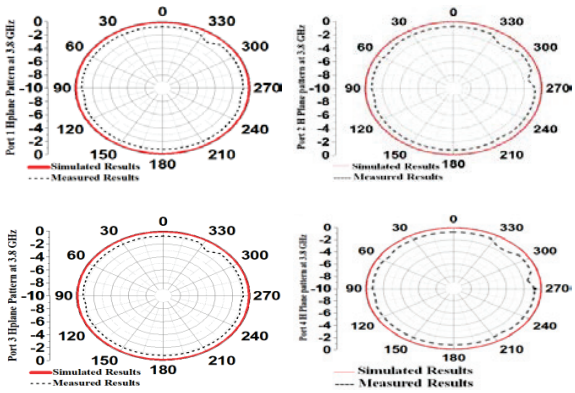

Fig. 16. (a) *H*-plane pattern of Port 1, Port 2, Port 3, and Port 4 of the proposed UWB MIMO antenna at 3.8 GHz.

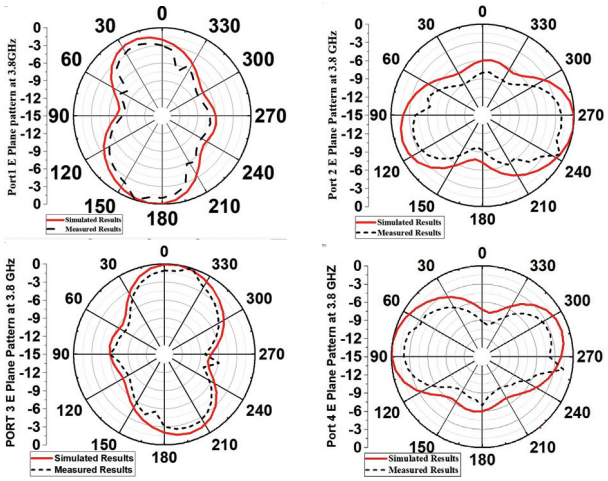

Fig. 16. (b) E-plane pattern of Port 1, Port 2, Port 3, and Port 4 of the proposed UWB MIMO at 3.8 GHz.

Table 2 presents the comparative chart for the proposed antenna design with the reported antenna. In this comparison, it is observed that the proposed antenna has

Table 2: Comparison table

Ref	Ports	Size (mm^2)	Isolation (dB)	TARC (dB)	ECC	CCL (bits/s/Hz)	GHz
1	4	40×40	>17	-	<0.03	-	2.94–14
2	4	39×39	>22	<-20	<0.02	<0.2	2.3–13.7
3	4	70×41	17	<-9	<0.012	<0.4	3.1–12
4	4	40×40	20	-	-	-	3–11.5
5	4	40×40	10	-	-	-	3–11
6	4	36×36	15	-	-	-	3.1–10.6
7	4	56×56	20	-	-	-	3–11
8	4	50×39	17	-	-	-	2.7–12
9	4	75×75	-	-	<0.1	-	3.1–17.3
10	4	35×35	=20	-	<0.5	-	3–12
11	4	40×40	=20	-	<0.04	-	2.9–12.1
12	4	24×24	=20	-	<0.5	-	3.1–10.5
15	2	13.5×34	=19	<-4	-	-	3–11
17	2	56×56	>22	-	<0.001	-	–
18	2	50×85	>20	-	<0.03	-	2–9.5
19	2	42×24	=15	-	<0.5	-	3.1–10.9
20	4	40×40	>20	-	<0.001	-	3.1–10.6
23	2	18×34	>22	<-20	<0.001	-	2.93–20
Prop	4	35×35	>35	<-20	<0.001	<0.4	3.1–11

achieved significant results in terms of CCL of less than 0.4 bits/s/Hz, TARC of < -10dB, ECC of 0.001, DG of 9.999 dB, and MEG of < 3 dB.

IV. CONCLUSION

The antenna elements are arranged in orthogonal, and then it appears to be the most effective solution to diminish the mutual coupling between UWB MIMO antennas and hence achieve compact size. The mutual coupling value of the proposed antenna is less than -35 dB and has been achieved successfully. The radiating antenna with compact size has been fabricated using the dimensions of 35×35 mm^2 having the thickness of the substrate 1.6 mm, and this antenna is used for diversity applications.

REFERENCES

[1] Saad, R. Ayman Ayd, and Hesham A. Mohamed. "Conceptual design of a compact four-element UWB MIMO slot antenna array," *IET Microwaves, Antennas & Propagation*, vol. 13, no. 2, pp. 208-215, 2019.

[2] Tang, Zhijun, Xiaofeng Wu, Jie Zhan, Shigang Hu, Zaifang Xi, and Yunxin Liu. "Compact UWB-MIMO antenna with high isolation and triple band-notched characteristics," *IEEE Access*, vol. 7, pp. 19856-19865, 2019.

[3] Yang, LingSheng, Ming Xu, and Chun Li. "Four-Element MIMO antenna system for UWB applications," *Radio engineering*, vol. 28, no. 1, pp. 60-67, 2019.

[4] Srivastava, Gunjan, Santanu Dwari, and B. K. Kanuijia. "A compact 4× 4 ultrawideband (UWB) band notched MIMO antenna," *In 2014 IEEE International Microwave and RF Conference (IMaRC)*, pp. 198-200, IEEE, 2014.

[5] Mao, Chun-Xu, and Qing-Xin Chu. "Compact coradiator UWB-MIMO antenna with dual polarization," *IEEE transactions on antennas and propagation*, vol. 62, no. 9, pp. 4474-4480, 2014.

[6] Zhang, Jing-Yi, Fan Zhang, and Wen-Peng Tian. "Compact 4-port ACS-fed UWB-MIMO antenna with shared radiators," *Progress In Electromagnetics Research Letters*, vol. 55, pp. 81-88, 2015.

[7] Li, Jian-Feng, Qing-Xin Chu, Zhi-Hui Li, and Xing-Xing Xia. "Compact dual band-notched UWB MIMO antenna with high isolation," *IEEE transactions on antennas and propagation*, vol. 61, no. 9, pp. 4759-4766, 2013.

[8] Khan, M. S., A. D. Capobianco, S. Asif, A. Iftikhar, B. Ijaz, and B. D. Braaten. "Compact 4× 4 UWB-MIMO antenna with WLAN band rejected operation," *Electronics Letters*, vol. 51, no. 14, pp. 1048-1050, 2015.

[9] Kayabasi, Ahmet, Abdurrahim Toktas, Enes Yigit, and Kadir Sabanci. "Triangular quad-port multi-polarized UWB MIMO antenna with enhanced isolation using neutralization ring," *AEU-International Journal of Electronics and Communications*, vol. 85, pp. 47-53, 2018.

[10] Zhu, Jianfeng, Shufang Li, Botao Feng, Li Deng, and Sixing Yin. "Compact dual-polarized UWB quasi-self-complementary MIMO/diversity antenna with band-rejection capability," *IEEE Antennas and Wireless Propagation Letters*, vol. 15, pp. 905-908, 2015.

[11] Yu, Jian-Feng, Xiang Long Liu, Xiao-Wei Shi, and Zedong Wang. "A compact four-element UWB MIMO antenna with QSCA implementation," *Progress In Electromagnetics Research Letters*, vol. 50, pp. 103-109, 2014.

[12] Srivastava, Gunjan, Akhilesh Mohan, and Ajay Chakraborty. "A compact multidirectional UWB MIMO slot antenna with high isolation," *Microwave and Optical Technology Letters*, vol. 59, no. 2, pp. 243-248, 2017.

[13] Wang, Xin, Zhenghe Feng, and Kwai-Man Luk. "Pattern and polarization diversity antenna with high isolation for portable wireless devices," *IEEE Antennas and Wireless Propagation Letters*, vol. 8, pp. 209-211, 2008.

[14] Y. Wu, K. Ding, B. Zhang, J. Li, D. Wu, and K. Wang, 2018. "Design of a compact UWB MIMO antenna without decoupling structure," *International Journal of Antennas and Propagation*, 2018.

[15] Wang, Fei, Zhaoyun Duan, Shifeng Li, Zhan-Liang Wang, and Yu-Bin Gong. "Compact UWB MIMO antenna with metamaterial-inspired isolator," *Progress In Electromagnetics Research C*, vol. 84, pp. 61-74, 2018.

[16] Christydass, Samuel Prasad Jones, and Nagarajan Gunavathi. "Dual-Band complementary split-ring resonator engraved rectangular monopole for GSM and WLAN/WiMAX/5G Sub-6 GHz band (new radio band)," *Progress In Electromagnetics Research C*, vol. 113, pp. 251-264, 2021.

[17] Jiang, Zhi Hao, Lei Zhang, Yan Zhang, Chao Yu, Longzhu Cai, Sidou Zheng, and Wei Hong. "A compact triple-band antenna with a notched ultra-wideband and its MIMO array," *IEEE Transactions on Antennas and Propagation*, vol. 66, no. 12, pp. 7021-7031, 2018.

[18] Zhao, Xing, Swee Ping Yeo, and Ling Chuen Ong. "Planar UWB MIMO antenna with pattern diversity and isolation improvement for mobile platform based on the theory of characteristic modes," *IEEE Transactions on Antennas and Propagation*, vol. 66, no. 1, pp. 420-425, 2017.

[19] Alsath, M. Gulam Nabi, and Malathi Kanagasabai. "Compact UWB monopole antenna for automotive communications," *IEEE Transactions on Antennas and Propagation*, vol. 63, no. 9, pp. 4204-4208, 2015.

[20] S. Kolangiammal, and G. Vairavel. "Compact planar monopole UWB MIMO antenna for diversity applications," *In Advances in Smart System Technologies*, pp. 281-291, Springer, Singapore, 2021.

[21] Singh, Amandeep, and Surinder Singh. "Design and optimization of a modified sierpinski fractal antenna for broadband applications," *Applied Soft Computing*, vol. 38, pp. 843-850, 2016.

[22] Solanki, Lakhvinder Singh, Surinder Singh, and Dharmendra Singh. "Modified wideband bowtie antenna for WLAN and high speed data communication applications," *Wireless Personal Communications*, vol. 95, no. 3, pp. 2649-2663, 2017.

[23] Chandel, Richa, Anil Kumar Gautam, and Karumudi Rambabu. "Tapered fed compact UWB MIMO-Diversity antenna with dual band-notched characteristics," *IEEE Transactions on Antennas and Propagation*, vol. 66, no. 4, pp. 1677-1684, 2018.

[24] Ibrahim, A. Ahmed, Jan Machac, and Raed M. Shubair. "UWB MIMO antenna for high speed wireless applications," *The Applied Computational Electromagnetics Society (ACES) Journal*, pp. 1294-1299, 2019.

[25] Tian, Ruiyuan, Buon Kiong Lau, and Zhinong Ying. "Multiplexing efficiency of MIMO antennas," *IEEE Antennas and Wireless Propagation Letters*, vol. 10, pp. 183-186, 2011.

[26] Singh, Amandeep, and Surinder Singh. "A modified coaxial probe-fed sierpinski fractal wideband and high gain antenna," *AEU-International Journal of Electronics and Communications*, vol. 69, no. 6, pp. 884-889, 2015.

[27] Song, Ze-Lin, Zhao-Jun Zhu, and Lu Cao. "High isolation UWB-MIMO compact microstrip antenna," *The Applied Computational Electromagnetics Society (ACES) Journal*, vol. 33, no. 3, pp. 293-297, Mar. 2018.

[28] CST Microwave Studio, ver. 2018, Computer simulation technology, Framingham, MA, 2018.

S. Kolangiammal received the M.Tech. degree from SRM University. She is currently working toward the Ph.D. degree with the Vel Tech Rangarajan Dr. Sagunthala R&D Institute of Science and Technology.

She is currently working as an Assistant Professor with the Department of ECE, SRMIST. Her research interests include antennas and propagation and wireless communications.

L. Balaji received the Ph.D. degree from Anna University.

He is currently an Associate Professor with the Department of ECE, Vel Tech Rangarajan Dr. Sagunthala R&D Institute of Science and Technology. His research interests include video coding, multimedia compression, and wireless communication and networking with IoT.

G. Vairavel received the Ph.D. degree from Anna University.

He is currently a Professor with the Centre for Applied Research in Education, SRMIST. His research interests include MIMO antenna design, software defined radio, and wireless communication.

Dynamic Force Calculation and Experimental Verification of Axial Bearings

Mingqi Wang, Jingjing Zhao, Xingnan Liu, Ni Mo, and Zhengang Shi*

Institute of Nuclear and New Energy Technology, Tsinghua University, Beijing 100084, China
Collaborative Innovation Center of Advanced Nuclear Energy Technology, Beijing 100084, China
The Key Laboratory of Advanced Reactor Engineering and Safety, Ministry of Education, Beijing 100084, China
wang-mq19@mails.tsinghua.edu.cn, zhao-jj@tsinghua.edu.cn, liuxingnan@tsinghua.edu.cn, moni@tsinghua.edu.cn, shizg@tsinghua.edu.cn (Corresponding author)*

Abstract – The axial bearing does not contain a laminated piece; so its dynamic performance is poor and often does not meet the load requirements. To accurately assess axial bearing performances during the design stage, it is necessary to accurately calculate the dynamic characteristics of the bearing, including amplitude, phase, and other parameters. Traditional studies have generally used the magnetic circuit method (MCM) or the finite element method (FEM) to analyze the dynamic performance of bearings, and few experimental measurements are carried out. Some experiments use a Guess meter to measure the magnetic field at local locations without directly measuring the electromagnetic force. In this paper, the dynamic force of axial bearing is measured by experiments, and the finite element calculation with Ansys Maxwell is carried out to study the influence of the gap, resonance, and other factors on the electromagnetic force. The comparison reveals a significant error in the calculation method using the initial gap because the gap between the stator and rotor changes with the dynamic force in the experiment. In this paper, the calculation method of "analyzing the dynamic performance of the bearing with the actual gap after the DC component is energized as the calculation gap" is proposed, which significantly reduces the calculation error and can ensure that the calculation error of amplitude and phase within 100 Hz is less than 5%. The method is of great significance for the engineering application of axial electromagnetic bearings.

Index Terms – Axial bearing dynamic performance, gap, resonance.

I. INTRODUCTION

Active magnetic bearings are widely used in various fields such as turbomachinery, vacuum systems, and high-temperature environments due to their advantages of no contact, no lubrication, and low loss [1]. The radial and axial bearings will control 5 degrees of freedom of the rotor, including radial and axial rotation and translation, respectively. Working in a changing magnetic field induces eddy currents in the stator and rotor, which will bring energy loss and affect the dynamic electromagnetic force and dynamic stiffness coefficient, thus affecting the dynamic characteristics of the system. However, considering the rotor strength and the feasibility of the manufacturing process, the stator and rotor of axial bearings are usually made of solid carbon steel or alloy steel [2], whose dynamic performance is poor and often fails to meet the load requirements. To accurately evaluate the dynamic characteristics of the axial bearing in the design stage, the dynamic forces in the axial direction, including parameters such as amplitude and phase, need to be accurately calculated. The magnetic field distribution around the rotor is far from the sinusoidal model, and its Fourier series expression will include many harmonics of the rotation angle. Moreover, magnetic bearings are generally driven by switching power amplifiers. The high-frequency ripple current caused by the switching power amplifiers and the dynamic control current with higher frequency will induce strong eddy currents in the bearing stator and thrust disc. Due to the skin effect of eddy current, mainly high-order harmonics will be driven out from the stack. The dynamic performance of axial bearings is challenging to evaluate accurately [3].

To study the dynamic performance of axial bearings, many scholars mainly use magnetic circuit method (MCM) and finite element method (FEM) to analyze and have achieved some results. Takeshi [4] uses FEM to analyze the eddy current problem when a simple magnetic bearing model uses solid steel as shaft material. Feeley *et al*. [5] present a simple dynamic model of eddy currents in a magnetic actuator, using the 2D eddy current equation to solve the uneven distribution of air gap magnetic field caused by eddy currents. Zhu *et al*. [2] develop an analytic model for a nonlaminated cylindrical magnetic actuator including eddy current effects by using the MCM. The frequency response of the analytic model is compared with the results of FEM. Sun *et al*.

Submitted On: June 7, 2021
Accepted On: March 21, 2022

https://doi.org/10.13052/2022.ACES.J.370412

[6] present a linear model including eddy current effects for a typical active magnetic thrust bearing (AMTB) and calculate the dynamic current stiffness and displacement stiffness using analytical method and transient finite element (FE) analysis. Zhu *et al*. [7] decompose the structure of the solid rotor actuator into the essential ring element and establish a magnetoresistance model considering the eddy current effect by solving the electromagnetic field within each essential element. Tian *et al*. [8] propose a fractional differential equation (FDE) model of the switching ripple current (SRC) considering the effects of eddy current and obtain a numerical solution by a predictor-corrector algorithm. The presented model can be applied to the studies of self-sensing of nonlaminated magnetic bearings. Han *et al*. [9] establish the dynamic factor models affected by the eddy currents for the hybrid thrust magnetic bearing (HTMB) with permanent magnets and subsidiary air gap, and the model's accuracy is verified by transient FE analysis. Henry *et al*. [10] mathematically formulate the problem of maximizing axial magnetic bearing actuator bandwidth through the choice of geometric and material properties.

However, the results of theoretical calculations and software simulations often differ significantly from actual engineering experiments, and there are few actual engineering experiments on dynamic electromagnetic force measurement of axial bearings.

Meeker *et al*. [11] formulate an augmented circuit model to account for eddy current, leakage, and fringing effects in radial active magnetic bearing. However, no analysis has been performed for axial bearing. Khoo *et al*. [12] propose a new concept, an active magnetic bearing with multiple parallel discs. The concept aims to solve the problem that the load-carrying capacity of traditional active magnetic bearings is limited by the saturation of magnetic flux density in iron. Yang *et al*. [13] present a new thrust actuator design for magnetic bearings. The actuator can produce high thrust but low radial attraction force. The actuator force characteristics are analyzed using FE analysis. Experimental verifications are also performed. Henry *et al*. [14] couple the nonlinear electromagnetic force measured in the experiment to a dynamic model. The Guess meter is used to measure the magnetic field at local locations but cannot directly measure the electromagnetic force. Wang *et al*. [15] propose a method to improve the measurement accuracy of imbalance identification. It uses a controllable electromagnet to generate the controllable electromagnetic force to attenuate the unbalance vibration synchronously. The equivalent magnetic circuit model of the electromagnet is established, and the relationship between the coil current and the dynamic electromagnetic force is analyzed by the FEM. Xu *et al*. [16] build a test platform for push-pull characteristics of a double-actuator electromechanical converter to test and analyze its static and dynamic characteristics.

To accurately analyze the axial bearing's dynamic characteristics: the dynamic force of the axial bearing at different AC frequencies, including parameters such as amplitude and phase, which reflect the real dynamic performance of the axial bearing in actual engineering experiments. Then use Ansys Maxwell to perform FE simulation to seek a simulation model that can truly reflect the actual experimental results. Experiments show that there are apparent errors in the method of calculating the dynamic force of the axial bearing by using the initial measurement of the gap because the stator and rotor gap will change with the dynamic force. In this paper, the calculation method of "analyzing the dynamic performance of the bearing with the actual gap after the DC component is energized as the calculation gap" is proposed. Considering the resonance of the table, we can calculate the dynamic characteristics of the axial bearing, which can significantly reduce the calculation error and ensure that the calculation error of amplitude and phase within 100 Hz is less than 5%. The above methods are of great significance to the engineering application of axial electromagnetic bearings.

II. INTRODUCTION TO THE EXPERIMENT

Theoretically, ignoring the core's magnetization and assuming that there is no electrical energy exchange between the coil and the power supply, assuming that the magnetic flux density remains constant. According to the principle of virtual displacement, the magnitude of the static axial force F generated by the axial bearing is equal to the partial derivative of the field energy W to the displacement of the core s:

$$F = \frac{\mathrm{d}W}{\mathrm{d}s} \approx \frac{\mu_0 A n^2 i^2}{4s^2} = k\frac{i^2}{s^2}, \tag{1}$$

where μ_0 represents permeability of vacuum, A and n are, respectively, the air gap area and winding turns of the core, i represents the control currents, and s represents the displacement of the core. The secondary term coefficients indicate the nonlinear relationship between the electromagnetic force and the displacement and control currents. In addition, the dynamic unbalance of the rotor, the gyroscopic effect of the rigid rotor, and the flexible rotor multi-order modes and vibration patterns also cause the above nonlinear relationship.

The rotor core is repeatedly magnetized several times in one revolution (determined by the axial bearing structure) during rotor rotation. The dynamic characteristics are nonlinear, with alternating currents of different frequencies passing through the windings. Moreover, the actual structure of the bearing is complex, and there are

other accidental factors. The FE analysis alone is not enough to correctly reflect the actual dynamic characteristics of the bearing. Therefore, the dynamic force measurement experiments of the solid structure axial bearings under different AC frequencies are carried out in this paper.

The schematic diagram of the experimental setup for dynamic force measurement of solid structure axial bearings is shown in Figure 1. The thrust disk is fixed on the base, and the axial bearing stator is connected to the base through three CL-YB-13T/100kg force measuring sensors. A nut adjusts the gap between stator and disk, and a stopper can measure the size of the gap with an error range of ± 0.02 mm. The axial force between the stator and rotor is obtained from the combined force of the three force sensors.

(a) Panoramic view of experimental facilities.

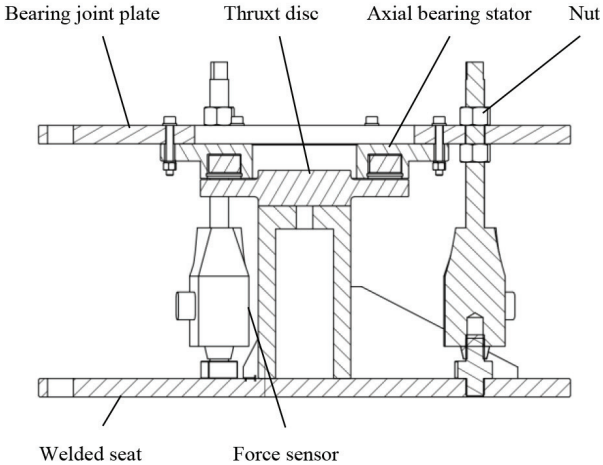

(b) Schematic diagram of the experimental setup.

Fig. 1. Schematic diagram of the experimental setup for dynamic force measurement of solid structure axial bearings.

Fig. 2. CL-YB-13T/100kg force measuring sensor.

Figure 2 shows the CL-YB-13T/100kg force sensor. The output signal of the measurement sensor can be obtained from the peak-to-peak value of the force sensor voltage and the peak-to-peak value of the sensor current. According to the relationship between the peak-to-peak value of sensor voltage and axial force, the peak-to-peak value of the actual axial force of the device at each moment can be obtained. In this paper, the environment is the atmosphere, and the room temperature is $15-20^{\circ}$C. The computer records the force signal through the force sensor, transmitter, and data acquisition card shown in Figure 2. The data sampling frequency is $10-10,000$ Hz. The initial gap of bearing is adjusted to 0.5 mm, and 5-A DC with an AC of amplitude 2 A is passed into the winding. The winding temperature is 30°C before the experiment, and the AC frequency is set to vary from 10 to 1000 Hz to record the force transducer signal. According to the transducer's signal characteristics, the axial bearing's dynamic performance can be obtained, that is, the peak-to-peak value and average phase of the dynamic force. Similarly, a total of four sets of experiments with different initial gaps and different winding currents are subsequently carried out. To avoid the contingency of experimental measurement and improve the accuracy of the experiment, we measured each group twice. Figure 3 shows the peak-to-peak values of the electromagnetic force measured by force measuring sensor concerning the input AC frequency under different experimental conditions. As shown in Figure 3 (a), the measurement results of Group 1 and Group 2 were the same, and the same

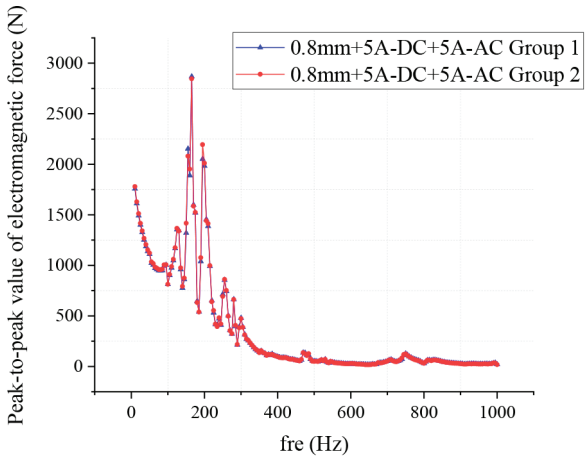

(a) Gap is 0.8 mm, input current DC component 5 A, and AC component 5 A.

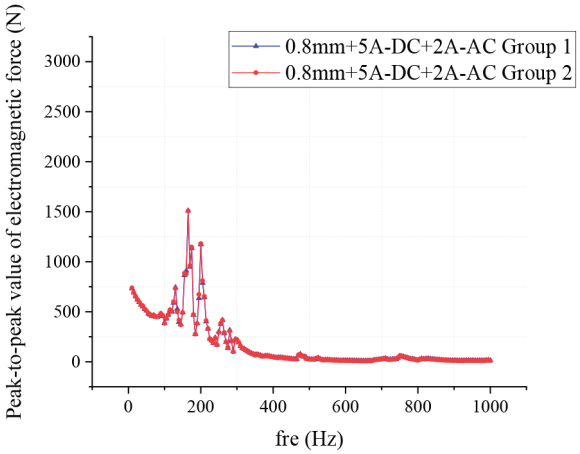

(b) Gap is 0.8 mm, input current DC component 5 A, and AC component 2 A.

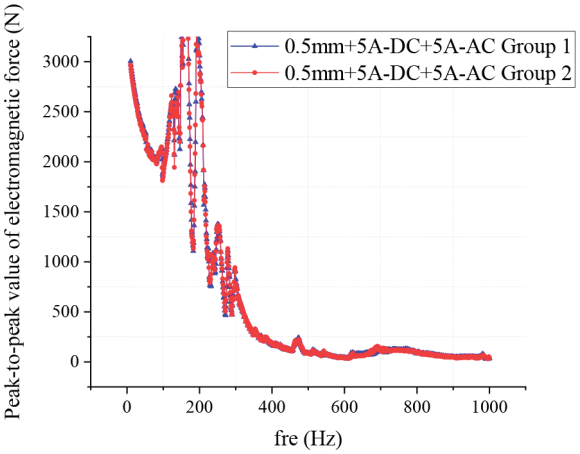

(c) Gap is 0.5 mm, input current DC component 5 A, AC component 5 A.

repeated experiments were also carried out for other groups.

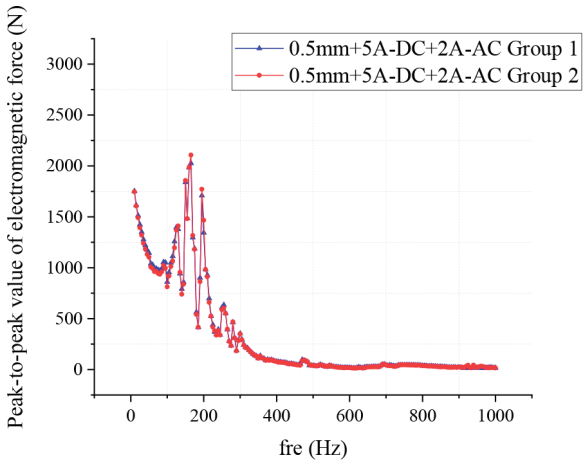

(d) Gap is 0.5 mm, input current DC component 5 A, and AC component 2 A.

Fig. 3. Peak-to-peak value of dynamic electromagnetic force for experimental measurement.

It can be concluded that the peak-to-peak value of the electromagnetic force tends to decrease gradually with the increase of the AC frequency. In the range of 400–1000 Hz, the peak-to-peak value of electromagnetic force is in the range of less than 200 N. The smaller the stator-rotor gap of the axial bearing, the larger the amplitude of the AC component of the input current in the winding, the larger the peak-to-peak value of electromagnetic force, which is more evident in the range of 0–400 Hz AC frequency, and there is no significant difference in the range of 400–1000 Hz. In the range of 100–200 Hz, the peak-to-peak value of electromagnetic force has significant fluctuations, which may be related to the self-oscillation frequency of the experimental bearing itself. The peak-to-peak value of electromagnetic force at the corresponding multiplier frequency also has certain fluctuation. Figure 4 shows the average phase between the electromagnetic force measured by the force measuring sensor and the input current under different experimental conditions as a variation of the input AC frequency.

It can be concluded that the average phase of the electromagnetic force generally tends to decrease gradually as the AC frequency increases, and this pattern is well maintained at 0–400 Hz. Due to the influence of the overall vibration, natural vibration frequency, and measurement error of the test structure, the average phase of electromagnetic force fluctuates in the range of 0–400 Hz. The influence is especially obvious in the range of 400–1000 Hz, where the average phase of the electromagnetic force has significant fluctuations. It can be seen from the results in the figure that the gap between stator and rotor of the axial bearing and the amplitude of the

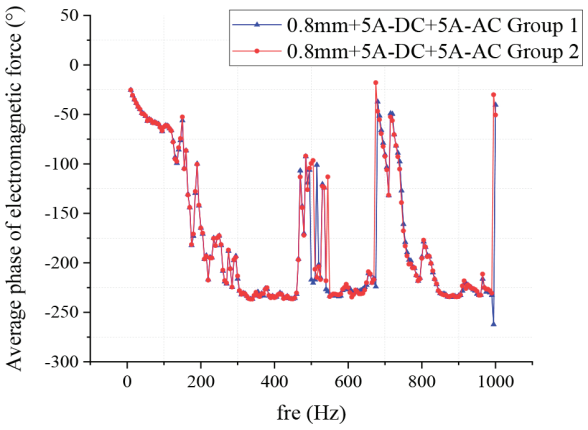

(a) Gap is 0.8 mm, input current DC component 5 A, and AC component 5 A.

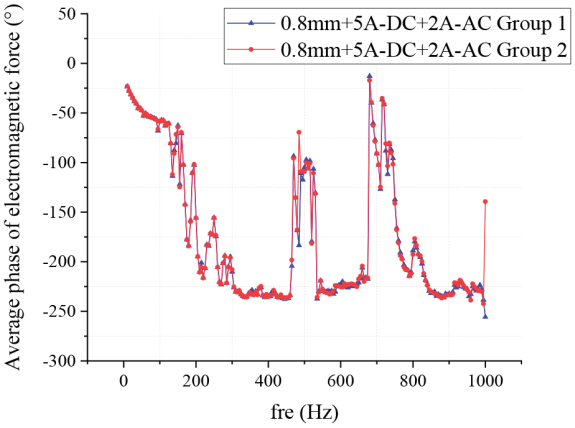

(b) Gap is 0.8 mm, input current DC component 5 A, and AC component 2 A.

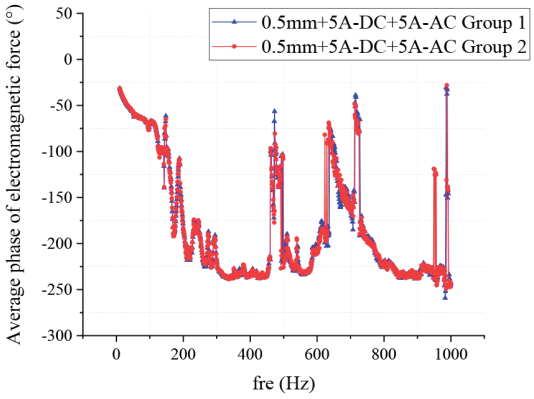

(c) Gap is 0.5 mm, input current DC component 5 A, and AC component 5 A.

AC component of the input current in the winding has little effect on the average phase of the electromagnetic force.

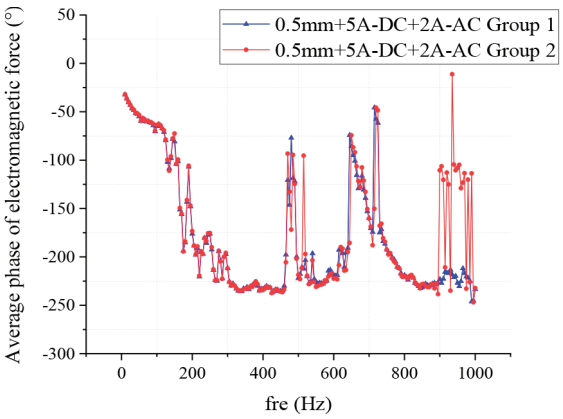

(d) Gap is 0.5 mm, input current DC component 5 A, and AC component 2 A.

Fig. 4. The average phase between dynamic electromagnetic force and the input current was measured experimentally.

III. FINITE ELEMENT CALCULATION MODEL AND CALCULATION METHOD

The FEM is used to analyze the dynamic harmonic field of the electromagnetic axial bearing. When studying the dynamic characteristics of axial bearings, it is necessary to simplify the actual problem studied, introduce reasonable assumptions, and turn the original problem into a solvable mathematical problem. Introduce the following assumptions related to the premises:

1. Ignore the temperature effect of conductor resistivity and assume that the conductor resistivity remains constant.
2. Reduce the actual three-dimensional field problem to a two-dimensional axisymmetric field problem.
3. Ignore the hysteresis effect of the material and the leakage effect in the loop.
4. The gap length between the stator and rotor is uniform.

The axial bearing of the experimental device is a circumferentially symmetric structure, and the loads in all directions can be regarded as uniform. Therefore, the axisymmetric field is used to calculate the FE solution using Ansys Maxwell. For this purpose, an FE model is established, as shown in Figure 5. In the selection of the size of the current winding, since the software can directly input the number of turns of the coil, the size of the model has no strict size. Just enter the number of turns to meet the actual working conditions. Figure 5 shows the simplified model of the experimental setup, and Table 1 shows the model's parameters.

For the electromagnetic axial bearing model, the coils are wound from copper wire, and the material used

Table 1: Basic parameters of the axial bearing model

Design parameters	**Numerical value**
Magnetic pole form	Single wire channel
Inner ring pole inner radius, r, mm	45
The outer radius of the inner ring pole, a, mm	55
The inner radius of the outer ring pole, b, mm	84
Outer pole outer radius, R, mm	90
Total stator thickness, H_{max}, mm	30
Wire groove depth, h, mm	21
Stator material	45 steel
The radius of thrust disk, R, mm	90
The thickness of thrust disk, m, mm	15
Thrust disc material	45 steel
Electromagnetic wire specifications, number of turns	∅1.2,135
Formula calculation 0.5 mm air gap bearing DC inductance, mH	72
Maximum current, A	10

Table 2: Simulation parameters of electromagnetism of axial bearing

Simulation parameters	**45 Steel**	**Pure copper**
Electrical conductivity, S/m	4.5 × 10 ^ 6	5.8 × 10 ^ 7
Resistivity, Ω*m	2 × 10 ^ –7	2.55 × 10 ^ –8

for the thrust disc and stator is 45 steel, respectively. The rest is air. Table 2 gives the relevant materials' required resistivity and relative magnetic permeability.

Time-varying currents flowing in a conductor produce a time-varying magnetic field in planes perpendicular to the conductor. In turn, this magnetic field induces eddy currents in the source conductor and any other conductor parallel to it. Eddy currents are calculated by solving for A and ϕ in the field equation:

$$\nabla \times \frac{1}{\mu}(\nabla \times A) = (\sigma + j\omega\varepsilon)(-j\omega A - \nabla\phi), \quad (2)$$

where A represents the magnetic vector potential, ϕ represents the electric scalar potential, μ is the absolute magnetic permeability, ω is the angular frequency at which all quantities are oscillating, σ is the conductivity, and ε is the absolute permittivity. The current plot of flux lines produced by eddy currents computed in a structure by Ansys Maxwell is shown below.

Substitute the structural parameters into Ansys Maxwell and run it to change the current frequency

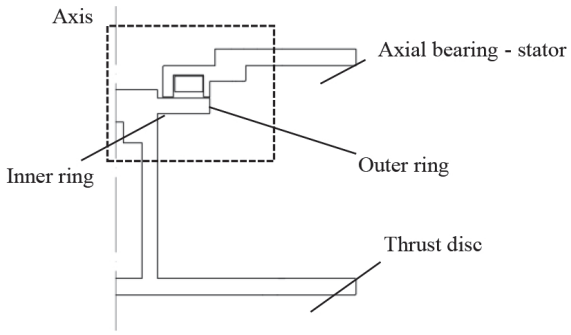

(a) Overall model.

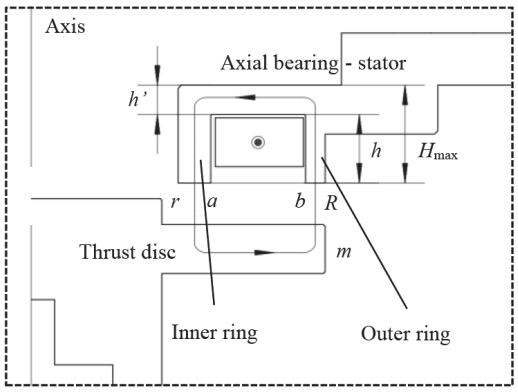

(b) Details of the model.

Fig. 5. Simplified model of the axial bearing.

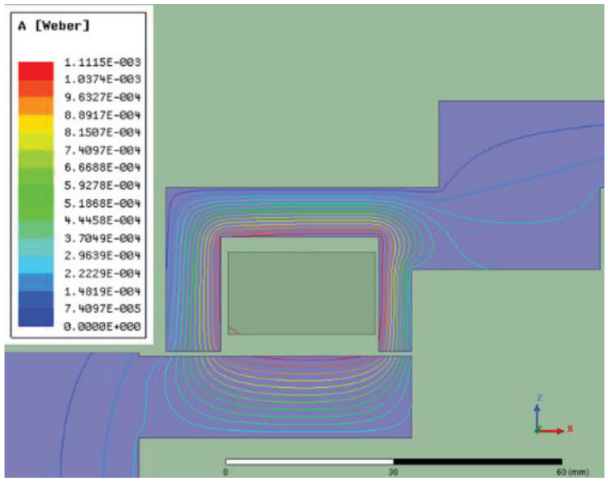

Fig. 6. Magnetic lines of force and magnetic field distribution of the test axial bearing.

of the input AC to obtain the dynamic characteristics of the axial bearing, such as electromagnetic force and phase under various frequency excitations. Differences between Ansys Maxwell calculations and experimental measurements are then analyzed.

IV. COMPARISON OF EXPERIMENTAL DATA AND CALCULATIONS

A. Static electromagnetic force and magnetic field conditions

The component of the Lorentz force due to current in a magnetic field is

$$F = \int_{\text{Vol}} (J \times B) d\text{Vol}, \tag{3}$$

where J represents the current density and B represents the magnetic flux density. Using Ansys Maxwell analysis, the gap between the stator and the thrust disk is 0.5 and 0.8 mm, and the comparison between the measured static force and the software calculated electromagnetic force when the input current of the experimental axial bearing is 1–10 A as shown in Figure 7.

While the current increases to a certain extent, the growth rate of the electromagnetic force decreases significantly, mainly due to the rise of the magnetic leakage flux, and the material reaches its magnetizing saturation. It is shown that the software simulation results are in good agreement with the experimental measurement results when calculating the static electromagnetic force. The static electromagnetic force becomes more significant with the increasing amplitude of the input DC in the winding. Meanwhile, the smaller the gap between the axial bearing stator and rotor, the larger the value of static electromagnetic force.

B. Comparison of experimental measurement and simulation of dynamic electromagnetic force

The virtual force in an eddy current problem is computed the same way as virtual force in a magneto-static problem. The only difference is that the average value of force over time is computed - not the instantaneous force at a given time. The time-averaged (or DC) force and AC force can be determined by

$$F = \frac{1}{2} \int Re \left| \vec{J} \times \vec{B} \right| dV. \tag{4}$$

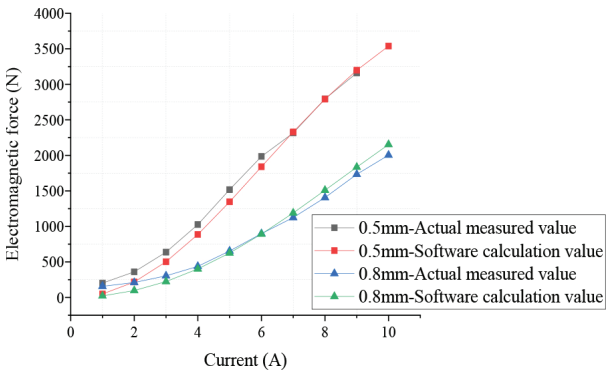

Fig. 7. Comparison of measured static force and software calculated electromagnetic force.

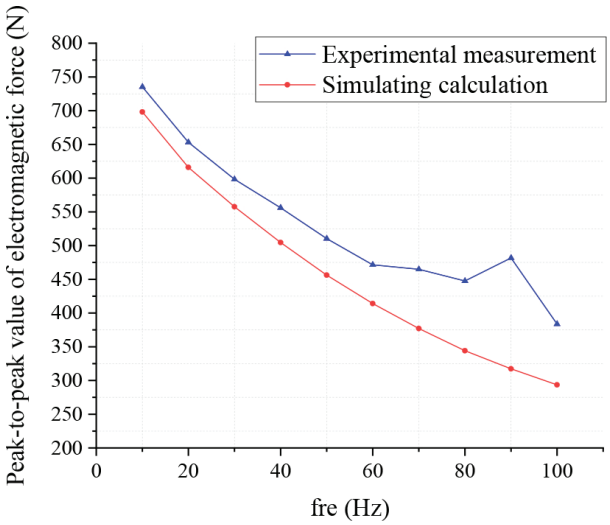

Fig. 8. Gap 0.8 mm, 5 A DC + 5 A AC simulation calculation compared with experimental measurement.

And instantaneous force is the sum of the time-averaged (or DC) force and the AC force:

$$F_{\text{INST}} = F_{\text{DC}} + F_{\text{AC}}. \tag{5}$$

The gap between the bearing stator and the thrust disk is set to 0.8 mm, and a 5-A DC and an AC of 2-A amplitude are passed into the winding. The calculation time is set to 1.5 s, the calculation step is 0.0005 s, and the AC frequency is varied from 10 to 100 Hz. Figure 8 shows a comparison between simulation calculation result and experimental measurement. The overall change trend of the two is consistent, and the electromagnetic force tends to decrease with the increase of the AC frequency. The causes of the errors are discussed below.

C. Error source: The gap between stator and thrust disk

Since the input current in the winding has both DC and AC components, the instantaneous value of the current in the winding is different at different moments, which causes the change of the transient electromagnetic force on the thrust disk at other moments. The gap between the stator and the thrust plate changes dynamically. Figure 9 shows the magnitude of static electromagnetic force calculated for different gaps at 100-Hz frequency. It can be concluded that the gap has a significant influence on the magnitude of axial electromagnetic force. The smaller the air gap, the larger the electromagnetic force. The gap and static electromagnetic force are approximately linearly distributed.

The variation of dynamic electromagnetic force under different gaps with the same excitation current is shown in Figure 10. Force oscillates at twice the fre-

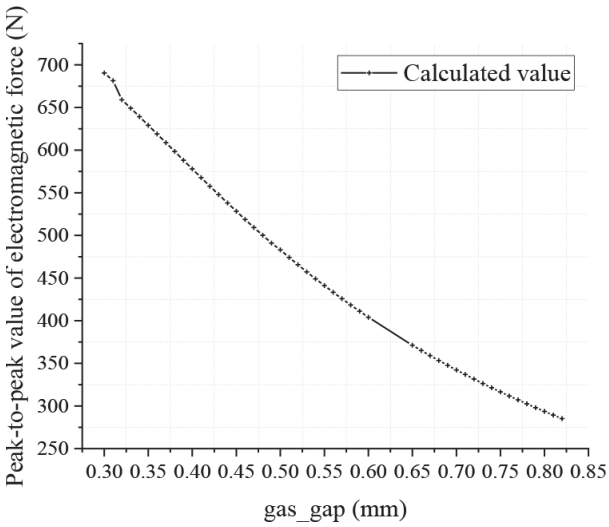

Fig. 9. Effect of the gap on the magnitude of static axial electromagnetic force.

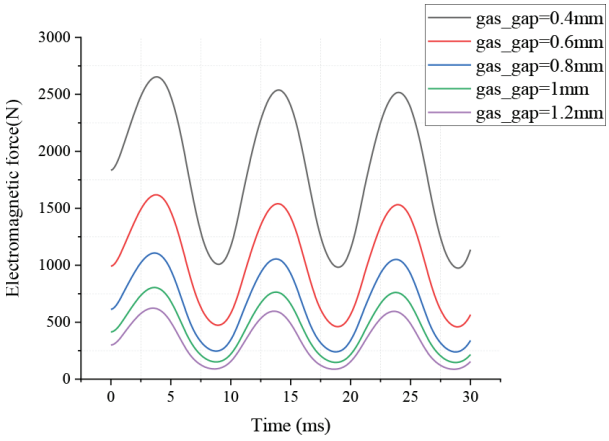

Fig. 10. Effect of the gap on the magnitude of the dynamic axial electromagnetic force.

quency of the source current and magnetic field:

$$f_F = \frac{1}{T_F} = 2f_S, \tag{6}$$

where f_F is the frequency of the force, f_S is the frequency of the source current and magnetic field, and T_F is the period of the force. The smaller the air gap, the larger the generated electromagnetic force, but the electromagnetic force waveform (half-sine wave) remains constantly.

If the actual value of the air gap between stator and thrust disk is considered in the simulation calculation, the calculation process is more complicated and time-consuming. Therefore, this paper will use the actual gap after the DC component is electrified as the calculation gap to analyze the dynamic performance of bearings. This means that applies a DC, which has the magnitude of the experiment's DC to the winding, and the actual gap between the stator and the thrust disk is measured at this time as the calculated gap.

Table 3: Effect of gap variation on stiffness for different currents

Current	**Gap**	**Static force**	**Stiffness, *K***
0 A	0.5 mm		
3 A	0.46 mm	1839 N	45975 N/m
5 A	0.43 mm	3539 N	50557.14 N/m
7 A	0.41 mm	4576 N	50844.44 N/m
10 A	0.39 mm	5933 N	53936.36 N/m
Current	**Gap**	**Static force**	**Stiffness, *K***
0 A	0.8 mm		
3 A	0.78 mm	893.3 N	44665 N/m
5 A	0.755 mm	2154 N	47866.67 N/m
7 A	0.735 mm	3175 N	48846.15 N/m
10 A	0.71 mm	4328 N	48088.89 N/m

The test clearance is measured by hand, and there may be some errors. To verify the accuracy of the measurement results, the axial bearing stiffness is calculated by measuring multiple sets of data using the characteristic of constant axial bearing stiffness. The accuracy of the measured gap values is verified by applying a DC with the magnitude of the experimental DC component to the winding. The axial bearing stiffness is as follows:

$$\text{Material stiffness}(K) = \frac{\text{static force}(F)}{\text{Gap change}(\delta)}. \tag{7}$$

As shown in Table 3, the stiffness values are calculated separately for each case.

The calculated values of the corresponding static force stiffness were mainly within the same range of values. It is considered that the above manual measurement gap results are more reliable. The gap between the stator and the thrust disk is held to be 0.5 mm, and 0.43 mm is used as the calculated gap for the Ansys Maxwell calculation when the current in the winding is 5-A DC component + 2 A/5 A AC components; the gap is 0.8 mm, and 0.755 mm is used as the calculated gap when the current in the winding is 5-A DC component + 2 A/5 A AC component.

D. Error source: The resonant frequency of the axial bearing itself and other

Due to the existence of resonant frequencies in the experimental bearing itself, the actual experimental measurement results have certain fluctuations. To compare with the simulation results, the experimental results should be somewhat smoothed and the AC frequencies in the resonant frequency range should be considered separately. In addition, the response frequency of the force transducer used in the experiment is less than 500 Hz, which will lead to a larger measurement error of the phase and amplitude of the electromagnetic force in the

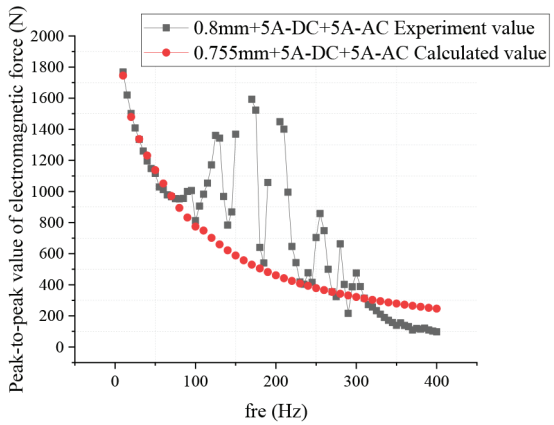

(a) 0.8-mm gap, peak-to-peak value of 5 A + 5 A axial force (the calculated gap is 0.755 mm).

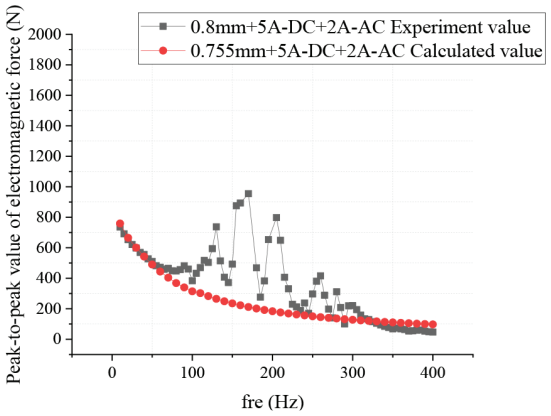

(b) 0.8-mm gap, peak-to-peak value of 5 A + 2 A axial force (the calculated gap is 0.755 mm).

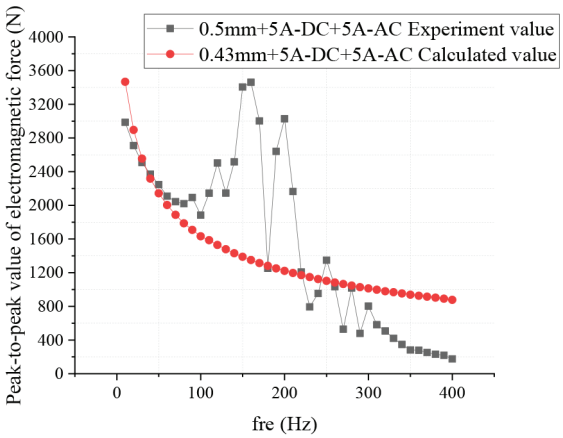

(c) 0.5-mm gap, peak-to-peak value of 5 A + 5 A axial force (the calculated gap is 0.43 mm).

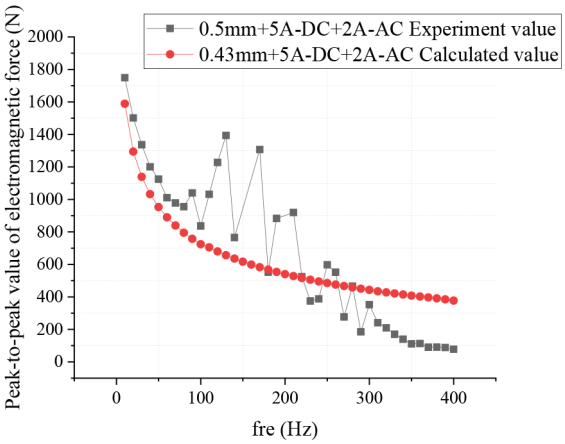

(d) 0.5-mm gap, peak-to-peak value of 5 A + 2 A axial force (the calculated gap is 0.43 mm).

Fig. 11. Comparison between the experimental results and simulation results of electromagnetic force peak-to-peak value.

larger AC frequency range. The calculated result of the electromagnetic force is only close to the measurement result in 100 Hz.

E. Comparison of electromagnetic force peak-to-peak experiment and simulation results

Based on the above error source analysis, the peak-to-peak value of electromagnetic force is simulated and the calculation result is shown in Figure 11.

The calculation error of electromagnetic force amplitude within 100 Hz is less than 5%. The amplitude of electromagnetic force within 100–300 Hz is influenced by the resonant frequency of the axial bearing itself, and the experimental results differ greatly from the simulation results. In the calculation range of more than 300 Hz, the experimental results are different from the simulation results due to the measurement error of the test force transducer and the simplification of the simulation model, but the overall trend of the two is the same. The simulation calculation results after certain error elimination are of great significance for the actual experimental measurement.

F. Comparison of experimental measurement and simulation of electromagnetic force mean phase

According to the experimental measurement diagram, the gap between the stator and rotor of the axial bearing has little effect on the average phase of the electromagnetic force. To further investigate the influence of the gap between the stator and rotor of the axial bearing on the average phase of the electromagnetic force, the influence on the average phase of the electromagnetic force at different gaps is calculated by using the software. Figure 12 shows the calculated values of the average phase of the electromagnetic force at different frequencies and gaps.

According to Figure 12, the phase difference between the axial bearing electromagnetic force and the input current is related to the AC frequency and has

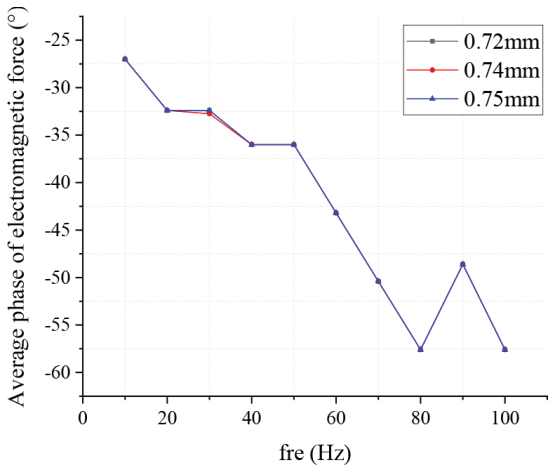

Fig. 12. Effect on the average phase of electromagnetic force with different gaps.

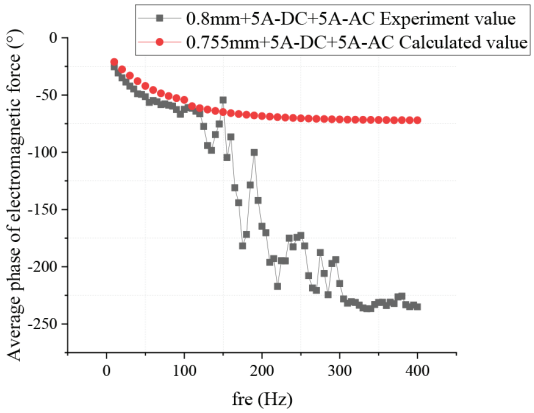

(a) 0.8-mm gap, 5 A + 5 A phase (calculated gap is 0.755 mm).

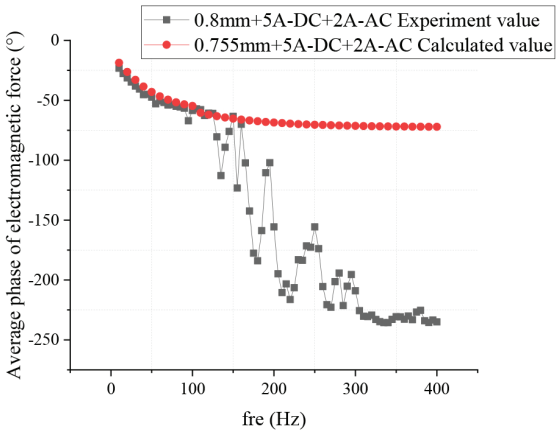

(b) 0.8-mm gap, 5 A + 2 A phase (calculated gap is 0.755 mm).

Fig. 13. Comparison between the experimental results and simulation results of the electromagnetic force phase.

little relationship with the gap between the stator and the thrust disc. To further investigate the comparison between the simulation calculation results and the experimental results of the average phase of electromagnetic force after the above error analysis, the comparison between the simulation calculation results and the experimental results of the average phase of electromagnetic force at 0.8-mm gap is calculated by using Ansys Maxwell as shown in Figure 13.

The calculation error of the electromagnetic force phase is similar to its amplitude calculation. When the AC frequency is within 100 Hz, the error between the calculated simulation results and the experimental measurement is less than 5%. When the AC frequency in the circuit is greater than 100 Hz, the calculation results of the electromagnetic force phase deviate from the experimental measurement results due to resonance and measurement errors. The phase deviation between the electromagnetic force and the current may be reversed by 180° because of the limitation of the measuring instrument. The measurement error of the phase is not discussed in detail here. If this part of the deviation is considered, the actual measurement results of the phase and the simulation results will also have better compliance in a larger range of AC frequency. It can be seen that the simulation calculation results after eliminating certain errors are of great significance to the actual experimental measurement.

V. CONCLUSION

To accurately evaluate the axial bearing performance at the design stage and accurately calculate the dynamic performance of the bearing, including parameters such as amplitude and phase. This paper compares the differences between the experimental measurement results and the simulation results and finds that the simulation results are of good guidance for the actual measurement of the axial bearing electromagnetic force.

1. When calculating the static electromagnetic force, the software simulation results agree with the experimental measurement results. The larger the amplitude of the input DC in the winding, the larger the static electromagnetic force. Meanwhile, the smaller the gap between the axial bearing stator and rotor, the larger the value of static electromagnetic force.
2. To measure the dynamic electromagnetic force, this paper proposes a method to eliminate the error from the perspective of error sources. The calculation method of "analyzing the dynamic performance of the bearing with the actual gap after the DC component is energized as the calculation gap" is proposed. The calculation error of amplitude and

phase within 100 Hz is less than 5%, which greatly reduces the calculation error.

3. For the dynamic electromagnetic force measurement, this paper also proposes other possible factors causing the error: the influence of the overall vibration, natural vibration frequency, measurement error of the test structure, the measurement error of the force transducer, etc.
4. Through experimental measurement and simulation analysis, it is concluded that the gap between the stator and rotor of the axial bearing has little effect on the average phase of the electromagnetic force.
5. When the AC frequency in the circuit is greater than 100 Hz, the factors such as resonance, the influence of the overall vibration, natural vibration frequency, measurement error, and measurement instrument limitation lead to a large deviation between the calculation result and the experimental measurement result of the electromagnetic force phase.

After certain error elimination, the simulation calculation results are of great significance for the actual experimental measurement.

ACKNOWLEDGMENT

This paper is supported by the Young Talent Project of China National Nuclear Corporation(20212009054), the National Key R&D Program of China (2018YFB2000100), and National S&T Major Project of China (ZX069).

REFERENCES

[1] G. Schweizer, H. Bleuler, and A. Traxler (L. Yu and C. J. Yuan. translated), *Active magnetic bearings—basics, properties and application of active magnetic bearings*, New Time Press, Beijing, 1997.

[2] L. Zhu, C. R. Knospe, and E. H. Maslen, "Analytic model for a nonlaminated cylindrical magnetic actuator including eddy currents," *IEEE Transactions on Magnetics*, vol. 41, no. 4, pp. 1248-1258, 2005.

[3] T. Hou and M. Li, "Optimal design of soft magnetic composite thrust magnetic bearing," *Machine tool and hydraulic pressure*, (2), 2019.

[4] T. Yoshimoto, "Eddy current effect in a magnetic bearing model," *IEEE Transactions on Magnetics*, vol. 19, no. 5, pp. 2097-2099, 1983.

[5] J. J. Feeley, "A simple dynamic model for eddy currents in a magnetic actuator," *IEEE Transactions on Magnetics*, vol. 32, no. 2, pp. 453-458, 1996.

[6] S. Yanhua, Y.-S. Ho, and L. Yu, "Dynamic stiffnesses of active magnetic thrust bearing including eddy-current effects," *IEEE Transactions on Magnetics*, vol. 45, no. 1, pp. 139-149, 2009.

[7] L. Zhu, and C. R. Knospe, "Modeling of nonlaminated electromagnetic suspension systems," *IEEE/ASME Transactions on Mechatronics*, vol. 15, no. 1, pp. 59-69, 2010.

[8] T. Yongsheng, Y. Sun, and L. Yu, "Modeling of switching ripple currents (SRCS) for magnetic bearings including eddy current effects," *International Journal of Applied Electromagnetics and Mechanics*, vol. 33, no. 1-2, pp. 791-799, 2010.

[9] H. Bangcheng, S. Zheng, and X. Hu, "Dynamic factor models of a thrust magnetic bearing with permanent magnet bias and subsidiary air gap," *IEEE Transactions on Magnetics*, vol. 49, no. 3, pp. 1221-1230, 2013.

[10] S. Henry, R. Fittro, and C. Knospe, "Optimization of axial magnetic bearing actuators for dynamic performance," *Actuators*, vol. 7, no. 4, pp. 66, 2018.

[11] D. C. Meeker, E. H. Maslen, and M. D. Noh, "An augmented circuit model for magnetic bearings including eddy currents, fringing, and leakage," *IEEE Transactions on Magnetics*, vol. 32, no. 4, pp. 3219-3227, 1996.

[12] W. K. S. Khoo, K. Kalita, S. D. Garvey, R. J. Hill-Cottingham, D. Rodger, and J. Fred Eastham, "Active axial-magnetomotive force parallel-airgap serial flux magnetic bearings," *IEEE Transactions on Magnetics*, vol. 46, no. 7, pp. 2596-2602, 2010.

[13] Y. Sheng-Ming and Y.-H. Tsai, "Design of a thrust actuator for magnetic bearings with low radial attraction force," *IEEE Transactions on Magnetics*, vol. 48, no. 11, pp. 3587-3590, 2012.

[14] H. Jong-Boo and K.-J. Kim, "Influence of nonlinear characteristics of electromagnet and normal force of a linear induction motor on a magnetically levitated vehicle," *Journal of Mechanical Science and Technology*, vol. 30, no. 11, pp. 4893-4900, 2016.

[15] W. Qiuxiao, Z. Wu, D. Wang, and X. Fu, "Study of measurement method for large imbalance evaluation based on dynamic electromagnetic force," *Measurement: Journal of the International Measurement Confederation*, vol. 104, pp. 142-150, 2017.

[16] W. Xuping, L. Quan, S. Luan, and X. Xu, "Dynamic and static characteristics of double push rods electromechanical converter," *Chinese Journal of Mechanical Engineering*, vol. 32, no. 1, pp. 1-11, 2019.

Mingqi Wang got her bachelor's degree of Energy and Power Engineering in North China Electric Power University (Baoding) in 2019. She is now studying at Institute of Nuclear and New Energy Technology, Tinghua University, Beijing, China. Her research subject is magnetic bearing.

Jingjing Zhao got her master's degree of Precision Instrument and Machinery in Beihang University in 2005. She is now working in Institute of Nuclear and New Energy Technology, Tsinghua University, Beijing, China. Her main research direction is the measurement and control of electromagnetic bearings.

Zhengang Shi got his PHD of Materials Science and Engineering in Tsinghua University in 2011. He is now working in Institute of Nuclear and New Energy Technology, Tsinghua University, Beijing, China. His researching subject includes novel magnetic bearing, magnetic field analysis, rotor dynamics, auxiliary bearing and insulation of helium gas.

Mo Ni received the PHD degree in electrical engineering from Tsinghua University in 2009. He is currently working with the Institute of Nuclear and New Energy Technology, Tsinghua University, Beijing, China. His research interest is magnetic bearing applications.

Zhengang Shi got his PHD of Nuclear Science and Technology in Tsinghua University in 2003. He is now working in Institute of Nuclear and New Energy Technology, Tsinghua University, Beijing, China. Dr. Shi's research subject is magnetic bearing.

Substrate Integrated Waveguide Antenna at Millimeter Wave for 5G Application

Yaqdhan Mahmood Hussein[1,2], Mohamad Kamal A. Rahim[1], Noor Asniza Murad[1], Hatem Oday Hanoosh[3,4], and Norsaidah Binti Muhamad Nadzir[1]

[1]Advance RF and Microwave Research Group (ARFMRG), School of Electrical Engineering, Faculty of Engineering, Universiti Teknologi Malaysia, UTM Johor Bahru, Johor 81310, Malaysia
Yaqthanm.79@gmail.com, mdkamal@utm.my, noorasniza@utm.my, norsaidah2@graduate.utm.my

[2]Information Technology and Communication (ITC) Al-Furat Al-Awsat Technical University, Sammawah, Iraq

[3]Department of Computer Techniques Engineering, College of Information Technology, Imam Ja'afar Al-Sadiq University, Samawah 66001, Al Muthanna, Iraq
Hatem.altaee1990@gmail.com

[4]College of Engineering Electronics and Communications Engineering, Al Muthanna University, Iraq

Abstract – This paper presents a dual-band slot antenna using substrate integrated waveguide (SIW) technology at 26 and 28 GHz. High loss is one of the main challenges faced by 5G base station network due to the severe path loss at high frequency. Hence, high gain antennas are required for 5G base station applications to overcome path loss issue. Hence, this work designs a high gain SIW antenna based on slot technology to excite dual-bands with high gain capability. The antenna is designed with two slots shaped to resonate at two different frequencies: 26 and 28 GHz. The antenna is analyzed using CST software and fabricated on Roger RT5880 substrate with permittivity of 2.2 and lost tangent of 0.0009 with thickness of 0.508 mm. The design operates at 26 and 28 GHz with measured reflection coefficients less than -10 dB. Measured high gains of 8 and 8.02 dB are obtained at 26 and 28 GHz, respectively. Overall, the antenna showed good performance that would benefit the fifth-generation applications.

Index Terms – Millimeter-wave antenna, SIW technology, (5G) applications.

I. INTRODUCTION

With the development of wireless communication technology, the dual-band and multiband antennas have the tendency for future communications due to the advantages of compactness, high integration, and low cost. Recently, several promising millimeter-wave bands have been released for 5G wireless communication systems. Therefore, broadband dual-band antennas are in demand for future millimeter-wave wireless applications. For the design of dual-band antennas, there are two basic technical challenges which limit the use of this technology. This includes simultaneous operation with a compact configuration and broadband operation in each of the bands.

Several types of dual-band antenna have been investigated in literature. Normally, two types of dual-band solutions, namely hybrid antennas and multimode antennas are used. The hybrid dual-band antenna is the combination of antennas resonating at different frequencies, respectively, but simultaneously fed by only one port. Furthermore, these antennas operate at different types of mode or appear to be arranged in a separated aperture. Different types of antennas have been combined and different types of resonant mode of antennas have been employed for the dual-band operation, such as the slot monopole [1], dielectric resonator antenna (DRA) slot [2], and slot patch [3]. In addition to that, the same types of antennas with different shapes or sizes have also been proposed for dual-band operation by using different modes of transmission line and separated placement, such as the substrate integrated waveguide (SIW) fed slots [4]. An antenna of a modified cavity with two layers was proposed to realize resonance and directional radiation patterns over a frequency band at millimeter wave in [5–7]; however, these papers come with complex design and bulky size.

This paper introduces SIW antenna with slot. This antenna was implemented using SIW technology with roger RT 5880 as substrate with thickness of 0.508 mm. The design is on a fully ground plane, the reflection coefficient of it is less than -10 dB as the result of reflection

Submitted On: April 12, 2021
Accepted On: March 21, 2022

https://doi.org/10.13052/2022.ACES.J.370413

coefficient were obtained from dual-band. The operating frequency dual-band resonates at 26 and 28 GHz. The paper is organized as follows. Section II gives a brief overview of the methodology for the antenna designed consideration. The simulated and measured results are summarized in Section III. Finally, Section IV draws conclusions.

II. ANTENNA DESIGN

Figure 1 shows the general structure of SIW which consists of a rectangular waveguide, two rows of periodic holes, and a substrate in between metal planes [8]. The proposed SIW antennas are designed using Rogers RT5880 substrate with dielectric constant of 2.2 and loss tangent of 0.0009, and thickness of 0.508 mm. The vias diameter, D, and spacing, S, are calculated using equations in [9]. Figure 2 shows the dimensions of the proposed antennas at millimeter wave with dual-band performance. This design comes with two different shapes of slot according to different position at the top of metal. Since SIW design generally works in TE1, 0 mode, m = 1, n = 0. Therefore, the equation for cutoff frequency is reduced to

$$f_c = \frac{c}{2a}, \tag{1}$$

where a is the total broad side dimension of the rectangular waveguide. Next, a_d is the width of dielectric field waveguide (DFW)

$$a_d = \frac{a}{\sqrt{\varepsilon_r}}. \tag{2}$$

The design equations for SIW, which are found by W_{siw}, are the separation between via rows (center to center)

$$W_{\text{siw}} = a_d + \frac{D^2}{0.95S}. \tag{3}$$

Then, the equations for the separation distance "S" and diameter "D" control the radiation loss and return loss are as follows:

$$\lambda_g = \frac{\mathbf{c}}{\mathbf{f}\sqrt{\varepsilon_r}}, \tag{4}$$

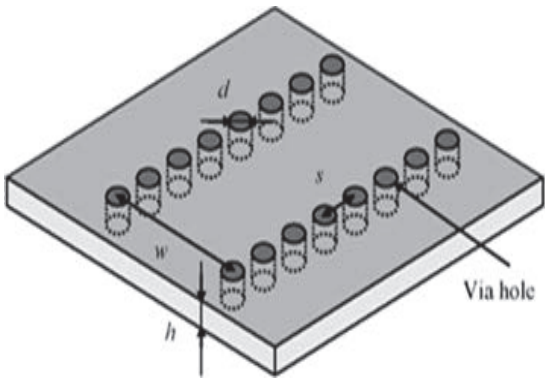

Fig. 1. General structure of a substrate integrated waveguide [10].

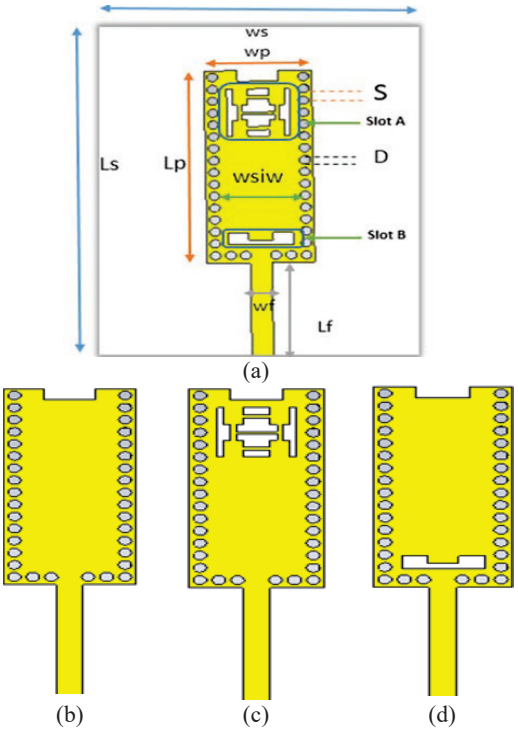

Fig. 2. Simulation structure of the SIW antenna. (a) Main structure with slots A and B. (b) Design without slot. (c) Design with slot A. (d) Design with slot B.

$$D \leq \frac{\lambda_g}{5}, \tag{5}$$

$$S \leq 2D, \tag{6}$$

Figure 2 (a) refers to main shape structure which consists of two columns as vias at both edges of the structure to prevent signal from passing through the edges of the patch, especially when millimeter-wave frequency loss becomes higher than lower frequency. The final dimensions of the structure designed at 26 GHz are shown in Table 1.

III. DISCUSSION BASED ON PARAMETRIC STUDY

The distance between vias(s) enables the dual-band antenna to control losses. Whenever the gap(s) is smaller, the antenna will achieve less loss because at the top of vias edges, electric will reflect around vias where some of them is radiated at the top of patch and the rest will have pushed downwards to create unwanted feedback, which is represented in slot A and slot B, respectively, as can be seen in Figure 2. Slot A creates radiation at 26 GHz because it depends on the distance between slots and feed line, slot A has multi-different slots arranged equally on the middle of antenna to keep angle of the beam at (0°) and ensures that it focuses on the target substrate.

Table 1: Dimensions of main structure

Variable	Name	Size (mm)
W_s	Width of substrate	2.08 λ
L_s	Length of substrate	2.8253 λ
W_p	Width of patch	0.675 λ
L_p	Length of patch	1.54 λ
W_{siw}	Width of SIW	0.57 λ
D	Diameter	0.069 λ
S	Space between vias	0.095 λ
W_f	Width of feed line	0.268 λ
L_f	Length of feed line	0.136 λ
Thickness of the substrate		0.044 λ

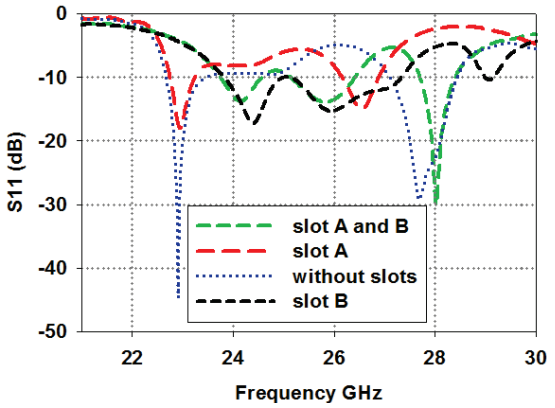

Fig. 3. Different reflection coefficient of the SIW structure with vias diameter (0.6 mm) depends on the different cases slots.

Slot B produces radiation at 28 GHz because of its size and position. Slot B has greater effect on radiation because of its position closer to the feed line. This shows that it is located closer to the main surface current (red zone). In addition, slot B proved high bandwidth.

The main parameter of this design study is the diameter of vias. When vias is 0.6 mm as can be seen in Figure 3 design has slot A, slot B and without slots the reflection coefficient becomes narrow band and it does not resonate at 26 and 28 GHz. As can be seen in Figure 4, when the diameter of vias is 1 mm and it has two slots (slot A and slot B), the reflection coefficient will not achieve dual-band frequency. When the diameter of vias is 0.8 mm, the design achieves dual-band resonance at (23-28) which can be seen in two cases. Based on Figure 5, this happens when design has slot A and without any slots.

The structure (prototype) of the proposed antenna design has been fabricated through standard single-layer PCB process, as shown in Figure 6, whereas their corresponding simulated and measured $|S11|$ are plotted.

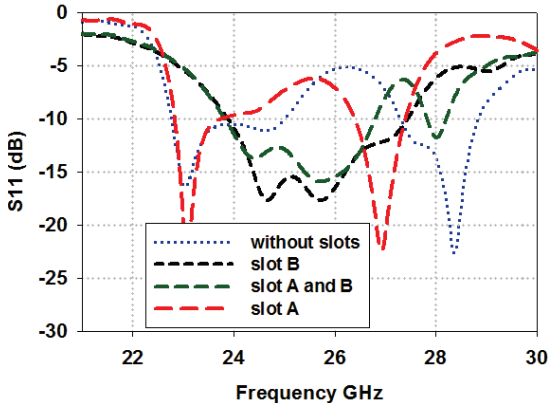

Fig. 4. Different reflection coefficient of the SIW structure with vias diameter (1 mm) depends on the different case slots.

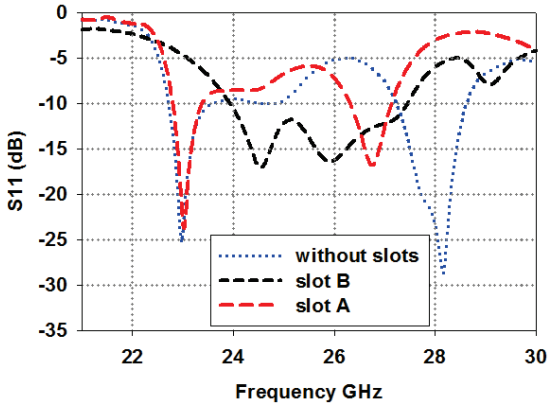

Fig. 5. Different reflection coefficient of the SIW structure with vias diameter (0.8 mm) depends on the different cases slots.

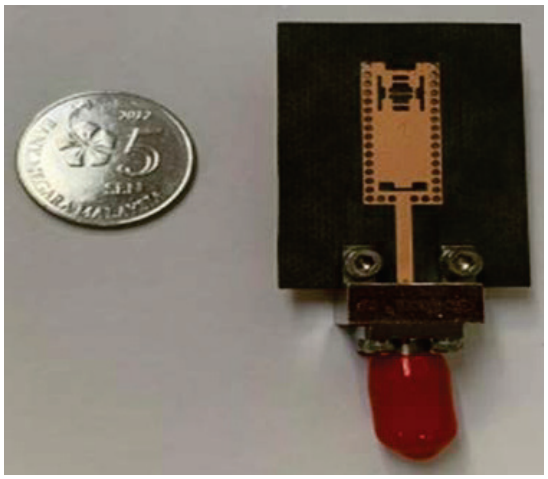

Fig. 6. The fabricated SIW antenna.

The antenna has only one port working as a feeder, and both the simulated and measured results indicate that a good impedance match is achieved when the dual-band 26 to 28 GHz is under the criteria of −10 dB, for both selected prototypes.

IV. SIMULATION AND FABRICATION RESULTS

Figure 7 shows the comparison between the simulated and measured reflection coefficients of the antenna structure in different forms. Through the different design of antenna structure, the authors anticipate getting *S*11 of less than −10 dB over high frequency and suitable bandwidth. Both results demonstrate that the reflection coefficient stayed below −10 dB at 26 GHz.

Next, Figure 8 shows the measured efficiency and gain performance of the front-end module. The measured gains of the front-end module have frequency dependency from −180° to 180°, when the line is a curve fitting result. The fitting curve has the center frequency

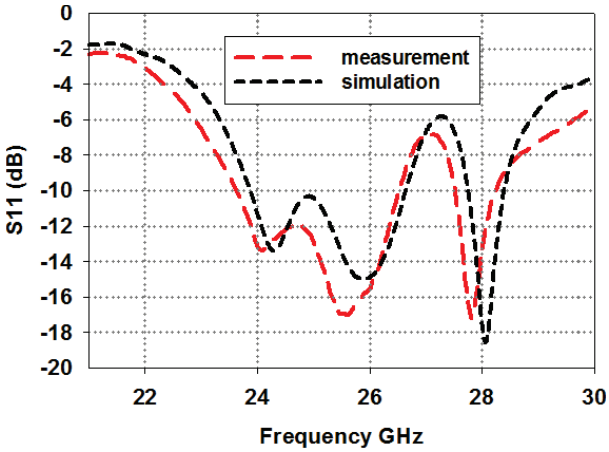

Fig. 7. Simulated and measured *S*11 of the main structure which has slot A and B with diameter of vias 0.8 mm.

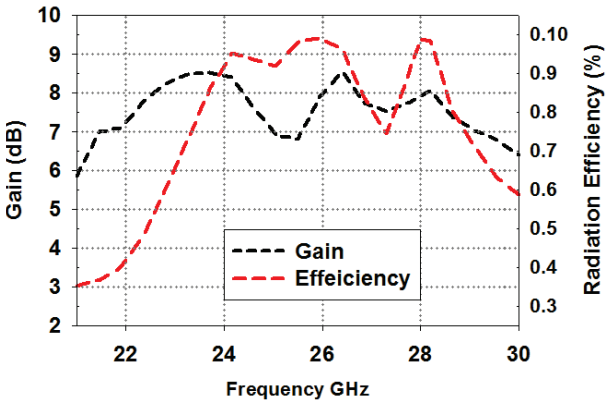

Fig. 8. Gain and efficiency performance.

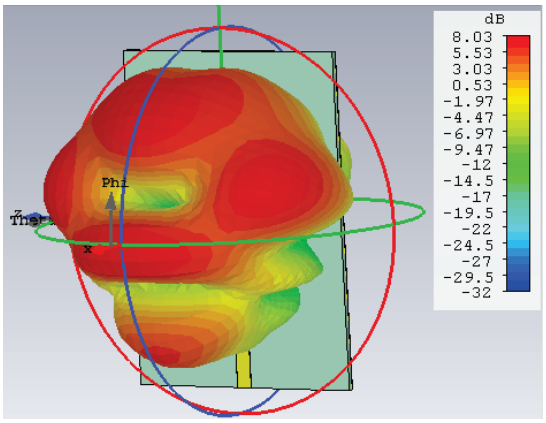

Fig. 9. Simulated 3D radiation pattern of the main structure.

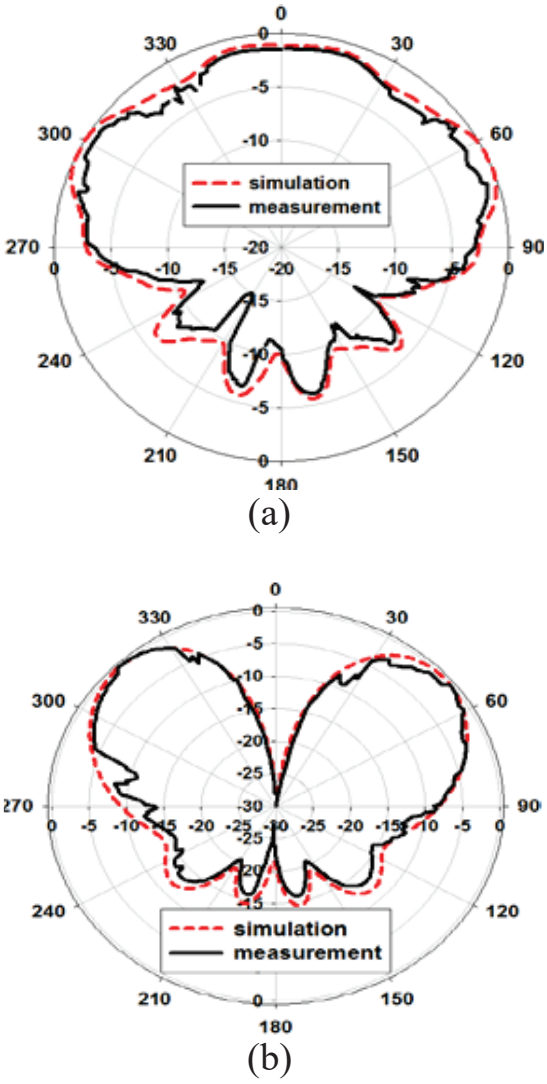

Fig. 10. Simulated and measured 2D radiation pattern (polar) for (a) *E*-plane and (b) *H*-plane at 26 GHz.

of about 26 GHz, and the SIW antenna achieved gains of 8 dB at 26 GHz and 8.03 dB at 28 GHz.

Normally, the radiation pattern of the antenna will take shape from the edges of the patch, but for SIW, the majority comes from the slots of the main structure as shown in the simulated 3D radiation pattern in Figure 9. The lengths of all slots were around 4.5 mm. The results proved that the width of the slots is suitable to achieve dual-band at millimeter wave and suitable for 5G applications.

The simulated *E*-plane and *H*-plane patterns computed at 26 and 28 GHz are presented in Figures 10 and 11. Figure 10 shows the comparison between the simulated and measured radiation pattern in *E*- and *H*-planes which comes from (slot A) radiating at 26 GHz. Meanwhile, Figure 11 indicates the comparison between

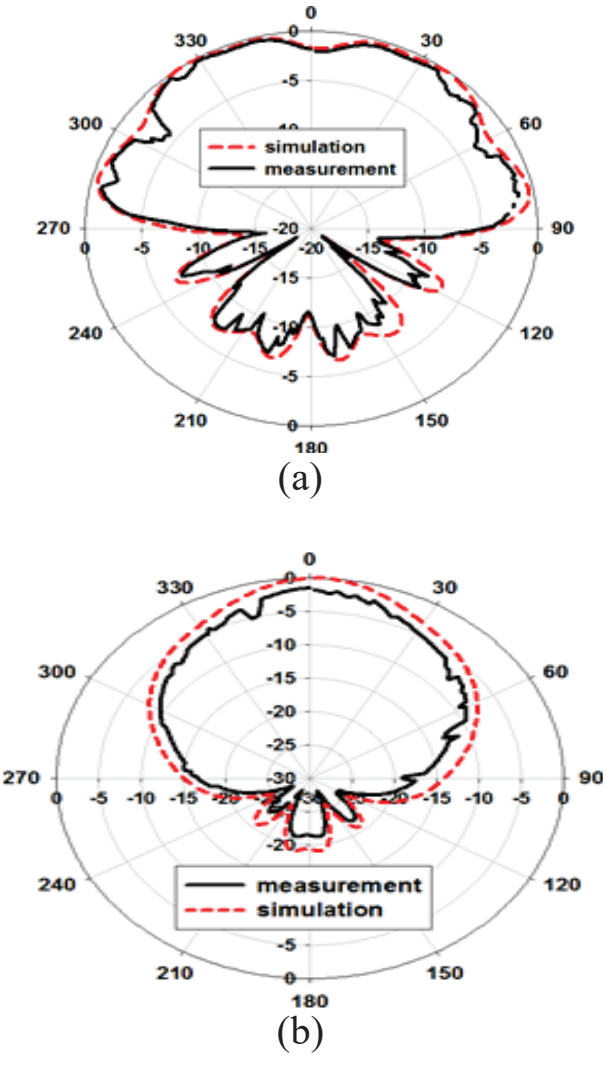

Fig. 11. Simulated and measured 2D radiation patterns (polar) for (a) *E*-plane and (b) *H*-plane at 28 GHz.

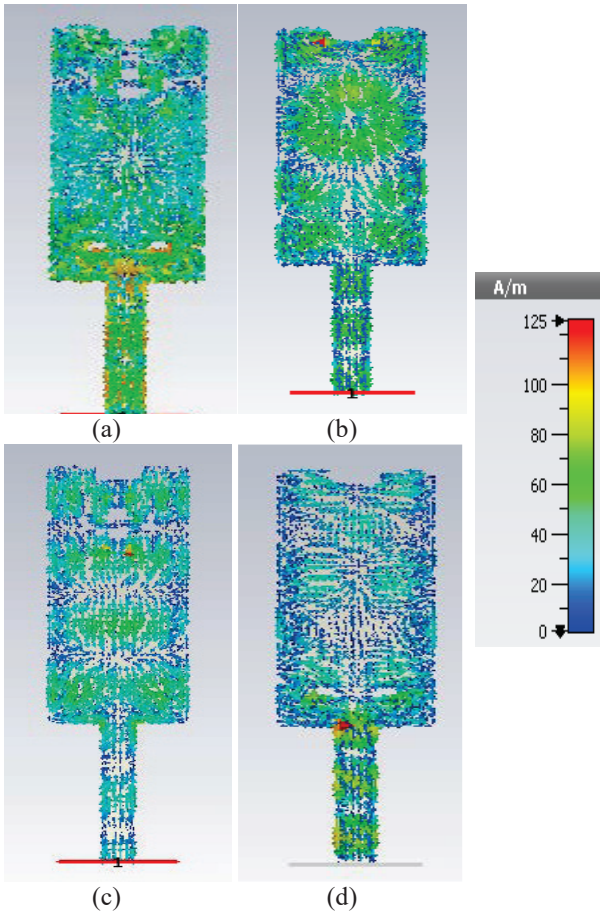

Fig. 12. Simulated current distributions on the SIW surface of the surface current when (a) design with slots A and B, (b) design without slots, (c) design with slot A, and (d) design with slot B.

the simulated and measured radiation pattern coming from (slot B) which radiates at 28 GHz. From 2D radiation (polar), the shape of the main beam can be visualized. This is one of the requirements for 5G application.

Due to the difference in the slot lengths, two different resonant modes with perturbed fields are excited within the SIW. Slot A, having longer slot length, radiated at 26 GHz and slot B at 28 GHz. These phenomena can be better understood with the help of surface current distribution on the top surface of the antenna at two resonant frequencies. Figure 12 shows that the surface current density becomes dominant on the lower half of the antenna and is mostly concentrated around the boundary of slot B. However, the surface current is almost negligible in the vicinity of slot A. It can be explained in a similar fashion, where surface current is mostly concentrated along the boundary of slot B.

Table 2: Comparison between this work and some previous dual-frequency/-band millimeter-wave

Ref.	Center freq. (GHz)	BW (GHz)	Gain (dB)	No. element
11	28/38	20.4/2.64	13.2/14.6	2×2
12	37.5/47	1.1/1.4	5.0/5.7	1
13	2.45/5.19	0.2/0.5	5.02/4.09	1
14	21/26	0.7/0.8	16/17.4	3×1
This work	26/28	2.8/0. 6	8/8.03	1

A comparison between the proposed design and previous works on dual frequency band millimeter-wave antennas is carried out in Table 2.

V. CONCLUSION

SIW antenna with slots is presented in this work. The antenna is meant to prove the concept of SIW antennas performance to be followed for millimeter-wave applications. Roger RT 5880 substrate is suitable for higher frequency because of the loss. Suitable width of slots and patch were identified to achieve better results of the 5G application with high gain and directivity with dual-band frequency. Gain that was achieved at 26-28 GHz are 8-8.03 dB, the directivity of dual-band is 8.18-8.22 dB, and also design provides sufficient impedance bandwidths at 2.8-0.6 GHz.

ACKNOWLEDGMENT

The authors would like to thank the Ministry of Higher Education (MOHE), School of Postgraduate Studies (SPS), Research Management Centre, Advanced RF and Microwave Research Group, School of Electrical Engineering, and Universiti Teknologi Malaysia (UTM), Johor Bahru, for the support of the research under Grant 09G19/06G15/04G65.

REFERENCES

[1] X. C. Lin and C. C. Yu, "A dual-band CPW-fed inductive slot-monopole hybrid antenna," *IEEE Transactions on Antennas and Propagation*, vol. 56, no. 1, pp. 282-285, 2008.

[2] Y. Ding and K. W. Leung, "On the dual-band DRA-slot hybrid antenna," *IEEE Transactions on Antennas and Propagation*, vol. 57, no. 3, pp. 624-630, 2009.

[3] I. Yeom, J. M. Kim, and C. W. Jung, "Dual-band slot-coupled patch antenna with broad bandwidth and high directivity for WLAN access point," *Electronics Letters*, vol. 50, no. 10, pp. 726-728, 2014.

[4] X. Zhang, Y. Chen, Y. Xie, and L. Liu, "An improved E-plane waveguide power divider design for 94GHz dual-pyramidal horn antenna," *The Applied Computational Electromagnetics Society (ACES) Journal*, pp. 1897-1903, 2019.

[5] Y. M. Hussain, M. K. A. Rahim, N. A. Murad, H. O. Hanoosh, and H. H. Keriee, "Substrate integrated waveguide cavity slot antenna at millimeter wave for 5G application." In *2021 International Symposium on Antennas and Propagation (ISAP)*. IEEE, pp. 1-2, Oct., 2021.

[6] Y. M. Hussein, M. K. A. Rahim, N. A. Murad, M. M. Jawad, H. O. Hanoosh, H. A. Majid, and H. H. Keriee, "Substrate integrated waveguide and microstrip antennas at 28 GHz," *Bulletin of Electrical Engineering and Informatics*, vol. 9, no. 6, pp. 2462-2468, 2020.

[7] H. O. Hanoosh, M. K. A. Rahim, N. A. Murad, and Y. M. Hussein, "Multi-beams waveguide slot antennas at X-band for wireless communications systems," *The Applied Computational Electromagnetics Society (ACES) Journal*, pp. 797-802, 2020.

[8] M. A. Rahim, I. M. Ibrahim, R. A. A. Kamaruddin, Z. Zakaria, and N. Hassim, "Characterization of microstrip patch array antenna at 28 GHz," *Journal of Telecommunication, Electronic and Computer Engineering (JTEC)*, vol. 9, no. (2-8), pp. 137-141, 2017.

[9] S. Moitra, A. K. Mukhopadhyay, and A. K. Bhattacharjee, "Ku-band substrate integrated waveguide (SIW) slot array antenna for next generation networks," *Global Journal of Computer Science and Technology*, 2013.

[10] M. Bozzi, A. Georgiadis, and K. Wu, "Review of substrate-integrated waveguide circuits and antennas," *IET Microwaves, Antennas & Propagation*, vol. 5, no. 8, pp. 909-920, 2011.

[11] T. Hong, Z. Zhao, W. Jiang, S. Xia, Y. Liu, and S. Gong, "Dual-band SIW cavity-backed slot array using TM 020 and TM 120 modes for 5G applications," *IEEE Transactions on Antennas and Propagation*, vol. 67, no. 5, pp. 3490-3495, 2019.

[12] Q. Wu, J. Yin, C. Yu, H. Wang, and W. Hong, "Low-profile millimeter-wave SIW cavity-backed dual-band circularly polarized antenna," *IEEE Transactions on Antennas and Propagation*, vol. 65, no. 12, pp. 7310-7315, 2017.

[13] Y. Ding and K. W. Leung, "On the dual-band DRA-slot hybrid antenna," *IEEE Transactions on Antennas and Propagation*, vol. 57, no. 3, pp. 624-630, 2009.

[14] W. Li, K. Da Xu, X. Tang, Y. Yang, Y. Liu, and Q. H. Liu, "Substrate integrated waveguide cavity-backed slot Array antenna using high-order radiation modes for dual-band applications in $ K $-band," *IEEE Transactions on Antennas and Propagation*, vol. 65, no. 9, pp. 4556-4565, 2017.

Yaqdhan Mahmood Hussein was born in Samawah, Iraq, in 1991. He received the B.S. degree in computer techniques engineering in 2014-2015 from Islamic University College, Najaf city, and the M.S. degree in electronic engineering (telecommunication system) from Universiti Teknikal Malaysia Melaka (UTeM), Malaysia, in 2018, respectively, and he is currently working toward the Ph.D. degree in electronic engineering with Universiti Teknologi Malaysia (UTM), Johor Bahru city. His current research interests include millimeter-wave antennas, base station antennas, and SIW technology with butler matrix.

Mohamad Kamal A. Rahim received the B.Eng. degree in electrical & electronics from the University of Strathclyde, U.K., in 1987. He received the M.Eng. degree in science from the University of New South Wales, Australia, in 1992 and the Ph.D. degree in electrical engineering from University of Birmingham, U.K., in 2003.

He is a Professor in RF & Microwave and Antenna at School of Electrical Engineering, Universiti Teknologi Malaysia. His research interest includes the areas of radio frequency, microwave and antennas.

He has been awarded with top research publication in 2015, 2017, and 2020. In 2018, he was honored as "Tokoh Penyelidik" at CITRA KARISMA UTM, and in the same year, he was awarded with Top Research Scientist Malaysia (TRSM) award by Academy Science of Malaysia.

Noor Asniza Murad received her first degree, Bachelor of Engineering (Electrical – Telecommunications), in 2001 from Universiti Teknologi Malaysia (UTM). Shortly after graduation, she served UTM as a tutor. She graduated with Master of Engineering (Electrical) in 2003 from the same university and has been appointed as a Lecturer in April 2003. She joined Emerging Device Technology Group, University of Birmingham, U.K., and obtained the Ph.D. degree in 2011 for research on micromachined millimeterwave circuits. She attached to HID GLOBAL Sdn Bhd for one year under Research and Development specifically working on RFID tag design, testing, and development. Her research interests include antenna design for RF and microwave communication systems, millimeter-wave circuits design, RFID, and antenna beamforming. Currently, she is a senior member of IEEE (MIEEE), MBOT Professional Technologist, and an Associate Professor with the School of Electrical Engineering, Universiti Teknologi Malaysia (UTM).

Hatem Oday Hatem (H. O. Hanoosh) was born in Samawah, Iraq, in 1991. He received the B.S. degree in computer techniques engineering in 2014-2015 from Islamic University College, Najaf City. He received the M.S. degree in electronic engineering (telecommunication system) from University Technical Malaysia Melaka (UTEM), Malaysia, in 2018, respectively, and he is currently working toward the Ph.D. degree in electronic engineering with University Technology Malaysia (UTM), Johor Bahru City. His current research interests include millimeter-wave antennas, base station antennas, and waveguide slot antennas.

Norsaidah Binti Muhamad Nadzir was born on March 12, 1993. She received the Master of Philosophy degree in electrical engineering from Universiti Teknologi Malaysia, Johor Bahru, Malaysia, in 2019. She is currently working toward the Doctor of Philosophy degree in electrical engineering with the same university. Her research interests include radio frequency identification (RFID) systems, RFID antennas, and compact millimeter-wave antennas. Her focus is on millimeter wave antenna with beamforming devices.

Research on EMI of Traction Network Transient Current Pulse on Shielded Cable Terminal Load

Yingchun Xiao[1,2], Feng Zhu[1,*], Shengxian Zhuang[1], and Yang Yang[1]

[1]School of Electrical Engineering
Southwest Jiaotong University, Chengdu, 611756, China
1134748712@qq. com, zhufeng@swjtu.cn, sxzhuang@swjtu.edu.cn, 280899254@qq.com

[2]Lanzhou City University, Lanzhou, 730070, China

Abstract **–** The transient current pulse (TCP) caused by the traction network short-circuit fault (TNSF) will produce a high-strength transient electromagnetic field (TEMF). The electromagnetic field will interfere with nearby weak current equipment through the shielded cable. In this paper, a transient circuit model (TCM) for the short-circuit traction network is proposed to calculate the transient current. The short circuit is equivalent to a ring, and the TEMF transient electromagnetic field is calculated based on the magnetic dipole. The current response of the TEMF transient electromagnetic field on the shielded cable is deduced based on the transmission line theory and verified by experiments. The electromagnetic interference (EMI) of a TEMF transient electromagnetic field to the shielded cable terminal load were was studied under various incidence angles, azimuth angles, and polarization angles. The results demonstrate that the greater the incident angle and azimuth angle, the greater the EMI on the terminal load. The horizontal distance between the shielded cable head and the short-circuit point should be greater than 6 m, and the incident angle should be greater than 45°. This method can provide a theoretical basis for the electromagnetic compatibility research of traction power supply systems and their nearby weak current equipment.

Index Terms **–** Traction network short-circuit current pulse, transient electromagnetic field, shielded cable, current response, electromagnetic interference (EMI).

I. INTRODUCTION

Cables are the medium for the effective transmission of energy and information between systems. Due to its special structure, it is easy to couple with external electromagnetic signals, causing interference or even damage to the terminal equipment [1]. Cables are also the main way to introduce electromagnetic interference (EMI) [2, 3]. Shielded cables cannot completely shield external magnetic signals. The induced current on the shielding layer can be coupled to the inner conductor through transfer impedance [4, 5]. In the traction network system, the harmonic current of the rail will interfere with the communication system nearby. Generally, there are multiple grounding branches to avoid the interference of harmonic currents [6]. However, when a short-circuit fault occurs in the traction network, or a short-circuit experiment, the amplitude of the short-circuit current increases rapidly [7], and transient current pulses (TCP) will be generated. The large transient current propagates along the transmission line (TL), which will form a strong magnetic field and radio interference, thereby affecting electrical equipment through the cable [8–11]. Therefore, it is necessary to study the EMI of the transient electromagnetic field (TEMF) caused by the traction network short-circuit fault (TNSF) on the shielded cable terminal load.

In order to analyze the influence of the TNSF on the shielded cable terminal load, the traction network transient current and the coupling to the shielded cable need to be studied. The circuit model of traction power supply system mainly includes equivalent circuit model, generalized symmetrical component model, and chain circuit model. Among them, the chain circuit model is more suitable for the simulation calculation of the traction network, and the generalized symmetric component model is more suitable for the theoretical analysis of the multi-rail traction network [12]. These models are mostly used to calculate current at 50 Hz. When analyzing transient processes induced by TNSF, however, the parameters at 50 Hz are insufficient, and transmission TL frequency characteristics must be studied in depth. The electromagnetic transients program (EMTP) is used to simulate a short-circuit fault by establishing an equivalent circuit of a substation in [6]. However, the TEMF caused by short-circuit current pulse is not discussed. Many studies investigate the transmission TL"s radiation problem by treating the contact line as a long wire made up of an infinite number of unit dipoles. For example, based on transmission TL theory, [13] established a radiation model under impedance matching. An improved

Submitted On: January 7, 2022
Accepted On: May 5, 2022

https://doi.org/10.13052/2022.ACES.J.370414

approximation method based on Hertzian dipole and a numerical method based on the finite element method algorithm are proposed to calculate the radiation of a coaxial cable [14, 15]. The circuit model for conducted and radiation interference on an electric railway contact line under the condition of overvoltage is established in [16], and the two types of interference are analyzed using the finite difference time domain method and segmented line technology, with the induced voltage on the cable calculated. However, when the traction network is short-circuited, a short-circuit loop will be formed. The electromagnetic radiation model of the contact wire based on the long wire has limitations.

The coupling models of electromagnetic field to cables include the classic Taylor Model [17], Agrawal Model [18], and Rachidi Model [19]. These three coupling models consider electromagnetic coupling in different ways but predict the same results in terms of total voltage and total current [20]. In [21], the electromagnetic radiation generated by the off-line arc of the electrified railway pantograph is equivalent to the parallel wave excitation. The induced current distribution on the contact line is studied based on the TL distributed parameter circuit. A closed time-domain coupling model is proposed in [22], which can effectively calculate the time-domain voltage generated by a pulsed electromagnetic plane wave on an ideal conductive plane. In [23], the exposed cable is equivalent to a vertical monopole antenna and studied the coupling model of nuclear electromagnetic pulses to the exposed cable. These methods assume that the shielded cable is parallel to the TL and do not analyze the EMI of the electromagnetic field on the cable terminal load when it is under different conditions.

In order to study the EMI of the traction network TCP on the shielded cable terminal load, a transient circuit model (TCM) is established and the shielded cable terminal response is calculated. The main contributions are summarized as follows:

1) Taking into account the single reignition when the circuit breaker is opened, a TCM for the short-circuit traction network is established to calculate the time-domain transient current;.
2) The short-circuited contact wire loop is equivalent to a loop antenna, and the TEMF is calculated based on the magnetic dipole;.
3) Considering the transfer impedance and transfer admittance between the shielding layer and the inner conductor, calculate the current response of the shielded cable based on the Agrawal Model, and analyze the EMI according to the power of the shielded cable terminal load.

The remainder of the paper is organized as follows. Section II briefly introduces the transient current and TEMF after the traction network is short-circuited. The response of the TEMF to the shielded cable terminal load is described in Section III. Section IV verifies the methods proposed in this article through simulation experiments and test experiments, and conclusions are drawn in Section V.

II. THE TRANSIENT PROCESS OF THE SHORT-CIRCUIT TRACTION NETWORK

The circuit breaker of the traction substation will open due to a short-circuit fault in the traction network, cutting off the contact wire. The electromagnetic field and electromagnetic energy will change as a result of the short circuit and the circuit breaker opening. The generated electromagnetic wave propagates along the line, causing a transient oscillation process. The frequency of the oscillation is determined by the transmission TL"s wave impedance, transmission time, and associated capacitance and inductance. A TCM for the short-circuit traction network is established to calculate the transient current and the TEMF.

A. TCM for short-circuit traction network

In addition to contact wire and rail, there are other auxiliary wires in the traction network. According to the Carson theory [24], each wire forms a loop with the ground, and the self-impedance of each wire and the mutual impedance between them can be calculated. Due to the admittance between the rail and the ground, part of the rail current flows into the substation to form a ground current. A part of the ground current returns to the substation through the grounding network. Taking into account the leakage reactance of the rail to the ground, the simplified double-wire traction network circuit model is shown in Figure 1. z_{I} and z_{II} are the self-impedances of the two contact wire-ground loops, and $z_{\mathrm{I}} = z_{\mathrm{II}}$. z_{III} is the impedance of the rail-ground loop. $z_{\mathrm{I-III}}$ is the mutual impedance between the two loops. The admittance per unit length between the rail and the ground is Y. Z_E is the grounding resistance of the traction substation, and Z_0 is the characteristic impedance of the rail.

According to the contact wire I-rail circuit, we can get,

$$\begin{aligned}\dot{U}_1 - \dot{U}_1' &= z_{\mathrm{I}}\dot{I}l - \int_0^l z_{\mathrm{I-III}}\dot{I}_T(x)\,dx \\ &+ \int_0^l z_{\mathrm{III}}\dot{I}_T(x)\,dx - z_{\mathrm{I-III}}\dot{I}l \\ &= \left(z_{\mathrm{I}} - \frac{z_{\mathrm{I-III}}^2}{z_{\mathrm{III}}}\right)\dot{I}l + \frac{(z_{\mathrm{III}} - z_{\mathrm{I-III}})^2}{2z_{\mathrm{III}}\sqrt{z_{\mathrm{III}}y}} \\ &\cdot \left[\left(1 - e^{-\gamma l}\right) - \frac{2Z_E + Z_0 e^{-\gamma l}}{Z_0 + 2Z_E}\left(e^{-\gamma l} - 1\right)\right]\cdot \dot{I}.\end{aligned} \tag{1}$$

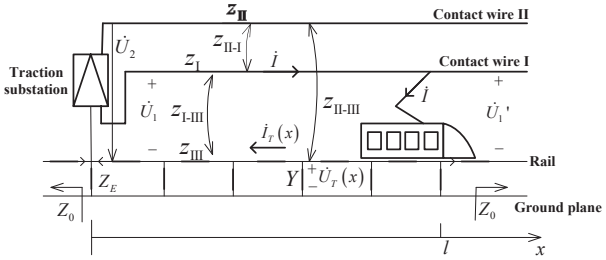

Fig. 1. Circuit model of double-wire traction network.

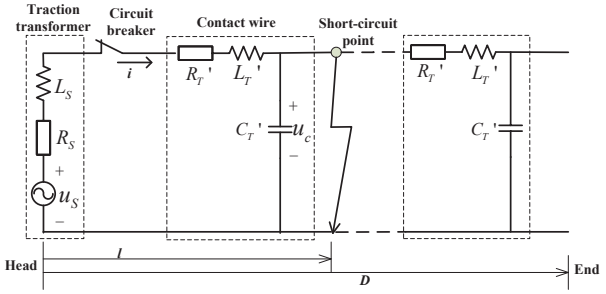

Fig. 2. TCM for traction network short-circuit.

Therefore, the impedance per unit length of the contact wire is

$$\begin{aligned} Z'_T &= R'_T + j\omega L'_T = \frac{\dot{U}_1 - \dot{U}'_1}{\dot{I}l} \\ &= \left(z_{\mathrm{I}} - \frac{z_{\mathrm{I-III}}^2}{z_{\mathrm{III}}}\right) + \frac{(z_{\mathrm{III}} - z_{\mathrm{I-III}})^2}{2z_{\mathrm{III}}\sqrt{z_{\mathrm{III}}\bar{y}}} \\ &\cdot \left[\left(1 - e^{-\gamma l}\right) - \frac{2Z_E + Z_0 e^{-\gamma l}}{Z_0 + 2Z_E}\left(e^{-\gamma l} - 1\right)\right] \cdot \frac{1}{l}, \end{aligned} \tag{2}$$

where γ is the propagation coefficient of the trail. $\gamma = \sqrt{z_{\mathrm{III}}\bar{y}}$, and $Z_0 = \sqrt{z_{\mathrm{III}}/y}$. Traction network impedance includes linear components and nonlinear components. It can be seen that when l is large, the nonlinear components can be ignored in a sinusoidal steady state circuit. However, when the current frequency is high, the nonlinear components cannot be ignored. z_{I}, z_{II}, z_{III}, and $z_{\mathrm{I-II}}$ can all be calculated according to the traction network parameters [25].

When the traction network is short-circuited, the contacts of the circuit breaker will be disconnected, and an arc will be generated. The arc will be extinguished when the current crosses zero. Circuit breaker arc is the main cause of high-frequency transient current and TEMF. The frequency of multiple reignitions caused by circuit breaker opening can reach 1 MHz [26]. The electromagnetic wave wavelength λ is 300 m. Based on the lumped parameter model of the contact wire, we established a TCM for traction network short-circuit, as shown in Figure 2.

It includes traction transformers, circuit breakers, and contact wires. D is the length of a power supply arm, and the distance between the short-circuit point and the substation is l. u_S is a 27.5 5-kV AC voltage source provided by the substation for the contact wire. R_S and L_S are the equivalent resistance and inductance of the transformer in the substation, respectively. They can be calculated by the electrical parameters of traction transformer.

C'_T is the capacitance per unit length of the contact line to the ground, and it is

$$C'_T = \frac{2\pi\varepsilon_0}{\ln\left(2h/a\right)}, \tag{3}$$

where a and h are the radius and height of the contact wire, and ε_0 is the vacuum dielectric constant.

B. The transient current

Suppose that when $t = 0$, the traction network is short-circuited, and when $t = t_1$, the contacts of the circuit breaker are disconnected. Before the traction network is short-circuited, the traction system works normally. The voltage on the contact wire is $u_S(t) = U_S \sin(\omega t + \psi_{0u})$, and the frequency is 50 Hz. The impedance of the train body is X, while the equivalent resistance, equivalent inductance, and ground capacitance of the short-circuit point to the substation are R_T, L_T, and C_T, respectively. As a result, the current flowing across the contact wire is

$$i_{(t\le 0)}(t) = \frac{U_S \sin(\omega t + \psi_{0u} - \varphi_0)}{\sqrt{(R_S + R_T)^2 + \left(\omega L_S + \omega L_T + \omega C_T - \frac{1}{X}\right)^2}}. \tag{4}$$

The voltage on the C_T is

$$u_{c(t\le 0)}(t) = \frac{U_S \left|\omega C_T - \frac{1}{X}\right| \cos(\omega t + \psi_{0u} - \varphi_0)}{\sqrt{(R_S + R_T)^2 + \left(\omega L_S + \omega L_T + \omega C_T - \frac{1}{X}\right)^2}}, \tag{5}$$

where ψ_{0u} is the initial phase of u_s, and φ_0 is the phase difference between the voltage and current before the contact wire is short-circuited. So,

$$\tan\varphi_0 = \frac{\omega(L_S + L_T + CT) - \frac{1}{X}}{R_S + R_T}. \tag{6}$$

When $t = 0$, the contact wire is short-circuited. According to Figure 2, the transient circuit can be expressed as

$$\begin{aligned} &(L_S + L_T) C_T \frac{d^2 u_c(t)}{dt} + (R_S + R_T) \\ &C_T \frac{du_c(t)}{dt} + u_c(t) = u_S(t). \end{aligned} \tag{7}$$

According to the initial values provided by equation (4) and (5), the current $i(t)$ when $0 < t \le t_1$ can be calculated, as

$$\begin{aligned} i_{(0<t\le t_1)}(t) &= \frac{U_S \cos(\omega t + \psi_{0u} - \varphi_1)}{W_1} \\ &+ A_1 P_1 C_T e^{P_1 t} + A_2 P_2 C_T e^{P_2 t}, \end{aligned} \tag{8}$$

where φ_1, W_1, P_1, P_2, A_1, and A_2 are,

$$\varphi_1 = \arctan\frac{\omega(L_S + L_T) - \frac{1}{\omega C_T}}{R_S + R_T}, \tag{9}$$

$$W_1 = \sqrt{(R_S+R_T)^2 + \left(\omega(L_S+L_T) - \frac{1}{\omega C_T}\right)^2}, \quad (10)$$

$$P_1 = -\frac{R_S+R_T}{2(L_S+L_T)} + \sqrt{\left(\frac{R_S+R_T}{2(L_S+L_T)}\right)^2 - \frac{1}{(L_S+L_T)C_T}}, \quad (11)$$

$$P_2 = -\frac{R_S+R_T}{2(L_S+L_T)} - \sqrt{\left(\frac{R_S+R_T}{2(L_S+L_T)}\right)^2 - \frac{1}{(L_S+L_T)C_T}}, \quad (12)$$

$$A_1 = \frac{1}{P_1-P_2}\left[W_2 - P_2\left(W_3 - \frac{U_S\sin(\psi_{0u}-\varphi_1)}{\omega C_T W_1}\right)\right], \quad (13)$$

$$A_2 = \frac{1}{P_2-P_1}\left[W_2 - P_1\left(W_3 - \frac{U_S\sin(\psi_{0u}-\varphi_1)}{\omega C_T W_1}\right)\right]. \quad (14)$$

In A_1 and A_2, W_2 and W_3 are, respectively,

$$W_2 = \frac{U_S\sin(\psi_{0u}-\varphi_0)}{C_T\sqrt{(R_S+R_T)^2+\left(\omega L_S+\omega L_T+\omega C_T-\frac{1}{X}\right)^2}} - \frac{U_S\cos(\psi_{0u}-\varphi_1)}{C_T W_1}, \quad (15)$$

$$W_3 = \frac{U_S\left|\omega C_T - \frac{1}{X}\right|\cos(\psi_{0u}-\varphi_0)}{\sqrt{(R_S+R_T)^2+\left(\omega L_S+\omega L_T+\omega C_T-\frac{1}{X}\right)^2}}. \quad (16)$$

When $t = t_1$, the contact of the circuit breaker is disconnected and an arc is generated. When the current crosses zero, the arc is extinguished, and the contact wire is truly disconnected. According to Figure 2, we can get,

$$L_S C_T\frac{d^2u_c(t)}{dt} + R_S C_T\frac{du_c(t)}{dt} + u_c(t) = u_S(t). \quad (17)$$

Therefore, it can be deduced that the current when $t > 0$ is

$$i_{(t>t_1)}(t) = \frac{U_S\sin(\omega(t-t_1)+\psi_{0u}-\varphi_1-\varphi_2)}{\sqrt{R_S^2+\left(\omega L_S-\frac{1}{\omega C_T}\right)^2}} + A_3P_3C_Te^{-P_3(t-t_1)} + A_4P_4C_Te^{-P_4(t-t_1)}, \quad (18)$$

where φ_2, P_3, P_4, A_3, and A_4 are, respectively,

$$\varphi_2 = \arctan\frac{\omega L_S - \frac{1}{\omega C_T}}{R_S}, \quad (19)$$

$$P_3 = -\frac{R_S}{2L_S} + \sqrt{\left(\frac{R_S}{2L_S}\right)^2 - \frac{1}{L_S C_T}}, \quad (20)$$

$$P_4 = -\frac{R_S}{2L_S} - \sqrt{\left(\frac{R_S}{2L_S}\right)^2 - \frac{1}{L_S C_T}}, \quad (21)$$

$$A_3 = \frac{1}{P_3-P_4}\left[\frac{i_{0<t\le t_1}(t_1)}{C_T} - P_4(W_5-W_4)\right], \quad (22)$$

$$A_4 = \frac{1}{P_4-P_3}\left[\frac{i_{0<t\le t_1}(t_1)}{C_T} - P_3(W_5-W_4)\right]. \quad (23)$$

In A_3 and A_4, W_4 and W_5 are, respectively,

$$W_4 = \frac{U_S}{\sqrt{R_S^2+\left(\omega L_S-\frac{1}{\omega C_T}\right)^2}}, \quad (24)$$

$$W_5 = \frac{U_S\sin(\omega t_1+\psi_{0u}-\varphi_1)}{\omega C_T W_1} + A_1e^{P_1t_1} + A_2e^{P_2t_1}. \quad (25)$$

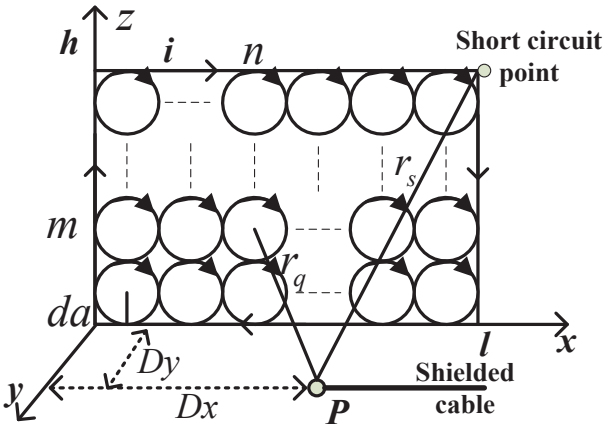

Fig. 3. Segmentation calculation of the electromagnetic field in a loop circuit.

After the arc is extinguished, the current quickly decays to zero. Through Fast Fourier Transform (FFT) transformation, the frequency spectrum of transient current can be obtained.

C. The transient electromagnetic field

The oscillating wave generated by the transient current becomes the disturbance source, radiating the TEMF energy to the surrounding space. When the distance between the short-circuit point and the substation is less than $\lambda/4$, and the height between the circuit point and the ground is less than $\lambda/4$, the current direction at all points on the line can be considered to be same. Therefore, we take the closed loop as a loop antenna and divide it into Q small circles, as shown in Figure 3. The radius of the small circle is da and meets $da << \lambda$. The shielded cable head is P. The horizontal distance from the substation is D_x. r_q is the distance from the q-th small circle to P. D_y is the vertical distance between the shielded cable and the rail.

The electromagnetic field at P is the superposition of the electromagnetic fields generated by each small ring. r_s is the distance from P to the short-circuit point, which can be expressed as

$$r_s = \sqrt{h^2 + D_y^2 + |l-D_x|^2}. \quad (26)$$

Let ϕ_q be the angle between the x x-axis and the projection of r_q on the xoy plane, and θ_q be the angle between r_q and the z z-axis. According to the electromagnetic field theory, when the shielded cable is in the near field of the radiation field, the electromagnetic field at P can be expressed as

$$E = \sum_{q=1}^{Q} dE_{\phi_q} = \sum_{q=1}^{Q} -jk\eta\frac{Ida^2}{4r_q^2}\sin\theta_q e^{-jkr_q}, \quad (27)$$

$$H = \sum_{q=1}^{Q} \sqrt{dH_{r_q}^2 + dH_{\theta_q}^2} = \sum_{q=1}^{Q} \frac{Ida^2}{2r_q^3} \sqrt{(\cos\theta_q)^2 + \frac{1}{4}(\sin\theta_q)^2} \cdot e^{-jkr_q}, \tag{28}$$

where I and f are the effective value and frequency of the transient current, and c is the speed of the wave in free space. $\eta \approx 377\,\Omega$ for wave impedance in free space, $k = 2\pi f/c$ for propagation constant. Q small circles are represented in the form of a matrix. The distance between the small circle in m row and n column to P can be expressed as,

$$r_{mn} = \sqrt{((2m-1)\,da)^2 + D_y^2 + |D_x - (2n-1)\,da|^2}, \tag{29}$$

where $1 \le m \le h/2da$, $1 \le n \le l/2da$.

Let $D_{xx} = |D_x - (2n-1)\,da|$, $D_{xx} = |D_x - (2n-1)\,da|$; the TEMF at P can be expressed as

$$E = \sum_{m=1}^{h/2da} \sum_{n=1}^{l/2da} \frac{-j60\pi^2 f \cdot Ida^2}{cr_{mn}^3} \sqrt{D_y^2 + D_{xx}^2} \cdot e^{-jkr_{mn}}, \tag{30}$$

$$H = \sum_{m=1}^{h/2da} \sum_{n=1}^{l/2da} \frac{Ida^2}{2r_{mn}^4} \sqrt{(2m-1)^2 da^2 + \frac{1}{4}D_y^2 + \frac{1}{4}D_{xx}^2} \cdot e^{-jkr_{mn}}. \tag{31}$$

It can be seen that the TEMF generated by the TNSF on the shielded cable is related to the height of the contact wire, the distance from the short-circuit point, the amplitude and frequency of the transient current, and the location of the shielded cable.

III. THE RESPONSE ON THE SHIELDED CABLE

If the cables of weak-current equipment are exposed, they are easily coupled by electromagnetic fields. Disturbance voltage and disturbance current are induced and enter the equipment along the inner conductor to cause EMI. We calculated the response of the TEMF on the shielded cable based on the transmission TL theory. A shielded cable includes a shielding layer and an inner conductor, which is defined as two independent transmission TLs. The electromagnetic field generates current and voltage on the shielding layer. The voltage and current on the shielding layer generate current and voltage on the inner conductor through transfer impedance and transfer admittance.

A. The voltage and current on the shielding layer

Let the incident angle, the azimuth angle, and the polarization angle of the electromagnetic field be φ, ψ, and α, respectively. The Agrawal model decomposes the incident field into the excitation field component that does not depend on the shielding structure and the scattered field component due to the induced charge and induced current on the shielding layer. Treating the shielding layer as an external transmission line (ETL), the equivalent circuit coupled to the shielding layer is shown in Figure 4. Cable length is L. h_c is the height from the ground. V_1 and V_2 are the lumped voltage sources at the ETL's two ends, and $V_S'(x)$ is the excitation voltage source along the direction of the ETL. Load impedances at both ends of the ETL are Z_{e1} and Z_{e1}, respectively. Z_e' and Y_e' are the ETL's unit impedance and unit admittance, which can be calculated using the shielded cable's parameters. The scattering field voltage is $V_{\rm sc}(x)$, the incident field is $E_{\rm in}$, and the ground reflection field is $E_{\rm re}$. $\hat{k}$ represents the direction of the plane wave generated by the electromagnetic field.

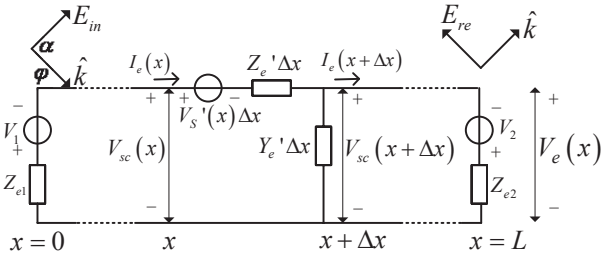

Fig. 4. The equivalent circuit of the shielding layer.

Assume that the incident field spectrum is $E_0(\omega)$. According to the components of $E_{\rm in}$ and $E_{\rm re}$ along the ETL, $V_S'(x)$, V_1, and V_2 can be deduced.

$$V_S'(x) = jk2h_cE_0(\omega)\sin\varphi \cdot \begin{pmatrix} \cos\alpha\sin\varphi\cos\psi \\ +\sin\alpha\sin\psi \end{pmatrix} e^{-jk_xx}, \tag{32}$$

$$V_1 \approx -2h_cE_0(\omega)\cos\alpha\cos\varphi, \tag{33}$$

$$V_2 \approx V_1 e^{-j\cos\varphi\cos\psi kL}, \tag{34}$$

where $k = 2\pi/\lambda$, $k = 2\pi/\lambda$ and $k_x = k\cos\varphi\cos\psi$. From Figure 4, we can get

$$\frac{d}{dx}\begin{bmatrix} V_{\rm sc}(x) \\ I_e(x) \end{bmatrix} + \begin{bmatrix} 0 & Z_e' \\ Y_e' & 0 \end{bmatrix}\begin{bmatrix} V_{\rm sc}(x) \\ I_e(x) \end{bmatrix} = \begin{bmatrix} V_S'(x) \\ 0 \end{bmatrix}. \tag{35}$$

Referring to [27], the current $I_e(x)$ and scattered voltage $V_{\rm sc}(x)$ at the x of the TL can be expressed in the form of Green's function. Therefore, $I_e(x)$ and $V_{\rm sc}(x)$ can be expressed as

$$I_e(x) = K_1e^{r_ex} + K_2e^{-r_ex} + K_3e^{-j\cos\varphi\cos\psi kx}, \tag{36}$$

$$V_{\rm sc}(x) = -\frac{1}{Y_e'}\begin{bmatrix} K_1r_ee^{r_ex} - K_2r_ee^{-r_ex} \\ -jk\cos\varphi\cos\phi K_3e^{-j\cos\varphi\cos\psi kx} \end{bmatrix}, \tag{37}$$

where $r_e = \sqrt{Z_e'Y_e'}$ is the propagation constant of the ETL. K_1, K_2, and K_3 are

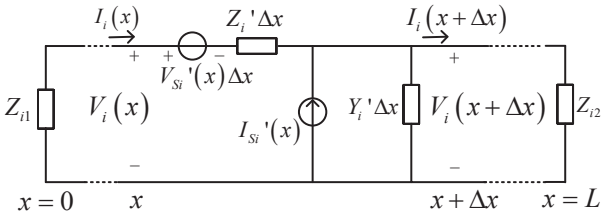

Fig. 5. The equivalent circuit of the inner conductor.

$$K_1 = \frac{1}{2Z_{e0}\left[1-\rho_{e1}\rho_{e2}e^{-2r_eL}\right]} \left\{ \begin{array}{l} V_x' \left[\begin{array}{l} -e^{-r_e^+L}\left(\frac{1}{r_e^+}+\frac{\rho_{e1}}{r_e^-}\right) \\ +\rho_{e2}e^{-2r_eL}\left(\frac{1}{r_e^-}+\frac{\rho_{e1}}{r_e^+}\right) \end{array} \right] \\ +V_1 \left[\begin{array}{l} (1-\rho_{e1})\rho_{e2}e^{-2r_eL} \\ +(1-\rho_{e2})e^{-r_e^+L} \end{array} \right] \end{array} \right\}, \tag{38}$$

$$K_2 = \frac{1}{2Z_{e0}\left[1-\rho_{e1}\rho_{e2}e^{-2r_eL}\right]} \left\{ \begin{array}{l} V_x' \left[\begin{array}{l} \rho_{e1}e^{-r_e^+L}\left(\frac{1}{r_e^+}+\frac{\rho_{e1}}{r_e^-}\right) \\ -\left(\frac{1}{r_e^-}+\frac{\rho_{e1}}{r_e^+}\right) \end{array} \right] \\ -V_1 \left[\begin{array}{l} (1-\rho_{e1}) \\ +(1-\rho_{e2})\rho_{e1}e^{-r_eL} \end{array} \right] \end{array} \right\}, \tag{39}$$

$$K_3 = \frac{V_x'}{2Z_{e0}}\left(\frac{1}{r_e^-}+\frac{1}{r_e^+}\right). \tag{40}$$

V_x' is

$$V_x' = j2kh_cE_0(\omega)\sin\varphi \left(\begin{array}{l} \cos\alpha\sin\varphi\cos\psi \\ +\sin\alpha\sin\psi \end{array} \right). \tag{41}$$

$Z_{e0} = \sqrt{Z_e'/Y_e'}$ is the characteristic impedance of the ETL. ρ_{e1} and ρ_{e2} are the reflection coefficients at the two ends of the ETL, and they are

$$\rho_{e1} = \frac{Z_{e1}-Z_{e0}}{Z_{e1}+Z_{e0}}, \tag{42}$$

$$\rho_{e2} = \frac{Z_{e2}-Z_{e0}}{Z_{e2}+Z_{e0}}. \tag{43}$$

The propagation constants r_e^+ and r_e^- are,

$$r_e^+ = r_e + jk\cos\varphi\cos\psi, \tag{44}$$

$$r_e^- = r_e - jk\cos\varphi\cos\psi. \tag{45}$$

The total voltage at the x of the TL is

$$\begin{aligned} V_e(x) &= V_{\rm sc}(x) - \int_0^{h_c} E_{\rm in}dz \\ &= V_{\rm sc}(x) - h_cE_0(\omega)\cos\alpha\cos\varphi. \end{aligned} \tag{46}$$

B. The voltage and current on the inner conductor

The current on the shielding layer penetrates into the shielded cable and generates an excitation source on the inner conductor. Taking the inner conductor as the Inner Transmission Line (ITL), its equivalent circuit model is shown in Figure 5.

Load impedances at both ends of the ITL are Z_{i1} and Z_{i2}. Z_i' and Y_i' are the ITL's unit impedance and unit admittance, which can be calculated using the shielded cable's parameters. $V_{Si}'(x)$ and $I_{Si}'(x)$ are the excitation voltage source and current source on the ITL.

$$V_{Si}'(x) = Z_t'I_e, \tag{47}$$

$$I_{Si}'(x) = -Y_t'V_e, \tag{48}$$

where Z_t' and Y_t' are transfer impedance and transfer admittance, and their values refer to [28] and [29]. According to the Baum–Liu–Tesche (BLT) equation [30], the current and voltage at both ends of the ITL can be deduced as

$$\left[\begin{array}{l} I_i(0) \\ I_i(L) \end{array} \right] = \frac{1}{Z_{i0}} \left[\begin{array}{cc} 1-\rho_{i1} & 0 \\ 0 & 1-\rho_{i2} \end{array} \right] \left[\begin{array}{cc} -\rho_{i1} & e^{r_iL} \\ e^{r_iL} & -\rho_{i2} \end{array} \right]^{-1} \left[\begin{array}{l} S_{i1} \\ S_{i2} \end{array} \right], \tag{49}$$

$$\left[\begin{array}{l} V_i(0) \\ V_i(L) \end{array} \right] = \left[\begin{array}{cc} 1+\rho_{i1} & 0 \\ 0 & 1+\rho_{i2} \end{array} \right] \left[\begin{array}{cc} -\rho_{i1} & e^{r_iL} \\ e^{r_iL} & -\rho_{i2} \end{array} \right]^{-1} \left[\begin{array}{l} S_{i1} \\ S_{i2} \end{array} \right], \tag{50}$$

where Z_{i0} is the characteristic impedance of the ITL. ρ_{i1} and ρ_{i2} are the reflection coefficients at the two ends of the ITL. $r_i = \sqrt{Z_i'Y_i'}$ is the propagation constant of the ITL. S_{i1} and S_{i2} can be obtained by integrating $V_{Si}'(x)$ and $I_{Si}'(x)$, which are

$$\begin{aligned} S_{i1} &= \frac{1}{2}K_1\left(Z_t'-Z_{ef}'\right)\frac{e^{(r_i+r_e)L}-1}{r_i+r_e} \\ &+\frac{1}{2}K_2\left(Z_t'+Z_{ef}'\right)\frac{e^{(r_i-r_e)L}-1}{r_i-r_e} \\ &+\frac{1}{2}K_3\left(Z_t'+Z_{ef}'\frac{jk_x}{r_e}\right)\frac{e^{(r_i-jk_x)L}-1}{r_i-jk_x}, \end{aligned} \tag{51}$$

$$\begin{aligned} S_{i2} &= \frac{1}{2}e^{r_iL}K_1\left(Z_t'-Z_{ef}'\right)\frac{e^{(r_e-r_i)L}-1}{r_e-r_i} \\ &-\frac{1}{2}e^{r_iL}K_2\left(Z_t'-Z_{ef}'\right)\frac{e^{-(r_i+r_e)L}-1}{r_i+r_e} \\ &-\frac{1}{2}e^{r_iL}K_3\left(Z_t'-Z_{ef}'\frac{jk_x}{r_e}\right)\frac{e^{-(r_i+jk_x)L}-1}{r_i+jk_x}, \end{aligned} \tag{52}$$

where $Z_{ef}' = jr_er_iS_s/\omega$, $Z_{ef}' = jr_er_iS_s/\omega$ and $k_x = k\cos\varphi\cos\psi$. When ignoring the propagation loss of the ETL and the ITL, then $Z_{ef}' = jk^2S_s/\omega$. S_s is the electrostatic shield leakage parameter of the shielded cable. Through the inverse FFT transform, the current response in the time domain can be obtained.

When the impedance of the shielded cable terminal load is Z, its power is

$$P_{\rm dBW} = 10\lg\left(i_i(t)^2\cdot Z\right). \tag{53}$$

If $P_{\rm dBW}$ exceeds the rated power of the terminal load, the terminal load will be disturbed or even damaged.

IV. EXPERIMENT

The TNSF can be simulated by a short-circuit experiment, and the traction network short-circuit

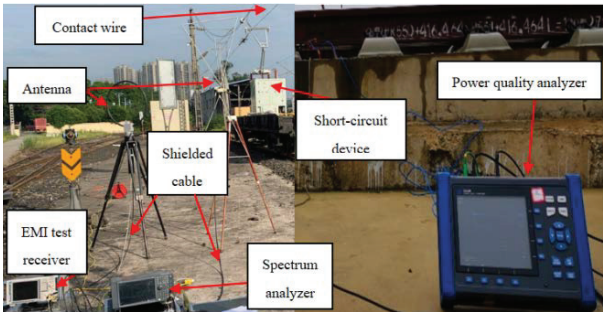

Fig. 6. The experimental site.

experiment is realized by a short-circuit device and a high-voltage circuit breaker. The short-circuit device is composed of a pantograph, a high-voltage electrical cabinet, and a short-circuit grounding shoe. It is placed at the short-circuit point to realize the connection between the contact wire and the rail. The experimental site is shown in Figure 6. The power quality analyzer (E6100) is used to test the short-circuit current. The EMI test receiver is used to test the current generated by the low-frequency magnetic field, and the spectrum analyzer is used to test the voltage generated by the high-frequency electric field. The distance from the short-circuit point to the substation is 30 m. The length of the shielded cable is 5 m, the height of the head is 1 m, and the vertical distance from the rail is 2 m. The impedance of the spectrum analyzer is 50 Ω, and the rated power is 30 dBm. The traction network short-circuit experiment process is shown in Figure 7.

Based on the actual traction network parameters, we calculate the transient current and the response of the shielded cable through the method proposed in Sections II and Section III. The calculated results are compared with the experimental results. The EMI on the terminal load is also analyzed.

A. Transient current

In the short-circuit experiment, the traction network's power supply is a direct power supply with a return line. Contact wire (CW), messenger wire (MW), return wire (RW), and rail (R) make up the majority of the traction network. These conductors are distributed in parallel. Tables 1 and Table 2 show the major parameters of the traction transformer and traction network conductors in the experiment. Figure 8 shows the traction network's spatial distribution.

The parameters of the TCM in Figure 2 can be calculated using the distance between the traction network conductors and the parameters in Tables 1 and Table 2, as shown in Table 3.

When a short-circuit fault occurs, let the initial phase angle of u_s be 0° and the duration of the short-circuit process be 0.15 s. Figure 9 shows the computed and measured values of the short-circuit current in the time domain.

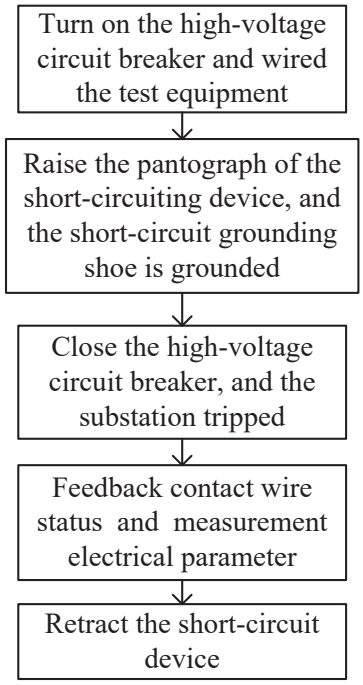

Fig. 7. Traction network short-circuit experiment process.

Table 1: Major parameters of the traction transformer

Parameters	Value
Short-circuit losses	146.49 kW
Short-circuit voltage	16.48 %
Rated voltages	220/2 × 27.5 kV
Rated current	227.27/909.08 A

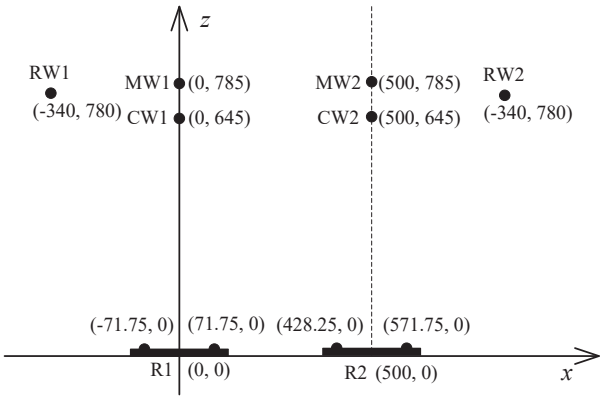

Fig. 8. Spatial distribution of traction network conductors (unit: cm).

Table 2: Major parameters of traction network conductors

Conductor	Type	DC resistance (Ω/km)	Calculate radius (cm)
CW1/ CW2	CTS-150	0.159	0.72
MW1/MW2	JTMH-120	0.242	0.70
RW1/RW2	LBGLJ-185/25	0.145	0.945
R1/ R2	P60	0.135	1.279

Table 3: Equivalent component parameters of TCM

Circuit component	Value
R_S	0.18 Ω
L_S	32 mH
R'_T	0.335 Ω/ km
L'_T	0.2944 Ω/ km
C'_T	0.0074 μF / km

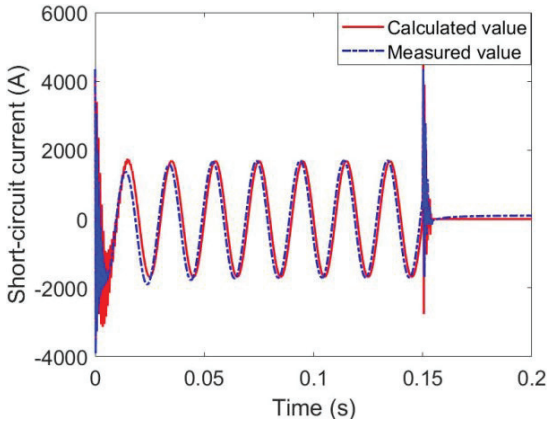

Fig. 9. Short-circuit current.

It can be seen that when a TNSF occurs, there is a small error between the calculated value and the measured value of the short-circuit current phase and amplitude. Since the actual circuit breaker has an arc extinguishing device, the calculated value is greater than the measured value. However, the waveform of the short-circuit current calculated value is in good agreement with the measured waveform. The maximum value of the short-circuit current is about 1644 A, the maximum value of the transient current is about 4351 A, and the duration of the transient process is about 0.015 s. The transient process of short-circuiting and circuit breaker opening produces a high-frequency current, and the frequency component of the measured data is more complicated due to the contingency of the arc in the actual test.

Table 4: Major parameters of shielded cable

Parameter	Value
The radius of the shield	0.37 cm
The thickness of the shield	0.127 mm
DC resistance	4.0 mΩ / m
Hole inductance	0.25 nH / m
leakage parameters	16 m /μF

Table 5: The calculated and measured value of the current response

Frequency (MHz)	Calculated value (dBμA)	Measured value (dBμA)
0.01	49.83	50.09
0.1	48.65	46.67
0.5	47.75	46.65
1	34.55	33.62
5	21.05	20.83
10	17.3	14.82
20	14.15	11.19
30	−18.66	−18.88
40	−21.69	−20.28
50	−26.60	−25.68

B. The terminal current of the shielded cable

When calculating the current response of the shielded cable, the height of the contact wire and the distance from the shielded cable head to the short-circuit point are the same as in the actual test experiment. The radius of the small circle is 0.005 m. The type of the shielded cable in the experiment is RG-214(I), and its major parameters are shown in Table 4. Both ends of the shielding layer are grounded through the antenna and the instrument casing. The impedance of the inner conductor matches the characteristic impedance of the shielded cable, which is 50 Ω.

When the incident angle, azimuth angle, and polarization angle of the electromagnetic field are, respectively, 30°, 0°, and 0°, and D_x is 10 m, the calculated and measured values of the shielded cable terminal current at some frequency points are shown in Table 5. It can be seen that the calculated values are in good agreement with the measured values, which verifies the method in this article. The higher the frequency, the smaller the current response. The value is larger when the current is below 1 MHz.

C. Analysis of EMI on terminal load

The current response of the shielded cable generates power on the shielded cable terminal load. If the power exceeds its rated power, the terminal load will be disturbed or even destroyed. We calculate the power of the shielded cable terminal load under different conditions

and analyze the EMI of the transient magnetic field generated by TNSF on the shielded cable terminal load.

Assume that the incident angle, azimuth angle, and polarization angle of the electromagnetic field are 30°, 0°, and 0°, respectively. When the distance between the shielded cable head and the short-circuit point is 7 m, 8.6 m, 10 m, and 11 m, respectively, the terminal current response of the shielded cable is shown in Figure 10 (a). The power generated by the terminal current on the spectrum analyzer is shown in Figure 10 (b). The fluctuations and discontinuities of the current waveform and power waveform in the figure are caused by the reflection of the current in the cable. It can be seen that when r_s is 8.6 m, the terminal current reaches its maximum value of 0.1879 A, and then the terminal current decreases as r_s increases. The maximum power can reach 32.33 dBm,

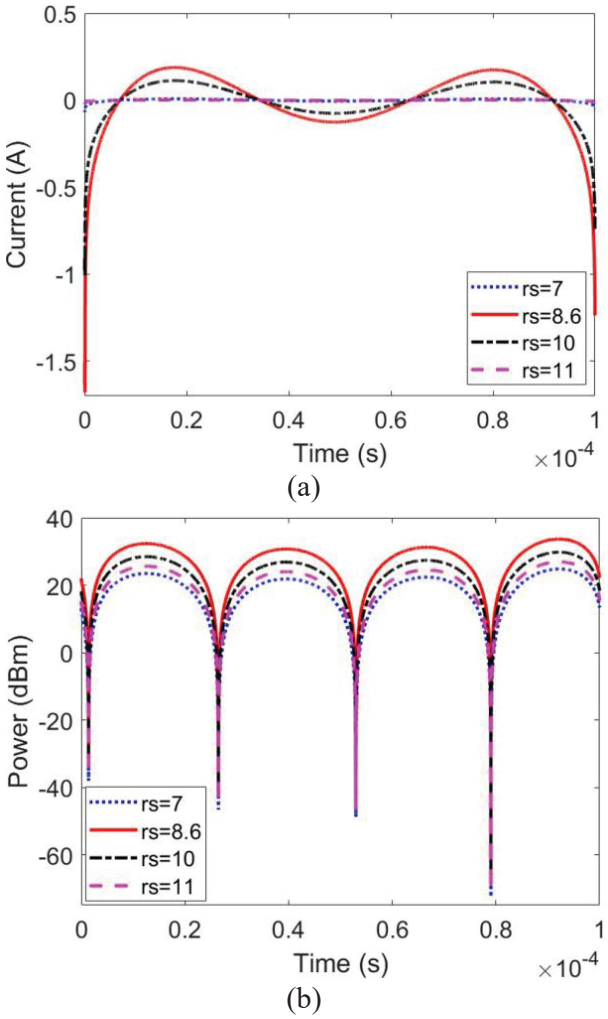

Fig. 10. (a) Terminal current of shielded cable under different r_s. (b) Spectrum analyzer power under different r_s.

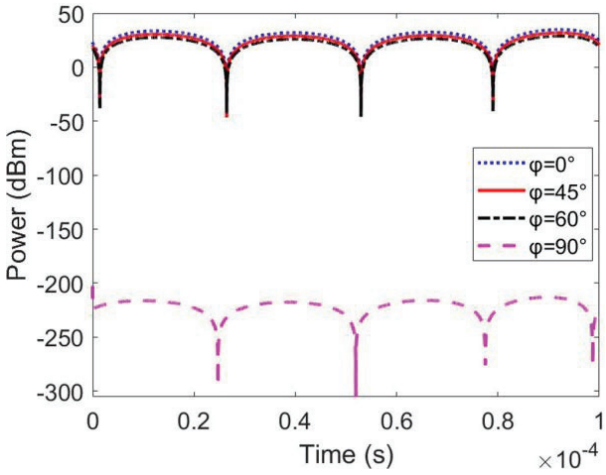

Fig. 11. Spectrum analyzer power under different incident angles.

which exceeds the rated power of the spectrum analyzer. According to equation (26), the horizontal distance between the shielded cable head and the short-circuit point must be more than 6 m to avoid damaging the spectrum analyzer.

If the distance between the shielded cable head and the short-circuit point is 8.6 m, the azimuth angle and the polarization angle are both 0°. When the incident angles are 0°, 45°, 60°, and 90°, the power of the spectrum analyzer is shown in Figure 11. It can be seen that the larger the incident angle, the smaller the terminal load power. When the incident angle is 45°, the power is 30.58 dBm, which exceeds the rated power of the spectrum analyzer. In order to avoid damage to the spectrometer, the incident angle should be greater than 45°.

If the distance between the shielded cable head and the short-circuit point is 8.6 m, the incident angle is 30°, and the polarization angle is 0°. When the azimuth angles are 0°, 45°, 60°, and 90°, the power of the spectrum analyzer is shown in Figure 12. The maximum power can reach 33.55 dBm, which also exceeds the rated power of the spectrum analyzer. The azimuth angle has less influence on the terminal load power. But when amplifying a part of the power waveform, it can be seen that the larger the azimuth angle, the smaller the power generated on the terminal load.

If the distance between the shielded cable head and the short-circuit point is 8.6 m, the incident angle is 30°, and the azimuth angle is 0°. When the polarization angles are 0° and 90°, the spectrum analyzer power generated by the terminal current is shown in Figure 13. It can be seen that, compared with the vertical polarization mode, the terminal load power in the horizontal polarization mode is smaller.

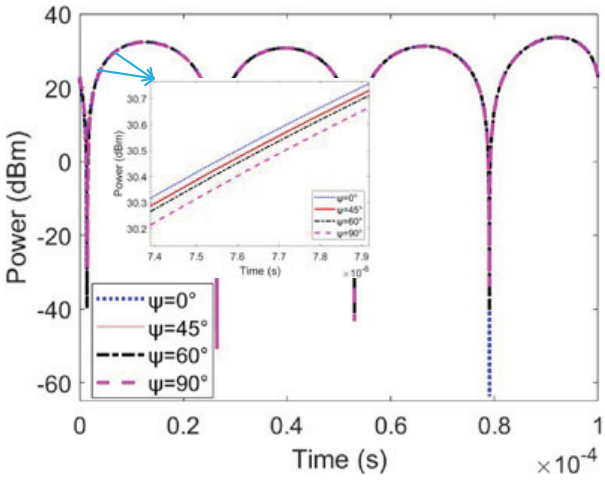

Fig. 12. Spectrum analyzer power under different azimuth angles.

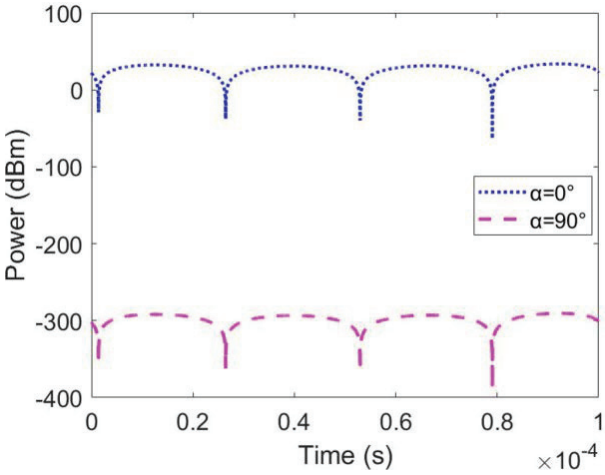

Fig. 13. Spectrum analyzer power under different polarization angles.

Fig. 14. Damaged spectrum analyzer.

Let the polarization angle be 0°, the azimuth angle be less than 90°, and the incident angle be less than 45°. We changed the relative position of the shielded cable and the short-circuit point to conduct many experiments. When the horizontal distance between the shielded cable head and the short-circuit point is about 5.3 m, the power generated by the terminal current of the shielded cable on the spectrum analyzer exceeds its rated power, which damages the RF input port of the spectrum analyzer. As shown in Figure 14.

V. CONCLUSION

1) This paper proposed a TCM for the short-circuit traction network to calculate the transient current. The model is validated by comparing the calculated and measured short-circuit current. The maximum value of transient current is about 4351 A, while the short-circuit current peaks at roughly 1644 A, and the transient process lasts about 0.015 s.
2) The TEMF was formed by the TCP caused by the TNSF. The current response of the TEMF on the shielded cable is calculated using transmission lineTL theory and verified by experiments. The horizontal distance between the shielded cable head and the short-circuit point should be greater than 6 m to avoid damaging the terminal load.
3) The change in the relative location of the shielded cable and the contact wire will cause the TEMF angle to shift. The larger the incident angle and the azimuth angle, the smaller the terminal load power will be. The azimuth angle has little effect on the terminal load power. When the polarization angle is 0°, greater power is generated on the terminal load. Therefore, to avoid damage to the terminal load, the incident angle should be greater than 45°.

ACKNOWLEDGMENT

The work was supported by National Key R&D Program of China under Grant No. 2018YFC0809500.

REFERENCES

[1] H. Xie, J. Wang, R. Fan, and Y. Liu, "A Hybrid FDTD-SPICE Method for Transmission Lines Excited by a Nonuniform Incident Wave," *IEEE Transactions on Electromagnetic Compatibility*, vol. 51, no. 3, pp. 811-817, Aug. 2009.

[2] B. X. Zhang, P. Xiao, D. Ren, and P. A. Du, "An Analytical Method for Calculating Radiated Emission of Discontinuous Penetrating Cable," *The Applied Computational Electromagnetics Society (ACES) Journal*, vol. 34, no. 01, pp. 25-32, 2021.

[3] G. Zhang, J. Bai, L. Wang, and X. Peng, "Stochastic Analysis of Multi-conductor Cables with Uncertain Boundary Conditions," *The Applied Computational Electromagnetics Society (ACES) Journal*, vol. 33, no. 08, pp. 847-853, 2021.

[4] H. Xie, J. Wang, R. Fan, and Y. Liu, "SPICE Models to Analyze Radiated and Conducted Susceptibilities of Shielded Coaxial Cables," *IEEE Transactions on Electromagnetic Compatibility*, vol. 52, no. 1, pp. 215-222, Feb. 2010.

[5] H. Xie, J. Wang, R. Fan, and Y. Liu, "SPICE Models for Prediction of Disturbances Induced by Nonuniform Fields on Shielded Cables," *IEEE Transactions on Electromagnetic Compatibility*, vol. 53, no. 1, pp. 185-192, Feb. 2011.

[6] S. R. Huang, Y. L. Kuo, B. N. Chen, K. C. Lu, and M. C. Huang, "A short-circuit current study for the power supply system of Taiwan railway," *IEEE Transactions on Power Delivery*, vol. 16, no. 4, pp. 492-497, Oct. 2001.

[7] X. Tian, X. Li, and Y. Li, "Current Waveform Feature and Fault Identification for Overhead Contact Line in Electrified Railway," 2010 International Conference on Electrical and Control Engineering, 2010, pp. 3516-3519.

[8] C. Tejada, P. Gomez, and J. C. Escamilla, "Computation of Radio Interference Levels in High Voltage Transmission Lines with Corona," *IEEE Latin America Transactions*, vol. 7, no. 1, pp. 54-61, March 2009.

[9] T. Lu, Y. Zou, H. Rao, and Q. Wang, "Analysis of electromagnetic radiation from HVAC test transmission line due to corona discharge," Digests of the 2010 14th Biennial IEEE Conference on Electromagnetic Field Computation, 2010, pp. 1-1.

[10] V. Šmidl, Š. Janouš, and Z. Peroutka, "Improved Stability of DC Catenary Fed Traction Drives Using Two-Stage Predictive Control," *IEEE Transactions on Industrial Electronics*, vol. 62, no. 5, pp. 3192-3201, May 2015.

[11] Y. X. Sun, Q. Li, W. H. Yu, Q. H. Jiang, and Q. K. Zhuo, "Study on Crosstalk Between Space Transient Interference Microstrip Lines Using Finite Difference Time Domain Method." *The Applied Computational Electromagnetics Society (ACES) Journal*, vol. 30, no. 08, pp. 891-897, 2021.

[12] Z. Liu, G. Zhang and Y. Liao, "Stability Research of High-Speed Railway EMUs and Traction Network Cascade System Considering Impedance Matching," *IEEE Transactions on Industry Applications*, vol. 52, no. 5, pp. 4315-4326, Sept.-Oct. 2016.

[13] R. Ianconescu and V. Vulfin, "Simulation and theory of TEM transmission lines radiation losses," 2016 IEEE International Conference on the Science of Electrical Engineering (ICSEE), 2016, pp. 1-4.

[14] P. Taheri, B. Kordi and A. M. Gole, "Electric field radiation from an overhead transmission line located above a lossy ground," 2008 43rd International Universities Power Engineering Conference, 2008, pp. 1-5.

[15] Q. Jin, W. Sheng, C. Gao, and Y. Han, "Internal and External Transmission Line Transfer Matrix and Near-Field Radiation of Braided Coaxial Cables," *IEEE Transactions on Electromagnetic Compatibility*, vol. 63, no. 1, pp. 206-214, Feb. 2021.

[16] H. Lu, F. Zhu, Q. Liu, X. Li, Y. Tang, and R. Qiu, "Suppression of Cable Overvoltage in a High-Speed Electric Multiple Units System," *IEEE Transactions on Electromagnetic Compatibility*, vol. 61, no. 2, pp. 361-371, April 2019.

[17] C. D. Taylor, R. S. Satterwhite, and C. W. Harrison, "The response of a treminated two-wire transmission line excited by a nonuniform electromagnetic field," *IEEE Trans. Antennas Propag.*, vol. AP-13, no. 6, pp. 987-989, Nov. 1965.

[18] A. K. Agrawal, H. J. Price, and S. H. Gurbaxani, "Transient response of multiconductor transmission lines excited by a nonuniform electromagnetic field," *IEEE Trans. Electromagn. Compat.*, vol. 22, no. 2, pp. 119-129, May 1980.

[19] F. Rachidi, "Formulation of the field-to-transmission line coupling equations in terms of magnetic excitation fields," *IEEE Trans. Electromagn. Compat.*, vol. 35, no. 3, pp. 404-407, Aug. 1993.

[20] F. Rachidi, "A Review of Field-to-Transmission Line Coupling Models With Special Emphasis to Lightning-Induced Voltages on Overhead Lines," *IEEE Transactions on Electromagnetic Compatibility*, vol. 54, no. 4, pp. 898-911, Aug. 2012.

[21] X. Li, F. Zhu, H. Lu, R. Qiu, and Y. Tang, "Longitudinal Propagation Characteristic of Pantograph Arcing Electromagnetic Emission With High-Speed Train Passing the Articulated Neutral Section," *IEEE Transactions on Electromagnetic Compatibility*, vol. 61, no. 2, pp. 319-326, April 2019.

[22] M. Štumpf, "Pulsed EM Plane-Wave Coupling to a Transmission Line Over Orthogonal Ground Planes: An Analytical Model Based on EM Reciprocity," *IEEE Transactions on Electromagnetic Compatibility*, vol. 63, no. 1, pp. 324-327, Feb. 2021.

[23] B. van Leersum, J. van der Ven, H. Bergsma, F. Buesink, and F. Leferink, "Protection Against Common Mode Currents on Cables Exposed to HIRF or NEMP," *IEEE Transactions on Electromagnetic Compatibility*, vol. 58, no. 4, pp. 1297-1305, Aug. 2016.

[24] J. R. Carson, "Wave propagation in overhead wires with ground return," *The Bell System Technical Journal*, vol. 5, no. 4, pp. 539-554, Oct. 1926.

[25] G. S. Lin and Q. Z. Li, "Impedance Calculations for AT Power Traction Networks with Parallel Connections," 2010 Asia-Pacific Power and Energy Engineering Conference, 2010, pp. 1-5.
[26] Y. G. Li, ATP-EMTP and its application in power systems. Beijing, China:China Electric Power Press, 2016.
[27] F. M. Tesche, Plane Wave Coupling to Cables. New York, USA: Academic Press, 1995.
[28] E. F. Vance, Coupling to Shielded Cables. R. E. Krieger, Melbourne, FI, 1987.
[29] B. J. Zhang, G. Wang, L. Duffy, A. Liu, and T. Shao, "Comparison of Calculation Methods of Braided Shield Cable Transfer Impedance Using FSV Method, " *The Applied Computational Electromagnetics Society (ACES) Journal*, vol. 30, no. 02, pp. 140-147, 2021.
[30] F. M. Tesche, and T. K. Liu, "Application of Multiconductor Transmission Line Network Analysis to Interaction Problems, " *Electromagnetics*, vol. 6, no. 1, pp. 1-20, 1986.

Yingchun Xiao was born in Gansu Province, China, in 1990. She received the B.S. degree in electronic information science and technology from the Lanzhou University of Technology, Lanzhou, China, in 2012, and is currently working toward the Ph.D. degree in electrical engineering at with Southwest Jiaotong University, Chengdu, China. At the same time, she is a lecturer Lecturer at with Lanzhou City College.

Her research interests include electromagnetic environment test and evaluation, electromagnetic compatibility analysis and design, and identification and location of electromagnetic interference sources.

Feng Zhu received the Ph.D. degree in railway traction electrification and automation from the Southwest Jiaotong University, Sichuan, China, in 1997.

He is currently a Full Professor with the School of Electrical Engineering, Southwest Jiaotong University.

His current research interests include locomotive over-voltage and grounding technology, electromagnetic theory and numerical analysis of electromagnetic field, and electromagnetic compatibility analysis and design.

Shengxian Zhuang received the M.S. and Ph.D. degrees from Southwest Jiaotong University and the University of Electronic Science and Technology of China in 1991 and 1999, respectively.

He is currently working with the School of Electrical Engineering at, Southwest Jiaotong University as a Professor. He got his M.S and Ph.D degrees, respectively, at Southwest Jiaotong University and the University of Electronic Science and Technology of China in 1991 and 1999. From 1999 to 2003, he did postdoctoral research at Zhejiang University and Linkoing University of Sweden. He was a visiting Professor at with Paderborn University in Germany in 2005 and at with the University of Leeds, U.K., in 2017.

His research interests include power conversion for sustainable energies, motor control and drive systems, power electronics and systems integration, and modeling, diagnosis, and suppression of electromagnetic interference of power electronic converters.

Yang Yang was born in Shanxi, China on April 19, 1989. She received her the bachelor's degree in measurement and control technology and instrumentation from the Shaanxi University of Science and Technology in 2011 and her the master's degree in control theory and control engineering from Northwestern Polytechnical University in 2014. She is currently working toward a the Ph.D. degree in electrical engineering at with Southwest Jiaotong University, Chengdu, China.

Her research interests include electromagnetic environment testing and evaluation, electromagnetic compatibility analysis and design, and electromagnetic compatibility problems in the field of railway power supply and rail transit.

Analysis of Symmetric Two and Four-coil Magnetic Resonant Coupling Wireless Power Transfer

Azuwa Ali[1], Mohd Najib Mohd Yasin[2], Ali Hanafiah Rambe[3], Ismahayati Adam[2], Nurulazlina Ramli[4], Hasliza A. Rahim[2], Thennarasan Sabapathy[2], Mohd Natashah Norizan[2], and Sharizal A. Sobri[5]

[1]Faculty of Electrical Engineering Technology, Universiti Malaysia Perlis, Pauh Putra Campus, 02600 Arau, Perlis, Malaysia
azuwa@unimap.edu.my

[2]Faculty of Electronic Engineering Technology, Universiti Malaysia Perlis (UniMAP), Pauh Putra Campus, 02600 Arau, Perlis, Malaysia
najibyasin@unimap.edu.my, ismahayati@unimap.edu.my, haslizarahim@unimap.edu.my, thennarasan@unimap.edu.my mohdnatashah@unimap.edu.my

[3]Department of Electrical Engineering, Universitas Sumatera Utara, Medan, Indonesia
ali3@usu.ac.id

[4]Faculty of Engineering and the Built Environment (FoEBE), SEGI University, Kota Damansara, 47810 Petaling Jaya, Selangor, Malaysia
azlinaramli@segi.edu.my

[5]Advanced Material Research Cluster, Faculty of Bioengineering and Technology, Universiti Malaysia Kelantan, Jeli Campus, 17600 Jeli, Kelantan, Malaysia
sharizal.s@umk.edu.my

Abstract – This study examined the efficiency of power transfer for two-coil and four-coil spiral magnetic resonant coupling wireless power transfer (WPT) using distance to coil diameter (D/d_m) ratio and reflection coefficient, S_{21} value. Adding resonators reduced the total resistance in the two-coil WPT system while increasing the S_{21} values of the whole system. A same-size spiral coil was proposed for the system and simulated using computer simulation technology (CST). A prototype with similar specifications for a four-coil design was implemented for verification. The proposed method yielded an optimal efficiency of 76.3% in the four-coil system, while the two-coil WPT yielded a 23.2% efficiency with a 1.33 D/d_m ratio.

Index Terms – Two-coil, four-coil, resonator, wireless power transfer.

I. INTRODUCTION

The wireless power transfer (WPT) technology uses a physical electromagnetic field to transmit energy. WPT was initiated by Nikola Tesla between 1891 and 1904. Tesla's WPT generated high alternating current using inductive coupling. In his experiment, Tesla lit three lamps at a 100-ft transfer distance using "Tesla Tower" [1]. Today, WPT is highly sought after for charging small electronic devices.

In 2007, the Massachusetts Institute of Technology (MIT) powered a 60-W light bulb ata 2-m distance from a transmitting coil via WPT [2]. This technology continued to expand in 2012 as the US Transportation Department used WPT to charge vehicles on railways and highways [4]. Studies on WPT are undertaken across many countries, particularly in the US, South Korea, China, and Japan [3, 4]. The ever-increasing demand for modern electronic devices (e.g., electric vehicles, mobile phones, and smart watches) becomes a driver for WPT, especially after its adoption for multiple applications.

Despite its high demand, WPT cannot transfer power over a long distance. Deterioration of power transfer efficiency (PTE) when distances exceed the coil diameter [21, 23]. This drawback may be resolved by incorporating an impedance matching network or inserting more loops except for a bulky outlook [2].

This study assessed the PTE of magnetic resonant coupling (MRC) WPT using two-coil and four-coil systems of the same size but without variable impedance matching. This MRC system consisted of

Submitted On: August 31, 2021
Accepted On: April 18, 2022

https://doi.org/10.13052/2022.ACES.J.370415

two independent coils,i.e., receiver and transmitter resonating together. Both coils were wirelessly separated by air. Identifying the attributes of the magnetic field was essential since MRC depended on the magnetic coupling. Specifically, the magnetic field would substantially affect the coupling coefficient, mutual inductance, and, eventually, the overall MRC performance.

Apart from the design and shape, adding a resonator to each of the two coils was essential to enhance the system's efficiency [22, 24]. Adding two or multiple resonators generated a magnetic field and flux distribution of higher values, thus affecting system efficiency. A circular spiral coil shape was selected [7, 11, 13, 14, 20] in this study due to its exceptional performance. With less resistance,this spiral coil improved the mutual inductance value. Adding a resonator to the transmitter and receiver would increase the intensity of the magnetic field MRC, improving the power transfer capability. Enhancing the power transfer capability would increase the coverage of effective distance. Recognizing the importance of embedding a resonator to MRC, this study incorporated two and four spiral coils to assess their effects on MRC performance based on S_{21} values using via computer simulation and experimental validation.

II. MUTUAL INDUCTANCE, REFLECTION, AND TRANSMISSION COEFFICIENT

Mutual inductances happen when the magnetic flux from a transmitter coil cuts across the receiver coil to induce the voltage and current in the receiver coil. In some cases, the leakage inductance exceeds the mutual inductance in a loosely coupled system, reducing the magnetizing flux [1, 3].

Figure 1 shows the resonant coupled four-coil system as an analogous circuit model using lumped parameters (L_i, C_i, and R_i). The interactions of the transmitter and receiver coils are the most crucial for power transfer, and the efficiency is virtually determined by the distance between them. When all four coils resonate together, their inductive and capacitive reactance become equal, allowing the receiver coil to cut the oscillating field created in the transmitter coil sufficiently to transmit the power to the load. Therefore, the mutual inductance, M, and the coupling coefficient, k, are related by following equation:

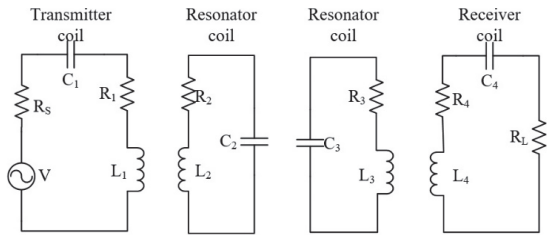

Fig. 1. The equivalent circuit model of a four-coil system.

$$M = kvL_1L_4, \tag{1}$$

where L_1 is the inductance of the receiver coil and L_4 is the inductance of the transmitter coil. Higher M means higher efficiency of the MRC. Meanwhile, the reflection coefficient, S_{11}, denotes the amount of power reflected from the receiver to the transmitter, whereas the transmission coefficient, S_{21}, signifies the amount of power transmitted to the receiver from the transmitter. Therefore, a lower return loss generates a higher S_{21} and promotes more power transfer.

The S_{21} parameter [eqn(2)] below is used to compute PTE

$$S_{21}\text{dB} = 20\log S_{21}, \tag{2}$$

$$n_{21} = S_{21}^2 \times 100\%. \tag{3}$$

Eqn (2) denotes S_{21} in dB value but converted to percentage in eqn (3) to compare performance. Therefore, this study measured S_{21}, inductance, and k of the system for investigating the performance of MRC with two-coil and four-coil WPTs. Several methods are used to determine inductance. They include Maxwell formula, Grover's method, Neumann's integrals, and finite element analysis (FEA) [1].

Several authors [3] attempted to derive accurate equations for$k$, yielding complicated formulas due to the complexity of the coupling mechanism in multi-turn structure [1, 3]. In general, knowing the frequency range of the application is crucial. At very low frequencies, the capacitive (electric) coupling also affects k [2]. Thus, a full-wave simulation remains essential for predicting the whole system's performance even though$M$ and $k$could be computed [using eqn(1)–(3)].

In this study, two software packages were used. The first was the FEA software known as An soft Maxwell (version x, name of developer, country). It determined k and M. The second one was the computer simulation technology (CST) software (version x, name of developer, country). It determined the S_{21} value. These software packages were used to model the MRC for the two-coil and four-coil in simulation in a three-dimensional (3D) environment. The FEA software was chosen because this technique did not require complex manual calculation while yielding consistent and reliable outputs for different types of systems.

III. METHODOLOGY

The comparative study impact of resonator on the performance of WPT was compared using An soft Maxwell. This software assessed the coupling factor effect on the WPT system. Figure 2 shows the plane view of the coil design for the two-coil and four-coil systems.

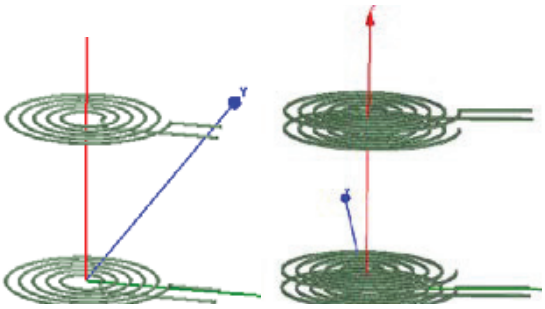

Fig. 2. The simulation of two-coil and four-coil systems using Ansoft Maxwell.

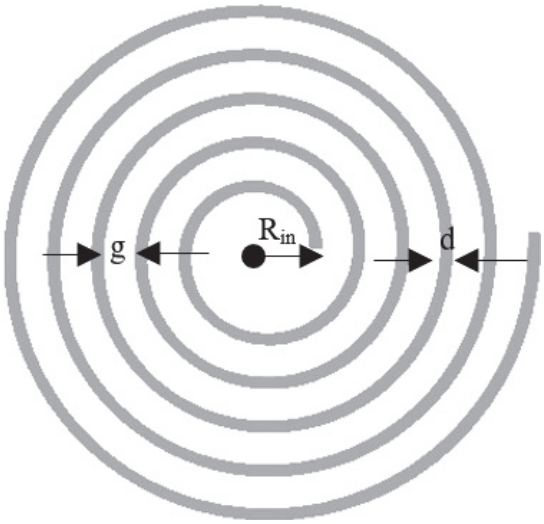

Fig. 3. The proposed geometry of the spiral coil.

Table 1 gives the specifications upon which coils were designed.

The radius of the wire and the coil thickness followed the exact Litz wire for small applications. Following the study of [11], no additional capacitor was added to tune the frequency of these coils for simultaneous resonance. PTE was compared with the CST software to assess the resonators' performance.

Figure 3 shows the geometry of the spiral coil geometry based on the parameters of Table 1 parameter use Litz wire as the coil prototype. Figure 4 shows the

Table 1: The proposed coil parameters for the simulation

Coil parameter (cm)	
Wire diameter, d	0.1
Coil progress/gap, g	0.4
Inner radius, R_{in}	0.5
Number of turns, n	5

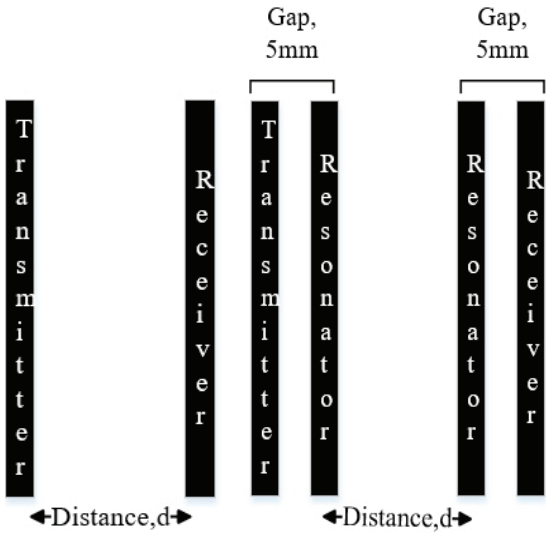

Fig. 4. The distance measurement for the two-coil and four-coil systems.

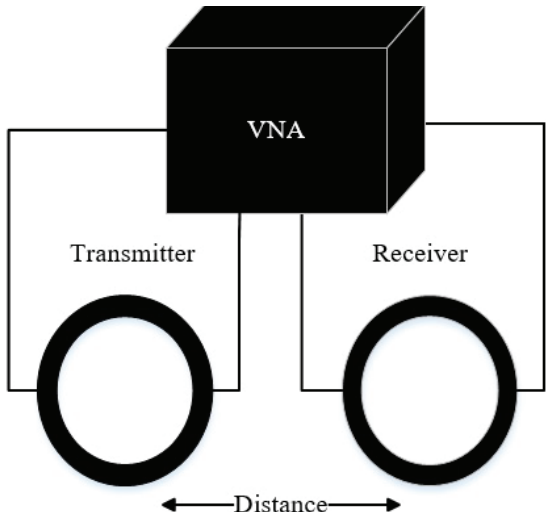

Fig. 5. The measurement setup.

distance measurements for the two- and four-coil systems for simulations and experiments. For the four-coil system, the distance was measured from the transmitter's resonator to the receiver's resonator. The distance between the coils and the resonator for the transmitter and receiver was set at a maximum of 5 mm, and the distance varied from 5 to 7cm.

Figure 5 shows the measurement setup for the experiments. The vector network analyzer (VNA) was connected to the transmitter and receiver for measuring S_{11} and S_{21}.

The distance from the receiving to the transmitting coils was altered manually. Values of S_{21} were recorded

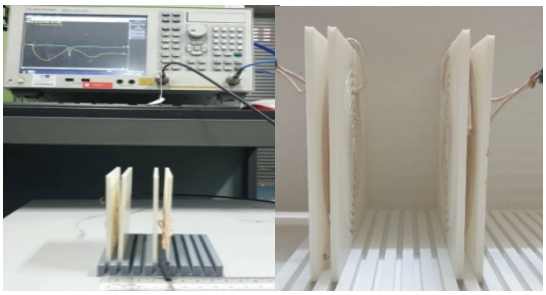

(a) (b)

Fig. 6. The measurement setup for the four-coil MRC.

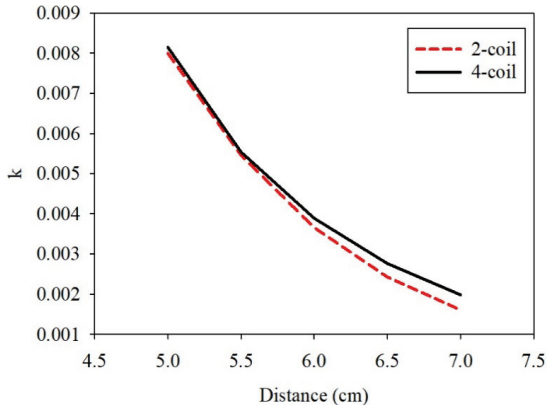

Fig. 7. Comparison of the coupling coefficient (k) for the two-coil and four-coil WPTs.

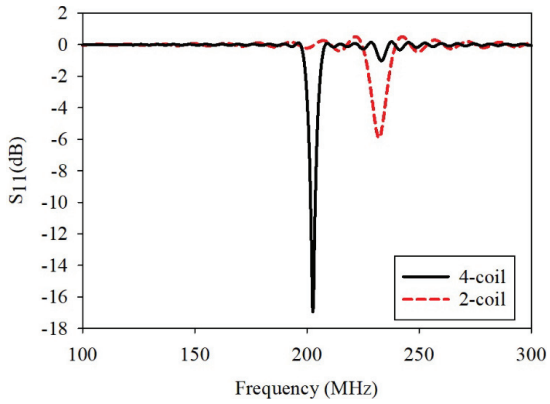

Fig. 8. The S_{11} parameter.

based on the distance variation. The performance of each system was experimentally evaluated using the setup of Figure 6.

IV. RESULTS AND DISCUSSION

Figure 7 shows the simulation of k for the two- and four-coil WPTs based on eqn (1). The values of

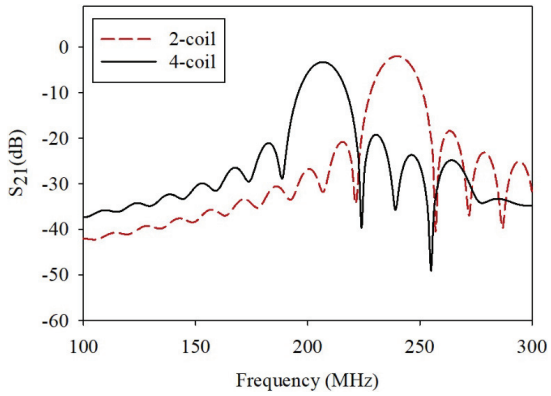

Fig. 9. S_{21} parameter.

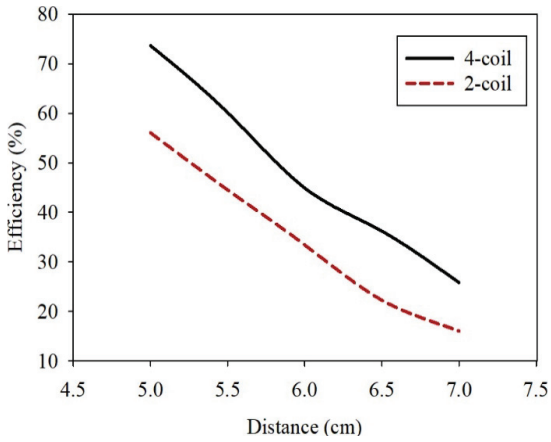

Fig. 10. Simulation results of the two-coil and four-coil systems.

k decreased exponentially when the distance increased. In general, the four-coil WPT performed better than the two-coil WPT.

The two-coil system results served as reference values to compare the improvement before and after incorporating the resonator. The CST material was composed of pure copper. The distance varied from 5 to 7 cm with a 0.5-cm increment.

Figures 8 and 9 show the simulation values of S_{11} and S_{21} for the two- and four-coil systems, respectively. In general, the four-coil WPT performed better than the two-coil system.

Figure 10 shows the simulation outcomes for both systems,yielding a 25.8% efficiency for the four-coil and a 16.0% efficiency for the two-coil system at a 7-cm distance. The four-coil system's efficiency increased by 9.8%, indicating that the resonator coil had enhanced the performance of the MRC system.

An experimental model was built to verify the accuracy of modeling. The coil was measured using VNA,

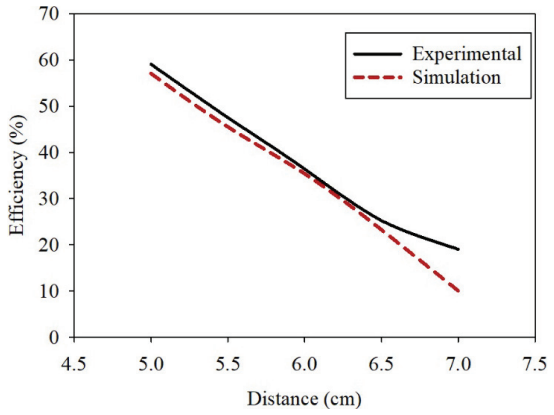

Fig. 11. Simulation and experimental results for the two-coil system.

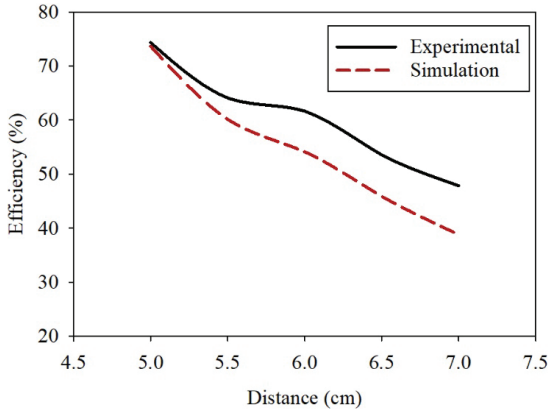

Fig. 12. Simulation and experimental results for the four-coil system.

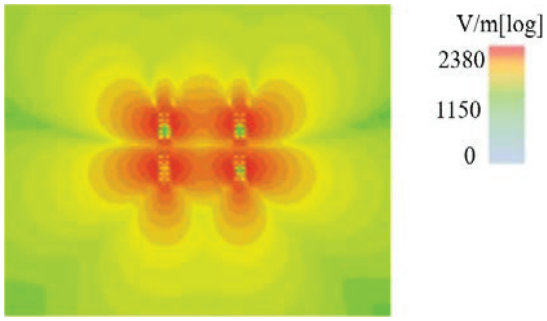

Fig. 13. The cross-sectional distribution of the electric field (E-field) at a 5-cm distance.

and the S_{21} value was recorded. The efficiency performance plotted against distance is illustrated in Figures 11 and 12 which show the efficiency performance versus the distance for the two- and four-coil systems, respectively. The system's efficiency improved by 24% when

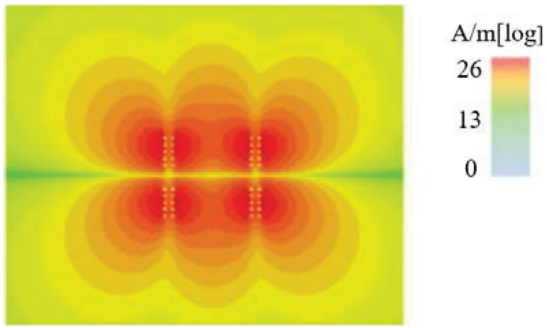

Fig. 14. The cross-sectional distribution of the magnetic field (H-field) at a 5-cm distance.

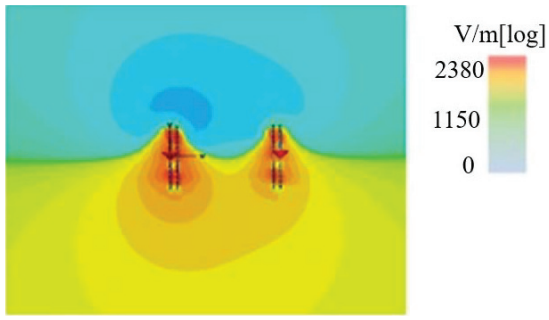

Fig. 15. The cross-sectional distribution of the electric field (E-field) view at a 7-cm distance.

the four-coil WPT was used. The efficiency exceeded 50% at a 6.5-cm distance, indicating that this design performed better even when the distance exceeded the coil size. This design performed better than several other systems (Table 2). In general, the efficiency deteriorates rapidly, not exceeding 0% if the ratio of distance (D) to coils is higher than the coil diameter, d_m [13]. Thus, PTE decreased substantially when $D>d_m$.

The coil used in the simulation consisted of copper, while the Litz wire was used in the experimental validation. Consequently, the simulation and the actual measurements varied slightly. A higher PTE for a longer distance was probably because the Litz wire could reduce the skin effect [11, 13], increasing the magnetic field.

Figures 13 and 14 show the cross-sectional distribution of the electric field (E-field) and magnetic field (H-field) of the four-coil system, respectively, based on the CST simulation at a 5-cm distance. Strong E-field and H-field were distributed and concentrated near the transmitter and receiver coils with the resonator.

Figures 15 and 16 show the cross-sectional distribution of the E-field and H-field of the four-coil system, respectively, based on the CST simulation at a 7-cm distance. A lower distribution of E-field and H-field indicated weak or low PTE.

Table 2: Comparison of the proposed design with related previous works

No	**Efficiency and distance**, D(cm)	**Coil type and size**, d_m (cm)	**Resonator type and size**, d_m (cm)	D/d_m	**Advantages/ Shortcoming**
1. (J. Zhang & Cheng, 2016)	30 cm distance with 55% PTE	Helical, 11 turns, 31.5	Helical, 11 turns, 31.5	D/d_m = 0.95	Big, bulky design
2. (Chung, Lee, Kang, & Park, 2016)	25cm distance with 80% PTE	Helical, 30	Helical, 30	D/d_m = 0.833	Resonator position varies to 15cm and 25cm from the transmitter PTE value not mentioned
3. (Dang & Qahouq, 2015)	50 cm distance with 85% PTE	Spiral, 10 turns, 40	Spiral, 10 turns, 40	D/d_m = 1.25	Big design
4. (Moghadam & Zhang, 2016)	100cm distance with 60% PTE	Planarized, 14	Planarized, 60	D/d_m = 1.67	Big design
5. (Jonah, Member, Georgakopoulos, & Member, 2013)	10 cm distance with 56.4% PTE	Circular copper, 10	Circular copper, 10	D/d_m = 1	Vary the position of resonator
6. (C. Zhang, Zhong, Liu, & Hui, 2014)	60cm distance with resonator in the middle 53.1% PTE, closer to receiver coil 69.3% PTE	Helical, 11 turns, 30	Helical, 11 turns, 30.	D/d_m = 2	Big, bulky design Resonator position 0.38 cm near to receiver coil
7. (Jolani, Chen, & Yu, 2015)	10cm distance with 83% PTE	Planar rectangular spiral, 2 turns, 5.9	Planar rectangular spiral, 5.9	D/d_m=1.67	3-layer planar resonator and loaded with capacitor
8. (Liu & Wang, 2016)	45 cm distance with 51.3% PTE	Helical, 11 turns, 11	Helical, 11 turns, 11	D/d_m = 4	Resonator position in the middle of transmitter and receiver. Big, bulky design with wire height 5.8cm
9. (Chin, Chung, Shuenn, Soon, &Lih, 2017)	1 cm distance with 19.1% PTE	Printed spiral coil, 3 turns, 0.5	Helical, 3 turns,0.5	D/d_m = 2	Efficiency is very low Bulky design Wireless implantable application
10. (Chen & Zhang, 2015)	15.2 cm distance with 70% PTE	Spiral, 10 turns, 5.5	Spiral, 10 turns, 12.5	D/d_m=1.22	Big design
11. This work	7 cm distance with 76.34% PTE	Spiral, 5 turns Transmitter= Receiver= 5	Spiral, 5 turns Resonator= 5	D/d_m=1.4	Same size of transmitter, receiver and resonator Resonator position is close to transmitter and receiver

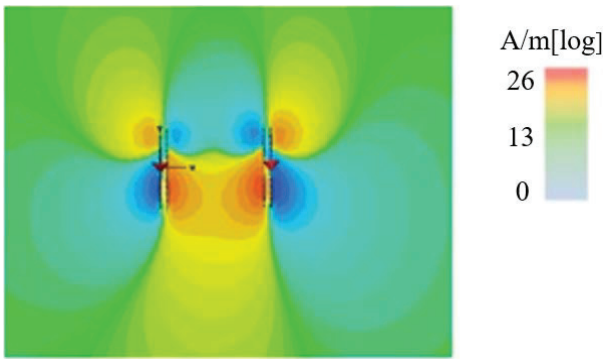

Fig. 16. The cross-sectional distribution of the magnetic field (H-field) view at a 7-cm distance.

The distance as a ratio of the coil diameter using the proposed design was 1.33 higher than the experimental result in the ratio (Table 2). The studies of [8] and [10] also yielded a higher ratio, but their bulky design was unsuitable for WPT applications. Likewise, the study of [11] yielded a higher ratio,but the system was optimized with a capacitor-loaded WPT with the resonator placed between the transmitter and receiver coils in [6]. Such an implementation is impractical for the actual application. By contrast, in this study, no capacitor was added to reduce the complexity in hardware implementation, thus yielding a small and compact design. Besides, both resonator coils in this study were similar in size, with the transmitter and receiver coils positioned close to both receiver and transmitter coils. The results appeared promising,with a consistent resonant frequency recorded despite the varied distance, along with improved PTE.

V. CONCLUSION

The design proposed in this study suits the MRC WPT concept with additional benefits in size and simplicity. This study recorded MRC WPT with a high PTE of 76.3% at a transfer distance exceeding 1.33 times the coil diameter. Overall,incorporating a resonator increased the PTE efficiency,enhancing the distance beyond the coil diameter, particularly when compared with the two-coil system.

ACKNOWLEDGMENT

This study was supported by Universiti Malaysia Perlis (UniMAP) and the Ministry of Higher Education (MoHe) under a Grant Number FRGS 9003-00850 (FRGS/1/2020/ICT09/UNIMAP/02/3).

REFERENCES

[1] N. Tesla, "The transmission of electrical energy without wires as a means for furthering peace," *Electrical World and Engineer*, pp. 21, 2005.

[2] L. Sun, D. Ma, and H. Tang, "A review of recent trends in wireless power transfer technology and its applications in electric vehicle wireless charging," *Renewable and Sustainable Energy Reviews*, vol. 91, pp. 490-503, 2018.

[3] H. Wang and X. Li, "Review and research progress of wireless power transfer for railway transportation," *Transactions on Electrical and Electronic Engineering (IEEJ),* vol. 4, no. 14, pp. 475-484, 2019.

[4] A. B. D. Arthur, "Review and evaluation of wireless power transfer (WPT) for electric transit applications," *FTA Report No. 0060*; FTA-0060, 2018.

[5] X. Chen and G. X. Zhang, "Middle range wireless power transfer systems with multiple resonators," *Journal of Central South University*, vol. 22, no. 6, pp. 2127-2136, 2015.

[6] C. Y. Do, C. Y. Lee, H. Kang, and Y. G. Park, "Design considerations of superconducting wireless power transfer for electric vehicle at different inserted resonators," *IEEE Transactions on Applied Superconductivity*, vol. 26, no. 4, pp. 1-5, Jun. 2016.

[7] Z. Dang and J. A. A. Qahouq, "Range and misalignment tolerance comparisons between two-coil and four-coil wireless power transfer systems," *Applied Power Electronics Conference and Exposition (APEC)IEEE*, pp. 1234-1240, 2015.

[8] M. R. V. Moghadam and R. Zhang, "Multiuser wireless power transfer via magnetic resonant coupling: performance analysis, charging control, and power region characterization," *IEEE Transactions on Signal and Information Processing over Networks*, vol. 2, no. 1, pp. 72-83, 2016.

[9] O. Jonah, S. Member, S. V. Georgakopoulos, and S. Member, "Wireless power transfer in concrete via strongly coupled magnetic resonance," *IEEE Transactions on Antennas and Propagation*, vol. 61, no. 3, pp. 1378-1384, 2013.

[10] C. Zhang, W. Zhong, X. Liu, and S. Y. R. Hui,, "A fast method for generating time-varying magnetic field patterns of mid-range wireless power transfer systems," *IEEE Transactions on Power Electronics*, vol. 30, no. 3, pp. 1513-1520, 2015.

[11] F. Jolani, Z. Chen, and Y. Yu, "Enhanced planar wireless power transfer using strongly coupled magnetic resonance," *Electronics Letters*, *51*(2), vol. 13, pp. 1648-1651, 2014.

[12] X. Liu and G. Wang, *Senior Member, IEEE,* "A novel wireless power transfer system with double intermediate resonant coils," *IEEE Transactions on*

Industrial Electronics, vol. 63, no. 4, pp. 2174-2180, 2016.

[13] C. Yang, C. Chang, S.-Y. S. Chang, and L. Chiou, "Efficient four-coil wireless power transfer for deep brain stimulation," *IEEE Transactions on Microwave Theory and Techniques*, vol. 65, no. 7, 2017.

[14] X. Chen and G. X. Zhang, "Middle range wireless power transfer systems with multiple resonators," *Journal of Central South University*, vol. 22, pp. 2127-2136, 2015.

[15] N. J. Grabham, Y. Li, L. R. Clare, B. H. Stark, and S. P. Beeby, "Fabrication techniques for manufacturing flexible coils on textiles for inductive power transfer," *IEEE Sensors Journal*, vol. 18, no. 6, pp. 2599-2606, 2018.

[16] D. Kim, J. Kim, and Y. Park, "Optimization and design of small circular coils in a magnetically coupled wireless power transfer system in the megahertz frequency," *IEEE Transactions on Microwave Theory and Techniques*, vol. 64, no. 8, pp. 2652-2663, 2016.

[17] T. Mizuno, T. Ueda, S. Yachi, R. Ohtomo, and Y. Goto', "Dependence of efficiency on wire type and number of strands of litz wire for wireless power transfer of magnetic resonant coupling," *IEEJ Journal of Industry applications*, vol. 3, pp. 35-40, 2014.

[18] B. H. Waters, B. J. Mahoney, G. Lee, and J. R. Smith, "Optimal coil size ratios for wireless power transfer applications," *IEEE International Symposium on Circuits and Systems (ISCAS)*, pp. 2045-2048, 2014.

[19] J. P. K. Sampath and A. Alphonesand Hitoshi Shimasaki, "Coil design guidelines for high efficiency of wireless power transfer (WPT)," *IEEE Region 10 International Conference TENCON*, pp. 726-729, 2016.

[20] M. A. Houran, X. Yang, and W. Chen, "Magnetically coupled resonance WPT?: Review of compensation topologies, resonator structures with misalignment, and EMI diagnostics," *Electronics* vol. 7, no. 11, pp. 296, 2018.

[21] S. Y. R. Hui, W. Zhong, and C. K. Lee, "A critical review of recent progress in mid-range wireless power transfer," *IEEE Trans. Power Electron.*, vol. 29, no. 9, pp. 4500-4511, 2013.

[22] A. Kurs, A. Karalis, R. Moffatt, J. D. Joannopoulos, P. Fisher, and M. Solja, "Wireless power transfer via strongly coupled magnetic resonances," *Science*, vol. 317, pp. 83-86, 2017.

[23] D. Seo, "Comparative analysis of two- and three-coil WPT systems based on transmission efficiency," *IEEE Access*, vol. 7, pp. 151962-151970, 2019.

[24] X. Zhang, S. L. Ho, and W. N. Fu, "Quantitative design and analysis of relay resonators in wireless power transfer system," *IEEE Transactions on Magnetics*, vol. 48, no. 11, pp. 4026-4029, 2012.

Azuwa Ali received B.Eng. degree in electrical and electronic engineering (Computer System) in 2004 from Universiti Teknologi Petronas (UTP) and the master's degree in electrical electronic engineering (communication & computer) in 2007 from Universiti Kebangsaan Malaysia (UKM).

She is a Lecturer with the Faculty of Electrical Engineering Technology, Universiti Malaysia Perlis (UniMAP). Her current research work includes the development of renewable harvesting system and wireless communication.

Mohd NajibMohd Yasin United Kingdom, and the Ph.D. degree from the University of Sheffield, Sheffield, U.K., in 2007 and 2013, respectively.

Since 2013, he has been a Lecturer withthe Faculty of Electronic Engineering Technology, Universiti Malaysia Perlis (UniMAP). His research interests include computational electromagnetics, conformal antennas, mutual coupling, wireless power transfer, array design, and dielectric resonator antennas.

Ali Hanafiah Rambe (Member, IEEE) was born in Medan, Sumatera Utara, Indonesia, in 1978. He received the bachelor's degree in telecommunication engineering from Universitas Sumatera Utara (USU), in 2003, the master's degree from the University of Indonesia, in 2008, and the Ph.D. degree from USU, in 2014.

He is currently a Lecturer and a Researcher with the Department of Electrical Engineering, Faculty of Engineering, USU. His research interests include microstrip antennas, electronic telecommunication, and radar.

Ismahayati Adam received the bachelor's degree in electrical-electronic and telecommunication engineering in 2006 and the M.Eng. degree in electronic telecommunication engineering in 2008 from Universiti Teknologi Malaysia (UTM). She received the Ph.D. degree in communication engineering from Universiti Malaysia Perlis, Malaysia, in 2018.

Since 2008, she has been with the Faculty of Electronic Engineering Technology, Universiti Malaysia Perlis (UniMAP) as a Lecturer. Her research interest includes antenna design, RF energy harvesting, mutual coupling, and wireless propagation.

Nurulazlina Ramli was born in Sri Aman, Sarawak, Malaysia, in 1984. She received theB.Eng. degree in electrical engineering (telecommunications) from the Universiti Teknologi Malaysia (UTM), Malaysia, in 2008. She pursued the M.Sc.degree in telecommunications and information engineering in 2011, and the Doctor of Philosophy degree in electrical engineering from Universiti Teknologi Mara (UiTM), Shah Alam, Malaysia, in 2015.She has been a Lecturer with the Faculty of Engineering, Built Environment, and Information Technology (FoEBEIT) at SEGi University, Malaysia, since September 2015. She is a Member of Institute of Electrical and Electronics Engineers (IEEE), a Graduate Member of the Institution of Engineers Malaysia (IEM), and a Registered Member of the International Association of Engineers (IAENG). Her research interests are in the areas of communication antenna design, reconfigurable/wearable antennas, electromagnetic radiation analysis, indoor/outdoor propagation modeling, dielectric resonator antenna, and wireless power transfers.

Hasliza A. Rahim received the bachelor's degree in electrical engineering from the University of Southern California, Los Angeles, CA, USA, in 2003, the master's degree in electronics design system from Universiti Sains Malaysia, Pulau Pinang, Malaysia, in 2006, and the Ph.D. degree in communication engineering from Universiti Malaysia Perlis, Perlis, Malaysia, in 2015.

Hasliza A. RahimIn 2006, she joined the Faculty of Electronic Engineering Technology, Universiti Malaysia Perlis (UniMAP), as a Lecturer, where she is currently an Associate Professor. She is a Chartered Engineer, Professional Technologist, Research Fellow with the Advanced Communication Engineering (ACE) Centre of Excellence and Head of Bioelectromagnetics Group under ACE. Her research interests include wearable and conformal antennas, metamaterials, antenna interaction with human body, on-body communications, green microwave absorbers, wireless body area networks, bioelectromagnetics, artificial intelligence (AI) optimization, and physical layer protocols for wireless communications.

Thennarasan Sabapathy received the B.Eng. degree in electrical telecommunication engineering from the Universiti Teknologi Malaysia, in 2007 and the M.Sc.Eng. degree from Multimedia University, Malaysia, in 2011. He pursued thePh.D. degree in communication engineering from Universiti Malaysia Perlis in 2014. He is currently an Associate Professor with the Faculty of Electronic Engineering Technology, Universiti Malaysia Perlis. His current research interests include antenna and propagation, millimeter-wave wireless communications, and fuzzy logic for wireless communications.

Mohd Natashah is a Senior Lecturer withthe Faculty of Electronic Engineering Technology (FTKEN), Universiti Malaysia Perlis (UniMAP), Malaysia. He received the bachelor's degree in electronic engineering from UniMAP, Malaysia, in 2008, theM.Sc.degree in microelectronics from Universiti Kebangsaan Malaysia (UKM), Malaysia, in 2011, and the Doctor of Engineering degree in sustainable energy and environmental engineering from Osaka University, Japan. He is active in volunteering work with IEEE Malaysia Section, acting as the Senior Member of IEEE and a committee member of the IEEE Malaysia Section Sensors and Nanotechnology Joint Councils Chapter. He is a member of the Institution of Engineering and Technology (IET), United Kingdom, Graduate Engineer of the Board of Engineers Malaysia (BEM), Malaysia, Chartered Engineer of the Engineering Council, United Kingdom, and Professional Technologist of the Malaysia Board of Technologist (MBOT), Malaysia.

SharizalA. Sobri is from the Faculty of Bioengineering and Technology, Universiti Malaysia Kelantan (UMK). He received the Ph.D. degree in mechanical engineering from the University of Manchester, U.K., and is currently one of the researchers in Advanced Material Research Cluster at the faculty. In January 2020, he was lucky to be chosen as a Fellow of CEO@FacultyProgramme 2.0 Cycle 3. He is proud that this time Huawei Malaysia has chosen him to fulfill his vision as an innovative leader. For six months, he was assigned to the Department of Public Affairs and Communication (PACD) and he had many incredible moments.

Analysis of a Sinusoidal Rotor Segments Axial Flux Interior Permanent Magnet Synchronous Motor with 120-degree Phase Belt Toroidal Windings

Yansong Wang[1], Wenbing Zhang[1*], Rui Nie[1], Jikai Si[1], Wenping Cao[2], and Yingsheng Li[3]

[1]Department of Electrical Engineering
Zhengzhou University, Zhengzhou 450001, China
wys1711@outlook.com, zwenbing@zzu.edu.cn*(corresponding author), ruinie1994@126.com,
sijikai@zzu.edu.cn

[2]Department of Electrical Engineering and Automation
Anhui University, Hefei 230601, China
19122@ahu.edu.cn

[3]Zhengzhou Runhua Intelligent Equipment Co., Ltd.
Zhengzhou 450004, China
xdlys@vip.sina.com

***Abstract* –** Axial flux permanent magnet (AFPM) motors are widely applied in many applications due to their performance advantages. A novel AFPM which owns a special winding form (120-degree phase belt toroidal windings) and a distinct rotor structure (sinusoidal rotor segments) is proposed in this paper to further improve the torque density of this kind of machine. First, the structure and working principle of the 120-degree phase belt toroidal windings sinusoidal rotor segments AFPM interior synchronous motor (120D-TWSRSAFPMISM) are clarified. Then, the design formula and crucial parameters of the motor are presented. Subsequently, the cogging torque is optimized by dividing the magnet grouping. Finally, the characteristics of the 120D-TWSRSAFPMISM are analyzed and compared with those of the traditional toroidal windings sinusoidal rotor segments AFPMISM (T-TWSRSAFPMISM) and another T-TW motor without the sinusoidal rotor segments (T-TWAFPMISM) by finite element method (FEM). The results show that the 120D-TW can significantly increase the back electromotive force (EMF) compared with the T-TW, and the sinusoidal rotor segments can increase the air-gap flux density compared with the traditional interior rotor. Therefore, the 120D-TW and sinusoidal rotor segments are combined in the AFPM motor. This combination can further increase the torque density compared with the contrast motors.

***Index Terms* –** 120-degree phase belt toroidal windings, axial flux permanent magnet (AFPM) motor, magnet grouping, interior motor, sinusoidal rotor segments, torque density.

I. INTRODUCTION

Axial flux permanent magnet (AFPM) motors are commonly used in various applications, including traction, power generation, and so on due to their flexible structure. Compared with the traditional permanent magnet motors, they have some noticeable benefits, such as higher power/torque densities, torque-to-weight ratios, geometrically higher aspect ratios, and so on. They have several alternative topologies, such as cored or coreless (slotted or slotless) or coreless stators, overlap or nonoverlap concentrated windings, and single or multiple rotors/stator [1–12]. By changing these alternatives to AFPM motors to improve torque density, it has become a hot spot on many researchers.

In the last few years, some topologies of AFPM motors have been proposed. For example, in [12], an AFPM motor with single stator and single rotor is proposed. It has the advantages of compact structure and small cogging torque, but it has the disadvantages of low torque density and insufficient mechanical strength. To solve this problem, the motor structure of single stator and double rotor has attracted many researchers' attention [13, 14]. In [13], a coreless AFPM motor with double rotors and single stator structure is proposed. Although it can effectively improve the torque density, its small air-gap flux, which needs to be improved to gain higher torque density. In [14], a new coreless axial flux interior permanent magnet synchronous motor with sinusoidal rotor segments is proposed. The sinusoidal rotor segmented structure is proposed to effectively improve the air-gap flux density of the interior motor by changing the rotor form, thus achieving the effect of improving

Submitted On: August 13, 2021
Accepted On: March 21, 2022

https://doi.org/10.13052/2022.ACES.J.370416

the torque density. However, it has the disadvantages of high copper loss due to its overlap winding structure, and the coreless structure limits further improvement of the torque density. Many researchers proposed the methods to reduce copper loss by varying slot configuration, change winding structure and displacement of conductors [15–17]. Meanwhile, to further improve the torque density by changing the stator core structure and winding form is a convenient and effective method.

The stator core structure is classified into slotted type and slotless type. In order to further improve the torque density, the slotted structure is selected. For the slotted motor, the winding form can be mainly divided into tooth-wound windings and core-wound windings (toroidal windings). In [17], a single stator and double rotor AFPM motor with tooth-wound windings and core-wound windings are compared and analyzed. It is shown that toroidal windings can save more copper, reduce copper loss, and improve efficiency. In order to further develop the advantages of toroidal windings, in [18], 120-degree phase belt toroidal windings (120D-TW) is proposed to increase torque density by increasing the amplitude of the back-EMF. If the sinusoidal rotor segments and 120-degree phase belt toroidal windings structures are combined with single stator and double rotor AFPM motors, it may further improve the torque density. Therefore, a 120-degree phase belt toroidal windings sinusoidal rotor segments AFPM interior synchronous motor (120D-TWSRSAFPMISM) is proposed and analyzed in this paper.

The paper is structured as follows. Section II introduces the motor structure, winding configuration, and operating principle of the proposed motor, the traditional toroidal windings sinusoidal rotor segments AFPMISM (T-TWSRSAFPMISM), and T-TW motor without the sinusoidal rotor segments (T-TWAFPMISM), and analyzes its structural advantages. Section III introduces the design formula and structural parameters of the motor. Section IV introduces an optimization method of permanent magnet grouping to reduce the cogging torque of the proposed motor and establishes a parametric model to obtain better structure parameters. Section V introduces the results of the 3D finite element analysis (3D-FEA). Finally, some conclusions are summarized in Section VI.

II. MOTOR STRUCTURE AND OPERATING PRINCIPLE

A. Motor structure

Figure 1 shows the structure of the proposed motors. Figure 1 (a) is the topology of the 120D-TWSRSAFPMISM. The proposed motor is an AFPM motor with single stator and double rotor. The stator is constructed with slotted and all windings are surrounded by toroidal on the stator yoke. The permanent magnet

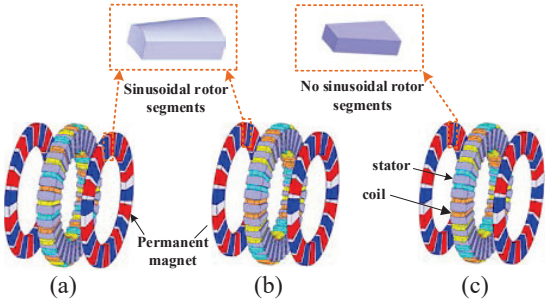

Fig. 1. Topology of the three motors. (a) 120D-TWSRSAFPMISM. (b) T-TWSRSAFPMISM. (c) T-TWAFPMISM.

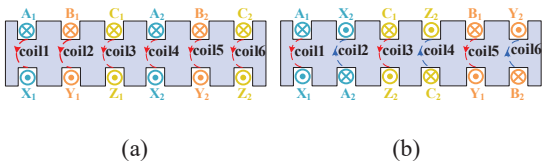

Fig. 2. Winding configurations of the two types. (a) 120-degree phase belt toroidal windings. (b) Traditional toroidal windings.

is inserted in two rotors with interior structure, which make the rotor like a wheel spoke. At the same time, the rotor is sinusoidal and divided by permanent magnet. Figures 1 (b) and (c) are proposed contrast motors: one is the T-TWSRSAFPMISM with sinusoidal rotor segment and other one is traditional toroidal windings interior permanent magnet axial flux permanent magnet synchronous motor (T-TWIPMAFPMSM) with no sinusoidal rotor segment.

B. Winding configuration

As shown in Figure 2, the winding configurations for the proposed motors are depicted. Figure 2 (a) is the winding configuration of the 120D-TWSRSAFPMSM. As can be seen from Figure 2 (a), the incoming line terminals (A, B, and C) of the 120D-TWSRSAFPMSM are all on the same side of the stator core and have the same winding direction. And its outcoming line terminals (X, Y, and Z) are all on the other side of the stator core. Figure 2 (b) is the winding configuration of contrast motors; its winding configuration is the traditional toroidal windings. And its positive side of coil and return side of coil are on either side of the stator.

Figure 3 shows the vector diagram of synthetic electromotive force (EMF) of the 1/5 model of 120D-TWSRSAFPMSM. As can be seen, the synthetic EMF of phases A, B, and C are all on the one side of the stator core, and synthetic EMF of phases X, Y, and Z are all on the other side of the stator core due to the special

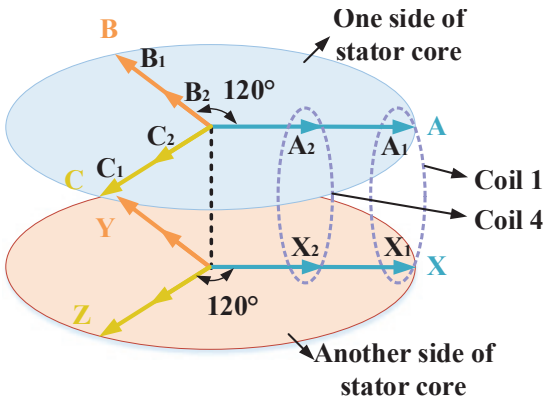

Fig. 3. Vector diagram of A-phase synthetic EMF of the 1/5 model of 120D-TWSRSAFPMSM.

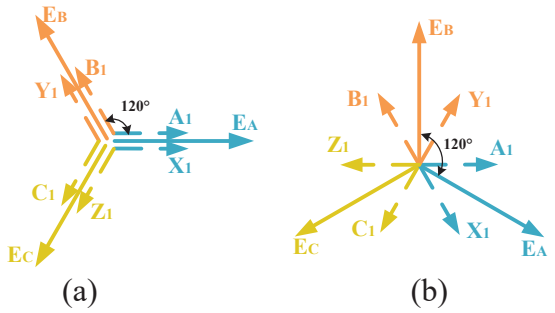

Fig. 4. Vector of diagram of EMF. (a) 120D-TW. (b) T-TW.

layouts of the novel toroidal windings. It should be noted that there is no space vector misalignment of coil-EMF, which can improve the synthetic EMF. After the three-phase symmetrical current is fed into the novel toroidal windings, both sides of the stator core will generate a rotating magnet field with the identical direction. Then the two rotors will rotate synchronously under the interaction between the armature field and permanent magnets field.

At the same time, the winding factor of the three winding types needs to be analyzed, which further illustrates the advantages of 120D-TW. First, the formula of winding factor is given by

$$K_n = K_d \times K_q, \tag{1}$$

where K_d is pitch-shortening factor, K_q is distribution factor, and K_n is winding factor.

The K_q can be expressed as

$$K_q = \frac{\sin\frac{q\alpha}{2}}{q\sin\frac{\alpha}{2}} \left(q = \frac{z}{2pm}, \alpha = \frac{p\times 360}{z}\right), \tag{2}$$

where z is stator slot number, p is pole pairs, and m is phase number. From the above formula, the distribution factor is related to the number of coils in the unit motor. Both the motor and the comparison motor are concentrated windings; so it is known that the distribution factor K_q is 1.

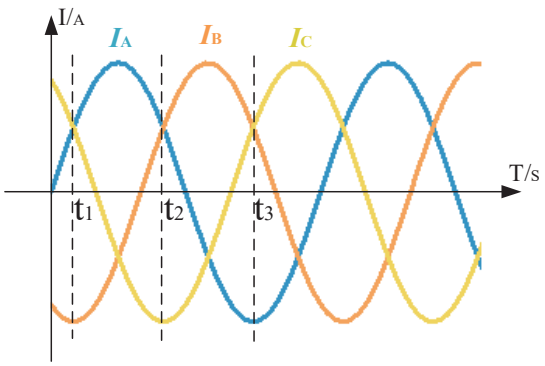

Fig. 5. Three-phase current I_A I_B, and I_C.

The K_d can be calculated by

$$K_d = \frac{1}{N}\sum_{k=1}^{N} e^{-j\theta_k}, \tag{3}$$

where N is the number of synthetic EMF for each phase EMF, and θ_k is the electrical degrees between the synthetic EMF. It can be seen from Figure 3 that the advantage of 120D-TW is that the angle between the coil$_1$ and coil$_4$ is 0°; then EMF of phase A is derived from the formula

$$\dot{e}_{A120D}(t) = \dot{e}_{coil1}(t) + \dot{e}_{coil4}(t). \tag{4}$$

According to formula (3), the formula of pitch-shortening factor K_{d1} of 120D-TW is given by

$$K_{d1} = \frac{1}{N}\sqrt{(1+\cos\theta_k)^2+\sin^2\theta_k}\,. \tag{5}$$

It shows that the pitch-shortening factor of 120D-TW of K_{d1} is 1. For the same reason and it can be seen that the angle between the coil$_1$ and coil$_2$ is 120 electrical degrees, the A phase EMF of the traditional toroidal winding is derived from the formula

$$\dot{e}_{ATW}(t) = \dot{e}_{coil1}(t) - \dot{e}_{coil2}(t) \tag{6}$$

$$K_{d2} = \frac{1}{N}\sqrt{(1-\cos\theta_k)^2+\sin^2\theta_k}\,. \tag{7}$$

It shows that the pitch-shortening factor of traditional toroidal winding of K_{d2} is 0.87. According to formula (1), the winding factors of 120D-TW and T-TW are 1 and 0.87, respectively. The winding factor of 120D-TW is 14.94% higher than that of T-TW, which means the 120D-TW has the ability to gain a higher back-EMF.

C. Operating principle

Figure 5 shows three moments of the three-phase current. Because the winding forms of the two contrast motors are the same (T-TW), only the armature magnetic field of one motor can be drawn. At the t_1, t_2, t_3 moments, the armature magnetic field of the 120D-TW and the T-TW is shown in Figure 6.

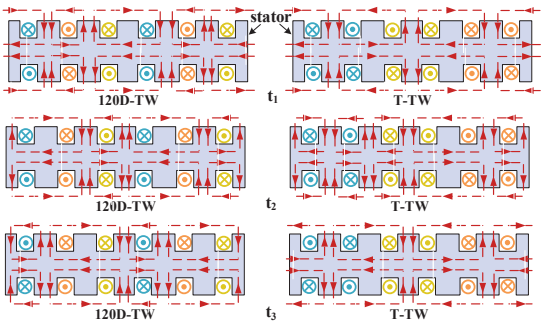

Fig. 6. The t_1, t_2, and t_3 moments of armature magnetic field.

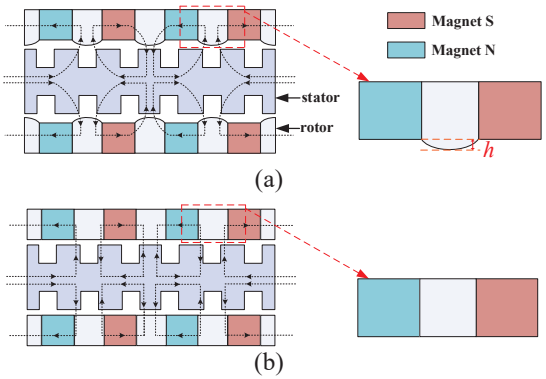

Fig. 7. Flux distribution of two rotor types. (a) Sinusoidal rotor segments. (b) Interior permanent magnet.

Figure 7 shows the 1/5 model of the rotor structure of the proposed motor and the contrast motor, respectively. Figure 7 (a) is a sinusoidal rotor segments structure adopted by 120D-TWSRSAFPMSM and T-TWSRSAFPMSM, and Figure 7 (b) is an interior permanent magnet structure by T-TWIPMAFPMSM. It can be seen that the permanent magnets of the two rotors are embedded in the rotor and distributed along the axial direction, and the permanent magnets of the same axial direction have the same polarity. Two strands of flux wire driven by permanent magnets inside the two rotors through the air gap, winding, and stator core. It can be seen that the sinusoidal rotor segment is compared with the interior permanent magnet, and the magnetic lines of the former converge toward the sinusoidal type rotor, while the latter diverges. It is shown that the sinusoidal rotor segments have the function of converging magnetic lines; so it can increase the air-gap flux density.

III. DESIGN OF THE PROPOSED MOTOR

The main design equations of the proposed motor are presented in this section.

The AFPM diameter ratio is defined as

$$D_o = \left[P_R / K_L \eta B_g A \frac{f}{p} \left(1-\lambda^2\right) \frac{1+\lambda}{2} \right]^{1/3}, \quad (8)$$

where D_i is the inner diameter, D_o is the outer diameter of the motor, λ is the ratio of D_i to D_o, P_R is the output power, A is the electrical loading, B_g is the air-gap flux density, and K_L is a constant incorporating winding factors. However, the winding form of 120D-TW is different from T-TW; the electrical load formula needs to be redefined. As shown in Figure 2, the windings of 120D-TW are winding in the same direction, similar to only out, and T-TW are winding in two directions, similar to in and out, resulting in the change in the number of series turns per phase; so the electric loading calculation formula should be changed accordingly.

The electric loading formula for the 120-degree phase belt toroidal windings is given by

$$A = mN \frac{2I_{rms}}{\pi(D_i+D_o)}. \quad (9)$$

The electrical load formula for the traditional toroidal windings is given by

$$A = mN \frac{I_{rms}}{\pi(D_i+D_o)}, \quad (10)$$

where N is the number of series turns per phase, and I_{rms} is current effective value. However, because the number of series turns per phase changes, the peak value of back-EMF formula also needs to change.The EMF for the 120-degree phase belt toroidal windings is given by

$$E_{pk} = K_n N B_g \frac{f}{p} \left(1-\lambda^2\right) {D_o}^2. \quad (11)$$

The EMF for the traditional toroidal windings is given by

$$E_{pk} = 2K_n N B_g \frac{f}{p} \left(1-\lambda^2\right) {D_o}^2. \quad (12)$$

The motor design is completed based on these fundamental sizing equations, and the initial motor design data are obtained. Then, contrast motors design is carried out by the same rotor D_o and the same amount of magnet volume. To verify the reasonability of the proposed motor, the 120D-TWSRSAFPMSM is compared with the contrast motors. The design of the three motors needs to follow some rules to ensure a fair comparison.

(1) The three motors have the same dimensions, including outer diameter and inner diameter of the stator and rotors, axial length, thickness of permanent magnet, and so on.
(2) The three motors are excited by a same current source and have the same materials.

Based on the principles above, the primary parameters of the 120D-TWSRSAFPMSM and contrast motors are presented in Table 1.

Table 1: Primary parameters of three motors

Parameters	120D-TWSRSAFPMSM	T-TWSRSAFPMSM	T-TWPMBAFPMSM
Rated speed	800 r/min	800 r/min	800 r/min
No. of phase	3	3	3
No. of poles	20	20	20
No. of winding coils	30	30	30
Turns of per coil	14	14	14
Outer diameter of stator core	148.0 mm	148.0 mm	148.0 mm
Inner diameter of stator core	100.0 mm	100.0 mm	100.0 mm

IV. OPTIMIZATION ANALYSIS

According to the primary parameters of the three motors presented in Table 1, first, the influence of sinusoidal rotor segments on the cogging torque is determined. Then, because all three motors are slotted, the cogging torque needs to be optimized. In this part, the magnet grouping division is used to reduce the cogging torque and establish a parametric model to obtain and analyze the results.

A. Sinusoidal rotor segments affect about cogging torque

Because both 120D-TWSRSAFPMSM and T-TWSRSAFPMSM adopt the rotor structure of the sinusoidal rotor segments, we need to determine the parameter about h of the rotor segment, then the parametric model can be established, which is shown in Figure 7 (a). Because the sinusoidal rotor parameter h has a great impact on the cogging torque and torque density. The simulation results are shown in Figure 8. Figure 8 (a) shows that when h is in 1 mm, the cogging torque is at turning point. Figure 8 (b) illustrates the influence of h on the fundamental harmonic and total harmonic distortion (THD) of air-gap flux density. It can be seen that with the increase of h, the fundamental harmonic and THD of air-gap flux density also gradually increase. With the increase of the parameter h, the fundamental harmonic of air-gap flux density and the cogging torque will be definitely increased. Accordingly, h is selected as 1 mm for increasing the torque output and reducing the cogging torque as much as possible.

B. Cogging torque optimization

Cogging torque is caused by interaction between magnets and stator slots. In other words, cogging torque is caused by the variation of the magnetic energy of the field due to the PM with the mechanical angular position of the rotor. Reducing cogging torque component is vital in PM motor design process especially at low speed and direct-drive applications.

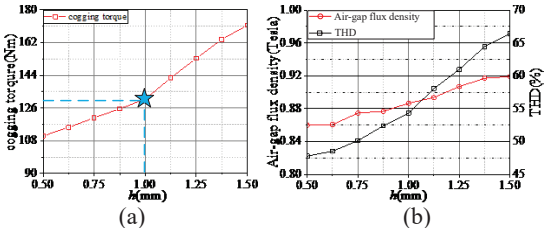

Fig. 8. Effect of the parameter h change on the sinusoidal rotor segments. (a) Cogging torque. (b) Fundamental harmonic of air-gap flux density and THD.

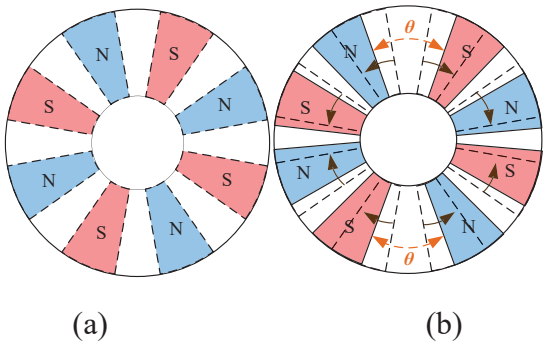

Fig. 9. Division of the permanent magnets into two groups. (a) Before the group. (b) After the group.

In addition, the proposed motor inevitably has cogging torque due to the slotted structure [19]. The dissatisfactory torque ripple may be obtained due to the cogging torque. Therefore, the torque ripple needs to be optimized. In [20], an optimization method for magnet grouping is proposed to reduce the cogging torque. It shows that by moving the permanent magnet and grouping it, an asymmetric air-gap magnetic density is formed, which can greatly reduce the cogging torque. At the same time, the avoidance of the irregular permanent magnet shape reduces the manufacturing difficulty of the permanent magnet.

This technique is illustrated in Figure 9 for a grouping method for a multipolar motor. By moving the permanent magnet and grouping it, forming an asymmetric air-gap magnetic density can greatly reduce the cogging torque. At the same time, the avoidance of the irregular permanent magnet shape reduces the manufacturing difficulty of the permanent magnet. The parameterization model of the motor is shown in Figure 10. It can be seen that the grouping angle is 10.5°, and the cogging torque ripple is 9.2%, which is the lowest in this data compared with other angles.

V. CHARACTERISTICS ANALYSIS

According to the primary parameters of the three motors presented in Table 1 and the result of optimiza-

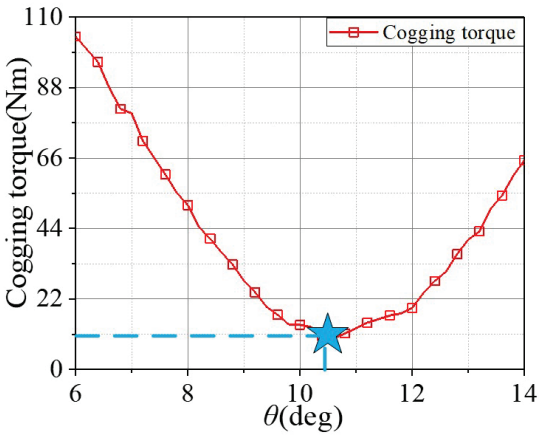

Fig. 10. Effect of the parameter θ change on the cogging torque ripple.

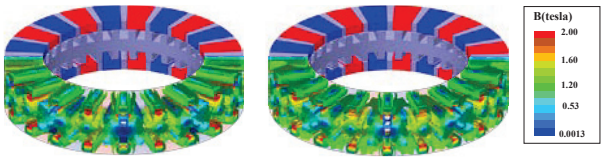

Fig. 11. No-load flux graph of motor. (a) Sinusoidal rotor segments. (b) Interior permanent magnet.

tion analysis, the 3D model of the three motors are established by 3D FEA software (ANSYS Maxwell). Subsequently, the operating characteristics under no-load and load conditions are analyzed, respectively.

A. No-load characteristics

Figure 11 shows the no-load flux graph of the two structures. It can be seen that the stator of two structures both have higher flux density in their teeth. However, the flux density of the stator core of the two structures is 1.41 T, and no magnetic saturation occurs

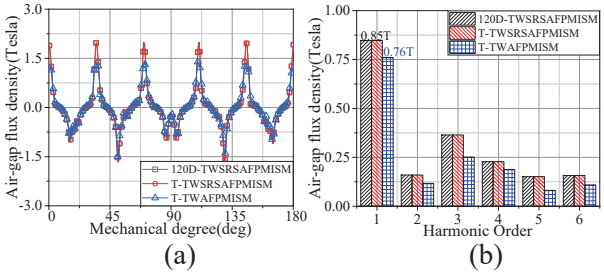

Fig. 12. Air-gap flux density and its harmonics distribution of the three motors under no-load condition. (a) Air-gap flux density. (b) Harmonics distribution.

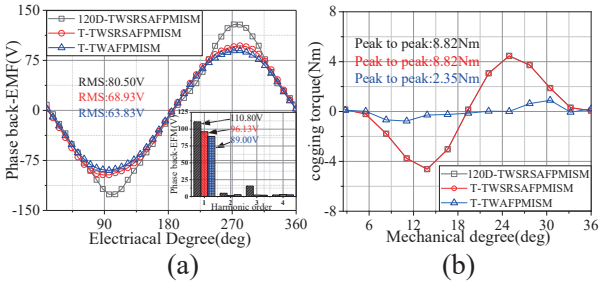

Fig. 13. (a) Back-EMF waveforms and its harmonics distribution of the three motors under no-load condition. (b) Cogging torque of the three motors.

Table 2: No-load characteristics of three motors

Parameters	120D-TWSRSAFPMISM	T-TWSRSAFPMISM	T-TWPMBAFPMISM
RMS of the back-EMF	80.50 V	68.93 V	63.83 V
Fundamental harmonic of the back-EMF	110.80 V	96.13 V	89.00 V
Total harmonic distribution (THD)	12.04%	5.09%	5.33%
Peak-to-peak value	8.82 Nm	8.82 Nm	2.35 Nm
No-load flux graph of the stator core	1.40 T	1.40 T	1.40 T

in the stator core. The air-gap flux density and its harmonics distribution of the three motors under no-load condition are presented in Figure 12. It can be seen from Figure 12 (a) that the air-gap flux density curve in the 120D-TWSRSAFPMISM is basically the same as that in the T-TWSRSAFPMISM, which is higher than T-TWAFPMISM. As shown in Figure 12 (b), the amplitudes of the fundamental harmonic of the air-gap flux density in the 120D-TWSRSAFPMISM and T-TWSRSAFPMISM are both 0.85 T, and the T-TWAFPMISM is 0.76 T. It can be seen that the first two increased by 11.84% compared with the latter, which can be seen that sinusoidal rotor segments can effectively increase flux density.

The no-load back-EMF, harmonics distribution, and cogging torque of the three motors are presented in Figures 13 (a) and (b), respectively. Comparative analysis results of the three motors are shown in Table 2. As shown in Table 2, it can be seen that the amplitudes of the fundamental harmonic of the back-EMF of the 120D-TWSRSAFPMISM are increased by 15.26% and 24.49% compared with the T-TWSRSAFPMISM and T-TWAFPMISM. In formula (8), it can be seen that the

Table 3: On-load characteristics of three motors

Parameters	120D-TWSRSAFPMSM	T-TWSRSAFPMSM	T-TWPMBAFPMSM
Average torque	113.67 Nm	98.38 Nm	91.67 Nm
Torque per ampere	2.84 Nm/A	2.46 Nm/A	2.29 Nm/A
Average torque density	25.43 kNm/m^3	22.01 kNm/m^3	20.51 kNm/m^3
Torque ripple	14.71%	17.10%	7.33%
Output power	9.52 kW	8.24 kW	7.68 kW

back-EMF is related to the winding coefficient K_n and the air-gap flux density B_g. Because the sinusoidal rotor segments can effectively improve the air-gap flux density, and combined with the advantages of high winding coefficient of 120D-TW, the fundamental harmonic of the back-EMF of 120D-TWSRSAFPMISM is greatly increased. And it is consistent with the analysis of the vector diagram of A-phase synthetic EMF of the three motors.

As shown in Table 2, the cogging torque of 120D-TWSRSAFPMISM and T-TWSRSAFPMISM are nearly the same, and the peak-to-peak values of both are 8.82 Nm. The cogging torque of T-TWAFPMISM is the smallest, and its peak-to-peak value is only 2.35 Nm. Compared with T-TWAFPMISM, the cogging torques of 120D-TWSRSAFPMISM and T-TWSRSAFPMISM both increased. Because the sinusoidal rotor segments structure increases the air-gap flux density, which also affects the cogging torque.

B. On-load characteristics

The torque curve and torque-current characteristic of the three motors are presented in Figures 14 (a) and (b), respectively. Comparative analysis results of the three motors are shown in Table 3.

As shown in Table 3, compared with the T-TWSRSAFPMISM and T-TWAFPMISM, the torque density of the 120D-TWSRSAFPMISM has increased by 15.54% and 24.0%, which can be seen that combining 120D-TW with sinusoidal rotor segments in the proposed motor can further improve torque density. And in Figure 14 (b), it shows the torque-current characteristic of three motors. As can be seen, within the whole current range, the 120D-TWSRSAFPMISM always has much higher average torque than the T-TWSRSAFPMISM and T-TWAFPMISM.

VI. CONCLUSION

In this paper, a 120D-TWSRSAFPMISM is proposed and presented. The structure and working principle of the proposed motor are defined. The cogging torque of the motor is reduced by dividing the permanent magnets into two groups and the 3D finite element

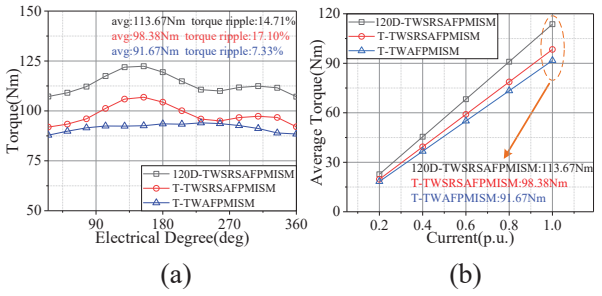

Fig. 14. (a) Torque curve of three motors at the same current. (b) Torque-current characteristic of three motors.

model of 120D-TWSRSAFPMISM and contrast motors are established. The no-load and load characteristics of the 120D-TWSRSAFPMISM are compared with contrast motors, which are designed with the same effective size.

In 120D-TWSRSAFPMISM, 120D-TW is combined with sinusoidal rotor segments. The difference between 120D-TW and T-TW lies in that the coil-EMF of 120D-TW has no space vector misalignment; so 120D-TW makes the amplitude of back-EMF increase by 14.94% compared with T-TW. The difference between sinusoidal rotor segments and traditional interior rotor is that the structure of sinusoidal rotor segments is sinusoidal, so that the flux field converges to the same place, making the air-gap flux density of structure sinusoidal rotor segments increase by 11.84% compared with the structure of traditional interior rotors. The simulation results show that the torque density of 120D-TWSRSAFPMISM increases by 15.54% and 24% compared with T-TWSRSAFPMISM and T-TWAFPMISM. Thus, the combination of the two structures in the proposed motor makes the torque density of the motor further improve compared with that of one structure.

ACKNOWLEDGMENT

This work is partially supported by Natural Science Foundation of China under Grant 51777060 and the China Postdoctoral Science Foundation under Grant 2020M682342, and in part by the Major Special Project for Collaborative Innovation in Zhengzhou under Grant 20XTZX12023.

REFERENCES

[1] F. Zhao, T. A. Lipo, and B. Kwon, "A novel dual-stator axial-flux spoke-type permanent magnet vernier machine for direct-drive applications," *IEEE Transactions on Magnetics*, vol. 50, no. 11, pp. Art ID. 8104304, Nov. 2014.

[2] V. Rallabandi, N. Taran, D. M. Ionel, and J. F. Eastham, "Coreless multidisc axial flux pm machine with carbon nanotube windings," *IEEE*

Transactions on Magnetics, vol. 53, no. 6, pp. Art ID. 8102904, Jun. 2017.

[3] X. Luo, S. Niu, and W. N. Fu, "Design and sensorless control of a novel axial-flux permanent magnet machine for in-wheel applications," *IEEE Transactions on Applied Superconductivity*, vol. 26, no. 7, pp. Art ID. 0608105, Oct. 2016.

[4] T. Rodrigo, D. S. Daniel, R. Oscar, and P. Rodrigo, "Dynamic modeling and parametric analysis of the magnetic stiffness on a radial heteropolar rotor magnetic bearing (RMB)," *Journal of Electrical and Computer Engineering Research*, vol. 1, no. 1, pp. 9-14, Jun. 2021.

[5] B. Rezaeealam and F. Rezaeealam, "Optimization of permanent magnet synchronous motors using conformal mappings," *Applied Computational Electromagnetic Society (ACES) Journal*, vol. 32, no. 10, pp. 915-923, Oct. 2017.

[6] G. D. Liu, Y. Z. Wang, X. P. Xu, W. Y. Ming, and X. Zhang,"The optimal design of real time control precision of planar motor," *Applied Computational Electromagnetic Society (ACES) Journal*, vol. 32, no. 10, pp. 948-954, Oct. 2017.

[7] J. L. Zhao, X. W. Quan, X. D. Sun, J. Li, and M. Y. Lin, "Design of a novel axial flux rotor consequent-pole permanent magnet machine," *IEEE Transactions on Applied Superconductivity*, vol. 30, no. 4, pp. Art ID. 5205506, Jun. 2020.

[8] J. Wang, X. Yuan, and K. Atallah, "Design optimization of a surface-mounted permanent-magnet motor with concentrated windings for electric vehicle applications," *IEEE Transactions on Vehicular Technology*, vol. 62, no. 3, pp. 1053-1064, Mar. 2013.

[9] H. Li, Z. Q. Zhu, and H. Hua, "Comparative analysis of flux reversal permanent magnet machines with toroidal and concentrated windings," *IEEE Transactions on Industrial Electronics*, vol. 67, no. 7, pp. 5278-5290, Jul. 2020.

[10] N. Taran, G. Heins, and D. M. Ionel, "Coreless and conventional axial flux permanent magnet motors for solar cars," *IEEE Transactions on Industry Applications*, vol. 54, no. 6, pp. 5907-5917, May 2018.

[11] B. Zhang, T. Seidler, R. Dierken, and M. Doppelbauer, "Development of a yokeless and segmented armature axial flux machine," *IEEE Transactions on Industrial Electronics*, vol. 63, no. 4, pp. 2062-2071, Apr. 2016.

[12] J. H. Choi, J. H. Kim, D. H. Kim, and Y. S. Bake, "Design and parametric analysis of axial flux PM motors with minimized cogging torque," *IEEE Transactions on Magnetics*, vol. 45, no. 6, pp. 2855-2858, Jun. 2009.

[13] Y. Zhang, N. Liu, S. Guo, J. Tong, and Q. Zhou, "Analysis and design of ironless axial flux permanent magnet synchronous motor," *IEEE 2018 10th International Conference on Intelligent Human-Machine Systems and Cybernetics.*, Hangzhou, China, pp. 170-173, Aug. 2018.

[14] M. Aydin and M. Gulec, "A new coreless axial flux interior permanent magnet synchronous motor with sinusoidal rotor segments," *IEEE Transactions on Magnetics*, vol. 52, no. 7, pp. Art ID. 8105204, Jul. 2016.

[15] M. Popescu and D. G. Dorrell, "Skin effect and proximity losses in high speed brushless permanent magnet motors," *IEEE Energy Conversion Congress and Exposition*, Denver, CO, USA, pp. 3520-3527, Sep. 2013.

[16] A. S. Thomas, Z. Q. Zhu, and G. W. Jewell, "Proximity loss study in high speed flux-switching permanent magnet machine," *IEEE Transactions on Magnetics*, vol. 45, no. 10, pp. 4748-4751, Oct. 2009.

[17] G. D. Donato, F. G. Capponi, and F. Caricchi, "Fractional-slot concentrated-winding axial-flux permanent-magnet machine with core-wound coils," *IEEE Transactions on Industry Applications*, vol. 48, no. 2, pp. 630-641, Apr. 2012.

[18] C. X. Gao, M. Z. Gao, J. K. Si, Y. H. Hu, and C. Gan, "A novel direct-drive permanent magnet synchronous motor with toroidal windings," *Energies*, vol. 12, no. 3, pp. Art ID. 432, Feb. 2019.

[19] W. Cheng, G. Gao, Z. Deng, L. Xiao, and M. Li, "Torque comparison between slotless and slotted ultra-high speed AFPM motors using analytical method," *IEEE Transactions on Magnetics*, vol. 58, no. 2, pp. Art ID. 8101805, May 2021.

[20] M. Gulec and M. Aydin, "Influence of magnet grouping in reduction of cogging torque for a slotted double-rotor axial-flux PM motor," *IEEE International Symposium on Power Electronics Power Electronics, Electrical Drives, Automation and Motion*, Sorrento, Italy, pp. 812-817, Aug. 2012.

Yansong Wang received the B.S. degree in automation from the Harbin University of Science and Technology in 2019. He is currently working toward the M.S. degree with the School of Electrical Engineering of Zhengzhou University, Zhengzhou, Henan.

His research interests include design, analysis, and control of axial-flux permanent magnet motors.

Wenbing Zhang (Non-member) majored in computer application from Nanjing Power Higher Specialized School, Nanjing, China, in 1994, and received the B.S. degree in computer science and technology from Zhengzhou University, Zhengzhou, China, in 2000.

His main research interests include numerical simulation and computation.

Rui Nie received the B.S. degree in electrical engineering from Henan Polytechnic University, Jiaozuo, China, in 2015, and the Ph.D. degree in electrical engineering from the China University of Mining and Technology, Xuzhou, China, in 2020. She is currently doing post-doctoral research at Zhenzhou University.

Her current research interests include linear motor design and control and renewable energy generation technology.

Jikai Si (Member, IEEE) received the Ph.D. degree in 2008 from the School of Information and Electrical Engineering, China University of Mining and Technology, Xuzhou, China, in 2008.

He is currently a Distinguished Professor with Zhengzhou University. His main research interests include the theory, application, and control of special motor. He has authored and co-authored over 160 technical papers in these areas. Prof. Si is a Member of the Green Motor System Professional Committee, China.

Wenping Cao (Senior Member, IEEE) received the B.Eng. degree in electrical engineering from Beijing Jiaotong University, Beijing, China, in 1991, and the Ph.D. degree in electrical machines and drives from the University of Nottingham, Nottingham, U.K., in 2004.

He was a Chair Professor of electrical power engineering and the Head of the Power Electronics, Machines, and Power System Group, Aston University, Birmingham, U.K. He is currently a Distinguished Professor with Anhui University, Hefei, China.

Yingsheng Li currently works in Zhengzhou Runhua Intelligent Equipment Co., Ltd, and is the legal representative of Zhengzhou Runhua Intelligent Equipment Co., Ltd. His research interests include the application, control of motor, and power electronics converters and control, and electrical motor drives.